Linking carbon and iron cycles by investigating transport, fate and mineralogy of iron-bearing nanoparticles and colloids from peat-draining rivers - Scotland as a model for high-latitude rivers

Deborah Anne Wood

January 2020

A thesis submitted for the degree of

Doctor of Philosophy

Biological and Environmental Sciences, Faculty of Natural Sciences

University of Stirling

Declaration of authorship

I, Deborah Anne Wood, declare that this thesis has been composed by me and it embodies the results of my own research. Where appropriate I have acknowledged the nature and extent of work carried out in collaboration with others.

……

Deborah Anne wood

20/10/2020

Abstract

Iron plays an integral role in ocean biogeochemistry, regulating carbon transport and sequestration, and primary productivity via particulate phases. These particulate phases comprise nanoparticles and colloids that range in size below the traditional operational filter cut-off of 0.45 μm for 'dissolved' species. This means they are difficult to characterise mineralogically and often neglected as 'dissolved iron'. Studies have investigated the covariation of iron with organic matter and the way that iron is transported from freshwater to saline systems. However, there remains a lack of understanding of the transport mechanisms. This understanding is imperative if we are to successfully apply iron biogeochemistry to climate models and begin to elucidate the role of iron in the environment. Therefore, there are ongoing efforts to find a reliable method to provide a mechanistic understanding of the transport of terrestrial, iron-bearing colloids and nanoparticles to the oceans.

In their comprehensive 2012 review of the iron biogeochemical cycle, Raiswell and Canfield urge that we adopt a more mineralogical view to define the role of colloids and nanoparticles in aquatic (freshwater and marine) environments. The aim of my project was to develop a novel method using synchrotron-based Mössbauer techniques to investigate the speciation and mineralogy of iron in the nanoparticle and colloidal components of river and coastal waters. A cascade of filtering techniques was used to isolate these particles, to enable their quantification and characterisation. Here, I present an evaluation of these techniques for their applicability, and the results of the first successful SMS measurements, conducted at the European Synchrotron Radiation Facility, Grenoble (ID18, Nuclear Resonance Beamline).

Acknowledgements

I am grateful to every person that has contributed to the completion of this thesis. There are indeed many of you.

Firstly, thank you to my supervisor, Christian Schröder, for his constant support, advice and sustained reassurance. And, for giving me this opportunity in the first place. I am forever grateful. Thank you to my other supervisors, Clare Wilson, Kirsty Crocket and Marc Stutter, for their continued support and advice. To Laura Hepburn, who has helped me so much in the field, the lab, over the phone, via email and over a beer or two. I would also like to thank the technicians. James for being an immense support whilst I got ready for the synchrotron, Ronnie - for everything you do, Stuart - for keeping my dosimeter up to date, Lorna, Ian, Sylvia, Pauline and Scott for all your support and advice, and Billy (Aquaculture) for bearing with me through my many questions and analyses.

To all my fellow students, past and present: Amanda (for chats at least every second day), Jess, Kat, Izzy, Matt, Kathleen, Pete, Tom…all the PhD folks. I have no words – you are all amazing and I hold you all as very dear friends - thank you! My list of thanks is huge. I am indebted to everyone at ID18 at the European Synchrotron Radiation Facility, to Roland Bol and everyone at IBG-3, Forschungszentrum Jülich, to the folks at SAMS, The Lyell Centre and JHI. I was also extremely grateful for the funding and support I received from The Scottish Alliance for Geoscience, Environment and Society (SAGES), the Marine Alliance for Science and Technology Scotland (MASTS), Stirlingshire Educational Trust, IBG-3 at Forschungszentrum Jülich, ERSF and The University of Stirling.

Thank you to my family. Mum and Dad, Chelsea, Hope, Allan, Mikey and of course, Frank the dog – my writing companion. Thank you for supporting me in more ways than I can say and for listening to me when I needed an ear, and for bailing me out when my funds ran dry. I am forever grateful to you all. Oh, and thank you to tea, coffee, chocolate and red wine!

Contents

Figures

Tables

1. Introduction

1.1 Iron in natural water environments

Iron is the 4th most abundant element in the Earth's crust. However, despite iron's ubiquity and its requirement by marine and terrestrial organisms as an essential nutrient, it is often found in forms which are not readily available for biological uptake (Pérez-Guzmán et al., 2010). Iron plays a key role in climate regulation and understanding of its role in the "biological pump" calls for a continued effort to understand its delivery to marine environments and relationships with the carbon and other element cycles. Intrinsically linked to primary biological productivity in the ocean, iron has the ability to influence its relationship with the biological carbon pump and removal of CO_2 from the atmosphere (Figure 1.1) (Breitbarth et al., 2010, Hendy, 2015, Tagliabue et al., 2017, Martin, 1990). Ocean iron inputs include, atmospheric dust (Hochella et al., 2008, Jickells et al., 2005, Mahowald et al., 2005), hydrothermal inputs (Yücel et al., 2011), diffusive fluxes from deep-sea sediments (Raiswell, 2006), submarine groundwater discharge (Charette and Sholkovitz, 2002), continental shelves (von der Heyden et al., 2012, De Jong et al., 2012, Jeandel et al., 2011), rivers (Hirst et al., 2017, Pokrovsky, 2016, Krachler et al., 2015, Yang et al., 2017, Zhu et al., 2017), glacial sediment , sea ice (Hawkings et al., 2014, Lannuzel et al., 2016) and permafrost melt (Salvadó et al., 2015). These inputs of iron to the global oceans are subject to changes in flux as climate changes (Hendy, 2015).

Martin (1990) proposed that the addition of iron to high-nutrient, low chlorophyll (HNLC) regions (low in iron) may stimulate phytoplankton growth, driving glacial-interglacial CO_2 change. Studies of both natural and artificial iron fertilisation of the oceans have since demonstrated that the low bioavailability of iron to phytoplankton can limit photosynthesis in HNLC (high-nutrient, low-chlorophyll) areas of the oceans, thereby influencing atmospheric CO_2 (Hendy, 2015, Salter et al., 2014). Although this clearly demonstrates the linkages between the bioavailability of iron to marine primary producers and the carbon cycle, the complexities of iron delivery to marine

environments and its relationship with the carbon cycle are still poorly understood (Lauderdale et al., 2020, Hirst et al., 2017).

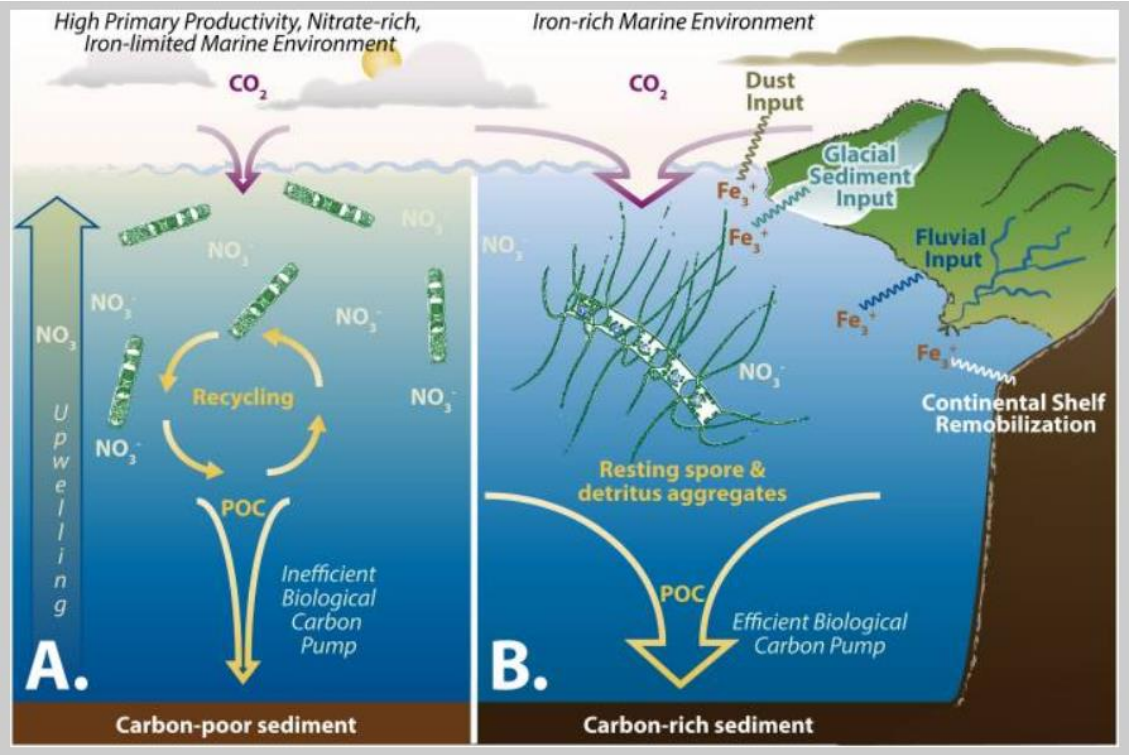

Figure 1.1. Iron and the global biological carbon pump: Iron plays a key role in the biological carbon pump. Iron availability affects primary productivity and the ocean's ability to remove CO_2 from the earth's atmosphere. A) In high primary productivity, nitrate-rich marine environments, where iron is limiting, silicified diatoms in the waters near the ocean's surface are recycled easily. This has a limiting effect on the efficiency of the biological pump. B) In iron-rich marine environments the diatom communities are composed of larger diatoms which form large chains with the ability to aggregate and sink, transferring carbon to the sea floor, enhancing the efficiency of the biological carbon pump (Hendy, 2015).

Resolving the speciation, mineralogy and particle size all play an integral part both in the understanding of the bioavailable fraction and the behaviour of more recalcitrant phases. Wells and Goldberg (1994) suggested that to begin to understand ocean biogeochemical cycling (of iron,

carbon and other element cycles) it is necessary to probe the chemical behaviour of physical size fractions (soluble, colloidal and particulate) in sea water and Raiswell and Canfield (2012) state that if we are to better understand the role of iron in oceans it is imperative to better characterise iron mineralogy within these size fractions. Combining both the influence of size effects and knowledge of iron mineralogy should therefore further our understanding of iron transport mechanisms and associations with other element cycles.

1.2 Iron bearing nanoparticles and fine colloids in the water environment: the operationally defined dissolved fraction

"*Mineralogy has only been peripheral in this research agenda but understanding the role of iron (oxyhydr)oxides requires that it assume a leading role*" (Raiswell & Canfield, 2012).

Iron (oxyhydr)oxide aggregates have been shown to be important in the biogeochemical iron cycle. In natural water environments, reactive iron phases exist as suspended nanoparticles and colloids. These particles are generally amorphous, making them difficult to characterise using conventional geochemical techniques (Caraballo et al., 2015, Hochella et al., 2008, Von Der Heyden et al., 2019). Additionally, their increasingly dilute nature as salinity increases in coastal and ocean environments further hinders mineralogical investigation (von der Heyden et al., 2012, Schröder et al., 2016). Subsequently, iron-bearing nanoparticles and colloid interactions in natural waters can often be underestimated, misunderstood or completely overlooked as they are often included in the operationally defined dissolved fraction and reported as bulk interactions. Raiswell and Canfield (2012) have shown that these definitions are not discrete and colloidal/particulate iron exists along a size continuum, where environmental iron-organic matter (Fe-OM) bearing colloids are likely to exist even in the operationally defined aqueous range (Figure 1.2).

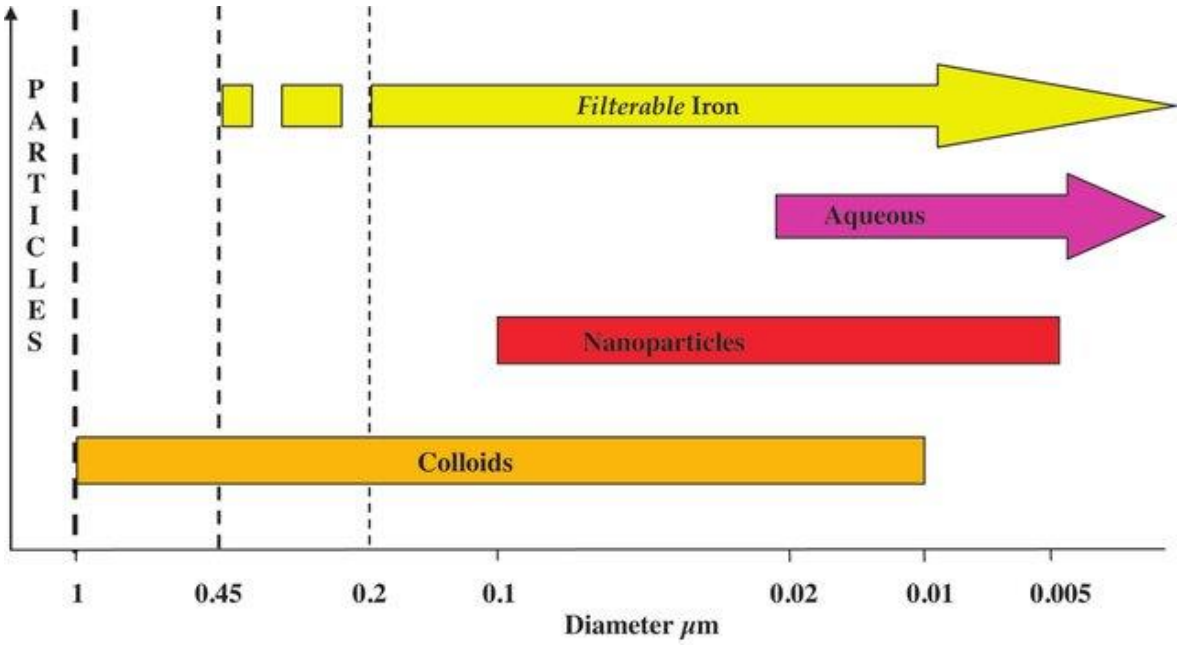

Figure 1.2. Particle size ranges: colloids, nanoparticles and aqueous species (Raiswell and Canfield 2012). Iron bearing particle size ranges are described on a continuum, with colloids and nanoparticles still being observable within the 'truly dissolved' (soluble) fraction i.e. below 0.02 μm.

The dissolved fraction contains other defined particle sizes: colloids, nanoparticles (less than 100 nm in one dimension) and aqueous species (Pokrovsky et al., 2014). The properties of the nanoparticulate iron phases very often differs from their bulk state as reactivity changes as a function of particle size (Figure 1.3) (Hochella et al., 2008, Wigginton et al., 2007, Caraballo et al., 2015). Studies of both natural and manufactured nanoparticles have advanced our understanding of these properties regarding their transport and fate within a range of environments, giving some insight into these interfaces such as those found in colloidal systems (Hirst et al., 2017, Hochella, 2008, Braunschweig et al., 2013).

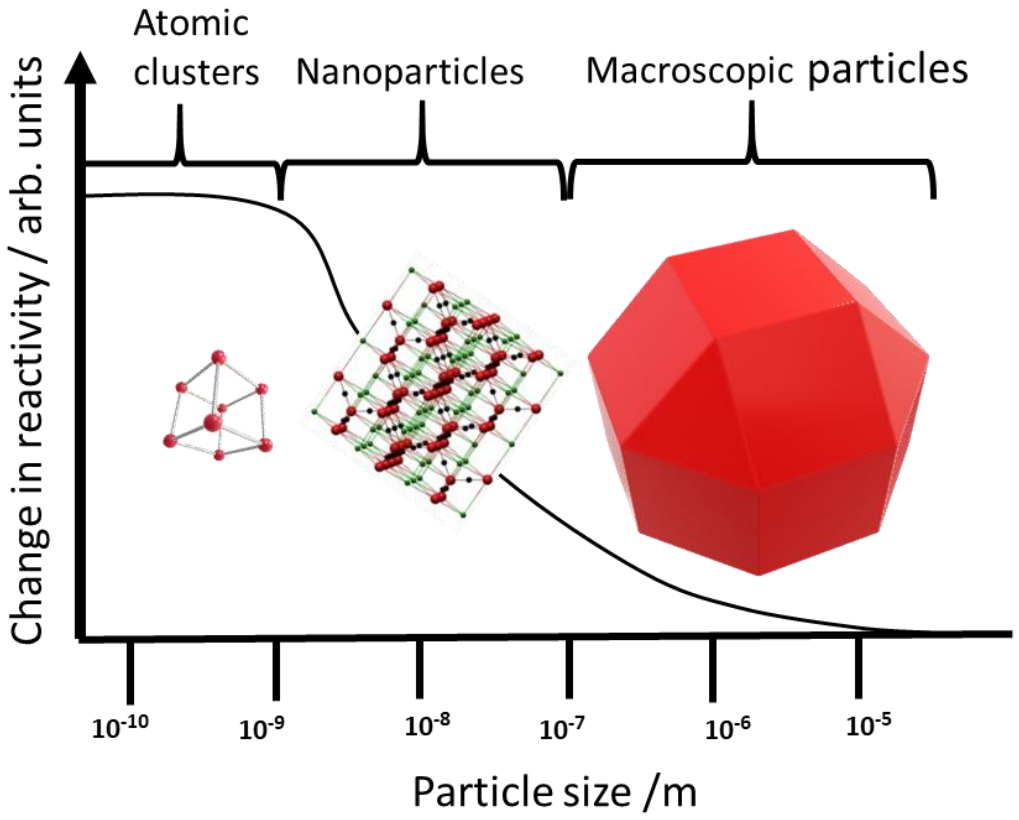

Figure 1.3. Size-dependent changes in reactivity of particles: atomic clusters to nanoparticle to macroscopic particles, and relative change in reactivity (adapted from Wigginton et al. (2007); nanoparticles image is Maghemite cubic, P4332/tetragonal, P41212 from Wu et al. (2015)).

There is an abundance of work for engineered iron nanoparticles, however, studies of iron mineralogy and speciation for iron-bearing nanoparticles (natural, released or incidental) and fine colloids in natural aqueous environments is lacking (Von Der Heyden et al., 2019). Part of the reason for this might be attributed to natural iron bearing nanoparticles and fine colloids being more difficult to investigate than engineered nanoparticles due to their amorphicity and dilute nature in some environments. Examples of this are found in recent studies of iron nanoparticles and fine colloids in the ocean (Von Der Heyden et al., 2019) and in glacial melt (Hawkings et al., 2014). These studies have employed the latest in synchrotron-based X-ray absorption spectroscopy but did not derive definitive mineralogy for many of the particles.

1.3 **Iron transport: terrestrial source, to rivers and on to the sea**

In sediments, iron minerals and organic matter mutually stabilise each other, forming a 'rusty carbon sink' (Lalonde et al., 2012). This stabilisation, whilst limiting mineral transformation and CO_2 emissions from soils and sediments, may also facilitate fluvial and estuarine transport of particulate iron to marine environments (Kritzberg et al., 2014, Jirsa et al., 2013, Schröder et al., 2016). It is at this interface, along the salinity gradient, that we can explore the transportation of terrestrially derived Fe-OM onward to the ocean. This transportation involves changes in iron complexation, therefore, speciation and mineralogy ultimately influence its ability to reach the ocean in bioavailable forms, or forms which may be potentially bioavailable (Batchelli et al., 2010, Rathgeb et al., 2016). Some studies have demonstrated that most of the iron from peatlands, "dissolved" in associated river systems, is bound in dispersed iron-humic colloids and survives flocculation through the mixing zone to the marine environment. Humic substances degrade slowly, protecting iron from coagulation (Jirsa et al., 2013, Kritzberg and Ekström, 2012, Lalonde et al., 2012). A proportion of humic iron(III) species of low-molecular weight have shown resistance to precipitation even in high salinities (Kritzberg et al., 2014, Herzog et al., 2017). Many of these studies are under laboratory induced conditions which, although informative, remove the complexities found in natural system. In fluvial networks, little is known about the transport mechanisms of iron from terrestrial sources, through the coastal mixing zone and to the open ocean. Increasing our understanding of these processes will better inform iron and carbon biogeochemistry models, and ultimately, better inform predictions of future climate scenarios (Muller, 2018).

Present calculations of global riverine iron delivery have been based on the "average world river". These calculations are made on major world rivers mostly at low latitudes, such as the Mississippi river. They are not representative of many high latitude rivers of Europe, Asia and North America which, are humic-rich and demonstrate iron-carrying capacities in the region of 3 orders of

magnitude higher than “global average river” (Krachler et al., 2010, Hunter et al., 1997). Studies that have been conducted on smaller temperate and boreal rivers, and peatland draining creeks suggest that these smaller rivers and creeks are an important source of iron to the coastal sea (Batchelli et al., 2010, Kritzberg et al., 2014, Krachler et al., 2016, Muller, 2018). Batchelli et al. (2010) discovered that most of the iron-humic complexes found in the greater than 5 kDa (approximately 3 nm) size fraction of the coastal plume of the River Thurso in NE Scotland, and associated with the Flow Country peatlands, were river-derived. Additionally, they found that the stability constants were uniform along the coastal plume at salinities of 28 to 35. Most of the iron in the described ‘truly dissolved’ fraction, attributed to less than 5 kDa, was reported as complexed to ligands of marine origin. The study also demonstrated the iron was bound strongly, albeit reversibly, to OM (humic substances) implying potential bioavailability (for example to siderophores) and, that the dissociation of the iron-humic associations might influence the conformation of colloids over time. Despite this important insight, the mechanistic details associated with the Fe-OM transport are not yet fully understood.

To better understand the transport mechanisms and processes involved, it is necessary to understand the iron mineralogy and its association with organic matter complexes in these environments (Muller, 2018). As discussed above, suitable methods and techniques to provide definitive mineralogy for these nanoparticles and fine colloids is lacking. The development of suitable methods to successfully probe the iron mineralogy in more iron rich waters will begin to close the knowledge gaps surrounding riverine iron transport to the coastal seas. Further development would then allow investigation of iron nanoparticles and fine colloids in their onward transport to the sea shelf and open oceans. This is particularly pertinent when considering the environmental impacts of climate change and anthropogenic inputs (Tagliabue et al., 2017, Pokrovsky et al., 2018).

1.3.1 **Iron in Peatlands and riverine delivery to the coastal oceans**

It is estimated that ~15-30% of the world's soil carbon is stored in the peatlands of boreal and sub-arctic regions (Limpens et al., 2008). Changes in anthropogenic land use and in climate are predicted to drive increases in greenhouse gas emissions (CO_2 and CH_4) from these regions to the atmosphere. Alongside this, these changes also promote losses of organic matter through fluvial networks (Krachler et al., 2015). Humic substances derived from peatlands are intrinsically bound with iron minerals, mutually stabilizing each other in soils and sediments (Lalonde et al., 2012, Pokrovsky et al., 2005). Examining the potential of rewetted peatlands as carbon sinks, Riedel et al. (2013) call for future studies to examine the age of the associated organic carbon to better describe the relationship with iron and the implications for carbon storage and sequestration: examining the aging of carbon can provide information as to its source i.e. biotic or abiotic and may give better understanding of Fe-OM preservation within sediments (Lalonde et al., 2012). However, this information is only part of the picture and, as discussed above, better understanding of the transport mechanisms and transformations are needed, from source to sea. The understanding of environmental (natural) iron nanoparticle and fine colloid mineralogy associated with this organic matter is still sparse despite it being an important component of environmental systems (Von Der Heyden et al., 2019).

1.4 **Project rationale**

The transport mechanisms of terrestrially derived nanoparticle and colloidal Fe-OM complexes along rivers to the coastal are not well constrained. This is, in part, due to the lack of understanding of the associated iron mineralogy and speciation: (i) the small particle size and their often amorphous, nature makes mineralogical characterisation challenging (ii) true nanoparticles fall below the traditional dissolved filter cut-off pore size (0.45 μm) and are often falsely classed as dissolved iron. Although investigating the nanoparticulate and fine colloidal fraction of Fe-OM material in natural water is pertinent to understanding its biogeochemical

cycling; isolating and characterising (in particular, defining the mineralogy) of these particles is difficult (Jirsa et al., 2013, Pokrovsky, 2016, Von Der Heyden et al., 2019). There are ongoing developments being made to methods and technologies to better quantify iron-bearing natural nanoparticles and fine colloids and to investigate their associated characteristics. Examples of these include: the use of dynamic light scattering (DLS), UV-Visible Absorption, fluorescence and inductively coupled plasma mass spectrometry (ICP-MS) coupled to field flow fractionation methods (Gottselig et al., 2017, Stolpe et al., 2012, Stolpe et al., 2013). Combined, or coupled technologies such as AF^4 coupled ICP-MS and carbon analysis in conjunction DLS has proved valuable in the characterisation of environmental nanoparticles from stream waters (Gottselig et al., 2017). This advance in physical size fractionation coupled analyses do not however, address mineralogical characterisation of water borne iron-bearing nanoparticles.

The importance of defining the mineralogy of iron in environmental nanoparticles and colloids has been discussed throughout this chapter. It is evident, therefore, that the addition of a suitable method to also investigate the iron mineralogy would, therefore, be valuable addition to these coupled and combined techniques used to better constrain these environmental particles. Iron in most natural waters is relatively dilute compared to soils and sediments, and becomes more so as salinity increases and mobility changes (Breitbarth et al., 2010). As discussed, this has implications for some analytical techniques, particularly those used to define iron mineralogy.

Mössbauer spectroscopy (MBS) is ideal for investigating the mineralogy of iron bearing nanoparticles, however, is not well suited to the investigation iron-bearing particles found in natural water environments due to their often dilute nature. To constrain measurements to workable timescales and ensure the feasibility of the analysis the optimal iron content in an MBS sample should be in the region of 10 mg cm^{-2} (Schröder et al. 2016). For sea water, achieving this amount of iron equates to filtering up to 1000 L of water. This means that there is a requirement for increased sample volumes when analysing dilute waters. An example of this would be with

increasing salinity as larger particulate matter is removed by flocculation and sedimentation , reducing the particle abundance and size range in the water column (Krachler et al., 2016).

The Synchrotron Mössbauer Source (SMS) at the European Synchrotron Radiation Facility (ESRF) requires only microscopic sample volumes for successful measurement. This negates the need to filter large volumes of water to gain a measurable sample. Schröder et al. (2016) demonstrated the ability of the SMS to define the iron mineralogy of the particulate size fraction from filtered coastal waters (> 700 nm). There are no studies to date presenting SMS techniques to investigate the nanoparticle and colloidal components of the operationally defined dissolved fraction (<450 nm) of water. Recent research calls for a technique with which to investigate the iron mineralogy within this size fraction (Muller, 2018, Von Der Heyden et al., 2019). The main driver for my PhD project was to develop successful SMS methods for the investigation of iron mineralogy of these environmental particles.

1.5 Aim, scope and structure of the thesis

Our understanding of iron biogeochemistry of water-borne environmental nanoparticles and colloids is poorly constrained, as has been highlighted in the preceding sections. In part this is linked to our lack of knowledge of iron mineralogy in these particles as it is particularly difficult to define and becomes increasing more so in dilute environments such as the oceans. Therefore, the main aim of this PhD study is to develop SMS methods which can be used to investigate the mineralogy in these particles.

Chapter 2. Size determination and mineralogical investigation: techniques for iron bearing nanoparticle characterisation

The motivation for this review chapter was to investigate the methods available for the characterisation of environmental iron-bearing nanoparticles with a view to elucidating knowledge and resource gaps. The review was approached from a particle size and mineralogical

perspective to evaluate techniques and instrumentation that was found to be most frequently employed.

Chapter 3. The behaviour of iron-bearing particles along a salinity gradient: Loch Etive

The main aim of this study was to gain insight into iron concentrations within physically defined size fractions of dissolved fraction of water at different salinities. As an initial stage of the SMS development, this study investigated associations between particle size and iron concentration to inform the physical size ranges associated with iron. Understanding the particle size ranges in which iron was partitioned helped to determine which particles of interest for SMS. The study was also used as a pilot to investigate particle isolation and concentration methods that could be applied to the SMS sample preparation.

Chapter 4. Distribution of iron between particulate size fractions in iron-rich rivers in the Flow Country

The main objectives for this study were to progress the method development initiated in Chapter 3 to i) quantify iron concentrations in size defined nanoparticle/colloidal fractions ii) determine which particle size fractions iron is associated with for both catchments studied: from source waters, through the rivers to the coastal plume iii) investigate relationships between organic and inorganic carbon concentrations in the nanoparticle/colloidal fractions were quantified and compared to the iron concentration results in the same size fractions and vi) investigate available isolation and concentration techniques for their effectiveness and applicability to SMS sample preparation.

Chapter 5. Investigation of environmental iron nanoparticles and colloids with the 57Fe Synchrotron Mössbauer Source – a proof-of-concept study

This chapter is the SMS development chapter, specific to sample development describes the processes involved, drawing the research conducted and described in Chapters 3 and 4. It also

presents the results of standard beamtime at ID18, ESRF, Grenoble in 2018 and the success of the developed SMS method. The chapter was also used to explore future sample optimisation options and applicability for future research.

Chapter 6: The concluding chapter explores the success of the methods used for size fractionation and iron concentrations. It discusses the isolation and enrichment of nanoparticles and fine colloids for subsequent SMS analysis. Lessons learned and the limitations of the developed methods and will be addressed with a view to exploring future development to further investigate iron mineralogy in Fe-OM nanoparticles and colloids riverine transport to the coastal oceans. Additionally, it discusses the feasibility of applying the methods to other systems such as lakes, sea ice and glacial melt, and even more dilute systems such the open ocean.

2. Size determination and mineralogical investigation: techniques for iron bearing nanoparticle characterisation

Nanoparticles and nanostructures are ubiquitous in nature (Hartland et al., 2013). As discussed in Chapter 1, iron oxide and oxyhydroxide nanoparticles and nanostructures are also ubiquitous in many of Earth's environments where they are often key components in biogeochemical processes (Guo and Barnard, 2013). The complexity of environmental iron bearing nanoparticles and structures necessitates the need for a diversity of techniques to examine the many properties that can influence their reactivity and function in biogeochemical processes thereby gaining a better understanding of their role in nature (Mourdikoudis et al., 2018). Increased understanding of environmental nanoparticles should also benefit the synthesis of engineered iron nanoparticles (Guo and Barnard, 2013), and ultimately allow predictions of engineered particle interactions upon their release into a range of different environments.

It is the complexity of nanoparticles and nanostructures that drives the need to examine a wide range of properties that have influence upon their reactivity, these physio-chemical parameters are extensive and include size and size distribution, shape, surface area, surface chemistry and element composition, speciation, coordination, aggregation, crystal structure (Mourdikoudis et al., 2018, Guo and Barnard, 2013, Hochella et al., 2008). This review provides an investigation into the suitability and effectiveness of techniques deemed to be most commonly employed for iron nanoparticle characterisation. Size, size distribution and mineralogical determination were the key characteristics selected as these were the main properties required for the development of SMS techniques for water borne environmental iron bearing nanoparticles.

Insight is given into the suitability of the techniques investigated regarding the characterisation of natural and engineered iron-bearing nanoparticles in the environment, and investigation under laboratory conditions. Consideration was given to appropriateness of application for targeted

properties of interest (size and mineralogy) alongside the advantages and limitations in different measurement environments or mediums. Method and instrument suitability for purpose, analytical success and any associated limitations is discussed in the above context, with an emphasis on suitability for size and mineralogical determination of natural nanoparticles in water environments. Suggestions for alternative techniques, and the potential for the combination of complementary techniques, where a multi analytical approach might be adopted, is also discussed.

2.1.1 **Background to characterisation and properties of iron-bearing nanoparticles**

Iron-bearing nanoparticles can be found as naturally occurring, incidental (e.g. those released to the atmosphere through combustion or as nanoparticulate matter from water and waste pipelines or filtration systems into the soils, sediments and water systems), synthesized (or engineered) particles and range from highly crystalline to amorphous; exist as single particles, agglomerates and aggregates which range in size (e.g. fine colloids). Within the nanoparticle size range, properties and behaviour can vary greatly (Abazari et al., 2015, Chatterjee et al., 2003, Hochella et al., 2008, Wigginton et al., 2007). Consideration must also be given to agglomerates (multi-granule), which exist as an assemblage of nanosized particles and although micro-sized, display a range of nanoscale properties over their surfaces and internally (Baalousha et al., 2008, Reichel et al., 2017). Crystal shape, mineralogy, physical size and domain structure all play a part in defining iron-bearing nanoparticle behaviour and there is a constant call for further investigation of these variables. This includes elucidating the theory of shape-size-structure interactions and effects on magnetic properties and, in the case of engineered nanoparticles, performance capabilities, toxicology and environmental implications (Uglov et al., 2016, Akbarzadeh et al., 2012). Optimization of the intended function and performance of engineered iron-bearing nanoparticles is dependent upon a combination of properties: particle size, crystal structure, geometry, morphology, porosity and specific surface area. Synthesis of these particles

with targeted properties is controlled by mineral growth mechanisms (transport processes and surface reactions) by manipulating the conditions in which they were produced. Iron nanoparticles are often selected over other magnetic nanoparticles for medical, industrial and environmental application due to their numerous useful properties, including a strong magnetic moment, biocompatibility, chemical stability, and pigmentation (Sun et al., 2006, Ali et al., 2016, Amstad et al., 2011, Hufschmid et al., 2015, Patsula et al., 2016).

Electromagnetic properties include: electrical conductivity/resistivity, optical absorption, energy-band structure/band gap/shift, dielectric, piezoelectric and ferroelectric properties, ζ(zeta)-potential (colloidal dispersion), hydrodynamic diameter (colloidal dispersion), surface charge, magnetic phase, hysteresis and magneto-optical. The influence of particle size on magnetic properties, even within the operationally defined nanoparticle range (1 to 100 nm), has been acknowledged for some time. There is a critical size for magnetic nanoparticles, at which the domain structure changes from single-(uniformly magnetized) to multi-domain (Kashuba and Pokrovsky, 1993, Gupta and Gupta, 2005). Magnetic properties of iron-bearing nanoparticles including saturation magnetization, saturation remanence blocking temperature and coercivity are highly influenced by the particle size and domain structure. Additionally, studies continue to explore the effect of crystal structure (shape and size) on critical size and, therefore, upon magnetic properties (Li et al., 2017, Uglov et al., 2016, Singh et al., 2017, Patsula et al., 2016). Better understanding these properties further elucidates the behaviour of magnetic nanoparticles in their environmental contexts (Anschutz and Penn, 2005, Chatterjee et al., 2003) and, for synthesized nanoparticles, can aid optimization of their potential application e.g. in medicine, agriculture, environmental remediation and industry (Patsula et al., 2016, Jain et al., 2005, Jain et al., 2003, Sabale et al., 2017). Atoms in nanoparticles are found on the surface, or near it, therefore, surface analysis is important in the characterization of iron-bearing nanoparticles i.e. surfaces and composition can provide a prediction of subsequent spatial and temporal, environmentally induced changes (Baer et al., 2010, Grainger and Castner, 2008).

There is an increasing diversity of techniques and measurements available to characterize iron-bearing nanoparticles, targeting specific properties such as magnetic, size, morphology, local structure and chemistry e.g. composition and thermal stability. Physical parameters such as size and surface area influence the chemistry of nanoparticles and therefore, their interactions in their environments. It is therefore imperative that we attempt to better understand these influences and effects through a rigorous set of applied measurements and subsequent modelling (Baer et al., 2010, Karakoti et al., 2006). As discussed in Chapter 1, bulk measurements or assumptions are often used to characterise iron bearing (and other) nanoparticles, however useful these are, they are limited in spatial resolution and nanoparticle surface properties are often out with the limitations of investigation due to sample preparation or instrument limitations. Additionally, the use of combined methods helps to provide more comprehensive analysis (Baer et al., 2010).

Nanoparticles are commonly defined as having one dimension which is less than 100 nm. This is the key reason for selecting size as a key property as this is where we can begin to investigate the size effects upon chemical and other behaviours, and to begin to explore size related reactivity in different environments (Von Der Heyden et al., 2019, Hochella et al., 2008). The effect of size alone does not define the behaviour of iron nanoparticles but it serves as a defined starting point. Consideration must be given to a suite of parameters if we are to fully understand iron nanoparticle behaviour in different environments. The complexities of understanding size effects are also compounded by other nanoparticle properties, the local environment and through aggregation/disaggregation mechanisms (Ali et al., 2016, Guo and Barnard, 2013).

2.2 **Review Methods**

Size and mineralogy formed the basis for the development of the SMS method, the main aim of my PhD project, which uses synchrotron based Mössbauer techniques to determine the iron mineralogy in water borne nanoparticles and colloids within defined particle size ranges. Size mineralogy are high level property descriptors and within these a number of further defined parameters can be measured. Although these are not exclusive properties for the investigation of nanoparticle behaviour they do, along with structural properties, encompass some of the key parameters for characterising nanoparticles (Modena et al., 2019, Mourdikoudis et al., 2018). Furthermore, they are specifically employed for the investigation of environmental iron nanoparticles (Guo and Barnard, 2013) and for those found in natural water environments (Von Der Heyden et al., 2019).

The techniques and instrumentation discussed in this review were selected using the literature search results (Appendices for Chapter 2) and their applicability to determine size, mineralogical speciation and structure for iron-bearing nanoparticles (Table 2.1). Investigation of all available techniques is out with the scope of this review. Those found to be more commonly employed are included. I performed a literature search to reveal the techniques and instrumentation most commonly cited for the characterisation of iron bearing environmental nanoparticles in aquatic environments. The search criteria and results are available in the Appendices for Chapter 2 (Table 7.1). Table 2.1 was adapted from Mourdikoudis et al. (2018) to demonstrate the range and diversity of measurable nanoparticle parameters. This table lists available instrumentation and techniques based used to characterise iron-bearing nanoparticles. The abbreviations used in Table 2.1 are listed in the Appendices for Chapter 2 (section 7.2.1).

Table 2.1. Nanoparticle parameters and associated techniques adapted from Table 2 in Mourdikoudis et al. (2018).

Parameter characterised	Techniques
Size (structural properties)	TEM, (μ)XRD, DLS, NTA, SAX, HR-TEM, SEM, AFM, EXAFS, FMR, DCS, ICP-MS, UV-Vis, MALDI, NMR, TRPS, EPLS, magnetic susceptibility, Raman
Shape	TEM, HRTEM, AFM, EPLS, FMR, 3D-tomography
Elemental/chemical composition	(μ)XRD, XPS, ICP-MS, ICP-OES, Raman, SEM-EDX, NMR, MFM, LEIS
Crystal structure	(μ)XRD, EXAFS, HR-TEM, Raman, electron diffraction, STEM
Size distribution	DCS, DLS, SAXS, NTA, ICP-MS, FMR, AF^4, superparamagnetic relaxometry, DTA, TRPS, SEM
Chemical state/oxidation state	XAS, EELS, XPS, Mössbauer
Growth kinetics	SAXS, NMR, TEM, cryo-TEM, *liquid-TEM*
Ligand/binding/composition/density/arrangement /mass, surface composition	XPS, FTIR, NMR, SIMS, FMR, TGA, SANS
Surface area, specific surface area	BET, liquid NMR
Surface charge	Zeta potential, EPM
Concentration	ICP-MS, UV-Vis, RMM-MEMS, PTA, DCS, TRPS
Agglomeration state	Zeta potential, DLS, DCS, UV-Vis, SEM, Cryo-TEM, TEM
Density	DCS, RMM-MEMS
Single particle properties	Sp-ICP-MS, MFM, HRTEM, liquid TEM, Raman
3D visualisation	3D-tomography, AFM, SEM
Dispersion of NPs in matrices	SEM, AFM, TEM
Structural defects	HRTEM, EBSD, Raman
Detection of NPs	TEM, SEM, STEM, EBSD, magnetic susceptibility
Optical properties	UV-Vis-NIR, PL, EELS-STEM
Magnetic properties	SQUID, VSM, Mössbauer, MFM, FMR, XMCD, magnetic susceptibility

Note: Red type indicates the techniques/instruments included in the discussion section (Section 2.4).

2.3 Iron-bearing nanoparticles

Advances in synthesized iron-bearing nanoparticle production are increasing, improving their success of application. The role of both natural and engineered nanoparticles has been acknowledged, and although our understanding is increasing, there is much more to understand about the role of nanoparticles in the environment. In some environments such as the oceans, this paucity of information might be in part due to their dilute nature which can lead to nanoparticles remaining unintentionally unobserved within the operationally defined dissolved

fraction (<0.45 μm). Hence, their influence and interactions might be underestimated and included in environmental modelling using bulk characterisation. Additionally, environmental and incidental (i.e. released as by-products of other processes) iron-bearing nanoparticles generally exist as poorly-crystalline or amorphous phases, which are often difficult to detect and characterize (Caraballo et al., 2015). These small particles are more than likely not contained in a closed system and might well be transient, albeit influential on the surrounding biogeochemistry. Therefore, development of *in situ* measurement techniques would be advantageous, and when combined with laboratory simulations, might provide invaluable insight into transport mechanisms and interactions with other element cycles in a diversity of changing environments.

There are no recognized standardized set of methods and metrics for nano-particle, -materials or -technology characterisation and labelling (for consumer goods), globally. Developing a suite of characterisation methods, sympathetic to both naturally occurring and engineered (synthesized) iron-bearing nanoparticles, targeting particular properties of interest, could provide an opportunity to forge collaborations amongst stakeholders: researchers, regulators and industry, and ultimately advance our overall understanding of iron-bearing nanoparticles (Vance et al., 2015). Firstly, we need to understand the properties and make decisions about which of those properties are important and, appropriate, to measure for given scenarios. Developing a suite of environmental nanoparticle data is of paramount importance for modelling and monitoring any success of engineered nanoparticle application, and for better understanding and prediction of transport and fate in the environment. On encountering natural or incidental iron-bearing nanoparticles *in situ*, we often have no, or very little idea about their characteristics, no definitive list of their constituents and limited understanding of their properties or transport mechanisms. Synthesized iron-bearing nanoparticles seem easier to constrain because we know their starting point. Therefore, there appears to be a benefit to further advancing our understanding of the characteristics and behaviours of these generally well defined particles. Modelling can begin from a defined starting position (known properties) compared to natural or incidental nanoparticles.

That holds strong until we begin to question spatial and temporal changes, potential for release in to other systems and any subsequent biogeochemical interactions. However, these nanoparticles still provide an advantageous starting point for controlled or manipulated investigations especially when we consider the potential for release (intentionally or inadvertently) into other environments and as an insight into naturally occurring nanoparticle behaviour. Providence of environmental and engineered iron-bearing nanoparticles, and our stewardship of them, can only be gained if we truly understand their size and mineralogically related properties and behaviour in order to inform stakeholders i.e. policy makers, industry, consumers (Vance et al., 2015, Froggett et al., 2014).

Iron-bearing nanoparticles exist as naturally occurring or synthetic. In natural environments: terrestrial i.e. soils, sediments, rocks, minerals (Raiswell and Canfield, 2012, Angelico et al., 2014, Chupakov et al., 2017, Claudio et al., 2017, Hochella et al., 2008, Pokrovsky et al., 2016, Rawat et al., 2018), biological (Claudio et al., 2017, Iravani, 2011, Zachara et al., 2002, Magro et al., 2018), extraterrestrial, planetary and as a result of space weathering (Schröder et al., 2016, Kohout et al., 2014, Schröder et al., 2006, Sasaki et al., 2001), atmospheric (Rubasinghege et al., 2010, Journet et al., 2008, Jickells et al., 2005), and in water environments including, groundwater, rivers, oceans, hydrothermal vents, sea ice etc. (Hawkings et al., 2014, von der Heyden et al., 2012, Hirst et al., 2017). However, engineered iron nanoparticles are being increasingly produced (both intentionally and unintentionally i.e. synthesized or incidental) and are becoming more prevalent in anthropogenically engineered environments, such as those targeted for remediation (Bryant et al., 2011, Chiang et al., 2001, Zhang et al., 2011), in medicine (Colombo et al., 2012) and also in industry and the production of consumer products (Gonzalez-Galvez et al., 2017). We need to acknowledge that these intended environments are often not, nor may they remain, indefinitely closed systems (Chekli et al., 2015). There are existing and potential cross overs and interactions through and within these environments that involve both natural and engineered nanoparticles. Von der Heyden et al. (2019) identified three 'broad' groups of iron nanoparticle mineralogy (in

natural aquatic environments): Fe(II)-rich nanoparticles, Fe(III)-rich nanoparticles, and magnetite nanoparticles. However, the authors highlight the complexities of underpinning the diverse iron speciation and mineralogy within aquatic systems and call for a research focus on Fe nanoparticle characterisation in an environmental context i.e. the need to elucidate the mechanics of observed ferrous iron (natural nanoparticle) stabilisation (organic functional group associations), or (microbial) production and the mechanics of ferric oxide stability (facilitating fluvial nutrient and contaminant transport), including their ability to harbour potentially bioavailable iron and transport it to the ocean.

Iron cycling and redox processes are abundant at interfaces, and ultimately chemical and physical changes within systems provide dynamic environments, which in turn influence other, connected systems and processes (Charlet et al., 2007, Luef et al., 2013, Pokrovsky et al., 2012, Scheinost and Charlet, 2008, Vasyukova et al., 2010). Understanding the transport mechanisms of iron-bearing nanoparticles and their interactions in specific environments is paramount to our modelling of their expected behaviour and any related effects. Iron can be a limiting nutrient in ecosystems as was outlined in Chapter 1. It is therefore critical that we better understand its role in our environments.

2.3.1 **Naturally occurring iron-bearing nanoparticles**

Despite iron's ubiquity and its requirement as an essential trace element by marine and terrestrial organisms, bioavailable iron on Earth is limited in oxygenated surface environments where iron phases exhibit low solubility (Frey and Reed, 2012, Hawkings et al., 2014). Iron exists in its main redox states: Fe(0), Fe(II) and Fe(III) (Raiswell and Canfield, 2012, Claudio et al., 2017, Viollier et al., 2000). Fe(III) is thermodynamically stable, although all states can exist in oxygenated environments due to low solubility. Ferric iron oxyhydroxide phases often occur as nanoparticles (Baalousha, 2009). Iron-bearing nanoparticle behaviour continually challenges our capabilities to strive for a better understanding of the spatial and temporal processes, interactions and effects.

They influence other element cycles in a diversity of environments (Hochella, 2008, Raiswell and Canfield, 2012). This is due, in part, to iron oxide nanoparticles in natural environments often being amorphous or poorly crystalline, displaying atypical morphologies to their bulk mineral counterparts, and including defects and impurities, making them challenging to characterize (Caraballo et al., 2015). In ground water, soils and sediments, naturally generated iron-bearing nanoparticles are ubiquitous, originating from mineral and rock weathering and as a product of organic matter decay and metabolism (Waychunas et al., 2005, Zachara et al., 2002, Nischwitz et al., 2016).

2.3.2 **Engineered (synthetic) iron-bearing nanoparticles**

Engineered iron and iron oxide nanoparticles have widespread application. They are often chosen above other magnetic nanoparticles due to their biocompatibility (showing only transient accumulation), ubiquity in nature, and unprecedented advances in control over their synthesis in terms of size and structure (Neamtu et al., 2018, Sabale et al., 2017, Teja and Koh, 2009). The properties of zero valent iron and magnetic iron oxide nanoparticles can be exploited through a diversity of uses in nanotechnology, from biomedicine to batteries (Lyubutin et al., 2018, Akbarzadeh et al., 2012, Barreto et al., 2011). Crystalline iron-bearing nanoparticles have well defined parameters upon synthesis, however, may be subject to changes such as, agglomeration, aggregation and disaggregation (Liu et al., 2018, Wang et al., 2018), mineralization (Chan et al., 2009), and crystallization (da Silva, 2016, Hue, 2015). Engineered magnetic iron nanoparticles, for example hematite (α-Fe_2O_3), maghemite (γ-Fe_2O_3), and particularly Magnetite (Fe_3O_4) are increasingly used, and their potential investigated for a diversity of applications (Ghazanfari et al., 2016), including: environmental remediation (e.g. soil, groundwater and wastewater treatment for removal of both organic and inorganic pollutants) (Neamtu et al., 2018, Reinsch et al., 2010); biomedical applications (e.g. targeted drug delivery, cancer treatment and diagnostics such as hyperthermia and Magnetic Resonance Imaging (MRI) (Zhan et al., 2018, Sabale et al., 2017),

biotechnology (e.g. biosensing) (Wu et al., 2008), and material science, engineering/industry (e.g. magnetic recording/data storage, pigments for printing) (Akbarzadeh et al., 2012). In surface functionalized iron-bearing nanoparticles, there has been success in stabilization controls i.e. to slow down aggregation processes thereby protecting their physical and chemical properties for longer periods, and within certain media like ferrofluids (Angelakeris et al., 2014).

Although predictions about the intended role of these nanoparticles can be made, there is still uncertainty surrounding their incidental interactions and fate in the environment (Caraballo et al., 2015, Wiesner et al., 2009, Magro et al., 2018). It is important to acknowledge that synthetic nanoparticles are designed and produced for a specific purpose, however, they may be intentionally, or unintentionally, released into the environment (Chekli et al., 2015, Gonzalez-Galvez et al., 2017, Westerhoff et al., 2018, Philippe and Schaumann, 2014, Rawat et al., 2018). Intentional release mechanisms include: remediation of ground water, industrial processes, drug delivery and medical diagnostics. Other synthetic iron-bearing nanoparticles found in the environment are often referred to as incidental nanoparticles. These are formed and released from anthropogenic inclusions/alterations to the environment, such as the rusting of pipework in water management systems (Westerhoff et al., 2018), combustion and other processes of industry, vehicle emissions, or commercial and residential heating systems (Smita et al., 2012). Engineered nanoparticles are usually more well-defined than incidental nanoparticles which, occur as by-products of other activities and, therefore, there are no imposed constraints on their formation or alteration.

Despite well-defined characteristics when initially produced, engineered nanoparticles are potentially subject to changes over time such as, agglomeration, aggregation and disaggregation in the same ways as natural nanoparticles (Liu et al., 2018, Philippe and Schaumann, 2014, Wang et al., 2018, Baalousha et al., 2008), mineralization (Chan et al., 2009) or crystallization (da Silva, 2016, Hue, 2015). Upon release, these particles may accumulate or be transported to other

environments where we know some of their effects. However, we do not yet fully understand the all of processes, or many of the potential impacts, and influences on their environments including: climate, toxicology, biotic systems and human health, element and nutrient cycles and the food chain. Anthropogenically produced nanoparticles (whether incidental or synthesized) are now recognized as being globally prevalent, interacting with, and influencing, both biotic and abiotic components (Baalousha et al., 2008, Philippe and Schaumann, 2014, Gonzalez-Galvez et al., 2017, Yang and Westerhoff, 2014, Rawat et al., 2018).

Concern about the effects and fate of nanoparticles has emerged and is now a focus of research i.e. the field of nanotoxicology which encompasses both anthropogenically and naturally produced nanoparticles. Nanotoxicology research plays a vital role in public perception and regulatory reform. Recognition is given to building better knowledge of nanoparticle properties; key to understanding their potential performance, influence on the global environment, and essential when informing industry, policy makers and future research and development (Hochella et al., 2008, Vance et al., 2015, Wiesner et al., 2009). Engineered (synthesized) nanoparticles might appear to pose less of a concern than incidental nanoparticles as the control on them is perceived to be more constrained. Furthermore, the body of work surrounding the synthesis of these particles informs the way they are expected to behave in a variety of different environments (Chekli et al., 2013, Chekli et al., 2015, Faraji et al., 2010, Manciulea et al., 2009). However, there are uncertainties surrounding the influence on, or from, receiving systems, whether those are environmental systems, or systems within their intended release environments e.g. biological organisms, remediation sites or technology (Hochella, 2008, Smita et al., 2012). As we discover more uses for iron-bearing nanoparticles, production expands, and with it the potential for synthesized nanoparticles being released from their intended environment inevitably increases and increases the complexity of receiving systems (Von Der Heyden et al., 2019).

2.4 Characterisation Techniques: size, structure and mineralogical determination

2.4.1 Dynamic Light Scattering (DLS) or Photon Correlation Spectroscopy(PCS)

DLS is used to determine particle size in colloidal suspension. It measures hydrodynamic diameter, not particle diameter. Diffusive movement of particles under Brownian motion is transferred to the particle size using the Stokes-Einstein relationship. DLS (conventional) is not ideal for particle size measurements in suspensions where there is a large ratio between the diameter of the particles held in suspension (i.e. 3:1 > 2:1). It is more reliably applied to monomodal rather than bimodal or polydisperse samples. However for monomodal samples it is a fast and reliable technique and therefore, is deemed more suitable for engineered and/or functionalized (surface coated) particles rather than natural or environmentally exposed ones (Hoo et al., 2008). In drug delivery, superparamagnetic iron oxide nanoparticles (SPIONs) need to be of a specific, uniform size, and DLS is a quick and reliable technique to measure these monodisperse samples for size consistency (Mahmoudi et al., 2011). DLS measures the intensity size average particle and from that the volume and number of particles can be calculated. Large particles (even a small number) can influence the intensity. However, this can usually be corrected by volume information (Hoo et al., 2008). It should be considered that nanoparticles, with a tendency to aggregate (agglomerate) might pose a problem with measurement in that you are measuring the aggregate size, even those which have been functionalized (Hinterwirth et al., 2013, Amstad et al., 2009), and changes to pH or ionic strength can affect particle surface charge and aggregation/disaggregation rates (Angelico et al., 2014). However, these issues are being overcome with the development of high-performance instrumentation (e.g. Zetasizer Nano ZS by Malvern Panalytical), and through the addition of solutions to slow down aggregation rates, selection of the correct parameters for suspension medium, considered and tested sample concentrations, and the use of software to deal with more polydisperse samples (Scotti et al., 2015). DLS is also often combined with zeta-

potential (ζ-potential) measurements in a single instrument. With these advances, DLS has been shown to be useful, not only for engineered iron-bearing nanoparticle e.g. in time-resolved aggregation behaviour studies (Mahmoudi et al., 2011), ground remediation studies (Tiraferri et al., 2008), engineered nanoparticles released to the environment (Hu et al., 2010) and soil/ground water (Angelico et al., 2014), but also for natural nanoparticles and fine colloids (Angelico et al., 2014, Gottselig et al., 2014).

2.4.2 **Asymmetric flow field flow fractionation (AF^4)**

AF^4 encompasses a variety of sub-techniques to provide separation of ~1 nm to ~1 μm particles. This size range is important because it allows for full investigation of the operationally defined dissolved phase (<0.45 μm), separating nanoparticles and (fine) colloids from the 'truly' dissolved phase (<1 nm). AF^4 can be used to separate and measure these particles by: size, mass, charge, density, diffusivity etc. for onward analysis. AF^4 provides hydrodynamic size distribution of a given sample (Giddings, 1993). It is frequently used to provide a (near) non-destructive fractionation of sample waters for particle analysis (von der Heyden et al., 2012, vd Kammer et al., 2005), including natural nanoparticles (Gimbert et al., 2005). It is often used as a complementary technique, or to validate other filtration techniques. AF^4 can also be used with, or coupled to, various on- or off-line measurement instruments to optimize, or further analyse a sample's components (Giddings, 1993, Singh, 2016, Jirsa et al., 2013) e.g. inductively coupled plasma mass spectrometry (ICP-MS), multi-angle static light scattering-differential refractometry (MALS-dRI), dynamic light scattering (DLS), size-exclusion chromatography (SEC) (Lohrke et al., 2008, Leeman et al., 2015). AF^4 coupled with inductively coupled plasma mass spectrometry (ICP-MS), organic carbon detector (OCD) and/or dynamic light scattering (DLS), have been developed as a tool to characterise particle bound metals such those found in iron-bearing nanoparticles and fine colloids in soil and water environments (Nischwitz et al., 2016, Gottselig et al., 2014, Jirsa et al., 2013). This demonstrates its usefulness for characterizing environmental samples where there are

chemical complexities over a broad range of particle sizes (Leeman et al., 2015, vd Kammer et al., 2005). AF^4 has also been successfully coupled with multi-angle laser light scattering for the investigation of environmental (natural and released/incidental) colloids and nanoparticles (vd Kammer et al., 2005, Baalousha et al., 2008).

An advantage of AF^4 is that it avoids the need for filtration and centrifugation, which have been shown to over- or underestimate particle concentrations due to effects of pore clogging (Zirkler et al., 2012, Gimbert et al., 2005). Furthermore, FFF is still often used with a pre-filtration step and it has been suggested that this pre-filtration step introduces an element of error with regard to under or over estimation of the particle size concentrations in the filtrate (Zirkler et al., 2012). However, successful size fractionation (with coupled analytical instrumentation), using a <5 μm pre-filtered sample has been developed, and demonstrated by (Gottselig et al., 2014, Gottselig et al., 2017). This minimises particle loss in the operationally defined dissolved fraction prior to onward analysis. Another advantage of AF^4 is that the size fractioned particles in solution can potentially be collected and subject to further offline analysis (Ponyik et al., 2013). Jirsa et al. (2013) suggested the potential for loss of organic matter in some aspects of AF^4, despite this, it has demonstrated pronounced advantages over traditional filtration methods and in characterising nanoparticles.

2.4.3 **Atomic Force Microscopy (AFM)**

AFM can characterize complex objects at the nanoscale and is used to determine particle size together with providing imaging. It can provide surface topography and is capable of imaging nanoparticles undergoing biological or other interactions in aqueous solution in a time-resolved manner (Hu et al., 2010, Lingamdinne et al., 2017, Carvell et al., 2010). For particle size measurements alone, the benefits of AFM over DLS is the ability to determine bimodal samples with ratios of between 8:1 and 5:1 (regardless of particle shape), whereas DLS is limited at ratios as low as 3:1 and 2:1 (Hoo et al., 2008). When combined with other techniques to investigate

aggregation and disaggregation in iron-bearing colloidal/nanoparticle suspensions AFM can provide powerful, real time, information adding understanding to the biogeochemical processes involved. AFM also has the potential to better inform environmentally released nanoparticle interactions and is often used to aid optimization of ground remediation using iron(-bearing) nanoparticles (Hu et al., 2010). Additions and adaptations to AFM include: scanning-probe microscopy (SPM), scanning tunnelling microscopy (STM) and ferromagnetic resonance (FMR). However, it should be noted that although the vertical resolution of AFM is ~0.1 nm, the lateral resolution is relatively low (~30nm) despite the vertical resolution achieving up to ~0.1nm (Mai, 2012).

2.4.4 **Scanning Electron Microscopy-Energy Dispersive spectrometry (SEM-EDS)**

This technique itself is non-destructive and sample preparation may not be needed when imaging samples in 'natural' or unaltered state (Rahman et al., 2011, Cardell and Guerra, 2016). Samples can be prepared uncoated and/or wet which is advantageous (and necessary) for some biological and environmental samples, however this is not generally the case. Analyses of dynamic experiments such as drying processes e.g. crystallization, are possible. SEM X-ray fluorescence from the elements within the sample surface is produced and employment of focusing optics e.g. polycapillary optics, can reduce spot size. SEM (morphology of a sample's surface) is often used in combination with EDS (or EDX). However, consideration must be given to chemical and physical conditions for samples and they must be related to reference materials or standard measurements (Cardell and Guerra, 2016). Issues can occur due to deterioration of a sample and/or interferences of the measurement environment (most common for environmental samples and those containing a high quantity of carbon). It is important therefore, to consider an adaptation option to SEM such as Environmental SEM (ESEM) or Field Emission SEM (FESEM). However, these come with their own limitations (Huang et al., 2014, Sheng et al., 2016, Tao et al., 2002). These adaptations can provide improved composition and structural analysis i.e. narrower

beam at both low and high electron energy, which also constrains sample damage and charging (Rahman et al., 2011); Electron Backscatter Diffraction (EBSD); Hyphenated SEM-Raman spectroscopy systems and, FIB/Dual-Beam (combined focused ion beam and SEM) (Young and Moore, 2005). Maximum resolution is often dependant on factors such as electron spot size and beam/sample interactions. Most benchtop SEM instruments resolution is ~20 nm, however, 1-20 nm resolution can be achieved with a full-sized SEM and advances in multibeam SEM for nanometre resolution investigation of bulk samples (Eberle et al., 2015). For example, with a voltage of 30 kV (beam emission from a tungsten cathode) the minimum beam diameter is about 10 nm. Although narrower beams are achievable, the addition of EDS requires a beam optimised by increased current for sensitivity. The optimum beam diameter for SEM-EDS therefore falls between 0.1 and 1 μm for qualitative analysis and 5 μm for quantitative analysis (Wassilkowska et al.).

2.4.5 Transmission Electron Microscopy (TEM) and High-resolution transmission electron microscopy (HR-TEM)

TEM investigates the internal composition of a sample (morphology, magnetic domains and stress) with higher resolution imaging, of ~0.2 nm, than SEM which, has a resolution between 1 and 20 nm (Mourdikoudis et al., 2018). Its application includes: nanotechnology; biology; medicine; industry (damage identification and product development); metallurgy; crystals and forensics. TEM provides extreme magnification, cryo-options are available, and the instrumentation has ease of use. However, sample preparation is extensive with the process being open to artefact accumulation (Riches and Drennan, 2006). TEM requires an extremely thin sample to allow electrons to pass through (samples must be electron transparent), tolerable of a vacuum environment and able to fit into the available vacuum chamber. Additionally, there is often a trade-off between the statistical analysis of particle size and the measurement of a whole population distribution (Pyrz and Buttrey, 2008) and the instrument itself is large and expensive

(Islam et al., 2013, Fu et al., 2011, Carvell et al., 2010, Angelico et al., 2014, Yang et al., 2012). HR-TEM nanoparticle characterisation provides information on the crystalline structures down to single particles, however, this is not always achievable where there is complexity in atom alignment and random orientation of crystals in relation to the electron source (Mourdikoudis et al., 2018, Carter and Williams, 2016, Rahman et al., 2011). TEM analysis can also be coupled with energy-dispersive X-ray spectroscopy (EDS) (Ribeiro et al., 2013).

Although TEM and HR-TEM can provide important information about the morphology and trace element concentrations of bulk samples, they cannot, as with X-ray power diffraction (XRD) or Raman, be used to examine molecular structure or chemical states at the surface. Complementary techniques such as time of flight secondary ion mass spectrometry (ToF-SIMS) can be used to gain this information and better characterize nanoparticles (Ribeiro et al., 2013). Additions and variations include: transmission electron cryomicroscopy (Cryo-TEM); Electron energy loss spectroscopy (EELS) (Prodan et al., 2013); electron diffraction, e.g. selected area electron diffraction (SAED) sometimes combined with X-ray power diffraction (XRD) analysis and atomic force microscopy (AFM) together with the Brunauer-Emmett-Teller (BET) surface area measurements.

2.4.6 **Sequential extraction procedures for iron**

Tessier et al. (1979) used bottom sediments as a proxy for suspended matter in sea water (due to the dilute nature of suspended particles), and stated this could conceptually be fractioned and subjected to sequential extraction techniques already developed for soils and sediments (Tessier et al., 1979). However, given this and despite this success and further development of these methods, there remains some uncertainty surrounding application to defining definitive environmental nanoparticle mineralogy in more dilute (iron) systems (Schröder et al., 2016, Raiswell and Canfield, 2012). It should also be acknowledged that there are a number of operational parameters that influence the success of sequential extraction methods such as, pH,

particles size, reagents used, temperature etc. which all leave the process open to both operator and instrument error (Filgueiras et al., 2002).Poulton and Canfield (Poulton and Canfield, 2005) devised a widely used method to selectively separate iron phases in sediment (rock) mixtures where other techniques are unable to provide physical separation (e.g. where laser ablation or micro-drilling are unable to target the complexities of the sample to separate it). This has been used as a proxy for mineralogy in environmental samples, where reactive iron species are often of an amorphous, colloidal or nanoparticulate nature that cannot be measured easily using XRD. However, many environmental samples comprise a diversity of grain sizes and crystallinities which influence solubility. Because sequential extraction procedures rely on distinct solubilities for each extracted mineral, there is the possibility that incomplete or overreaching extraction of minerals might occur during any of the extraction steps. This obviously sheds some uncertainty on the results (Schröder et al., 2016, Filgueiras et al., 2002, Poulton and Canfield, 2005). Schröder et al. (2016) demonstrated the usefulness of verifying each extraction using ^{57}Fe Mössbauer spectroscopy, thus complementing and validating results by combining the techniques. Where particulate iron is found in the nanoparticle range, and concentration is of a dilute nature e.g. in natural water environments, it is apparent that the Poulton and Canfield (2005) extraction method might not be easily applied, if indeed it is feasible at all. As discussed in the introduction (Chapter 1), the properties displayed by nanoparticles and fine colloids means their reactivity can differ greatly from their bulk counterparts. This is compounded by a general trend of environmental iron oxide nanoparticles displaying poor crystallinity, affecting solubility (Schwertmann, 1991).

2.4.7 **X- ray Absorption Spectroscopy (XAS)**

XAS techniques are used in many fields of investigation, including: general x-ray use, materials research, catalysis, molecular physics, biology/life sciences, environmental and geosciences, astronomy. They are used to measure the linear absorption coefficient μ(E), where XAFS is X-ray

Absorption Fine Structure is commonly used and is divided into the 'near edge' region: XANES (X-ray Absorption Near Edge Spectroscopy); NEXAFS (Near-Edge X-ray Absorption Fine Structure) and the 'extended' region, Extended X-ray Absorption Fine Structure (EXAFS) (Sassi et al., 2017). XAS methods can be used to identify and discriminate among crystallographically similar phases beyond the capabilities of XRD (Balasubramanian et al., 2014). Because these techniques do not require long range translational order, some success is possible when investigating amorphous materials, liquids, (poly)crystalline solids, and molecular gases. XAS is suited to synchrotron radiation sources as these can provide: an extremely intense, often well-collimated beam and a broad-spectrum to tune X-ray energy. However, interpretation and fitting are model dependent and well-known standards are often needed. Despite higher resolution, it can be difficult to separate contributions from different species and this can pose issues when spatial resolution is important i.e. resolution much lower than TEM: ~10 μm for EXAFS and 1 μm for XANES. Despite employing the latest in synchrotron-based X-ray absorption spectroscopy (XAS) to investigate the mineralogy of amorphous iron nanoparticles, for example, in glacial melt, some studies have (for a large fraction of these particles) been unable to derive definitive mineralogy (Hawkings et al., 2014). Fe L-Edge X-ray Absorption Spectroscopy demonstrates issues with defining mineralogy for amorphous nanoparticles and agglomerates in aquatic natural nanoparticles (Von Der Heyden et al., 2019).

2.4.7.1 Extended X-ray Absorption Fine Structure (EXAFS)

EXAFS is a particularly useful tool for the environmental chemistry and geochemistry fields as it can inform the location of a given atom in a crystal structure for example, the determination of location of (a given) atom in a crystalline or amorphous material with more than 1 type of cation site. However, there is limited information where there are relatively similar sites e.g. averaged metal-oxygen distances, and here alternative techniques should be sought other than single

crystal x-ray or neutron diffraction techniques (Gonzalez et al., 2014, Lu et al., 2011, Sheng et al., 2016, Teo, 2012).

2.4.7.2 X-ray Absorption Fine Structure (XANES)

XANES can determine an atom's valence/oxidation state and chemical state of elements even in microscopic quantities in bulk medium with large background. It is element specific and can be targeted to specific metals. XANES can provide formal valence (non-destructive), providing information on coordination environment, including subtle geometrical distortions (3D structure). There are some constraints, however, for example, there is potential for sample destruction. Additionally, the determination of oxidation state and scattering atom may be hindered due to multiple scatterings by photoelectrons and auger electrons which can occur if vacancies are induced by other interactions (Gonzalez et al., 2014, Reinsch et al., 2010, Sassi et al., 2017)

2.4.8 **Mössbauer spectroscopy (MBS)**

Mössbauer spectroscopy (^{57}Fe) (MBS) is used in iron mineralogy to quantitatively probe the electronic, magnetic, structural properties of a given material including: valence state and site occupancy of iron in a given site and/or individual mineral; coordination polyhedron type occupied by iron atoms and redox ratios (Murad, 2018, Long and Grandjean, 2013). A benefit of MBS (for iron mineralogy determination) is that iron is the only element detected, making it free from matrix effects (Gütlich et al., 2010).

Mössbauer spectroscopy is well suited for the mineralogical characterisation of iron-bearing nanoparticles in many environmental samples, despite this it may be pushed past reasonable expectations regarding sample collection, preparation and measurement times, when investigating nanoparticulate iron in more dilute systems and/or where the particles are amorphous. For example, iron-bearing nanoparticles found in the oceans, sea ice or glacial melt, rivers, lakes and ground water. Constraints of conventional MBS include it being a *bulk* technique

and sample material must be measured in the solid state, not ideal for water samples unless frozen or freeze dried. In addition, optimal experimental conditions must be achieved i.e. sample preparation and thickness are paramount to success. Although these are achievable for some samples, they are not always for others e.g. for those already discussed: amorphous nanoparticles, or samples where iron concentration is too dilute such as in natural water environments. There might also be situations where the determination of total Fe (atoms) is not possible due to the iron concentration related to other elements present (Bancroft, 1973, Long and Grandjean, 2013).

When analysing MBS spectra, different minerals' site geometries can be the same and require further analyses using complementary technique(s) (Jilbert et al., 2018). Despite the advantages of only iron being detected, this feature also restricts the analyses to only iron which (in some cases) calls for complementary analyses of the sample matrix. Despite this however, we acknowledge that a multi-analysis approach is usually needed for iron-bearing nanoparticle characterisation. Conventional Mössbauer spectroscopy (MBS) provides feasible options for determining definitive iron mineralogy in some natural samples (soil, rock and sediment), however the dilute nature of iron bearing nanoparticles and small colloids in natural water environments poses a significant issue regarding sample iron content, achievable sample volumes and particle amorphicity (Schröder et al., 2016). In conventional Mössbauer spectroscopy the ideal absorber contains 10 mg Fe per cm^2. Reasonable Mössbauer spectra can still be obtained from samples containing one order of magnitude less iron, but only if long measurement times are allowed for. The dilute nature of the iron-bearing particulate fraction in seawater demands filtration of up to 1000 litres of natural waters to gain enough material for a conventional Mössbauer measurement. In river systems with a high iron load, initial sample volumes are still in the range of 10s to 100s of litres. Collecting such large volumes of water destroys temporal and spatial relationships through uncontrolled mixing and condensing the particulate fraction onto a single filter, otherwise mm-sized sample volumes are not operationally feasible.

2.4.8.1 The ^{57}Fe Synchrotron Mössbauer Source (SMS)

The ^{57}Fe Synchrotron Mössbauer Source at the ESRF (European Synchrotron Radiation Facility, Grenoble, France) provides energy-domain Mössbauer spectroscopy using synchrotron radiation (Potapkin et al., 2012, Smirnov et al., 1997). The beam of filtered *γ* radiation required for the Mössbauer experiment is of high brilliance, can be focused to a 10 μm × 5 μm spot size, (and is fully resonant and fully polarized. In contrast to conventional Mössbauer spectroscopy, the micron-sized diameter beam of the SMS allows investigation of microscopic sample volumes that can be extracted from a few litres of water (2 to 10 L), ideal for dilute environmental samples. This ensures that spatial and temporal sample integrity are maintained. In addition, the high luminosity of the synchrotron beam and the absence of non-resonant photons in the SMS set-up provides a high data quality output achieved in a significantly shorter amount of time than possible with any conventional Mössbauer set up (Schröder et al., 2016, Cini et al., 2018, Potapkin et al., 2012). However, success of this method is dependent upon removal of most of the sample waters. The sample matrix must be in a solid state, which requires freezing of suspensions.

2.5 Discussion and conclusions

As previously discussed, characterisation of both naturally occurring and synthesized iron bearing nanoparticles is imperative if we are to understand their physical and chemical behaviour in their environments. Studies of both natural and manufactured nanoparticles are well documented and, have advanced our understanding of these properties regarding their transport and fate in differing environments. However, a better mechanistic understanding of nanoparticle iron transport is needed to inform models within the diverse array of systems in which these nanoparticles exist, interact with and influence their environments, including: atmospheric, soil, fluvial, lacustrine, ocean biogeochemical and climate processes, environmental hazards and toxicology, biomedical interactions, space and deep earth processes.

Mineralogical determination of iron(bearing) nanoparticles often requires pre-concentration and isolation steps. Prior to mineralogical characterisation, it is also necessary to determine the success of these methods and resolve the size fraction of interest. The defined 'size' of a nanoparticle covers an array of different measurements that can be applied to nanoparticles and can be correlated to a range of inherent and often interrelating properties. Nanoparticles are often defined as being <100 nm in one dimension but can also include aggregates and agglomerates (colloids) (Raiswell and Canfield, 2012). The most appropriate choice of technique and instrumentation must be considered when deciding which size boundaries i.e. internal or external, are important to measure to be able to determine size correlated properties to enhance engineered iron-bearing nanoparticle application, and to successfully investigate the properties of natural nanoparticles and colloids. Iron mineralogy is key to investigating the behaviour of iron bearing nanoparticles in a range of environments. Successfully modelling potential changes, transport and fate of natural and engineered particles is dependent upon the development of methods to provide constrained characterisation of these particles at the nanoscale.

Many of the size determination techniques described above do not allow for physical size fractionation of these particles to enable onward analysis of the mineralogy in each defined size fraction. However, DLS is shown to be useful for confirming the particles sizes eluted from AF^4 or from other filtration techniques to confirm separation success by further defining the separated size fractions based on hydrodynamic diameter. As discussed, the DLS technique is subject to an array of assumptions and can pose some extra difficulties when samples are polydisperse or prone to aggregation, as most natural nanoparticles and colloids in water samples are. By coupling DLS to AF^4 this can be somewhat mitigated. The advantage of AF^4 for particle size fractionation is that it mitigates some of the over, or under -estimation of particle (size) concentration, inherent with other methods of size fractionation discussed above e.g. filtration. Although microscopy i.e. SEM (3 dimensional sample surface information with ~0.5 nm resolution) and TEM (2 dimensional inner sample structure with greater resolution than SEM) techniques

better cope with polydispersity in samples and give direct (visualization) measurements, these techniques come with their own limitations. TEM analysis for particle sizing has a trade-off when statistical accuracy in sample populations is needed (Pyrz and Buttrey, 2008), and sample preparation can be extensive and destructive. TEM often requires a very thin sample. AFM offers an advantage over DLS in that it can cope better with non-monodisperse (bimodal or polydisperse) samples in aqueous solution. However, calculation of the ratio of sizes in a sample population from AFM scans is not always accurate, so estimation of the distribution of particles sizes might present an element of error. The benefit of DLS over AFM is that it can be adapted to cope with polydispersity. AFM analysis, however is not influenced by particle shape, making it a useful precursor to screen samples prior to full DLS analysis (Hoo et al., 2008).

Mineralogical investigation of engineered iron(-bearing) nanoparticles is well documented and synthesis is well constrained as discussed in section 2.3.2. However, obtaining definitive mineralogy of natural iron-bearing nanoparticles, or of released particles (engineered or incidental) presents a difficult task for the reasons discussed previously including, particle size and morphology (e.g. amorphous phases), dilute systems (e.g. natural water environments, particularly as salinity increases) or matrix interferences. Studies employing XAS (XANES and EXAFS) have demonstrated an inability to successfully resolve iron mineralogy of natural nanoparticles in natural water environments and in sea ice melt (Von Der Heyden et al., 2019).

Conventional Mössbauer Spectroscopy, although ideal for iron bearing nanoparticle mineralogy, becomes unfeasible due to sample volume constraints and iron concentrations found in more dilute systems such as the operationally defined dissolved fraction in natural water environments. However, SMS (synchrotron based Mössbauer techniques) have the potential to overcome these limitations by needing only microscopic volumes of sample material for a successful measurement. Some of the particle sizing techniques discussed in this review can potentially be combined with successful isolation and concentration techniques. For example, AF^4 coupled to

DLS and ICP-MS, for size and element analysis are shown to be successful techniques for natural nanoparticle characterisation. Success of these methods is optimal when using small sample volumes. It, therefore, appears feasible that a multi-analytical approach could provide a means for separation of size fractions for onward mineralogical analysis. Exploring the development of AF^4 to provide successful collection of particles, and optimising methods for effective water removal, might be a way to facilitate Mössbauer analysis of iron dilute water samples and optimisation of SMS sample preparation and techniques to provide definitive mineralogy in dilute systems such as rivers, sea ice and even open oceans.

3. The behaviour of iron-bearing particles along a salinity gradient: Loch Etive

3.1 Introduction

In the oceans inputs such as dissolved organic matter, major nutrients and trace elements such as iron are involved in key biogeochemical processes and can exert controls on primary productivity (Mori et al., 2019, Hendy, 2015). Over the last decade, studies have reported an increase of iron delivery to coastal waters in northern Europe evidenced by increasing iron concentrations in surface waters and estuaries (Ekström et al., 2016, Kritzberg and Ekström, 2012). It is suggested that this increase in exports also indicates increases of iron exported from soils, through rivers to the coastal oceans (Herzog et al., 2017). Despite these known increases in iron delivery there is marked variation in the iron transport capacity of different rivers (Krachler et al., 2016, Kritzberg et al., 2014). Estuarine systems connect rivers to the sea and play an important role in the delivery of organic and inorganic inputs to coastal waters (Abualhaija et al., 2015, Herzog et al., 2020).

It is generally accepted that most of the iron-organic matter particles within the operationally defined dissolved fraction of natural waters will aggregate and flocculate (sediment out) as salinity increases (Hunter et al., 1997, Keller et al., 2010, Yang et al., 2017). Studies have shown non-conservative behaviour of iron in estuarine systems (Daneshvar, 2015), and it is estimated that most of the riverine iron removal in estuaries (up to 95%) takes place at low salinities (~5 psu) (Sholkovitz et al., 1978, Sholkovitz, 1978). However, there is evidence to demonstrate that associations between iron and organic matter in rivers allow some submicron iron-bearing particles to transcend the salinity gradient and reach the coastal ocean (Batchelli et al., 2010, Jirsa et al., 2013, Oleinikova et al., 2018). Despite this, many of these biogeochemical interactions are still poorly understood and investigation is ongoing to elucidate which particles behave in this way, and why (Muller, 2018).

Estuaries are biogeochemically complex systems involving external inputs (e.g. from rivers or groundwater) and internal cycling (e.g. remineralisation, nutrient cycling) (Mori et al., 2019, Oldham et al., 2017). Recent research addresses a diversity of these biogeochemical processes and includes laboratory mixing experiments to achieve salinity values to investigate, for example, iron in algal growth measurements (Krachler et al., 2015, Krachler et al., 2016), iron speciation (Herzog et al., 2017, Kritzberg et al., 2014), ligand complexation (Hopwood et al., 2015) and iron mineralogy particle size effects (Hirst et al., 2017, Von Der Heyden et al., 2019). Despite the advances in our knowledge surrounding the connections between iron and organic matter, including the developing understanding of the ability for some particles to remain in suspension at higher salinities, definitive mineralogical characterisation of the iron phases in the Fe-OM particles is lacking. Von der Heyden et al. (2019) highlight the diverse iron speciation and mineralogy found in natural aquatic environments and urge ongoing investigation of iron speciation and biogechemical behaviour as being crucial to our interpretation of environmental change. Additionally, despite demonstrating that Fe-OM particles are more stable than iron (oxy)hydroxides at increased salinities, Herzog et al. (2017, 2020) found Fe-OM complexes in salinity induced aggregates and iron (oxy)hydroxide nanoparticles surviving in higher salinity waters. They suggest that alongside the influence of salinity, organic matter and the iron phase on the transport of these particles, there are other complexities such as particle size and chemical/organic matter composition variables influencing the way these particles behave. As discussed, characterising river-borne Fe-OM particles and transport capabilities is at the forefront of understanding their fate and potential interactions.

Study Area: Loch Etive

Sea lochs on the west coast of Scotland drain predominantly from peatland and organo-mineral catchments thus the rivers and streams entering the sea lochs likely carry a high load of organic matter (Smeaton et al., 2017). The short distance between many of these catchments and the

coastal ocean facilitates source-to-sea research, therefore, these catchments should provide a good analogue for high latitude fjordic systems for the investigation of the transport, fate, and mineralogy of iron-bearing nanoparticles and colloids. The study area of Loch Etive and two of its main tributaries: River Awe and River Etive was chosen for its potential to provide insight into an extended gradient of salinity for iron-organic matter (Fe-OM) delivery to the coastal ocean. Loch Etive is a fjordic sea loch and as such it differs from some other coastal water inputs, for example, the short distance for Fe-OM transport found in the peat draining creeks and rivers of the Flow Country (Krachler et al., 2016), or sea ice or glacial systems (Raiswell et al., 2018).

Loch Etive has a large organo-mineral/peat dominated catchment, the largest catchment of all the sea lochs in Scotland, with high freshwater runoff which is rich in organic matter. The runoff provides a flux of terrestrial organic carbon into and through the loch. Organic matter fluxes into and out of the loch from the coastal ocean, interacting with the loch itself, its sediments, and with the coastal marine area (McKee et al., 2002).

The study was conducted to inform the initial stages for the development of methods to employ synchrotron Mössbauer techniques to investigate iron mineralogy in water borne particles. The main aim of this study was to gain insight into iron concentrations within physically defined size fractions within the dissolved fraction of water at different salinities. Iron concentration data was used to investigate associations between particle size and iron concentration to inform size ranges where these particles reside. Understanding the particle size ranges in which iron is partitioned in a range of water environments formed the initial stage of investigation into characterising these particles.

3.2 Materials and Methods

3.2.1 Study area and sampling sites

The selection of Loch Etive and its catchment was made for the reasons outlined above: and included: consideration of the high runoff, rich in organic matter to the loch, Fe-OM associations, access to a salinity transect, ease of access to SAMS research vessels, laboratories and equipment for sample storage and processing. Figure 3.1 shows the site of Loch Etive on the west coast of Scotland.

Figure 3.1. Loch Etive sampling sites are within the red boxed area.

Loch Etive catchment properties

Loch Etive was formed during the retreat of glaciers from Scotland and is categorised as a glacially over-deepened trough. It has a larger rainwater catchment than any other Scottish fjord, with a total catchment area of approximately 1350 km^2 (Audsley et al., 2016). Three main rivers directly

discharge into the loch: River Etive, River Kinglass and River Awe. The River Awe drains into Loch Etive from Loch Awe, providing an estimated 60% of the total freshwater input. A hydro-electric scheme regulates the River Awe flow with the potential to significantly modify salinity at Bonawe (Figure 3.2, sampling point 3). The land cover in the Loch Etive upper catchment consists bog (~5%) and montane (~11 %) and in the lower catchment consists broadleaved woodland (~2%), coniferous woodland (~25 %), rough grassland (~ %), improved grassland (53%) (Morton et al., 2011).

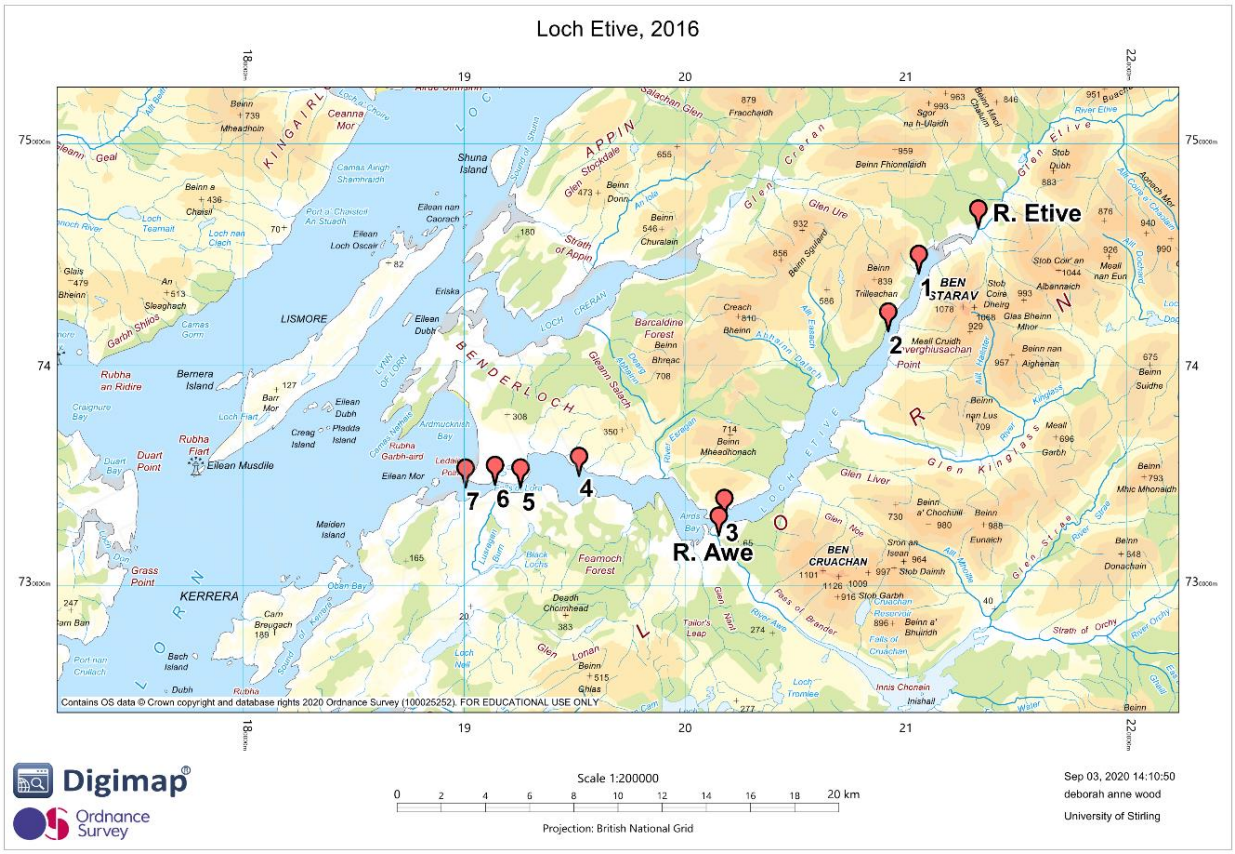

Figure 3.2. Loch Etive sampling sites (stations).

The topsoil organic carbon content for both the River Etive and River Awe is predominantly in the organo-mineral to the organic category, dominated by >35% organic soils in the mid to upper reaches of the catchments (Lilly and Donnelly, 2012). The most dominant soil types are podzols, which compose approximately 70% with some peats (21 %), brown earths (8 %) and gleys (1 %). (Soil Survey of Scotland, 1981). The following catchment geology associated with Loch Etive is

described based on BGS Geology. River Etive catchment geology comprises mainly felsic and mafic igneous intrusions with River Awe catchment geology comprising Argyll Group psammite, semipelite and pelite, extrusive mafic lava and tuff, Appin group quartzite, smaller felsic intrusions, Appin group graphitic pelite, calcareous pelite, calcsilicate rock and psammite. Superficial deposits are mainly (Diamacton) till, some sand and gravels and peat (from DiGMapGB-625, with the permission of the British Geological Survey ©UKRI. All rights Reserved).

3.2.2 **Field sampling**

3.2.2.1 Loch Etive sampling

Water samples were collected on a one day cruise in January 2016. The sampling and onsite measurements were conducted from the afterdeck of the Seòl Mara, The Scottish Association for Marine Science (SAMS) research vessel by winching a Seabird conductivity, temperature, and depth (CTD) profiler and rosette sampler loaded with Niskin bottles. This was set to sample and take measurements of a vertical profile of the water column at pre-specified depths of 1 m, 6 m and 10 m (station 1 also included the variables at 4m). Collected sample water was then transferred from the Niskin bottles directly to pre-cleaned Low-density polyethylene (LDPE) bottles. These were thrice rinsed using sample water from the Niskin bottle, filled (with no void space), capped, double bagged and placed in a cool box until being move to cold storage (at a temperature of 4°C) until initial processing the following day.

3.2.2.2 River sampling

River sampling and onsite measurements were also conducted in January 2016. Surface water samples were collected from each site. The sample container was held ~5 to 10cm below the water surface, upstream from the sampler whilst taking care to minimise disturbing the underlying sediment. Collection vessels were preconditioned with sample water (in triplicate) then fully filled, with no void space, closed, sealed with parafilm, double bagged and sealed with

cable ties. All samples were transported in a cooled and steady environment i.e. sample time of temperatures were maintained (without freezing) below the measured water temperatures at the sampling and then stored at 4 ^{o}C on arrival at the laboratory. Initial sample processing (filtration at 0.4 μm) was performed on return to the laboratory.

3.2.2.3 Onsite measurements: Loch Etive

Sampling positions were recorded using a handheld GPS and corroborated using the Seòl Mara's onboard navigation system. Salinity was initially checked using a Castaway mini CTD to test the approximate salinity of each proposed sample site. It was used to attain a suitable sampling position on the loch to provide a suitable salinity gradient, ensuring a range of salinities were sampled. The salinity measurements were taken using a salinity logger mounted to the CTD. Temperature and depth were also recorded using the logger attached to the CTD. Data was then downloaded once back onshore, using the logger's software. The pH was measured for each sample collected in the Niskin bottles by collecting the first litre of the sample in an acid clean, then thrice sample preconditioned LDPE bottle and calibrated portable pH probe was then used to record triplicate measurements.

3.2.2.4 Onsite measurements: Rivers Awe and Etive

For the Rivers Etive and Awe pH was measured using a HI-98127 pocket pH tester (Hanna Instruments Ltd, UK). Salinity was not measured as these are fresh water influxes, temperature (this was not recorded at sampling time) and bottom depth was not observed as only surface water sampling was conducted.

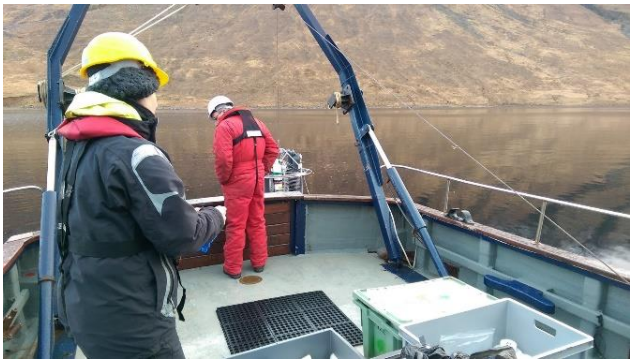

Figure 3.3. The Seòl Mara SAMS research vessel (top left photograph credit: SAMS). Photographs of after deck with CTD being winched into the loch (bottom left) and CTD loaded with Niskin bottles ready for deployment (right) (photograph credits: Deborah Wood, January 2016).

3.2.3 Sample processing

3.2.3.1 Physical size fractionation

Physical size parameters

To achieve consistency for data analysis, a conversion from kDa to nm was adopted for the purposes of this PhD project. The conversion is after Erickson (2009) and assumes particles are spherical: 0.66 nm ≈ 1 kDa. The assumption that the particles investigated in this study are likely spherical was adopted based on a study by Muller & Cuscov (2017), who demonstrated that the Fe-OM particles found in 0 PSU waters in the north east of Scotland, were in a size range between 200 nm and 1000 nm and were spherical in shape. This conversion in line with other recent

studies such as the data parameters that have been used for asymmetric flow field flow fractionation (AF^4) presented by Gottselig (2014) and Nischwitz (2016). There is no definite consensus in the available data over a number of aquatic colloid studies (Guo and Santschi, 2007). Particles sizes and their operationally defined size fractions used throughout this thesis are presented in Appendices for Chapter 3 (Figures 7.1 and 7.2).

Physical size fractionation

All samples were collected on the January 2016 cruise. The 400 nm filtration of the samples to isolate the 400 nm size fraction was processed by myself and the iron concentration for both the <400 nm and <3 nm fractions and the dissolved organic carbon (<700 nm) were measured at SAMS.

400 nm vacuum filtration (TFF)

Samples were vacuum filtered to remove the greater than 400 nm particulate fraction using 0.4 μm track-etched polycarbonate membranes.

- Aliquots of each unfiltered sample were stored (4^{o}C) for later analysis
- Aliquots of 400 nm filtrate were stored (4^{o}C) for later iron analysis

The remaining filtrate (<400 nm) was transferred to cleaned LDPE 2 L bottles and stored at 4^{o}C until further processing.

66 nm tangential flow filtration

2 L of the 400 nm filtrate for each sample was passed through a tangential flow filtration system, housing a 100 kDa (66 nm) hydrophilic ceramic cassette. The TFF system was run until 200 mL of retentate was achieved. The retentate and permeate were stored (4^{o}C), clean, for later analysis, including aliquots for iron and other element concentration measurements.

Iron and carbon concentration in water samples (SAMS)

Total iron concentration was measured using ICP-MS for acid digested water samples at SAMS. Acid digest protocols are in the Appendices for Chapter 3 (section 7.3.1). DOC measurements (<700 nm) were analysed and provided by SAMS. These data were presented at MASTS: Annual Science Meeting 31 October – 2 November 2018: *Do peat organics facilitate estuarine dissolved Fe transport? A case study from Loch Etive*, presented by Crocket et al., 2018, and are intended for future publication on which I am a co- author.

Freeze drying: Aliquots of the water samples from all size fractions were pre-frozen and freeze dried for subsequent analysis (iron concentration and determination of Fe(II) and Fe(III)) to investigate this process for SMS techniques development as a water removal method.

Iron concentrations (Stirling)

The acid digested water samples were analysed for total iron using a XSERIES 2 ICP-MS (Thermo Scientific, Germany) using collision cell technology (CCT) to mitigate potential polyatomic interferences. Multi element standards (Merck, Germany) certified by the National Institute of Standards and Technology (NIST), internal standards (scandium (Sc) and rhodium (Rh)) and total procedural and laboratory blanks were included in each run. ICP-MS (Thermo Fisher series 2) analysis was performed on microwave HNO_3 digested and resolubilised aliquots (MARS 6 Microwave Digestion System). This analysis was undertaken to quality check the filtration and concentration procedures and to provide a suite of iron concentrations by physical size fraction. Standards, all sample dilutions and reagent blanks for ICP-MS were prepared using sample protocols, with ultrapure HNO_3 and Milli-Q water in a 2% matrix for freshwater samples, with a dilution factor of 20 for saline samples. When not being processed or analysed, all samples and aliquots were stored, double bagged, in clean lock-tight plastic boxes at 4 °C in the dark prior to processing and analysis.

Ferrozine assay

Spectrophotometric determination of Fe(II) and Fe(III) (Stookey, 1970) was conducted on freeze dried material. The resulting retentate (>66 nm <400 nm) was initially freeze dried then resolubilised using 18 ΩM (milli-Q) water prior to the ferrozine assay. Calibration curves are in Appendices for chapter 3 (section 3.7.3).

3.2.1 **Statistical analysis and treatment of data**

Normality of data was tested using the Anderson-Darling method. Variance analysis of data (one-way ANOVA) and post-hoc Tukey tests (for were performed to determine if there were differences in the means of the measured variables for pH, iron, carbon. Where normal distributions of data were not present, a Kruskal-Wallis test was used to determine whether the medians of the groups differed and post-hoc Mann-Whitney tests were used to determine whether the population means of paired groups differed. Regression (Fitted Line Plot) analysis was used to investigate relationships between sets of variables. All statistical tests were performed using Minitab 19 Statistical Software.

3.3 **Results**

3.3.1 **Field measurements**

Table 3.1 shows each station location (grid reference: OS) and the measured variables (temperature, salinity and pH) at sampling depths from the Loch Etive cruise.

Loch Etive salinity

During the sampling it was not possible to cover a full salinity transect (i.e. up to ~35 psu) as anticipated, however, a narrower salinity transect was achieved which Loch Etive salinities ranging from 8.32 psu to 24.30 psu (Table 3.1). Station locations are given in Table 3.1 and shown on the map in Figure 3.2. Salinity was measured by sampling depth (m) at each sampling station for Loch Etive.

Table 3.1. Loch Etive sampling campaign, January 2016. Site variables: temperature (°C), pH and salinity (psu); station coordinates (grid reference: OS), sampling depth (m), bottom depth (m) of loch (ascertained from the research vessel's onboard navigation system).

Sampling station (designated number)	Sampling depth (m)	Grid reference (OS)	Bottom depth of loch (m)	Temperature (°C)	pH	Salinity (psu)
1	4	NN1063944097	21.0	9.42	7.70	15.45
1	1	NN1063944097	21.0	n/d	n/d	8.32
1	6	NN1063944097	21.0	9.79	7.67	16.65
1	10	NN1063944097	21.0	10.27	7.63	17.85
2	1	NN0927641483	25.0	6.71	7.69	9.74
2	6	NN0927641483	25.0	9.67	7.70	16.92
2	10	NN0927641483	25.0	10.07	7.72	18.51
3	1	NN0184833060	24.5	7.37	7.76	13.54
3	6	NN0184833060	24.5	8.00	7.93	18.13
3	10	NN0184833060	24.5	8.30	7.93	19.37
4	1	NM9526334972	22.7	7.35	n/d	17.10
4	6	NM9526334972	22.7	7.74	n/d	20.96
4	10	NM9526334972	22.7	7.98	7.97	24.03
5	1	NM9262234417	20.2	7.47	7.91	19.43
5	6	NM9262234417	20.2	7.54	7.95	20.02
5	10	NM9262234417	20.2	7.48	7.97	19.47
6	1	NM9147034535	21.3	7.43	7.95	19.17
6	6	NM9147034535	21.3	7.46	7.92	19.32
6	10	NM9147034535	21.3	7.51	7.97	19.80
7	1	NM9012234443	34.5	7.58	7.95	20.68
7	6	NM9012234443	34.5	7.61	8.00	20.99
7	10	NM9012234443	34.5	7.61	7.99	20.99
River Etive	n/a	NN1219845852	n/a	n/d	7.24	n/d
River Awe	n/a	NN0109332337	n/a	n/d	6.75	n/d

Salinity measurements (Table 3.1) for Loch Etive are plotted by station number at sampling depth (Figure 3.4) show a distinct stratification of the upper basin with denser (more saline) water found with increasing depth in the upper basin. West of the Falls of Lora (Figure 3.2) beyond station number 4, an observed accumulation of denser (saltier) water is found at depth, after which this distinct stratification is no longer observed.

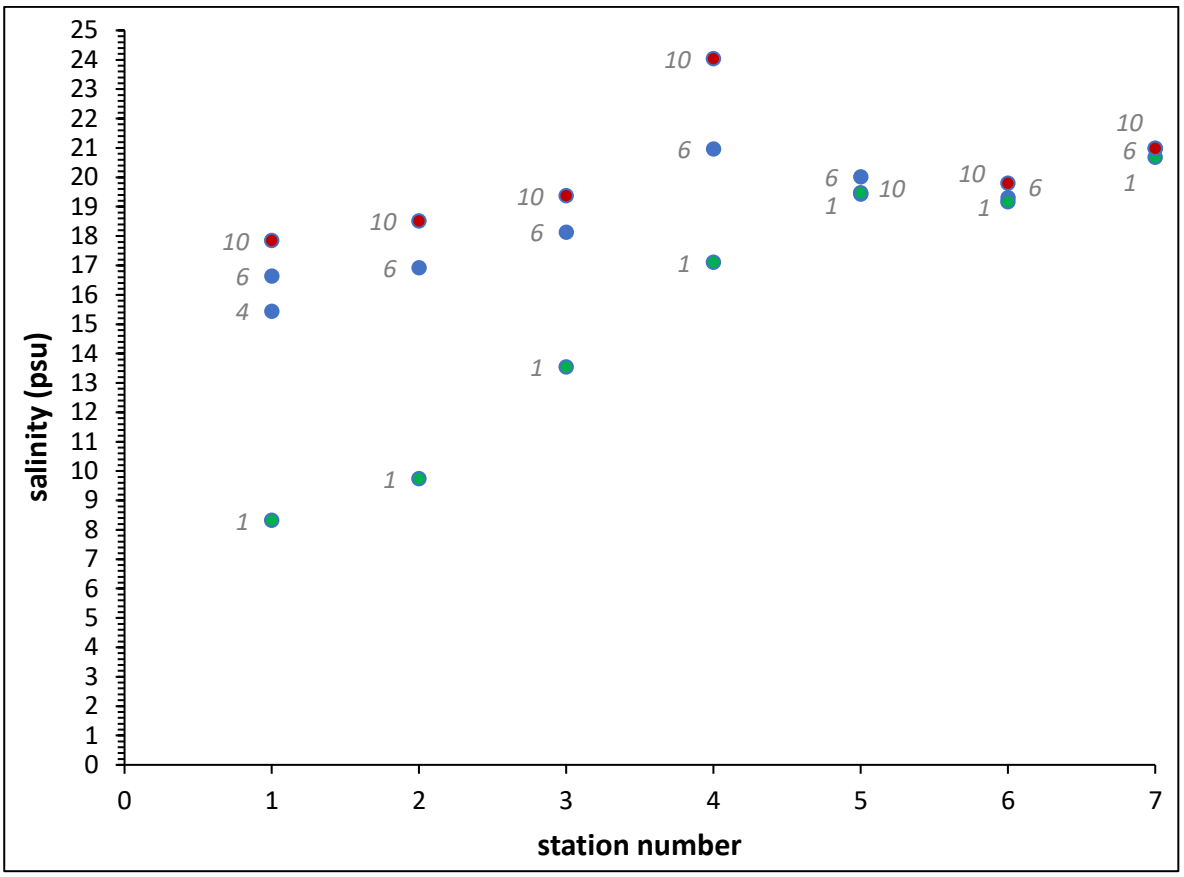

Figure 3.4. Loch Etive salinity (January 2016 sampling). Relationships between salinity (psu) and depth (m) by sampling station numbers: 1 (head of loch) to 7 (mouth of loch), situated within Loch Etive. Depth (m) is shown beside each closed circle symbol (red=10 m, blue=6 m and green=1 m) for each station (x-axis). Where x and y both equal 0, this is representative of the freshwater rivers Etive and Awe.

pH and salinity

As salinity increased, pH increased. A simple linear regression was calculated to predict pH based on salinity (Figure 3.5). A significant regression equation was found ($F(1,18)=86.67$, $p=0.000$, $R^2=0.83$). A Pearson's correlation was run to assess the relationship between pH and salinity. There was a strong positive correlation ($r(18)=0.910$, $p=0.000$).

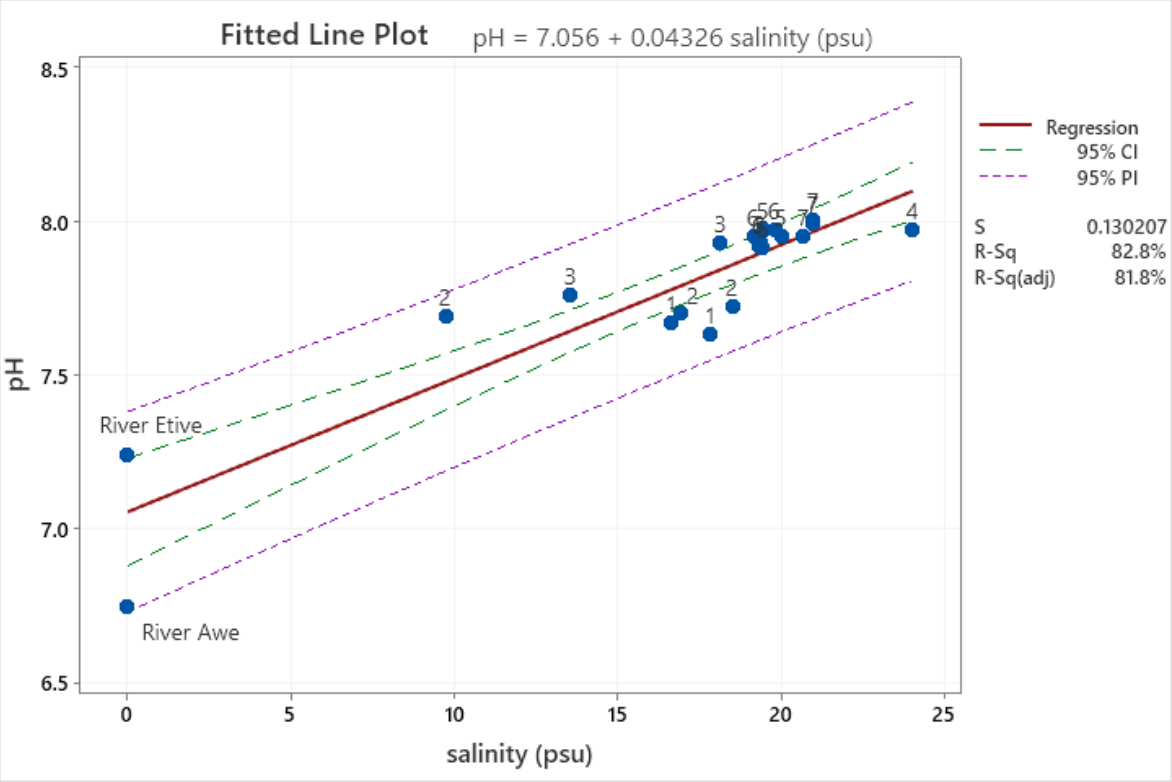

Figure 3.5. Loch Etive stations, River Etive and River Awe: regression analysis for pH as a response to salinity (R^2=0.83, *p*=0.000). Data labels are sampling station numbers (for individual measurements), CI = 95% confidence interval and PI = prediction interval i.e. 95% prediction bands.

Removal of the river sites (River Etive and River Awe) from the dataset presented above (Figure 3.5) produced the following results: a significant regression equation was found ($F(1,16)=15.46$, $p=0.001$, $R^2=0.83$). A Pearson's correlation was run to assess the relationship between pH and salinity. There was a strong positive correlation ($r(16)=0.701$, $p=0.001$).

3.3.2 Iron and dissolved organic carbon concentrations

Iron concentration

This section presents the iron and carbon concentration (measurements) conducted at the Scottish Association for Marine Science (SAMS).

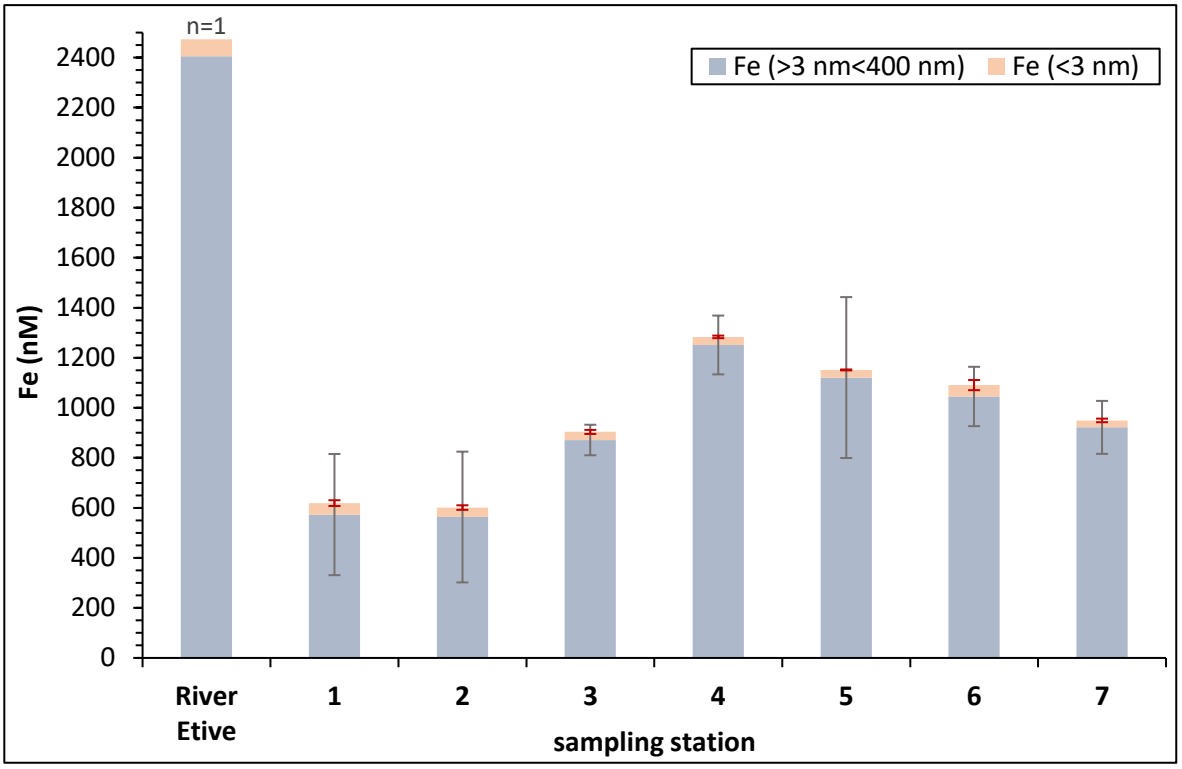

Figure 3.6. Iron concentrations from Etive sampling, 2016. Loch Etive iron concentrations (nM) for each sampling station: average iron concentrations of combined depths (1 m, 6 m and 10 m); <3 nm (pink) and >3 nm <400 nm (grey) physical size fractions (where n=3 the error bars represent 1x standard deviation). River Etive and the numbered stations represent the sampling sites along the length of Loch Etive with station 1 being at the head of the loch and 7 at the mouth.

River Etive iron concentration data was omitted from the following statistical analyses as there was only one recorded measurement in the <3 nm and <400 nm physical size fraction.

Table 3.2. Descriptive statistics for iron concentration (nM) for the less than 3 nm physical size fraction by station number for Loch Etive, 2018. Kruskal-Wallis test: H=7.10, 6 d.f., *p*=0.132 (the P value was calculated in Minitab 19 accounting for data constraints and the critical value for

H).

Station number	N	Median	Mean Rank	Z-Value
station 1	3	44.5640	16.7	1.71
station 2	3	36.0692	13.3	0.70
station 3	3	30.0146	9.0	-0.60
station 4	3	32.5528	10.0	-0.30
station 5	3	30.8825	8.0	-0.90
station 6	3	38.2994	14.3	1.01
station 7	3	26.6690	5.7	-1.61
Overall	21		11.0	

Iron concentration medians in the less than 3 nm physical size fraction for Loch Etive samples at each station (station numbers 1 to 7 in Figure 3.6) are not statistically different (Kruskal-Wallis test: H=7.10, 6 d.f., p=0.312). To compare the unique pairs of station data and to sense check the Kruskal-Wallis result, post hoc 2-sample Mann Whitney tests were conducted for all station pairs. These tests confirmed that there was no significant difference between each paired station median (p>0.05). Table 3.3 shows the summarised results.

Table 3.3. 2-sample Mann Whitney test: Fe (less than 3 nm physical size fraction) versus station. P values and achieved confidence (targeted confidence level = 95%).

Station number (n_1)	Station number (n_2)	P value	Achieved confidence (%)
1	2	0.663	91.91
1	3	0.190	91.91
1	4	0.190	91.91
1	5	0.081	91.91
1	6	0.386	85.11
1	7	0.190	91.91
2	3	0.663	91.91
2	4	0.663	91.91
2	5	0.383	91.91
2	6	0.773	85.11
2	7	0.190	91.91
3	4	1.000	91.91
3	5	1.000	91.91
3	6	1.000	91.91
3	7	0.663	91.91
4	5	0.663	91.91
4	6	0.773	85.11
4	7	0.383	91.91
5	6	0.773	91.91
5	7	0.663	91.91
6	7	0.386	85.11

There are differences in the iron concentration in the <400 nm size fraction (Figure 3.5) amongst the Loch Etive sampling stations 1 to 7 (one-way ANOVA: (F(6, 14)=4.95, p=0.06, R^2=0.68). Tukey pairwise comparisons (Table 3.4) show the mean groupings for the sites.

Table 3.4. Iron concentrations (nM) for the less than 400 nm physical size fraction by station number for Loch Etive, 2016. Tukey grouping information with 99.58% individual confidence

levels to obtain a 95% joint confidence level.

Station number	N	Mean Fe (nM)	Grouping
station 4	3	1283.6	A
station 5	3	1151	A B
station 6	3	1090.7	A B
station 7	3	949.5	A B
station 3	3	903.6	A B
station 1	3	619	B
station 2	3	601	B

Note: Means that do not share a letter are significantly different.

There are significant differences in the mean iron concentration between station 1 and station 4 and, between station 2 and station 4. There are no significant differences found between mean iron concentrations for all other paired stations (p>0.05) (Table 3.4).

Dissolved organic carbon

There are differences in the organic carbon concentration in the <700 nm size fraction amongst the Loch Etive sampling stations 1 to 7 (one-way ANOVA: (F(6, 14)=9.28, p=0.00, R^2=0.80). Tukey pairwise comparisons (Table 3.5) show the mean groupings for the sites.

Table 3.5. Carbon concentrations (nM) for the less than 700 nm physical size fraction by station number for Loch Etive, 2016. Tukey grouping information with 99.58% individual confidence levels to obtain a 95% joint confidence level.

Station (number)	N	Mean (nM)	Grouping
1	3	197202	A
2	3	182313	AB
3	3	165795	BC
5	3	156361	BC
6	3	152906	BC
7	3	146548	C
4	3	146029	C

There are significant differences in the mean carbon (less than 700 nm) (Table 3.5). Station 1, at the head of the loch, fed by the River Etive, has significantly higher carbon concentrations than

stations numbered 3 through to 4. Station 2 shares a grouping with station 1 but also a grouping with stations 3 to 6. However, both stations 7 and 4 (sharing a grouping) have significantly lower iron concentrations than stations 1 and 2 although the do share a grouping with stations 3 to 6. Carbon concentrations decrease from the head of the loch to the mouth.

Dissolved organic carbon and iron

Dissolved (less than 700 nm filtered particle size fraction) organic carbon concentrations were measured for sampling stations 1 to 7 (Figure 3.2).

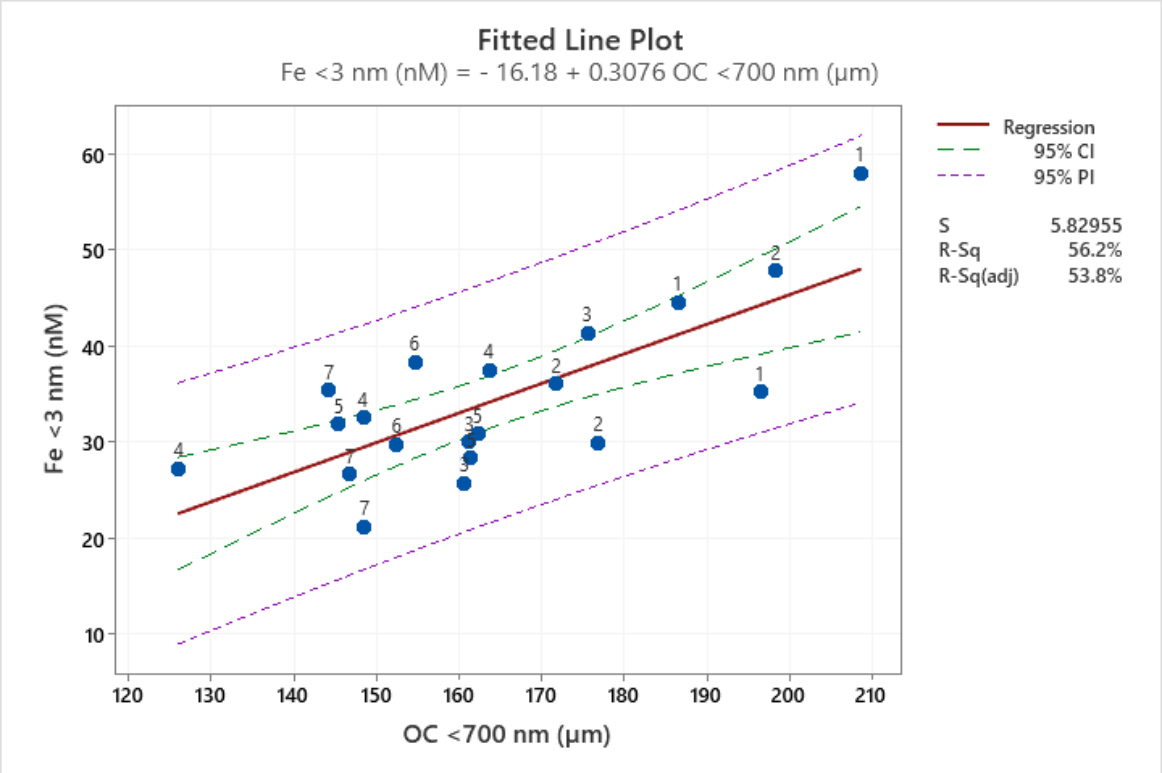

Figure 3.7. Loch Etive regression analysis for iron concentration in the less than 3 nm particle size fraction as a response to carbon concentration in the less than 700 nm particle size fraction (R^2=0.56, *p*=0.00). Data labels are sampling station numbers (for individual measurements), CI = 95% confidence interval and PI = prediction interval i.e. 95% prediction bands.

A simple linear regression was calculated to predict iron concentration in the less than 3 nm particle size fraction based on carbon concentration in the less than 700 nm particle size fraction (Figure 3.7). A significant regression equation was found ($F(1,18)=23.08$, $p=0.00$, $R^2=0.56$). A Pearson's correlation was run to assess the relationship between iron (<3 nm) and carbon (<700 nm). There was a strong positive correlation between iron and carbon ($r(18)=0.750$, $p=0.00$).

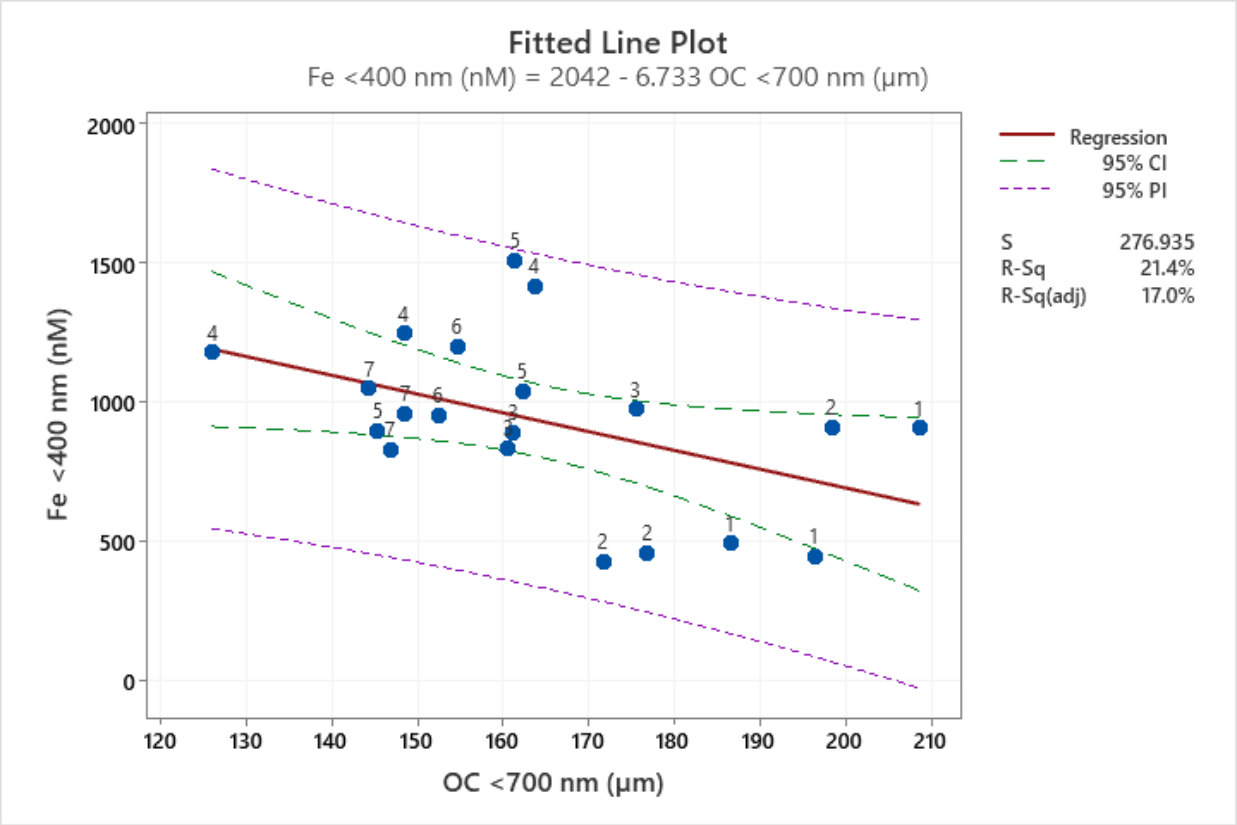

Figure 3.8. Loch Etive regression analysis for iron concentration in the less than 400 nm particle size fraction as a response to carbon concentration in the less than 700 nm particle size fraction ($R^2=0.21$, $p=0.04$). Data labels are sampling station numbers (for individual measurements), CI = 95% confidence interval and PI = prediction interval i.e. 95% prediction bands.

A simple linear regression was calculated to predict iron concentration in the less than 400 nm particle size fraction in response to carbon concentration in the less than 700 nm particle size fraction (Figure 3.8). A significant regression equation was found ($F(1,18)=4.90$, $p=0.04$, $R^2=0.21$).

A Pearson's correlation was run to assess the relationship between iron (<400 nm) and carbon (<700 nm). Iron shows a moderately weak negative correlation with carbon (in the less than 700 nm size fraction) ($r(18)= -0.463$, $p=0.04$).

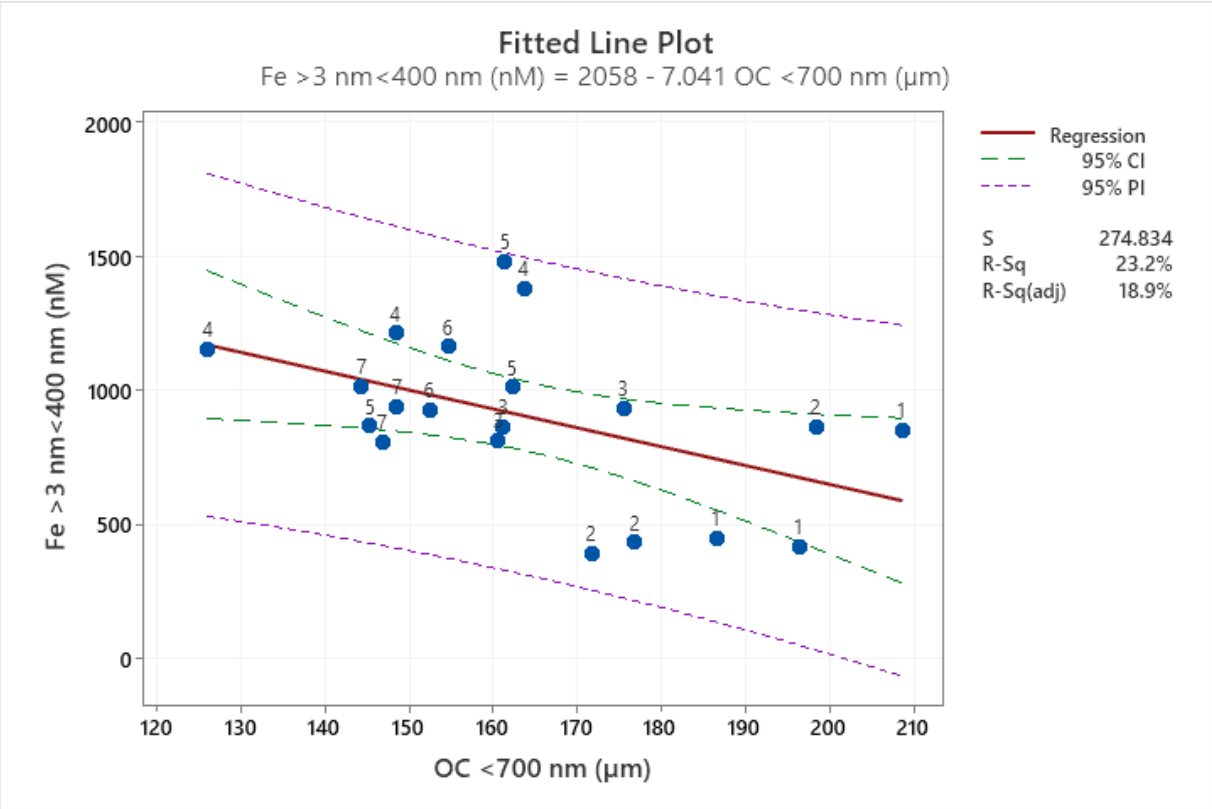

Figure 3.9. Loch Etive regression analysis for iron concentration in the greater than 3 nm, less than 400 nm particle size fraction as a response to carbon concentration in the less than 700 nm particle size fraction ($R^2=0.23$, $p=0.03$). Data labels are sampling station numbers (for individual measurements), CI = 95% confidence interval and PI = prediction interval i.e. 95% prediction bands.

A simple linear regression was calculated to predict iron concentration in the less than 3 nm, greater than 400 nm particle size fraction based on carbon concentration in the less than 700 nm particle size fraction (Figure 3.9). A significant regression equation was found ($F(1,18)=5.44$, $p=0.03$, $R^2=0.23$). A Pearson's correlation was run to assess the relationship between iron (>3

nm<400 nm) and carbon (<700 nm). There was a moderately weak negative correlation between iron and carbon ($r(18)= -0.482$, $p=0.03$).

Salinity and dissolved organic carbon

A simple linear regression was run to predict dissolved organic carbon concentration in the less than 700 nm particle size fraction based on salinity (Figure 3.10). A significant regression equation was found ($F(1,18)=62.03$, $p=0.00$, $R^2=0.78$). A Pearson's correlation was run to assess the relationship between dissolved organic carbon (<700 nm) and salinity. There was a strong negative correlation between dissolved organic carbon in the less than 700 nm size fraction and salinity ($r(18)= -0.880$, $p=0.00$). Organic carbon concentrations in the less than 700 nm physical size fraction decrease with increasing salinity.

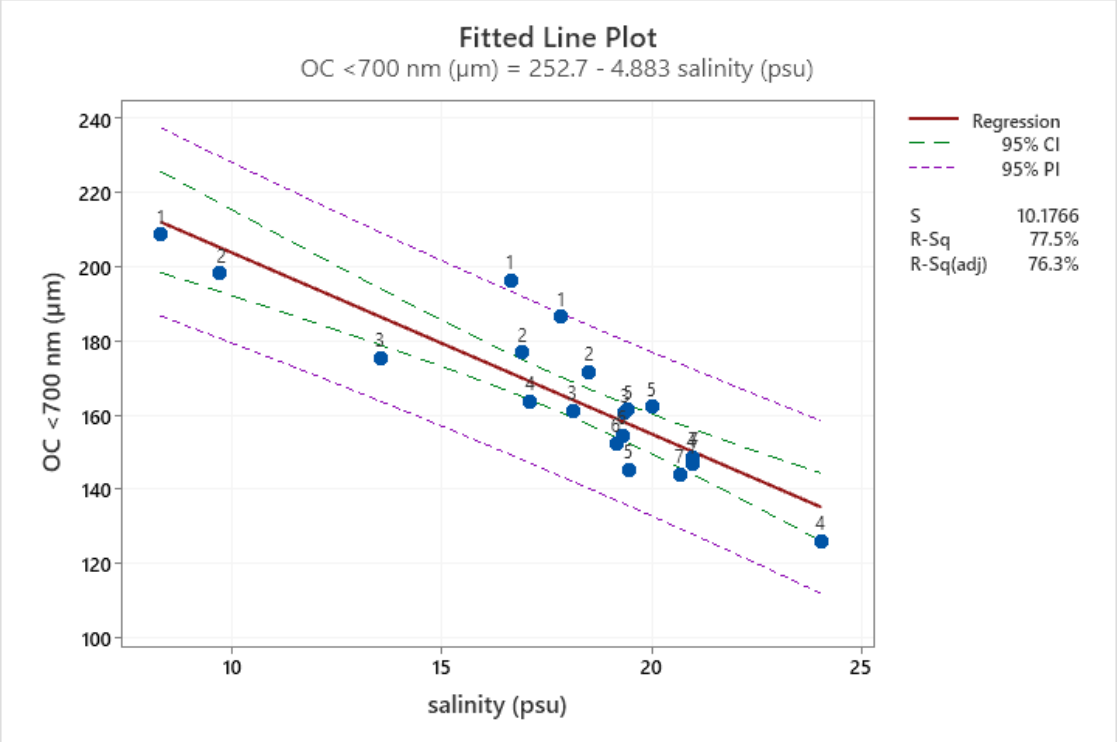

Figure 3.10. Loch Etive regression analysis for dissolved organic carbon concentration in the less than 700 nm particle size fraction as a response to salinity ($R^2=0.76$, $p=0.00$). Data labels are sampling station numbers (for individual measurements), CI = 95% confidence interval and PI = prediction interval i.e. 95% prediction bands.

Iron concentration and salinity

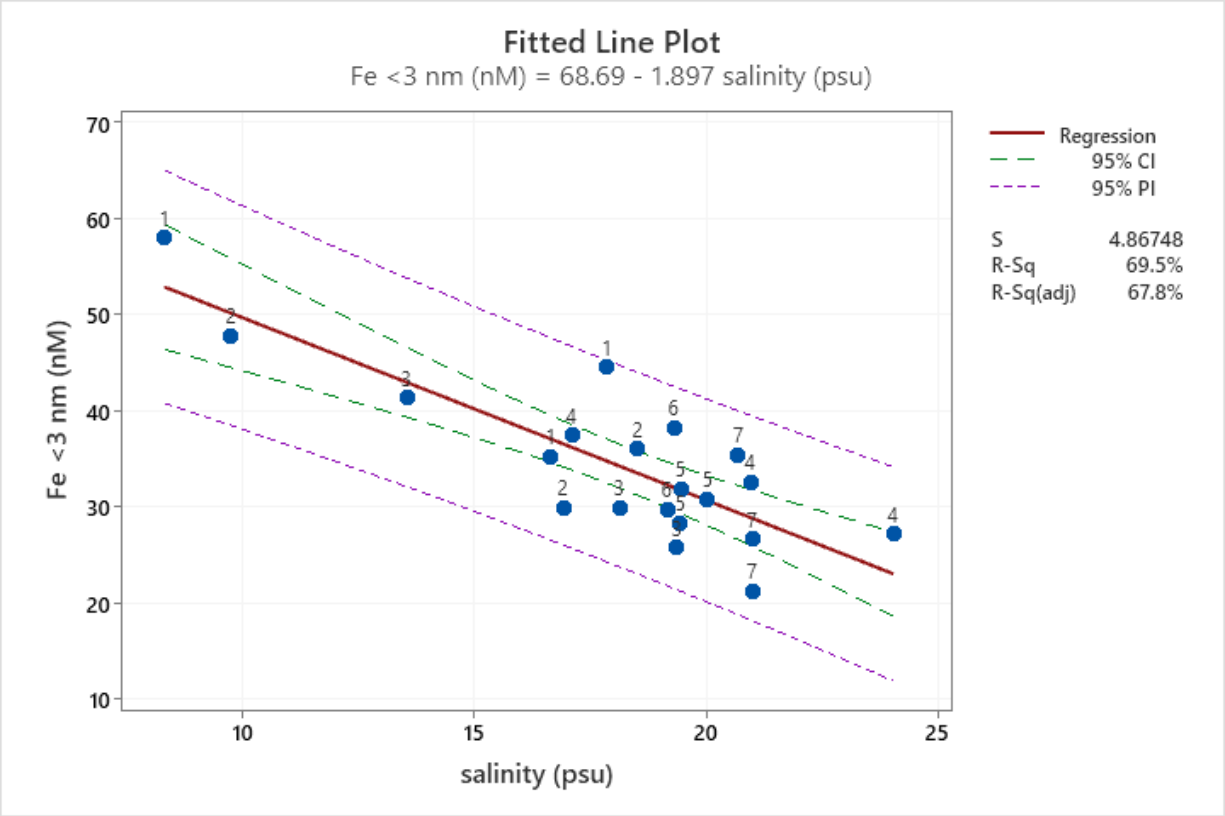

Figure 3.11. Loch Etive regression analysis for iron concentration in the less than 3 nm particle size fraction as a response to salinity (R^2=0.70, *p*=0.00). Data labels are sampling station numbers (for individual measurements), CI = 95% confidence interval and PI = prediction interval i.e. 95% prediction bands.

A simple linear regression was calculated to predict iron concentration in the less than 3 nm particle size fraction as a response to salinity (Figure 3.11). A significant regression equation was found ($F(1,18)=40.93$, $p=0.00$, $R^2=0.70$). A Pearson's correlation was run to assess the relationship between iron concentration (<3 nm) and salinity. There was a strong negative correlation between iron in the less than 3 nm size fraction and salinity ($r(18)= -0.830$, $p=0.00$). As salinity increases the iron concentration in the less than 3 nm physical size fraction decreases.

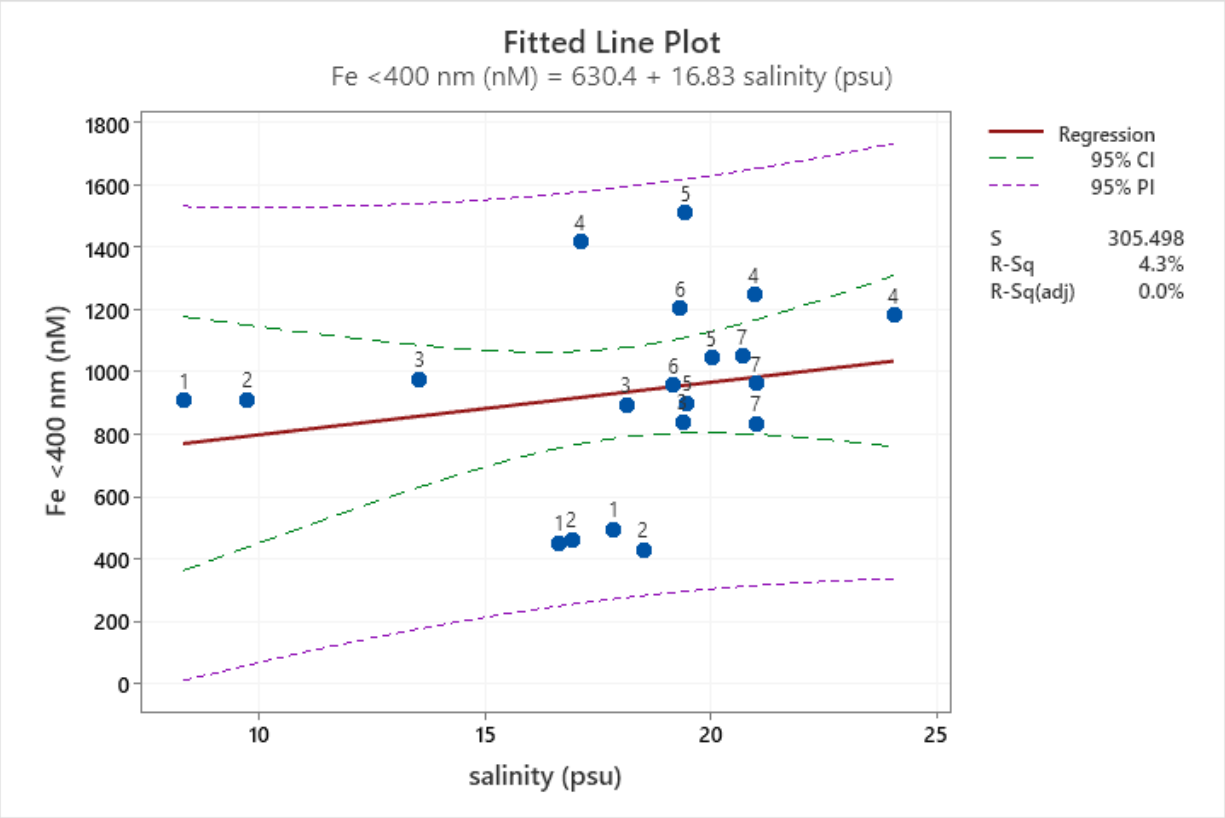

Figure 3.12. Loch Etive regression analysis for iron concentration in the less than 400 nm particle size fraction as a response to salinity (R^2=0.04, *p*=0.00). Data labels are sampling station numbers (for individual measurements), CI = 95% confidence interval and PI = prediction interval i.e. 95% prediction bands.

A simple linear regression was calculated to predict iron concentration in the less than 400 nm particle size fraction as a response to salinity (Figure 3.12). There was no significant relationship found ($F(1,18)=0.82$, $p=0.378$, R^2 of 0.04). A Pearson's correlation was run to assess the relationship between iron concentration (<400 nm) and salinity. There was no significant correlation between iron in the less than 400 nm size fraction and salinity ($r(18)= 0.208$, $p=0.38$).

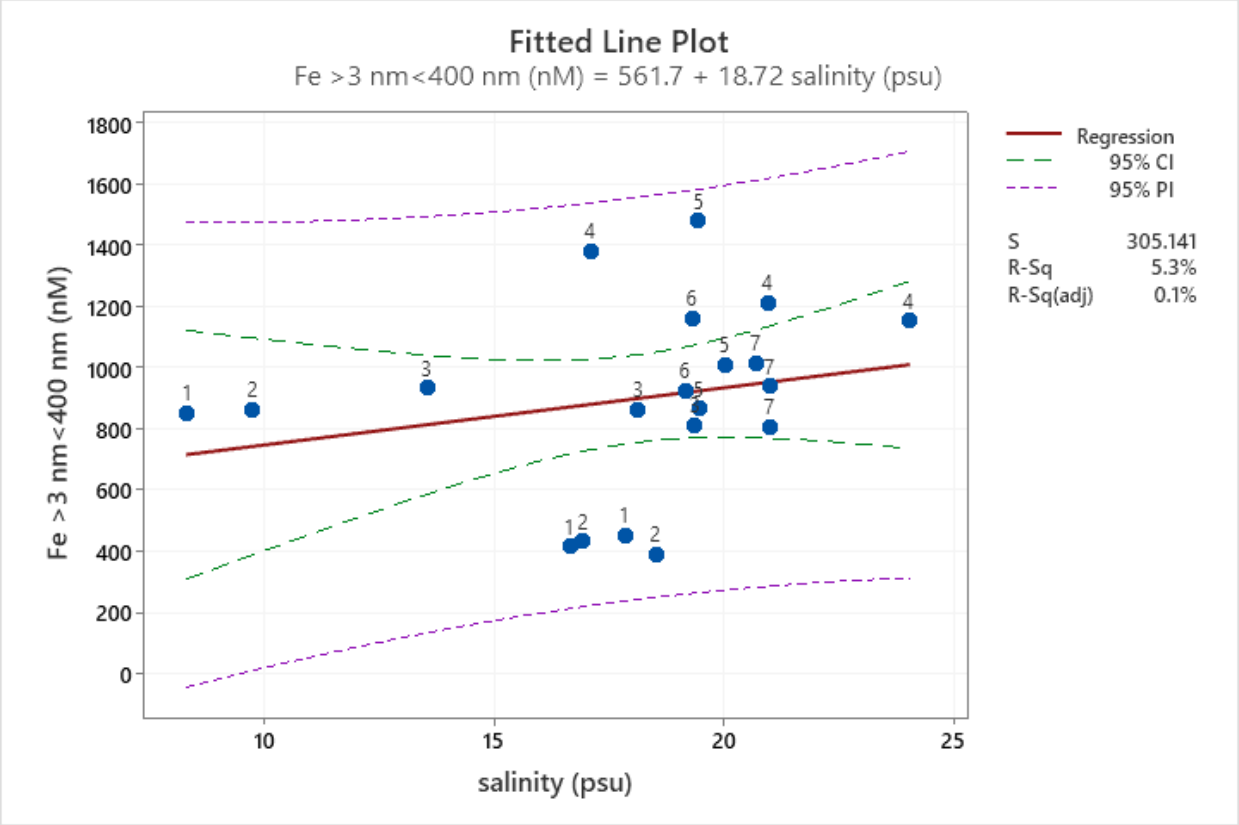

Figure 3.13. Loch Etive regression analysis for iron concentration in the less than 3 nm, greater than 400 nm particle size fraction as a response to salinity (R^2=0.05, *p*=0.33). Data labels are sampling station numbers (for individual measurements), CI = 95% confidence interval and PI = prediction interval i.e. 95% prediction bands.

A simple linear regression was calculated to predict iron concentration in the less than 3 nm greater than 400 nm particle size fraction as a response to salinity (Figure 3.13). There was no significant relationship found ($F(1,18)=1.01$, $p=0.33$, $R^2=0.05$). A Pearson's correlation was run to assess the relationship between iron concentration (>3 nm<400 nm) and salinity. There was no significant correlation between iron in the less than 3 nm, greater than 400 nm size fraction and salinity ($r(18)= 0.231$, $p=0.33$).

Iron concentrations (Stirling measurements)

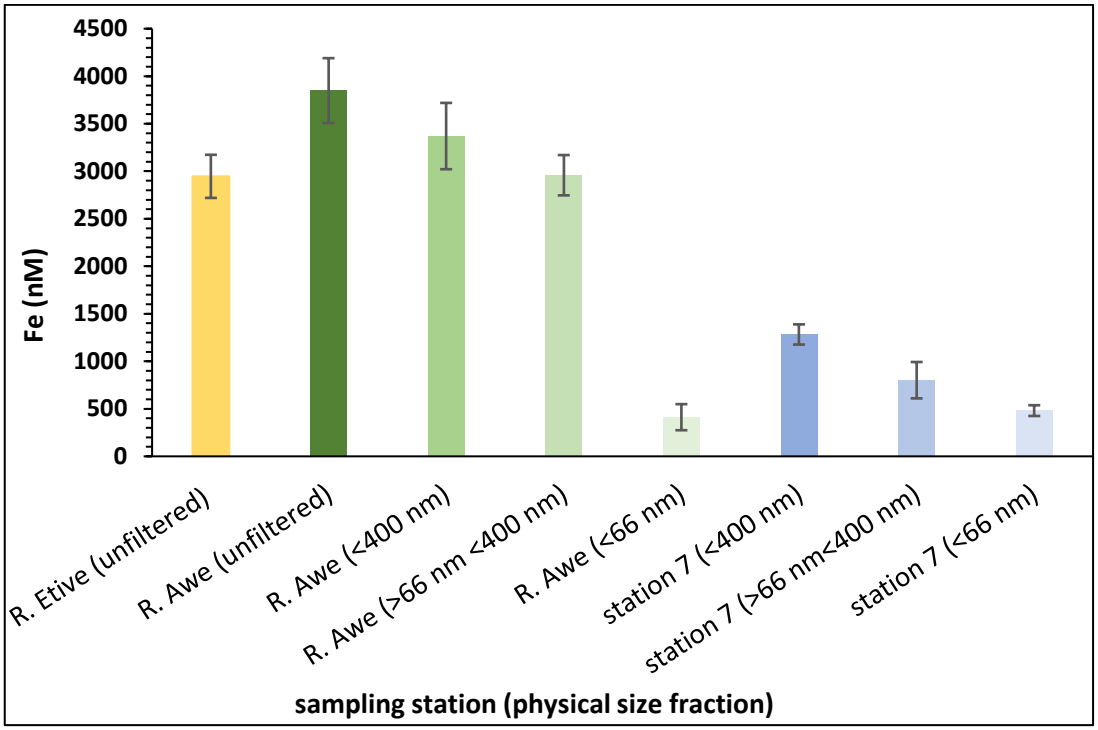

Figure 3.14. Iron concentrations, Etive, 2016 (by physical size fraction):

One-way ANOVAs were performed on the iron concentrations in the paired samples of the same physical size fraction for **1)** River Etive and River Awe (Unfiltered), **2)** River Awe and station 7 (less than 400 nm), **3)** River Awe and station 7 (greater than 66 nm less than 400 nm) and **4)** River Awe and station 7 (less than 66 nm) (Figure 3.14).

1) Iron concentration was different with a significantly higher concentration of iron in the unfiltered River Awe sample compared to River Etive ($F(1,4)=14.59$, $p=0.019$, $R^2=0.78$). A Tukey pairwise comparison confirmed the difference in groupings of means ($p=0.019$, CI = 95%).

2) Iron concentration in River Awe (less than 400 nm) and sampling station 7 (<400 nm) were different with a significantly higher concentration of iron in the River Awe ($F(1,4)=98.23$, $p=0.001$, $R^2=0.96$). A Tukey pairwise comparison confirmed the difference in groupings of means ($p=0.001$, CI = 95%).

3) Iron concentration in River Awe and sampling station 7 (greater than 66 nm less than 400 nm) were different with a significantly higher concentration of iron in the River Awe ($F(1,4)=171.18$, $p=0.000$, $R^2=0.98$). A Tukey pairwise comparison confirmed the difference in groupings of means ($p=0.000$, CI = 95%).

4) The iron concentration in River Awe and sampling station 7 (less than 66 nm) were not significantly different ($F(1,4)=0.66$, $p=0.463$, $R^2=0.14$). A Tukey pairwise comparison confirmed there was no difference in the grouping of means ($p=463$, CI = 95%).

SAMS iron concentrations versus Stirling iron concentrations

A difference was found when comparing the results from the SAMS iron concentration measurements with the Stirling university measurements for the less than 400 nm physically size fractioned samples from station 7 ($F(1,4)=14.25$, $p=0.020$, $R^2=0.78$ at 95% confidence level).

Iron concentrations (Stirling measurements): percentage iron concentration in physical size fractions

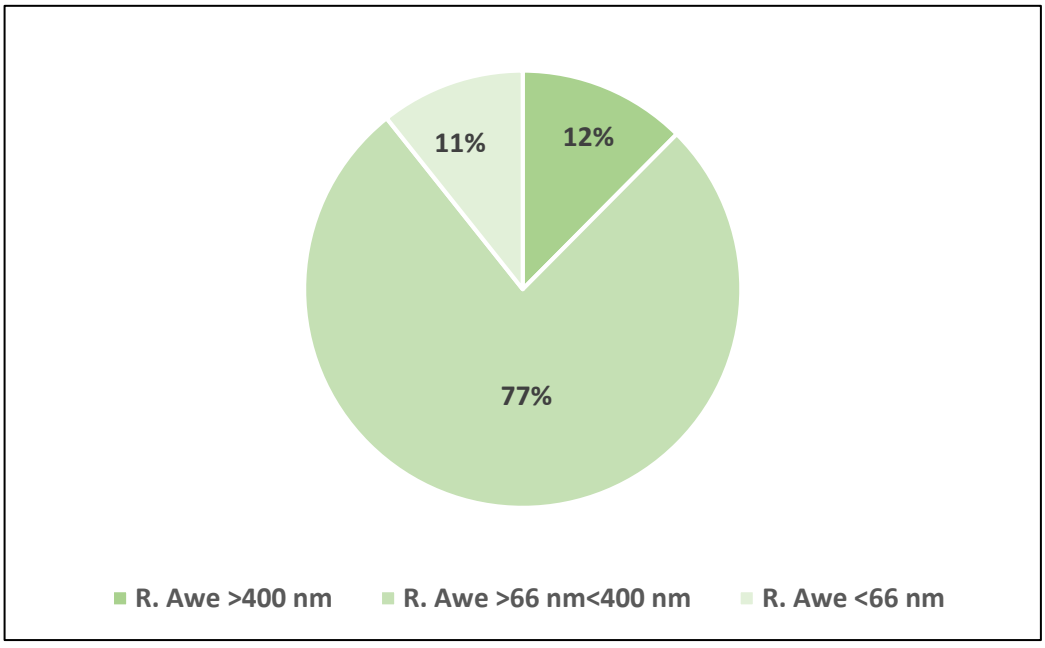

Figure 3.15. River Awe, January 2016: total iron in each physical size fraction as a percentage of the total iron in the unfiltered fraction (Stirling measurements).

Figure 3.15 shows the total iron in each physical size fraction as a percentage of the total iron in the unfiltered fraction for the River Awe. Most of the iron is found in the less than 400 nm physical size fraction (88%), with the majority of the iron found within this fraction being in the colloidal fraction i.e. greater than 66 nm (77%).

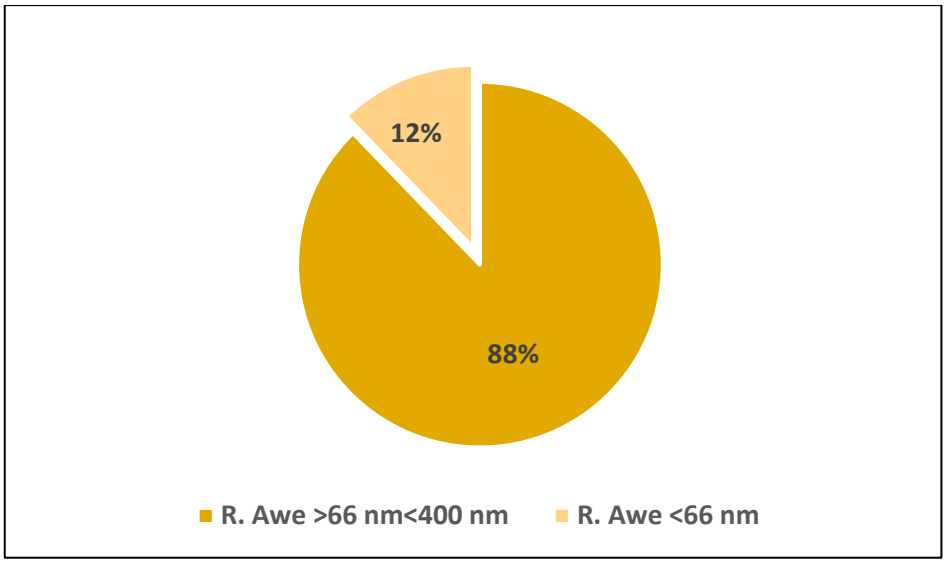

Figure 3.16. River Awe percentage iron in the total dissolved (<400 nm) fraction by size fraction: <66 nm and >66 nm<400 nm.

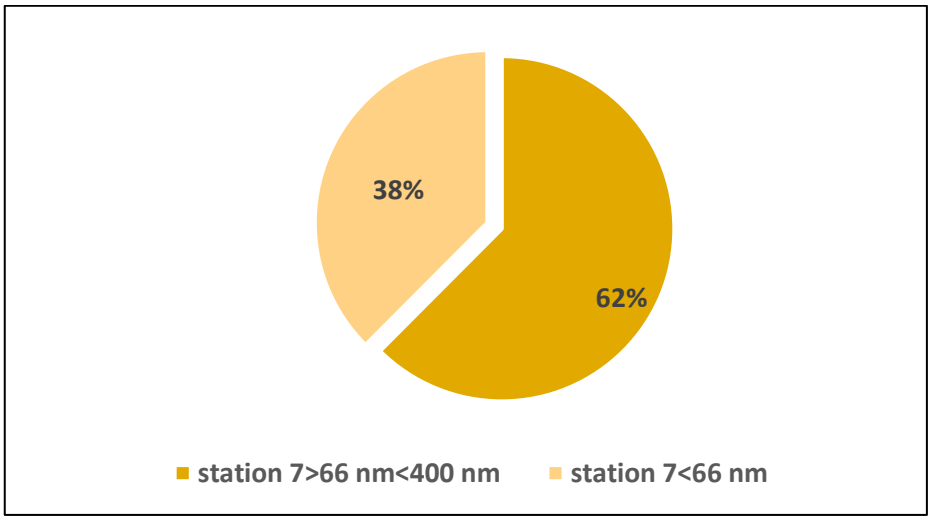

Figure 3.17. Station 7 percentage iron in the total dissolved (<400 nm) fraction by size fraction: <66 nm and >66 nm<400 nm.

Most of the iron in the dissolved (<400 nm) physical size fraction is held within the colloidal fraction (>66 nm<400 nm) for both Loch Etive station 7 and the River Awe, however, the distribution of the iron in the *dissolved* (<400 nm) fraction differs. River Awe has a higher percentage of iron held in the 66 to 400 nm physical size fraction (88%) compared to station 7 (62%).

3.3.3 **Fe(II) and Fe(III) determination: ferrozine assay**

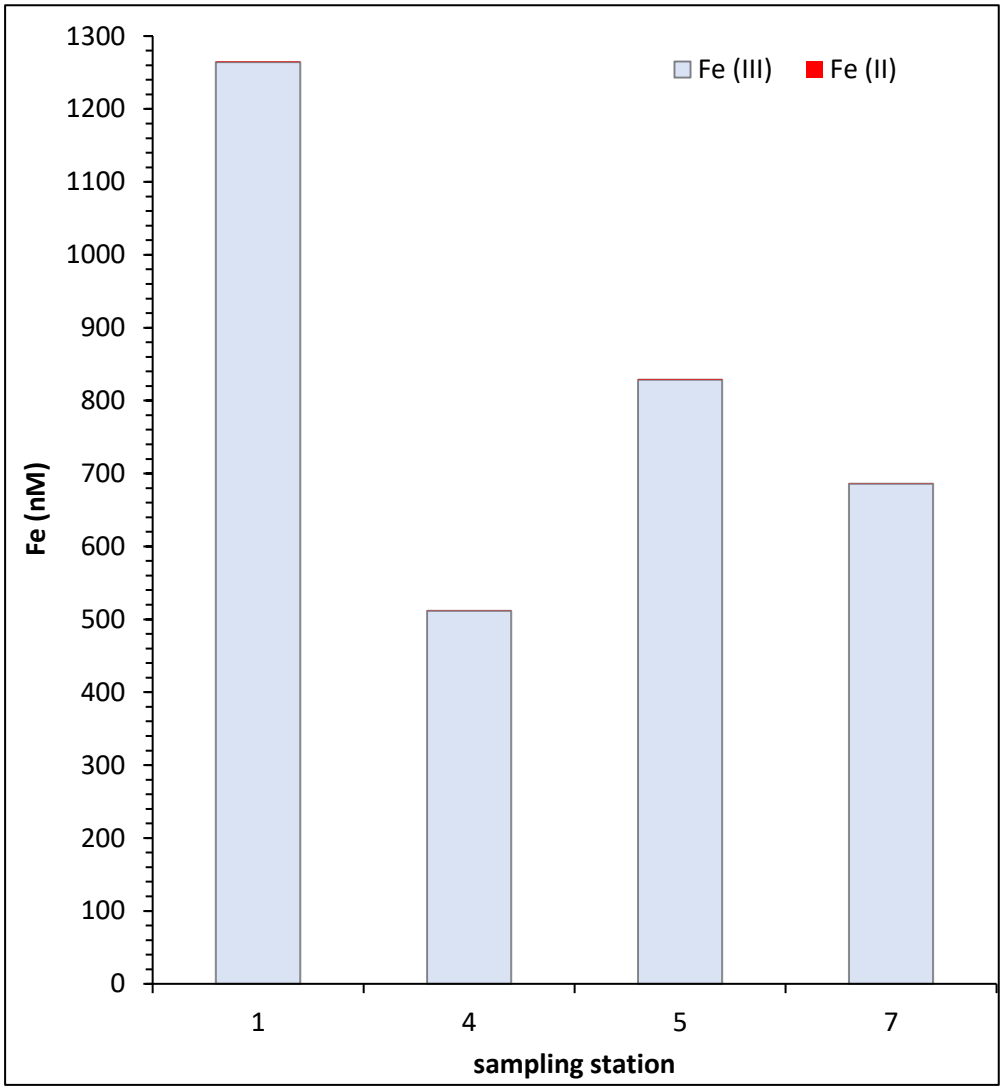

Figure 3.18. Ferrozine assay (Fe(II)/Fe(III) speciation) in the less than 400 nm resolubilised freeze dried physical size fraction from Loch Etive stations 1, 4, 5 and 7.

Table 3.6. Ferrozine assay percentages of Fe(II)/Fe(III) speciation in the less than 400 nm resolubilised freeze dried physical size fraction from Loch Etive stations 1, 4, 5 and 7.

station number	Fe(III) (%)	Fe(II) (%)
1	99.92	0.08
4	99.92	0.08
5	99.92	0.08
7	99.93	0.07

Spectrophotometric determination of Fe(II) and Fe(III)The ferrozine assay (Figure 3.18) were conducted on resolubilised freeze dried material. There were losses of material during the freeze-drying process. The majority of iron is fully oxidised in all samples as the percentage of Fe(II) is 0.08 in each case (Table 3.6).

3.4 **Discussion**

As stated in the introduction the aim of this study was to gain insight into iron concentrations within physically defined size fractions of the operationally defined dissolved fraction of water at different salinities. Iron concentration data was gathered to investigate associations between iron concentration and the particle size ranges where these particles reside. This study also informed the initial development of methods to employ synchrotron Mössbauer techniques to investigate iron mineralogy in water borne particles.

Salinity

Salinity measurements for Loch Etive plotted by station number at sampling depths (Figure 3.4) show a distinct stratification of the upper basin with denser (more saline) water found with increasing depth in the upper basin. West of the Falls of Lora (Figure 3.2) beyond station number 4, an observed accumulation of denser (saltier) water is found at depth, after which this distinct stratification is no longer observed. During the sampling it was not possible to cover a full salinity transect (i.e. up to ~35 psu) as anticipated. This is likely attributed to tidal influences on the

freshwater outflow (Boyd et al., 2010), Loch Etive's large annual fresh water inputs (from 12 rivers) and its topographically-restricted exchange which, causes stratifications in density in its upper basin leading to periods of hypoxia. Exchange events (flushing) in Loch Etive occur approximately every 16 months as a result of reduced freshwater inputs enabling the influx of denser coastal sea water to enter the upper basin, and displacement of its bottom waters. Partial flushing events also occur. The sequence of events described, massive freshwater inputs and flushing, affect the chemistry of Loch Etive including its salinity. Because of this, despite the large amount of research done in and around the Loch, there are still uncertainties surrounding the iron and carbon (and other element) cycling in and through the loch (Overnell et al., 2002, Loh et al., 2008). The uncertainties of the chemical investigations highlight difficulties that might be encountered if presenting Loch Etive as a proxy for other estuarine systems.

pH and salinity

pH increased as salinity increased (Table 3.1) (p=0.000, R^2=0.83) (Figure 3.5). Removal of the river sites from the regression analysis resulted in a weaker relationship between pH and salinity in the loch itself (p=0.001, R^2=0.49).

Iron concentrations (SAMS and University of Stirling)

Iron concentration in the less than 3 nm physical size fraction (Tables 3.2 & 3.3) for Loch Etive samples at each station are not significantly different (p=0.312). This suggests that the iron concentration in the less than 3 nm physical size fraction is sustained along the salinity gradient, from the lowest recorded salinity at station 1 (14.56 ± 4.28 psu) to the highest recorded at station 4 (20.70 ± 3.47 psu). However, the iron concentration in the less than 3 nm size fraction does decreases as salinity increases (Figure 3.11). The less than 3 nm (truly dissolved) fraction is not the main focus of this study. A complementary study to investigate this fraction from the data presented here is ongoing (see section 3.3.2).

The colloidal fraction (greater than 3nm, less than 400 nm) is the focus of my study. The data presented here demonstrate the ability of this fraction to carry more iron across the salinity gradient than the less than 3 nm size fraction. This is in agreement with a previous study by Muller and Cuscov (2017). It is also expected that there will be some transformation of iron from the colloidal to the truly dissolved fraction as salinity increases, possibly sustaining the truly dissolved fraction. The role of humic substances in iron transport is the subject of extensive ongoing research (Muller and Cuscov, 2017, Oldham et al., 2017, Oleinikova et al., 2018), however, in sea water it has proven difficult to select the terrestrial humic substances for investigation due to analytical constraints (Muller, 2018). Once this is possible, the determination of the iron mineralogy associated with these particles should prove revealing.

Unlike the 3 nm size fraction, significant differences in iron concentrations were found in the less than 400 nm size fraction. There was also no significant relationship (p=0.378) found with salinity (Figure 3.12). The less than 3 nm, greater than 4 nm iron concentrations behaved similarly to the less than 400 nm size fraction as a response to salinity (p=0.330). Iron concentrations at station 4 were significantly higher than the concentrations measured at stations 1 and 2, however, stations 3 to 5 are similar (Table 3.4). The only significant difference in iron concentration is found at station 4 when compared to both stations 1 and 2. This might be explained by a number of factors including the location of two of the main tributaries, River Awe and River Kinglass (Figure 3.19, adapted from Figure 3..4), and the influence of the Bonawe Sill which forms a topographically-restricted exchange between upper and lower loch basins (Audsley et al., 2016). Overall iron concentrations (<400 nm size fraction) at station 4 are the highest measured, reducing again from station 5 to 7. West of the Falls of Lora (Figure 3.4) beyond station number 4, an observed accumulation of denser (saltier) water is found at depth, after which, this distinct stratification is no longer observed. Station 5 iron concentrations show greater variability than station 4, possibly due to increased mixing, external inputs and internal cycling (Rijkenberg et al., 2014).

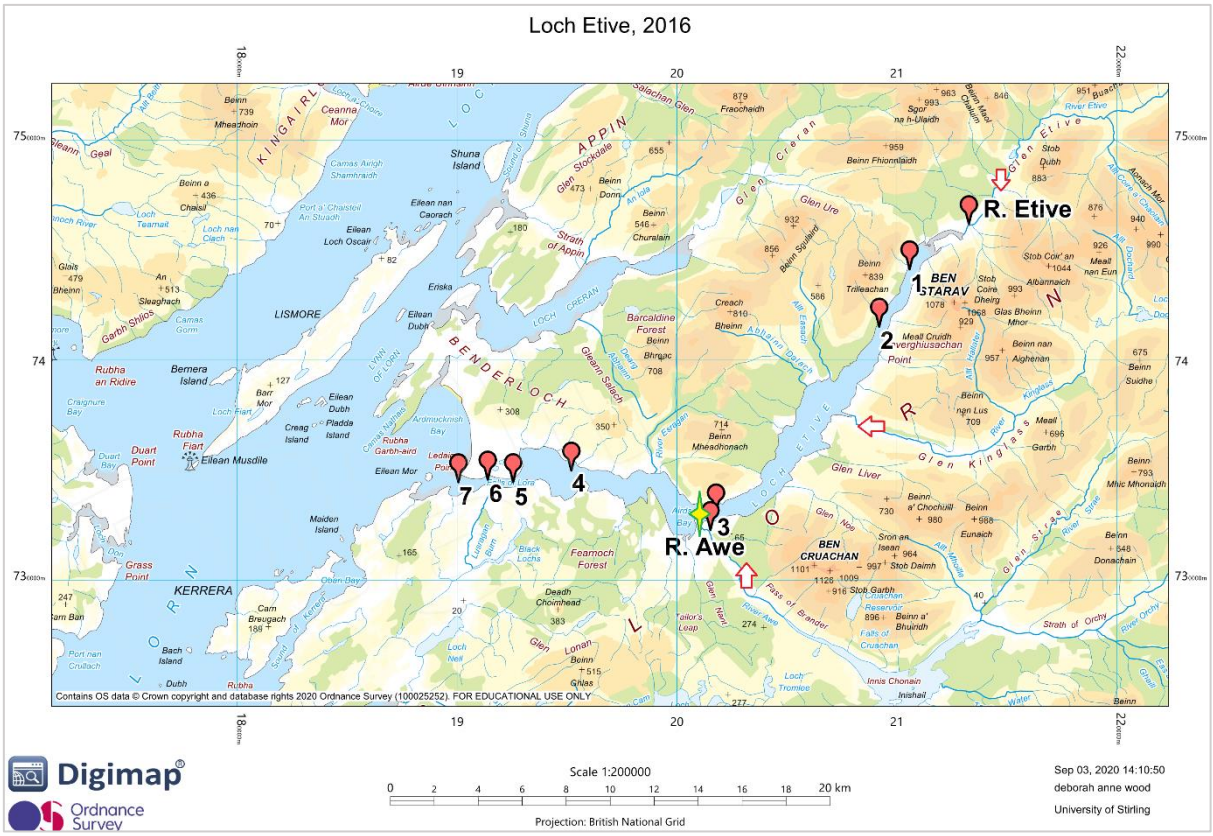

Figure 3.19. Loch Etive sampling stations (red marker pins). Red arrows denote the 3 main river inputs to the upper basin, east of the Bonawe Sill (green and yellow star): River Etive, River Kinglass and River Awe.

Iron concentrations (University of Stirling)

As stated in the methods (section 3.2.3), I produced a different suite of iron concentration data to facilitate research into the methods that might be employed for the development of synchrotron Mössbauer techniques. Only one comparison was made during this study and a significant difference in iron concentration was found for the less than 400 nm physically size fractioned samples from station 7 (p=0.020). On reflection, replicating the sample processes and measurements for the same physical size fractions on the collected samples would have provided useful data for a more thorough investigation of physical size fractionation methods. It is recommended that future studies include a more thorough investigation of the success of a range

of size fractionation methods in order to highlight any potential processing issues. Processing artefacts and contamination issues become increasingly critical as iron concentration decreases, for example in more dilute systems (as salinity increases) as discussed in Chapter1.

Iron concentration in the unfiltered samples from the River Etive was significantly lower than the River Awe (p=0.019), suggesting a higher initial iron load delivered to the loch from the River Awe compared to the River Etive. A significantly higher iron concentration was also found in the less than 400 nm River Awe sample compared to the same size fraction for sampling station 7 (p=0.001). In the greater than 66 nm, less than 400 nm size fraction, comparisons were made between the River Awe and station 7 where the River Awe had a significantly higher iron concentration (p=0.000). This result was not unexpected as station 7 was likely subject to salinity effects, and the processes of aggregation and flocculation, effectively removing larger particles from the water column as discussed in Chapter 1 (Sholkovitz, 1978). However, in the less than 66 nm size fraction, when again comparing the River Awe iron concentration with that of station 7 (Figure 3.14), there was no significant difference found (p=0.463).

Although overall iron concentrations in all measured size fractions decrease with increasing salinity and pH as is expected, the distribution of iron within the less than 400 nm filtered fraction shifts. The percentage iron in the smaller size fraction below 66 nm increases and iron concentration in the greater than 66 nm, below 400 nm decreases (Figures 3.15 to 3.16). There may be a number of explanations for this, indeed colloidal stability and aggregation kinetics of submicron particles associated with increased salinity are likely involved, for example, larger particles may be more prone to aggregation, and as they become greater in size the probability of collision and further aggregation is increased. (Hunter et al., 1997). However, this study has shown that nanoparticles and colloids, greater than the truly dissolved (<3 nm) fraction also persist. This is likely attributed to size properties (physical, thermal and chemical), and associated effects of Brownian, hydrodynamic and colloidal forces (Kovalchuk and Starov, 2012, Hunter et al.,

1997), although these are not yet fully understood in natural water environments. It is apparent that better understanding of the iron mineralogy (associated with solubility) and organic matter type (e.g. functional groups), or specific associations with other elements is needed.

This study has demonstrated that here are differences in the way iron bearing particles within different physical sizes behave throughout the operationally defined dissolved fraction, and at different salinities. The less than 400 nm physical size fraction behaves differently to its size fractioned components (e.g. nanoparticles, colloids, fine colloids) and confirms that assumptions made about the biogeochemistry of the operationally defined dissolved fraction might lead to under or over estimations in model predictions. Future studies into iron biogeochemistry in natural waters should continue strive to partition the operationally defined dissolved fraction in order to focus of specific particles of interest. Chapter 2 (section 2.4.2) describes AF^4 coupled to other analytical instrumentation which, is capable of informing the components of the dissolved fraction of water. This data can then be used in conjunction with other observed variables such as element concentrations and speciation, mineralogy, organic matter characteristics, salinity, pH, temperature etc. to better quantify transport processes and interactions within spatially and temporally defined systems.

Iron concentration and dissolved organic carbon

As was expected, as salinity increases, organic carbon in the less than 700 nm physical size fraction decreases (Figure 3.10). I investigated the response of iron in the different size fractions over the dissolved carbon (<700 nm) transect. This data was provided by SAMS from the January Loch Etive sampling cruise. As there were no carbon concentration measurements equivalent to the iron size fractions, the results presented here are limited as they do not fully describe the relationships between iron and carbon from the same size fraction. As discussed above, this would have provided greater insight into the relationship between iron and carbon for this study and is recommended for future studies.

A moderately strong positive relationship (p=0.00) with dissolved organic carbon concentrations was found for iron concentrations in the less than 3 nm filtered fraction (Figure 3.7). However, in the less than 400 nm filtered fraction (Figure 3.8) and in the greater than 3 nm, less than 400 nm fraction (Figure 3.9) the relationship was not well described by the regression analysis and there appeared to be a weak association between carbon and iron (p=0.04 and p=0.03 respectively). The data analysis on the samples processed at SAMS (Figure 3.6) show that the majority of the iron is held in the colloidal fraction (>3 nm <400 nm), and those processed at the University of Stirling show that the majority of the iron is held in the narrower colloidal fraction (>66 nm <400 nm) (Figures 3.15 to 3.17). However, the Stirling sample results show that iron-bearing particles in the less than 66 nm size fraction also persist at higher salinities (Figures 3.16 & 3.17), confirming the benefits of further define particle size fractions if we are to better understand their behaviour in natural water systems.

Ferrozine assay

Spectrophotometric determination of Fe(II) and Fe(III) (Figure 3.18) was conducted on resolubilised freeze dried material. The majority of iron is fully oxidised in all samples; Fe(II) is 0.08% or below, in each case (Table 3.6). It should be acknowledged that there were observed losses of material during the freeze-drying process, however, this loss is not expected to have affected the iron speciation ratio. It also possible that the freeze drying process would likely have had an effect on the iron speciation (Zhang et al., 2001). For this reason, it is suggested that freeze drying should be avoided for the SMS techniques. Despite these limitations, there is a significant difference between the Fe(II) and Fe(III) concentrations which cannot reasonably be explained by sample material losses. This result agrees with the expected levels of Fe(II) & (III) in our present oxygenated hydrosphere i.e. high levels of Fe(III) (fully oxidised) compared to Fe(II) (Emerson et al., 2012). It is advised that future spectrophotometric determination of Fe(II) and Fe(III) should be performed on unfiltered and filtered water samples, omitting the freeze drying process.

3.5 **Conclusions**

This study has demonstrated that majority of the iron in the waters of Loch Etive, reaching higher salinities (up to 20 psu), is associated with particles in the colloidal fraction. The colloidal fraction being broadly defined as the greater than 3 nm, less than 400 nm physical size fraction. There is general acknowledgment that the physical size fraction of Fe-OM particles transcending the salinity zone are submicron. This study has demonstrated that particles in the nanoparticle and colloidal size range persist in waters of increased salinity. Furthermore, it has distinguished a shift in particle size distribution as salinity increases when comparing iron concentrations held within the <66 nm size fraction compared to the <400 nm size fraction. Further studies should be carried out to ascertain the validity of these results in other estuarine and coastal settings. Characterisation of the nanoparticle and colloidal size fractions should also be pursued to give a better understanding of the mechanisms involved in their transport. When we consider the Fe-OM associations shown in this study, we only demonstrate the relationship of iron concentration in different size fractions, with dissolved carbon less than 700 nm size fraction only. It is suggested that to better understand this relationship, both iron and carbon concentrations should be measured in a range of physical size fractions below 400 nm. Ideally, this should be explored throughout a range of salinities and pH values i.e. from terrestrial source to sea.

4. Distribution of iron between particulate size fractions in iron-rich rivers in the Flow Country

4.1 Introduction

Rivers, were previously thought to be an insignificant source of iron to the oceans compared to atmospheric dust inputs (De Baar, 2001). Iron concentrations, in the less than 10 kDa (approximately 6.6 nm using the calculation described in Appendices for Chapter 3, section 7.3.1) size fraction, in the 'average world river', as defined by Hunter et al. (1997), were reported to be 40 nM (Dai and Martin, 1995). Based on this, de Baar and de Jong (2001) calculated the 'global riverine iron input' to be 1.5 x 10^9 mol y^{-1}. However, rivers in some regions of the globe have now been shown to provide relatively large fluxes of potentially bioavailable iron, and it is likely that the global iron flux from rivers to the ocean is underestimated. For example, Krachler et al. (2010) calculated the delivery of 'truly dissolved' iron (Fe-OM) from a peat draining creek to coastal waters, based on sampling in summer 2008 of the Rhian Burn, Kinloch River tributary, NE Scotland, to be 3300 nM. This is almost two orders of magnitude greater than the 'average world river calculations' reported by Dai and Martin (1995). Additionally, Kritzberg et al. (2014) reviewed studies on iron transport in boreal rivers and found that there was an increasing trend in iron concentrations over recent decades in some Swedish rivers of between 20% and 470% (i.e. increases of between 1 and 28 nM). The review also found that there was a variation in the ability of different boreal rivers to maintain iron in suspension at salinity and suggested a link to the characteristics of the associated organic matter and the iron phase (Kritzberg and Ekström, 2012). The authors called for future research to investigate these components including their source, transport and fate (Kritzberg et al., 2014).

As discussed in Chapter 1, although it was previously widely acknowledged that most of the iron transported by rivers is removed from the water column by aggregation and flocculation

(Sholkovitz et al., 1978), a number of studies have shown that some particles or colloids within the operationally defined dissolved fraction (the physical size fraction below 450 nm) successfully transcend this salinity 'barrier' reaching the coastal ocean (Krachler et al., 2016, Muller, 2018, Batchelli et al., 2010). Some studies have hypothesised, and begun to demonstrate, that the iron transported by rivers, surviving the mixing zone, is held within the 'truly dissolved' fraction and it appears that there is some assumption that this 'truly dissolved' fraction is temporally and spatially sustained (Batchelli et al., 2010, Krachler et al., 2015, Yang et al., 2017). However, as previously discussed, there are acknowledged, although not as yet fully understood, relationships between iron concentrations and particle size within Fe-OM bearing nanoparticles and colloids as they are transported by rivers and creeks from terrestrial source sites to coastal sites with increased salinity i.e. into and through mixing zones (Kritzberg et al., 2014, Pokrovsky et al., 2014, Muller and Cuscov, 2017).

Study Area: The Flow Country

The Flow Country in the north east of Scotland is subject to a range of recent research involving peatland processes and the influence of climate on peatland hydrology (Andersen et al., 2018, Gaffney et al., 2020). Although research in this region includes the source to sea iron-organic matter (Fe-OM) carrying capacity and potential iron bioavailability of the humic-rich river systems (Krachler et al., 2016, Muller and Cuscov, 2017), it has not as yet investigated the iron phases present in nanoparticles and colloids, and their source to sea transport. It is suggested that research in this geographical region will serve as a proxy for higher latitudes in the wake of global climate change. The NE of Scotland provides known iron-rich natural waters and Fe-OM associations ideal for the investigation of Fe-OM transport from source to sea, and as such was a driver for choosing this area for this study. The known high concentrations of iron in nanoparticles and colloids provided by the sample waters was also advantageous for the initial development of

synchrotron techniques to investigate the mineralogy of these submicron particles and colloids using the Synchrotron Mössbauer Source and supporting my PhD project aims.

The purpose of this study was to better understand how iron concentration is partitioned in defined physical size fractions of waters sampled from river source, the river itself and the receiving coastal waters. Additionally, this study investigates Fe-OM transport and whether carbon is similarly enriched in the same physical size fractions as the iron. In order to achieve this, several physical size fractionation methods were explored. Alongside the particle size fractionation, element specific (iron and carbon) concentration data were collected and analysed. This not only served to examine the success of the physical size fractionation, using mass balance calculations, it also provided iron and carbon concentrations by physical size fraction, and provided better understanding for the development of the SMS methods.

4.2 Materials and Methods

4.2.1 Field sampling

The study measured iron and carbon concentrations in defined particle size fractions of river waters, their sources and coastal sites in Spring 2017 and 2018 and was limited to a restricted sampling period. The main aim of my PhD being was to develop methods to employ synchrotron based Mössbauer techniques for the investigation of iron mineralogy in environmental iron bearing particles, therefore, sampling was also constrained by the PhD project time and by funding limits.

4.2.1.1 Sample sites

Sampling took place in April 2017 and March 2018 in the Flow Country. Water samples (10 L volume for each sample) were collected from two river catchments in the Caithness and Sutherland regions of the north east of Scotland: River Thurso and River Halladale (Table 4.1, Figures 4.1 and 4.2). The Flow Country covers an area of approximately 4,000 km^2 and is the

largest blanket bog in Europe (Lindsay et al., 1988, Andersen et al., 2018). The River Thurso has a catchment area of 412.8 km^2 and River Halladale catchment area is 204.6 km^2 (Kay et al., 2011). The sites sampled included surface waters from terrestrial source, riverine flows and coastal plumes.

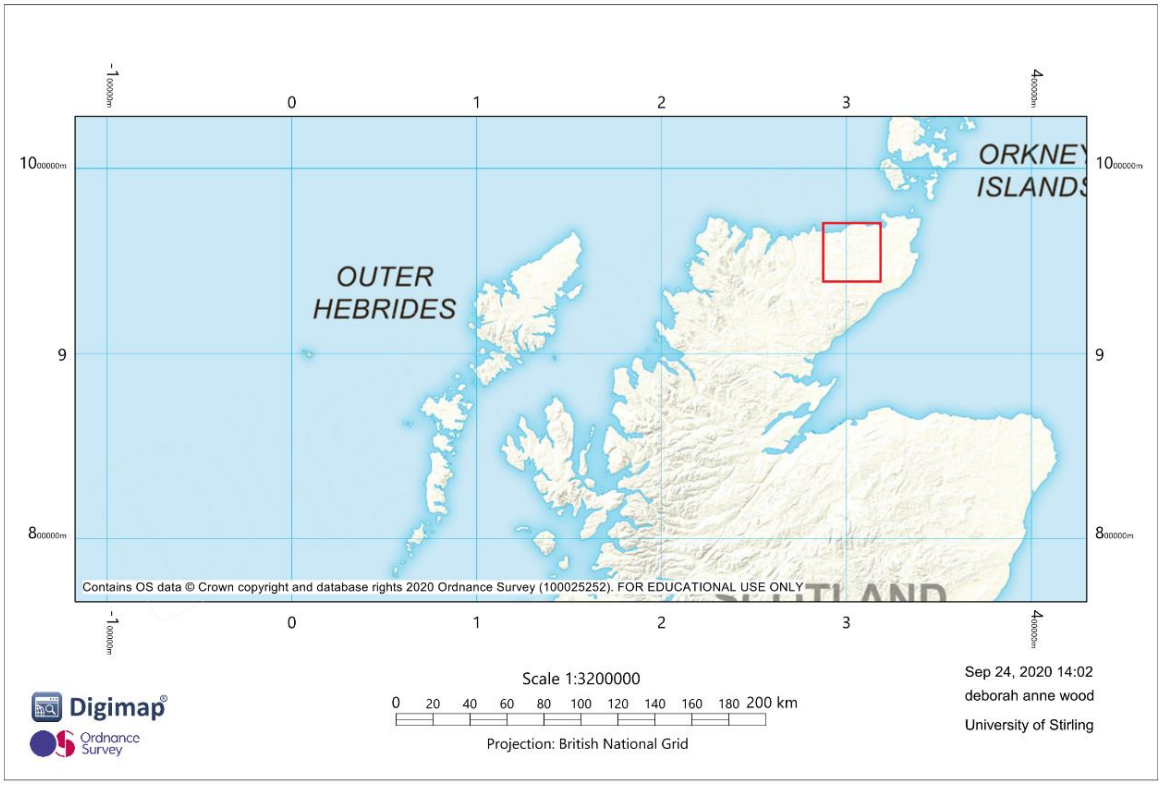

Figure 4.1. Sampling area 2017 and 2018: Caithness and Sutherland, north east Scotland.

Table 4.1. Sampling sites (2017 and 2018): catchment, site name, month and year sampled and Ordnance Survey (OS) grid reference.

Catchment	Site name	Month & year	Grid reference (OS)
Thurso	Loch More (peat bog water)	March 2018	ND0837446081
	River Thurso	*April 2017*	*ND1312359561*
	River Thurso	March 2018	ND1312359585
	Thurso estuary	March 2018	ND1223768803
Halladale	Halladale feeder stream	March 2018	NC9008460623
	River Halladale	*April 2017*	*NC8912556081*
	River Halladale	March 2018	NC8913756082
	Melvich Bay (coastal plume)	*April 2017*	*NC8911965094*
	Melvich Bay (coastal plume)	March 2018	NC8912065044

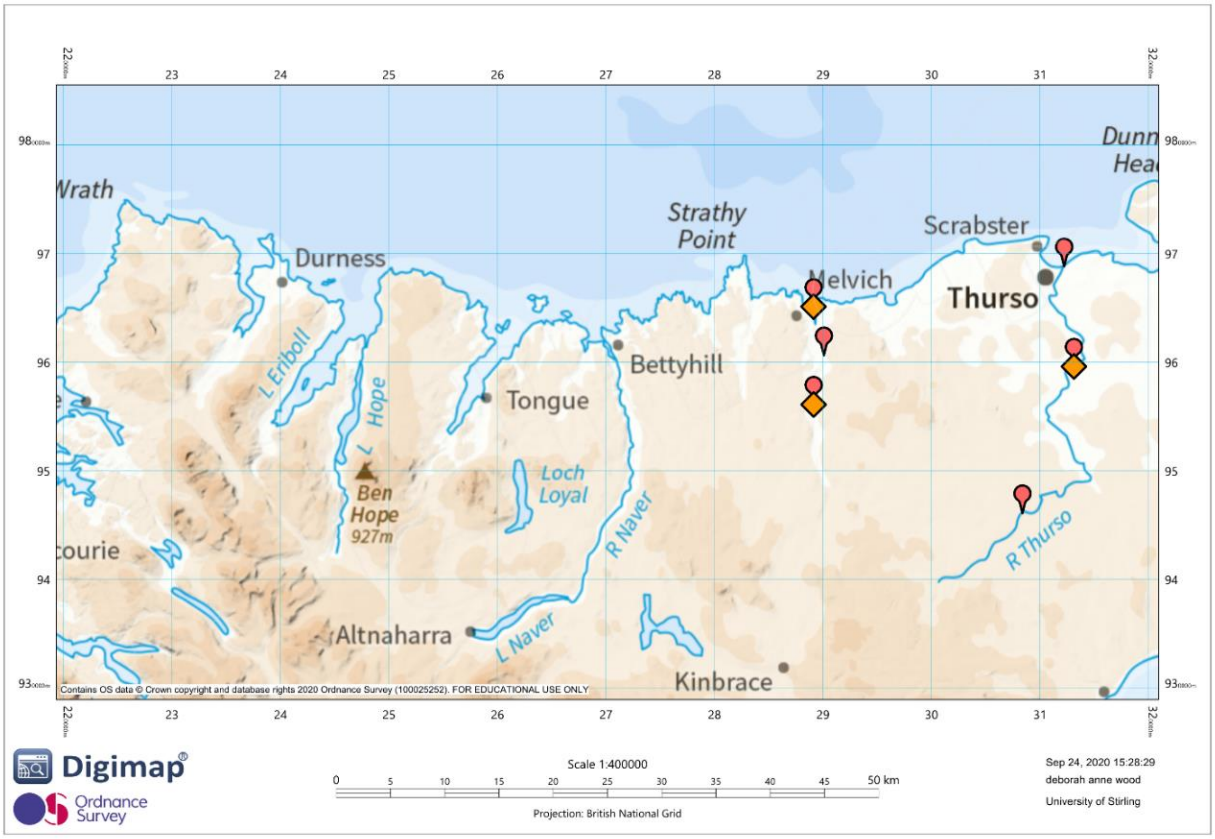

Figure 4.2. Sampling sites: Thurso and Halladale catchments, Scotland. Site markers: 2017 (orange diamonds) and 2018 (red pins).

4.2.1.2 Sample Collection

Samples were collected from locations shown in Table 4.2. Water samples were collected in pre-cleaned 10 L low-density polyethylene containers (LDPE), excepting the ones specifically for organic carbon analysis which were collected in pre-cleaned glass bottles. All LDPE sampling equipment was acid washed and rinsed with Milli-Q® (18.2 MΩ) water as per protocols adapted from the GEOTRACES Cookbook (Cutter et al., 2010). After cleaning the containers were filled with Milli-Q® water (no void space), double bagged and cable tied until their moment of use. A total procedural blank (TPB) was transported with the equipment to the sampling sites and returned unopened ready for processing using the same procedures as the collected water samples.

Surface water samples (from 5 to 10cm below the water surface) were collected from each site (Table 4.2). Each sample was collected upstream from the sampler taking care to cause minimal disruption to the underlying sediment. Collection vessels were preconditioned with sample waters (in triplicate) then fully filled, with no void space, closed, sealed with parafilm, double bagged and closed with cable ties. All samples were transported in a cooled and steady environment i.e. sample temperatures were maintained (without freezing) below the measured water temperatures at the time of sampling, and then stored at 4 ^{o}C on arrival at the laboratory. Initial sample processing of vacuum filtration (to isolate the operationally defined dissolved fraction) commenced within 24 hours of returning to the laboratory.

4.2.2 **Onsite measurements**

Measurements of water pH, temperature and specific electrical conductance were collected *in situ* using HI98130 pH/EC Combo pH Tester (Hanna Instruments Ltd, UK).

4.2.3 **Sample processing**

Blanks and standards

Total procedural blanks (TPB) were transported to and from the sampling sites and left unopened. Aliquots from the TBPs and fresh Milli-Q® (18.2 MΩ) blanks were processed and analysed, following the same procedures as the collected water samples. Iron concentration were measured using Inductively coupled plasma mass spectrometry (ICP-MS).

4.2.4 **Physical size fractionation**

450 nm (2017) & 400 nm (2018) : vacuum filtration

Physical size fractionation was performed on the water samples to achieve a suite of physical sizes that were relatable to the definitions of particle sizes within the *operationally defined dissolved* fraction. For the initial processing stage, isolating the operationally dissolved fraction, vacuum filtration was used. Due to existing laboratory stock availability of filter membranes and funding

constraints at the time, the 2017 filter membranes were pore size 450 nm. The reason for the change to 400 nm pore size in 2018 was that study received a donation of a number of 400 nm polycarbonate track-etched membrane filters. These were deemed to be suitable for purpose.

For the less than 66 nm physical fractionation

The methods employed were as follows: 2017 tangential flow filtration for 2017 samples and Jumbosep™ centrifugal devices for 2018 samples. 2 nm Amicon Ultra-15 centrifugal filter unit were used in 2018 to filter the <66 nm size fraction, effectively removing the truly dissolved fraction. Samples collected in 2018 were also used to test Asymmetrical flow field-flow fractionation coupled ICP-MS (AF^4- ICP-MS). AF^4 fractionation parameters were: ~1.2 to 20 nm, 20 to 60 nm and >60 nm (2018) after Gottselig et al. (2017).

The suspended particulate physical size fractions of the sampled surface water were isolated using a combination of different methods which were developed over sampling campaigns presented in Chapter 3 and in this chapter. On return to the laboratory the water samples were processed through pre-cleaned track-etched polycarbonate membranes in Nalgene vacuum filtration units (Figure 4.3). This process of filtration removed the larger particulates, isolating the defined dissolved fraction as described in Figure 4.3 ready for further processing and analysis.

- Aliquots of unfiltered sample were stored (4°C) for later analysis
- Aliquots of the filtrate were stored at 4°C for later analysis
- The filter membranes were stored at 4°C in individual petri dishes, sealed with parafilm and double bagged for later analysis
- The remaining filtrate (the *dissolved* fraction) was transferred to pre-cleaned LDPE 2 L bottles and stored at 4°C until processing through the further physical size

fractionation process steps as detailed below

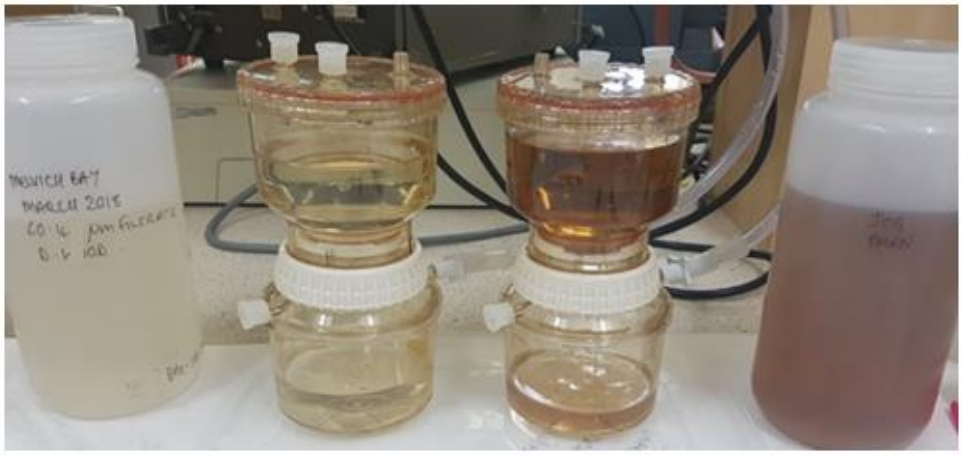

Figure 4.3. Isolation of the defined dissolved fraction for the 2018 water samples using Nalgene vacuum filtration units (photograph: D. Wood).

Isolation of colloids

Further physical size fractionation of the defined dissolved fraction (Figure 4.3) was undertaken using different systems for 2017 and 2018. For the 2017 samples a tangential flow filtration (TFF) in concentration mode (Scottish Association for Marine Science (SAMS), Oban) was employed, and for the 2018 samples Jumbosep Centrifugal Devices (Pall Corporation) were used. The Jumbosep devices were purchased for the 2018 sample processing as previous iron concentration analysis revealed issues with the iron mass balance calculation for TFF.

Tangential flow filtration

TFF for the 2017 water samples was performed in concentration mode using a 100 kDa (66 nm) hydrophilic ceramic cassette. The TFF system was operated until 200 mL of retentate (less than 450 nm and greater than 66 nm) was achieved. The retentate was clean stored at 4^{o}C for later analysis. The permeate (less than 66 nm) was also clean stored at 4^{o}C for further physical size fractionation and aliquots were reserved for further analysis.

Jumbosep™ Centrifugal Devices

For the 2018 water samples the 400 nm filtrate from the vacuum filtration process was further physically size fractioned using acid clean Jumbosep™ centrifugal devices with clean low protein-binding Omega™ membranes with polysulfone housing (MWCO of 100 kDa) yielding a filtrate with particle size of approximately 66 nm. The retentate collected equated to the condensed and isolated size fraction of less than 400 nm and greater than 66 nm and the filtrate produced was below 66 nm.

Separation of the truly dissolved fraction

The less than 66 nm filtrate was then processed through a 2 nm (3 kDa MWCO) physical size fractionation using Amicon Ultra-15 units (3 kDa MWCO). Aliquots of the retentate (greater than 2 nm and less than 66 nm) and of the *truly dissolved* fraction (less than 2 nm) were reserved and stored in acid clean Thermo Scientific Nalgene Round-bottom tubes for later analysis.

4.2.5 **Bulk acid digestion for total iron extraction**

A total acid digest was performed in acid clean Polytetrafluoroethylene (PTFE or Teflon) vials. All work was conducted in a combined laminar flow hood/fume cupboard. All hydrofluoric acid (HF) work was undertaken with the addition of fume scrubbers. **Hydrochloric acid (HCl) digestion**: hydrochloric acid dissolves many carbonates, oxides, hydroxides, phosphates, borates, and sulphides. Pre-weighed samples were transferred into acid-cleaned (10% HCl, rinsed thrice with deionised water) PTFE beakers and dried down. The initial sample vessel was rinsed 2 times with 3 mL concentrated hydrochloric acid into the PTFE beaker using a disposable LDPE Pasteur pipette. Samples were placed onto a hotplate and left overnight to flux at ~70 °C (thermostat T). The samples (open) were then left on the hotplate until it had dried completely (hotplate temperature was increased at this point). Once dry, each sample was removed from the hotplate and placed in a tray, covered and left to cool (~ 1 hour). **Aqua regia digestion** (3:1, concentrated hydrochloric

acid (HCl):concentrated nitric acid (HNO_3) by volume): aqua regia dissolves sulfides, phosphates, organic matter and many metals and alloys including gold, platinum, and palladium: 3 mL concentrated hydrochloric acid and 1 mL concentrated nitric acid were added to each sample, in the spillage tray, using disposable LDPE Pasteur pipettes. Samples were placed from the tray onto a hotplate and left overnight to flux at ~70 °C (thermostat T). The samples were then left on the hotplate (open) until they had dried completely (hotplate temperature was increased at this point). Once dry, the samples were removed from the hotplate into a tray and allow to cool, as per the above HCl digest. **Hydrofluoric acid digestion (HF) digest**: removal of silicon and destruction of silicates; dissolves oxides of Nb, Ta, Ti, and Zr also, Nb, and Ta ores: In a spill tray, 2 mL of hydrofluoric acid was added to each sample using a disposable LDPE Pasteur pipette. The samples were the transferred to a hotplate and left for 24 hours to specifically target the silicates (thermostat was set at ~70 °C). After this period the samples were left on the hotplate until dried completely, removed from hotplate and left to cool. **Nitric acid digestion**: Oxidises many metals and alloys to soluble nitrates; organic material oxidized slowly: Samples were re-dissolved, in the PTFE beakers with HNO_3 and digested as per the HCL and aqua regia stages. This process, including fluxing and drying on the hotplate was repeated twice for any samples that had been HF digested to ensure any remaining HF in the dried sample was removed by evaporation to fumes in a low-volatility acid (i.e. HNO_3). After this 3 mL of 2% HNO_3 was added to each sample and transferred to a LDPE bottle (with a LDPE closure). Residue from the PTFE beaker was then rinsed into the LDPE bottle with 2 mL concentrated nitric acid using a disposable LDPE Pasteur pipette. The HNO_3 digest also prepares samples for ICP-MS analysis (matrix is instrument/laboratory dependent). Further heating was not needed for this stage.

Stand-alone inductively coupled plasma mass spectrometry (ICP-MS)

The acid digested water samples were analysed for total Fe using a XSERIES 2 ICP-MS (Thermo Scientific, Germany) using collision cell technology (CCT) to mitigate potential polyatomic

interferences. Multi element standards (Merck, Germany) certified by the National Institute of Standards and Technology (NIST), internal standards (scandium (Sc) and rhodium (Rh)) and total procedural and laboratory blanks were included in each run. ICP-MS (Thermo Fisher series 2) analysis was performed on the digested and resolubilised aliquots. This analysis was undertaken to quality check the filtration and concentration procedures and to provide a suite of iron concentrations by physical size fraction. Standards, all sample dilutions (including nanoparticle standards) and reagent blanks for ICP-MS were prepared using sample protocols, with ultrapure HNO_3 and Milli-Q water in a 2% matrix for freshwater samples, with a dilution factor of 20 for saline samples. When not being processed or analysed, all samples and aliquots were stored, double bagged, in clean lock-tight plastic boxes at 4 °C in the dark prior to processing and analysis.

4.2.6 Asymmetric Flow Field Flow Fractionation (AF4) and Inductively Coupled Plasma-Mass Spectrometry (ICP-MS)

Asymmetric Flow Field Flow Fractionation (AF^4) and Inductively Coupled Plasma-Mass Spectrometry (ICP-MS) - Institute of Bio- and Geosciences Agrosphere (IBG-3), Forschungszentrum Jülich, Germany. This hyphenated technique provided size resolved detection of colloidal Al, Si, P, Ca, Mn and Fe in undigested water samples. The instrumentation comprises a quadrupole ICP-MS with collision cell technology (Agilent 7500, Agilent Technologies, Japan) coupled online to the AF^4. To gain total sample elemental concentrations prior to fractionation, offline ICP-MS measurements were performed on 5000 nm (MWCO) filtered samples. The samples were shaken to homogenise the particles and then filtered through a 5000 nm (5 μm) cellulose nitrate membrane to ensure there were no larger particles present that could potentially clog the instrument filter or the AF^4 tubing. The ICP-MS was attuned to the specialized low concentration measurements using a MicroMist nebulizer with helium (He) as collision gas. Integration times were adjusted per element phase as described in Nischwitz et al. (2016).

AF^4 size separation theory is based on the diffusion coefficient of the single particles, related to the mobility of a particle. At a low Reynolds-coefficient the mobility is the reciprocal drag-coefficient, described for spherical particles by the Stokes-equation. For non-spherical particles the drag-coefficient is related to the surface area of a particle due to its power of resistance. The diffusion of non-spherical particles is affected by their shape and surface size. The particle fractions and elution times are shown in Appendices for Chapter 4 (7.4.1). Particle fractions of environmental samples separated by AF^4 relate to the particle size and shape and are assumed as being spherical in this study (Gottselig et al., 2017). Calibration data regression parameters for AF^4 data are presented in Appendix 7.4.1.

4.2.7 *Dynamic Light Scattering*

Maximum particle sizes were also measured using DLS this study are reported in the results section using a Zetasizer Nano, Malvern, UK.

The samples where AF^4 was applied were analysed using dynamic light scattering (DLS) to measure the maximum hydrodynamic diameter (d.nm) of the included particles in the *unfiltered* samples (all samples were pre-filtered to 5 μm, excepting the River Thurso which, had been pre-filtered to <400 nm prior to analysis).

4.2.8 **Carbon analysis**

Organic carbon (total carbon: organic and inorganic carbon) were determined using an elemental micro-analyser (EA1108 CHNS-O, Carlo Erba Instruments, Milano, Italy) and PC-based Eager 300 software system. The 2017 analysis was performed on the less than 450 nm fraction only. The 2018 sample preparation extended the analysis to better complement the iron analysis of each physical size fraction described in Figure 4.3.

4.2.9 **Statistical analysis**

ANOVA and Welsh ANOVA with Tukey and Games-Howell comparisons were conducted to find any differences between samples. Pearson product-moment correlation conducted for correlation analysis between iron and carbon. All statistical analyses were performed using Minitab (19).

4.3 **Results**

4.3.1 **In-stream measurements**

In-stream measurements 2017

Table 4.2. in-stream pH measurements, 2017

site name	pH
River Thurso	8.4
River Halladale	8.3
Melvich Bay	8.6

In-stream measurements 2018

Table 4.3. Flow Country, 2018 sampling: in-stream measured variables: temperature, electrical conductivity and pH of waters at time of sampling.

site name	T (°C) (x)	sample T (°C) (σ)	EC (*µ*s) (x)	EC (*µ*s) (σ)	pH (x)	pH (σ)
Loch More (peat bog)	9.20	*0.55*	179.00	*18.36*	6.74	*0.35*
River Thurso	6.60	*0.10*	97.00	*15.59*	8.03	*0.05*
Thurso estuary	6.90	*0.10*	*nd*	*nd*	8.12	*0.39*
Halladale feeder stream	5.90	*0.10*	129.67	*0.58*	5.56	*0.16*
River Halladale	6.50	*0.10*	76.33	*11.93*	8.15	*0.04*
Melvich Bay (coastal plume)	6.78	*0.10*	942.50	*65.00*	8.03	*0.25*

Key: *nd = not determined due to instrument detection limits, T = temperature, EC = electrical conductivity.*

Electrical Conductivity 2018

A Welch ANOVA was conducted. Electrical conductivity (EC) amongst the sampled sites was found to be significantly different ($F(4,4.37)=123.58$, $p=0.000$). Table 4.3 presents the post-hoc Games-Howell pairwise comparisons. EC for the Thurso estuary site was not measured because the combined pH/EC meter was limited to maximum a conductivity of 3999 μS cm^{-1} (Table 4.4).

Table 4.4. Electrical conductivity (μS) by site (2018 sampling): grouping Information using the Games-Howell Method and 95% confidence.

Site name	N	Mean	Grouping
Melvich Bay (coastal plume)	4	942.50	A
Loch More peat bog	3	179.00	B
Halladale feeder stream	3	129.67	B C
River Thurso	3	97.00	C D
River Halladale	3	76.33	D

Means that do not share a letter are significantly different.

The measured Thurso catchment sites (2018) had significantly different EC results. The peat bog site EC was significantly higher than the River Thurso; EC for the River Thurso estuarine site was not successfully measured. The Halladale catchment sites were all significantly different. The Halladale feeder stream had a higher EC than the River Halladale and the EC for the Melvich Bay coastal site was significantly higher than all the other sites. Both catchments displayed the same patterns of EC where measurements were highest in the coastal sites followed by the source sites and the lowest measurements were recorded in the rivers.

pH 2017 and 2018

A one-way ANOVA showed significant differences in pH for the 2017 sampled sites ($F(2,8)=28.00$, $p=0.001$). A Tukey pairwise grouping confirmed that the River Thurso and River Halladale were not significantly different, however, Melvich Bay coastal site had a significantly higher pH.

pH values for the 2018 sampled sites had significant differences ($F(5,6.14)=113.04$, $p=0.001$). Table 4.5 presents the post-hoc Games-Howell pairwise comparisons for pH.

Table 4.5. pH by site (2018 sampling): Grouping Information Using the Games-Howell Method and 95% confidence.

Site name	N	Mean	Grouping
R. Halladale	3	8.15	A
Thurso estuary	3	8.10	A
Melvich Bay (coastal plume)	4	8.03	A
River Thurso	3	8.03	A
Loch More peat bog	4	6.74	B
Halladale feeder stream	3	5.56	C

Means that do not share a letter are significantly different.

In-stream measurements for 2017 and 2018 show an increase in pH from source sites to coastal sites. This is particularly evident for the River Thurso (2018). However, unlike the results, the pH for the Halladale coastal site at Melvich Bay does not differ significantly from the River Halladale for the 2018 results.

4.3.2 Iron and Carbon

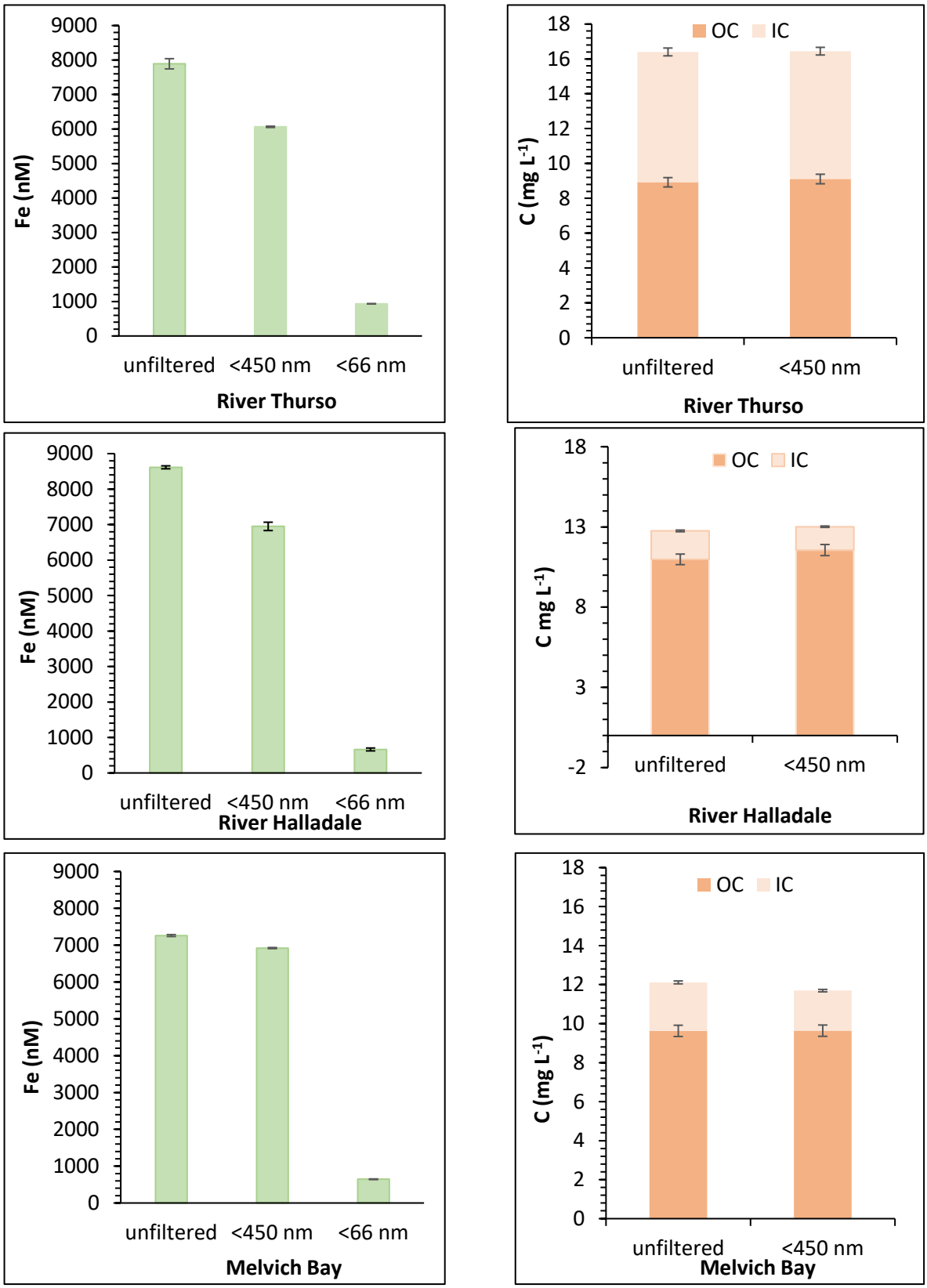

Figure 4.4. Iron (nM) and carbon (mg L^{-1}) concentrations, 2017.

Carbon 2017

Organic carbon (OC) and inorganic carbon (IC) in the less than 450 nm filtered operationally defined dissolved fraction (Figure 4.4).

DOC 2017

A Welch ANOVA was conducted. DOC amongst sampled sites were significantly different ($F(2,2.71)=17.43$, $p=0.028$).

Table 4.6. 2017 sampling. Grouping Information Using the Games-Howell Method and 95% confidence (equal variances were not assumed for analysis).

Site name	N	Mean (mg L^{-1})	Grouping
River Thurso	3	10.98	A
River Halladale	3	9.26	B
Melvich Bay (coastal plume)	3	8.92	B

Means that do not share a letter are significantly different.

There was no significant difference between the two Halladale catchment sites, however, River Thurso is significantly different to the Halladale catchment DOC (Figure 4.4 and Table 4.6).

DIC 2017

A Welch ANOVA was conducted. DIC at was significantly different for each site ($F(2,3.24)$, $p=0.000$).

Table 4.7. 2017 sampling. Grouping Information Using the Games-Howell Method and 95% confidence (based on equal variances were not assumed for analysis).

Site name	N	Mean (mg L^{-1})	Grouping
Melvich Bay (coastal plume)	3	7.48	A
River Halladale	3	2.49	B
River Thurso	3	1.77	C

Means that do not share a letter are significantly different.

The Melvich Bay coastal site had a significantly higher DIC concentration than the River Halladale. The River Thurso site had significantly lower DIC concentration than both Halladale catchment sites (Figure 4.4 and Table 4.7).

Iron 2017

Less than 66 nm: River Halladale, River Thurso and Melvich, 2017 (Figure 4.4)

Descriptive statistics for iron concentration (nM) for the less than 66 nm physical size fraction by site, 2017. A Kruskal-Wallis test was conducted (H=5.60, 2 d.f., p=0.061). 2-sample Mann Whitney tests confirmed medians did not differ significantly (p>0.05).

Greater than 66 nm, less than 450nm: River Halladale, River Thurso and Melvich, 2017 (Figure 4.4)

Descriptive statistics for iron concentration (nM) for the greater than 66 nm, less than 450 nm physical size fraction by site, 2017. Kruskal-Wallis test was conducted (H=5.60, 2 d.f., p=0.061). 2-sample Mann Whitney tests confirmed medians did not differ significantly (p>0.05).

Less 450nm (Figure 4.5): River Halladale, River Thurso and Melvich, 2017 (Figure 4.4)

Descriptive statistics for iron concentration (nM) for the less than 450 nm physical size fraction by site, 2017. A Kruskal-Wallis test was conducted (H=5.60, 2 d.f., p=0.061). 2-sample Mann Whitney tests confirmed medians did not differ significantly (p>0.05).

Unfiltered (Figure 4.5): River Halladale, River Thurso and Melvich, 2017 (Figure 4.4)

A one-way ANOVA was conducted. There were significant differences iron concentration in the unfiltered samples (F(2, 6)=168.90, p=0.000). Tukey pairwise comparisons (Table 4.8) show the mean groupings for the sites.

Table 4.8. Iron concentrations (nM) unfiltered sites, 2017. Tukey grouping information with 97.80% individual confidence levels to obtain a 95% joint confidence level.

Sample site (unfiltered)	N	Mean	Grouping
River Halladale	3	8614.7	A
River Thurso	3	7891.2	B
Melvich Bay	3	7260.9	C

Note: Means that do not share a letter are significantly different.

All sites (Table 4.8) have significantly different iron concentrations. The highest iron concentration was found in the River Halladale. Melvich Bay coastal plume had the lowest iron concentration. Iron concentrations in the Halladale catchment reduced from the river to the coast.

Carbon concentrations 2018

2018 carbon concentrations (Figure 4.5) were measured on the physically isolated size fractions: less than 400 nm and less than 66 nm.

Table 4.9. Carbon concentrations in the measured fractions blanks and standards.

Sample Name	TOC	TC	IC
Blank	0.213	0.4431	0.2299
TC 10	9.798	9.989	0.1914
Blank	0.091	0.3293	0.2387
TC 10	9.696	9.898	0.2026
IC 5	0.151	5.556	5.404
Blank	0.090	0.3438	0.2533
TC 10	9.567	9.76	0.1938
IC 5	0.0133	5.066	5.053
Blank	0.1374	0.3825	0.2451
TC 10	9.666	9.843	0.1768
IC 5	0.0613	4.981	4.92

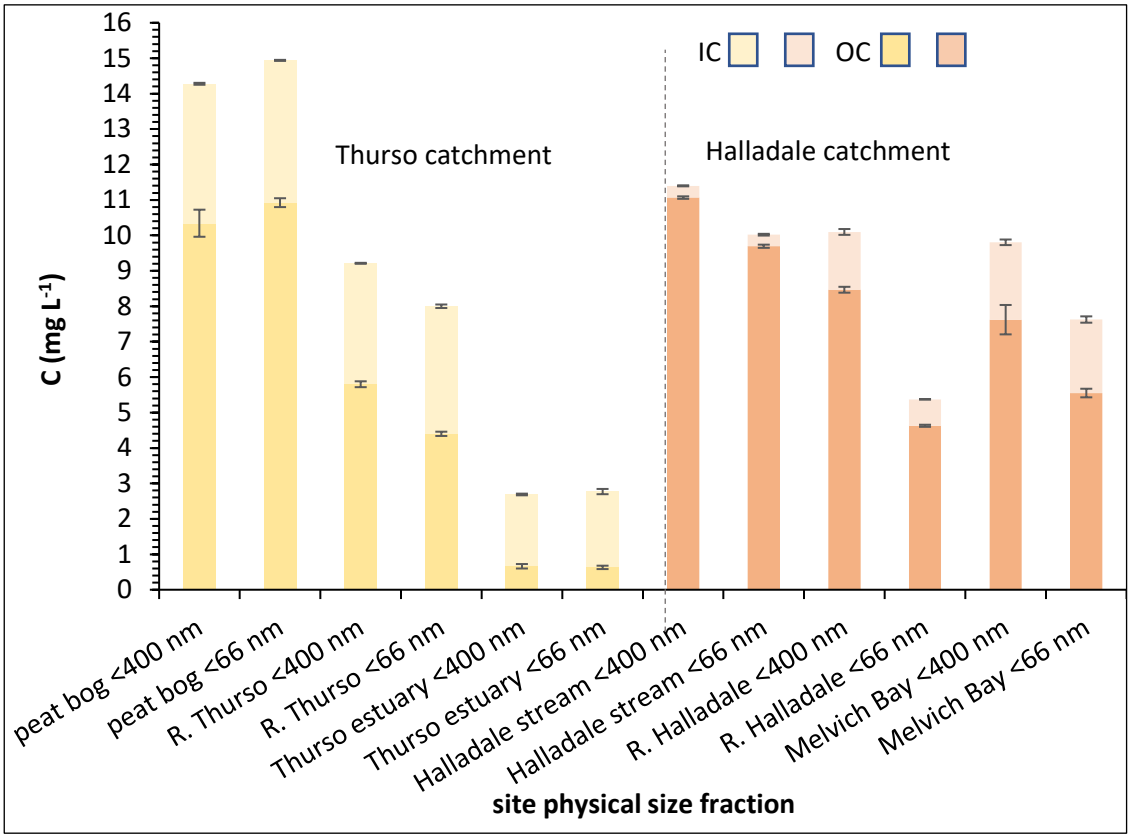

Figure 4.5. Inorganic and organic carbon (mg L^{-1}) for 2018: less than 400 nm and less than 66 nm physical size fractions. Error bars represent 1 x standard deviation. Total carbon for total procedural blank (TPB) = 0.78 (±0.21) mg L^{-1} and for Milli-Q® (18 MΩ) blank = 0.24 (±0.23) mg L^{-1}.

DOC 2018

A one-way ANOVA was conducted. DOC <400 nm concentrations for each site were significantly different ($F(5,12)=761.12$, $p=0.000$). Tukey Pairwise comparisons are shown in Table 4.10.

Table 4.10. DOC (2018) in the less than 400 nm physical size fraction. Tukey pairwise comparison table for all sites.

Factor	N	Mean	Grouping
Halladale stream OC <400 nm	3	11.0667	A
peat bog OC<400 nm	3	10.343	B
River Halladale OC <400 nm	3	8.4660	C
Melvich Bay OC <400 nm	3	7.621	D
River Thurso OC <400 m	3	5.7993	E
Thurso estuary OC< 400 nm	3	0.6625	F

DOC was highest in the source sites with the lowest concentrations being found in the coastal sites. DOC concentrations in the sample waters decreased from source to sea in both catchments (Figure 4.5 and Table 4.11).

DIC 2018

A one-way ANOVA was conducted. DIC <400 nm concentrations for each site were significantly different amongst all sites ($F(5,12)=2045.34$, $p=0.000$). Tukey Pairwise comparisons are shown in Table 4.11.

Table 4.11. DIC (2018) in the less than 400 nm physical size fraction. Tukey pairwise comparison table for all sites.

Factor	N	Mean	Grouping
peat bog IC<400 nm	3	3.9347	A
River Thurso IC<400 nm	3	3.41267	B
Melvich Bay IC <400 nm	3	2.1837	C
Thurso estuary IC <400 nm	3	2.0260	D
River Halladale IC <400 nm	3	1.6313	E
Halladale stream IC <400 nm	3	0.33173	F

DIC in the Thurso catchment was highest in the Peat bog source site, followed by the River Thurso and the Thurso estuarine site had the lowest concentration. In the Halladale catchment, the estuarine site (Melvich Bay) had the highest DIC concentration followed by the River Halladale; the Halladale stream source site had the lowest DIC concentration. The Thurso catchment was higher DIC concentrations in both the source and river sites when compared to the Halladale catchment equivalent sites, however, the coastal site in the Halladale catchment (Melvich Bay) has a higher DIC concentration than the Thurso estuary (Figure 4.5 and Table 4.11).

A one-way ANOVA conducted was conducted. Organic carbon (OC) concentrations in the less than 66 nm fraction were significantly different amongst all sites ($F(5,12)=6565.66$, $p=0.000$). Tukey Pairwise comparisons are shown in Table 4.12.

Table 4.12. OC (2018) in the less than 66 nm physical size fraction. Tukey pairwise comparison table for all sites.

Factor	N	Mean	Grouping
peat bog OC<66 nm	3	10.92	A
Halladale stream OC <66 nm	3	9.69	B
Melvich Bay OC <66 nm	3	5.55	C
River Halladale OC <66 nm	3	4.63	D
River Thurso OC <66 nm	3	4.40	E
Thurso estuary OC <66 nm	3	0.63	F

In the Thurso site OC concentrations in the less than 66 nm size fraction were highest in the peat bog site and the lowest are in the Thurso estuary. In the Halladale catchment the highest OC concentration is found in the Halladale stream source site. The coastal site at Melvich Bay had the lowest OC in the Halladale catchment. The Thurso catchment presents reducing OC concentrations from source to sea. The Halladale catchment followed the same initial trend, with a reduction in OC in the river compared to the source site, however, there was increased iron concentration from the river to the coastal site.

A one-way ANOVA conducted was conducted. There were significant differences in the inorganic carbon (IC) concentrations in the less than 66 nm fraction were significantly different amongst the sites ($F(5,12)=2325.32$, $p=0.000$). Tukey Pairwise comparisons are shown in Table 4.13.

Table 4.13. IC (2018) in the less than 66 nm physical size fraction. Tukey pairwise comparison table for all sites.

Factor	N	Mean	Grouping
peat bog IC <66 nm	3	4.02	A
River Thurso IC <66 nm	3	3.60	B
Thurso estuary IC <66 nm	3	2.14	C
Melvich Bay IC < 66 nm	3	2.07	C
River Halladale IC < 66 nm	3	0.75	D
Halladale stream < 66 nm	3	0.33	E

IC concentrations throughout the Thurso catchment were higher than those found in the Halladale catchment. In the Thurso catchment the highest IC is found was the peat bog source site and the lowest in the estuary, presenting a reducing trend from source to sea. In the Halladale catchment, the highest IC concentration was found in the Melvich Bay coastal site, and the lowest in the Halladale feeder source stream. The Halladale catchment presented increasing IC concentrations from the coastal site to the source site.

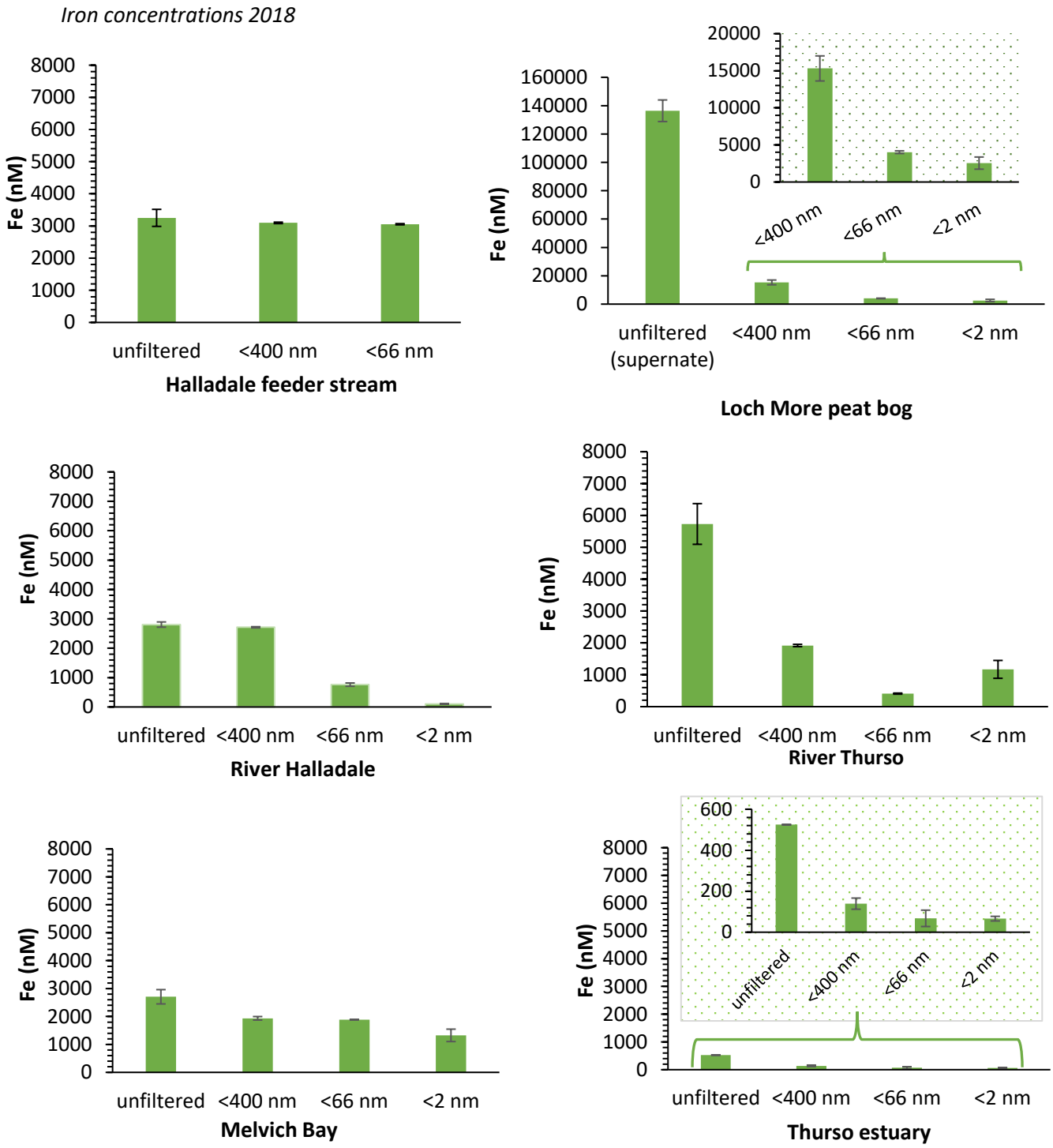

Figure 4.6. Iron concentrations (2018): Fe (nM) in River Halladale and River Thurso catchment by physical size fraction (ICP-MS). Physical size fractionation: 400 nm, 66 nm, 2 nm. Source sites are Halladale stream and peat bog, river sites are River Halladale and River Thurso, and coastal sites are Melvich Bay and Thurso estuary.

Iron in the less than 2 nm physical size fraction

A one-way ANOVA conducted was conducted. Iron concentrations in the less than 2 nm physical size fractions have significant differences ($F(4,10)=19.67$, $p=0.000$). Table 4.14 presents the Tukey groupings.

Table 4.14. Iron concentrations in the less than 2 nm size fraction: Tukey grouping Information 99.18% individual confidence levels to achieve a joint 95% confidence level.

Site	N	Mean	Grouping
Peat bog <2 nm	3	2551.00	A
Melvich Bay <2 nm	3	1326.00	B
R. Thurso <2 nm	3	1170.00	BC
R. Halladale <2 nm	3	104.68	CD
Thurso estuary <2 nm	3	66.11	D

Means that do not share a letter are significantly different.

Thurso catchment sites for the less than 2 nm fraction iron concentrations significantly differ from each other. Decreasing concentrations were observed from the source site to the coastal site. In the Halladale catchment, the available data are limited to the river and coastal sites. The coastal site was significantly higher in iron concentration compared to the river (Figure 4.6 and Table 4.14).

Iron in the less than 66 nm physical size fraction

A Welch ANOVA was conducted. Iron concentrations in the less than 66 nm physical size fractions are significantly different ($F(5,5.03)=5517.40$, $p=0.000$). Table 4.15 presents the post-hoc Games-Howell pairwise comparisons.

Table 4.15. Iron concentrations in the less than 66 nm size fraction: grouping Information using the Games-Howell Method and 95% confidence.

Site	N	Mean	Grouping
Peat bog <66 nm	3	4023.00	A
Halladale stream <66 nm	3	3054.50	B
Melvich Bay <66 nm	3	1887.14	C
R. Halladale <66 nm	3	761.20	D
R. Thurso <66 nm	3	409.37	E
Thurso estuary <66 nm	3	67.70	F

Means that do not share a letter are significantly different.

All sites across the two catchments had significantly different iron concentrations in the less than 66 nm fraction. The iron concentration decreased from source to sea in the River Thurso catchment. The source site (Halladale stream) had the highest iron concentration in the Halladale catchment, and the Halladale river presents the lowest iron concentration (Figure 4.6 and Table 4.15).

Iron in the less than 400 nm physical size fraction

A Welch ANOVA was conducted. Iron concentrations in the less than 400 nm size fractions are significantly different ($F(5, 5.47)$, $p=0.000$). Table 4.16 presents the post-hoc Games-Howell pairwise comparisons.

Table 4.16. Iron concentrations in the less than 400 nm size fraction: grouping Information using the Games-Howell Method and 95% confidence.

Site	N	Mean	Grouping
Peat bog <400 nm	3	15317.00	A
Halladale stream <400 nm	3	3096.70	B
R. Halladale <400 nm	3	2712.50	C
Melvich Bay <400 nm	3	1935.40	D
R. Thurso <400 nm	3	1919.40	D
Thurso estuary <400 nm	3	139.30	E

Means that do not share a letter are significantly different.

In the less than 400 nm size fraction, iron concentrations in the River Thurso catchment decreased from source to sea. The Halladale catchment displayed the same decreases from source site to

coastal site. The coastal site for the Halladale catchment had similar iron concentration to the Thurso river. All other sites had significantly different iron concentrations.

Iron in the unfiltered samples

A Welch ANOVA was conducted. Iron concentrations in the unfiltered samples have significant differences ($F(5,4.67)=467.22$, $p=0.000$). Table 4.17 presents the post-hoc Games-Howell pairwise comparisons.

Table 4.17. Iron concentrations in the unfiltered samples: grouping Information using the Games-Howell Method and 95% confidence.

Site	N	Mean	Grouping
Peat bog	3	136388.00	A
R. Thurso	3	5733.00	B
Halladale stream	3	3252.00	B C
R. Halladale	3	2805.40	B C
Melvich Bay	3	2706.00	C
Thurso estuary	3	524.69	D

Means that do not share a letter are significantly different.

In the unfiltered samples, the Thurso catchment unfiltered iron concentrations were significantly different to each other and reduced from source site to coastal site. The Halladale catchment followed the same trend and there was no significant difference in the concentrations found between the source site and the river.

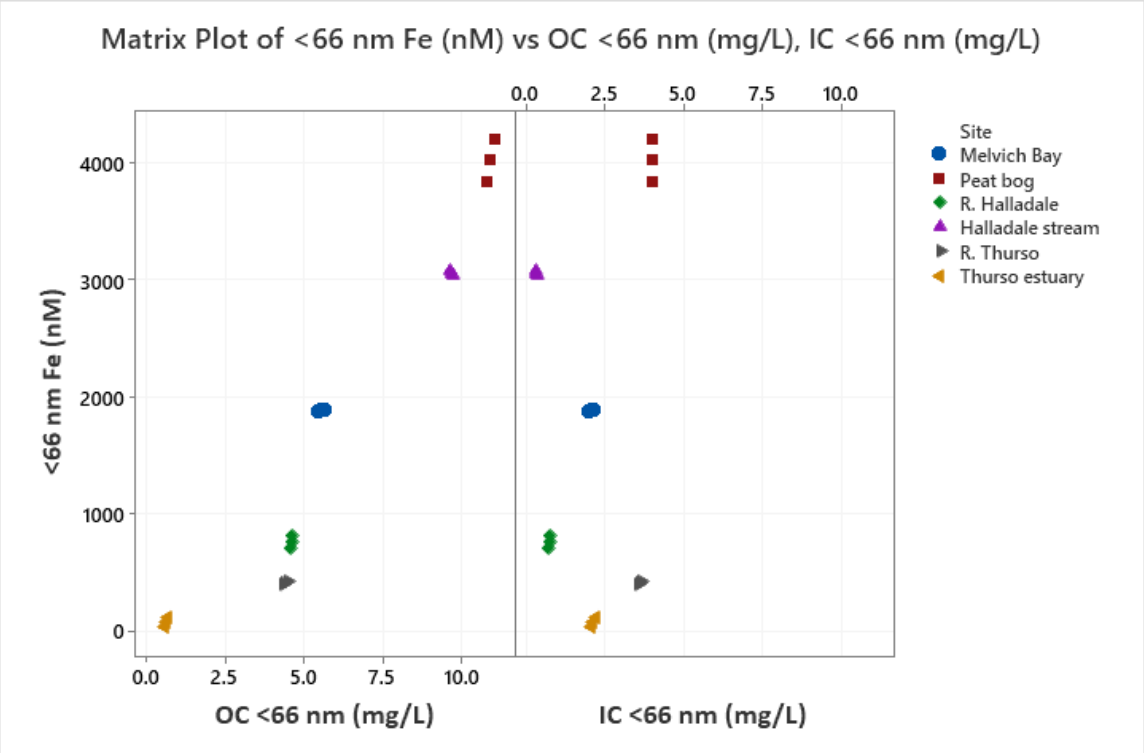

Figure 4.7. Matrix plot for iron and carbon in the <66 nm size fractions by sampled site, 2018.

Table 4.18. Pearson product-moment correlation coefficients were computed to assess the relationships between concentrations of iron and OC, iron and IC, and OC and IC in the <66 nm size fraction.

	Fe<66 nm (nM)	OC <66 nm (mg L^{-1})
OC <66 nm (mg L^{-1})	r=0.954, *p*=0.000	
IC <66 nm (mg L^{-1})	*r*=0.113, *p*=0.656	*r*=0.077, *p*=0.760

The results indicate that there is a positive correlation between iron and OC in the <66 nm size fraction. There was no correlation between iron and IC or IC and OC in the same size fraction (Figure 4.7 and Table 4.18).

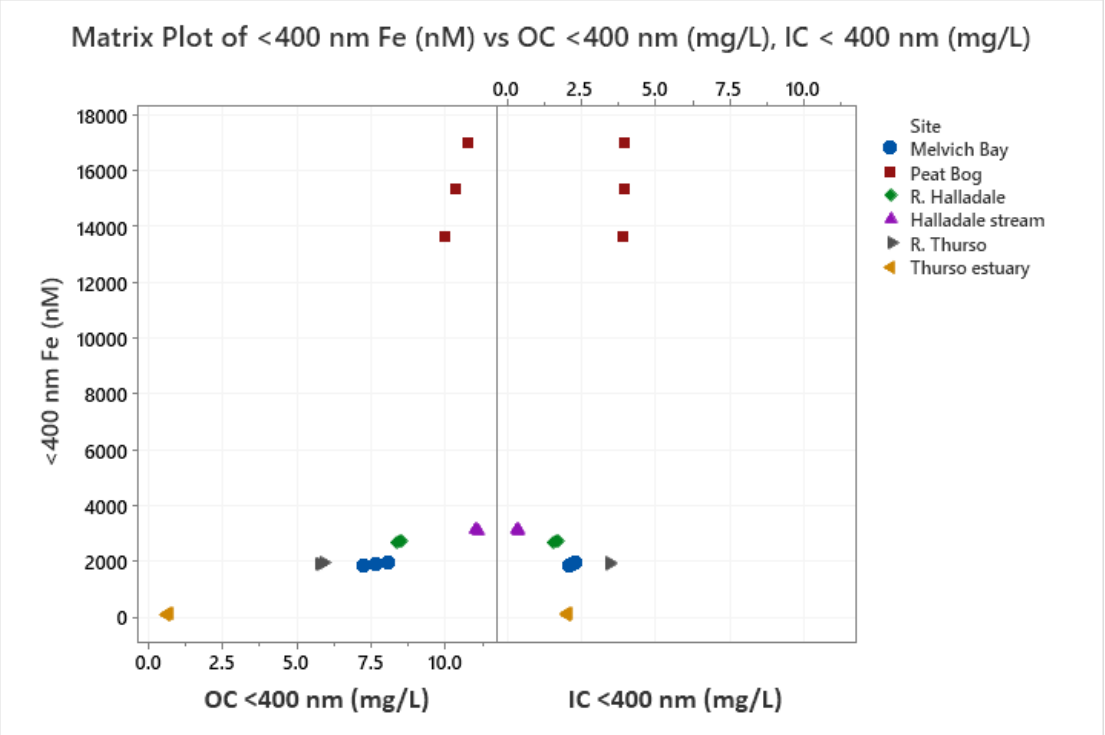

Figure 4.8 Matrix plot for iron and carbon (OC and IC) in the <400 nm size fractions by sampled site, 2018.

Table 4.19. Pearson product-moment correlation coefficients were computed to assess the relationships between concentrations of iron and OC, iron and IC, and OC and IC in the <400 nm size fraction.

	Fe<400 nm (nM)	**OC <400 nm (mg L^{-1})**
OC <400 nm (mg L^{-1})	*r*=0.550, *p*=0.018	
IC < 400 nm (mg L^{-1})	*r*=0.562, *p*=0.015	*r*= -0.126, *p*=0.619

The results indicate there is a positive correlation between iron and OC, and between iron and IC in the <400 nm size fraction. There was no significant correlation between iron IC and OC in the same size fraction (Figure 4.8 and Table 4.19).

Iron concentrations 2018: AF^4-ICP-MS

ICP-MS element screening prior to AF^4-ICP-MS

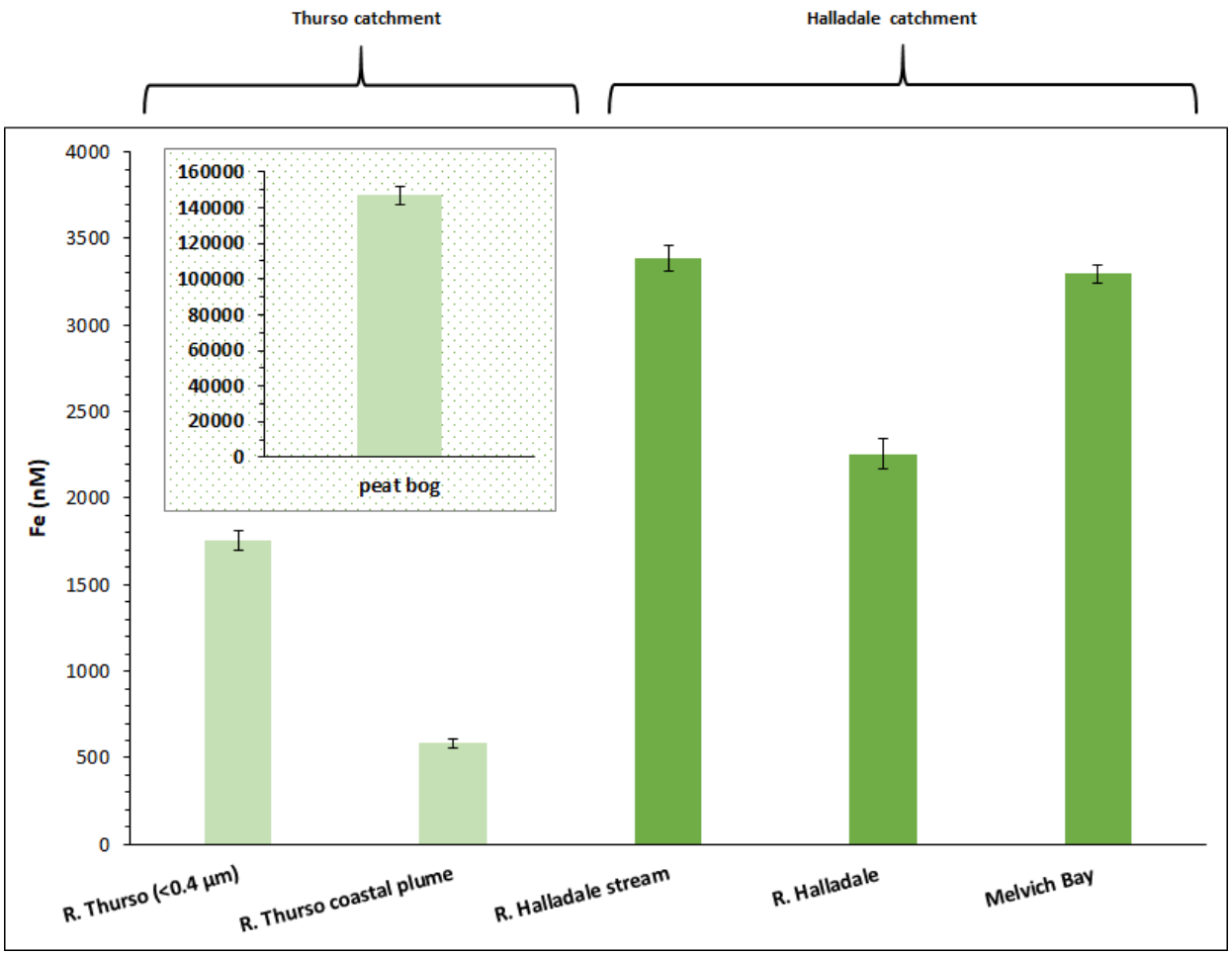

Figure 4.9. Total sample iron concentrations from element screening prior to AF^4-ICP-MS analysis. ICP-MS measured total iron concentrations in samples: Peat bog (<5000 nm), River Thurso (<400 nm), Halladale feeder stream (<5000 nm), R. Halladale (<5000 nm), Thurso coastal plume (<5000 nm) and Melvich Bay (<5000 nm).

Total iron concentrations on samples filtered to < 5000 nm (River Thurso <400 nm) are shown in Figure 4.9. The peat bog had the highest iron concentration and there was a reduction, by three orders of magnitude in the Thurso estuary concentration. In the River Halladale catchment, there

was a reduction in iron concentration from the feeder stream to the river, and then an increase again in the coastal plume.

A Welch ANOVA was conducted. Iron concentrations in samples filtered to <5000 nm (River Thurso has been excluded as there was no available unfiltered sample) are significantly different ($F(5,5.36)=1464.08$, $p=0.000$). Table 4.20 presents the post-hoc Games-Howell pairwise comparisons.

Table 4.20. Iron concentrations in **samples filtered to <5000 nm**: grouping Information using the Games-Howell Method and 95% confidence.

site	N	Mean	Grouping
Peat bog <5000 nm	3	146835.00	A
Halladale stream <5000 nm	3	3384.40	B
Melvich Bay <5000 nm	3	3294.80	B
River Halladale <5000 nm	3	2256.20	C
Thurso estuary <5000 nm	3	583.80	D

Means that do not share a letter are significantly different.

The iron concentration in the Thurso catchment samples decreased significantly from the Peat bog source site to the Thurso estuary. The iron concentration for the <400 nm fraction for River Thurso, measured during the screening, was 1754.86 (± 53.72) nM. The Halladale catchment had similar iron concentrations in both the Halladale source stream and the coastal site. The concentration in the Halladale River was lower than in the other two sites (Figure 4.9 and Table 4.20).

Measurements using Dynamic Light Scattering (DLS)

Particle size distribution was measured using dynamic light scattering (DLS) for samples shown in Figure 4.9. The mean hydrodynamic diameter (d.nm) of the included particles for the maximum zeta (ζ) average (Z-Average.) are presented in Table 4.21 .

Table 4.21. DLS analysis samples (<5000 nm filtered/River Thurso prefiltration was 400 nm): maximum Z-Average (zeta (ζ) average) d.nm (standard deviations for the <5000 nm prefiltered samples (River Thurso prefiltration was 400 nm). percentage of iron in each eluted fraction with

Site	**1st fraction** ***(% Fe)***	**2nd fraction** ***(% Fe)***	**3rd fraction = 60 nm to DLS max. average (d.nm) ± standard deviation** ***(% Fe)***
Peat bog	Approximately 1.2 nm to 20 nm *(1%)*	20 nm to 60 nm (48%)	1150.27 ± 2206.02 *(51%)*
River Thurso	Approximately 1.2 nm to 20 nm (*23%)*	20 nm to 60 nm (43%)	327.91 ± 1090.47 *(34%)*
Thurso estuary	Approximately 1.2 nm to 20 nm *(31%)*	20 nm to 60 nm (36%)	682.97 ± 99.20 *(33 %)*
Halladale stream	Approximately 1.2 nm to 20 nm *(60%)*	20 nm to 60 nm (26%)	2664.12 ± 2834.10 *(14%)*
River Halladale	Approximately 1.2 nm to *20 nm*	20 nm to 60 nm (48%)	1447.84 ± 2074.29 *(25%)*
Melvich Bay	Approximately 1.2 nm to 20 nm *(20%)*	20 nm to 60 nm (40%)	212.15 ± 458.46 *(40%)*

Fractograms: AF^4-ICP-MS

A

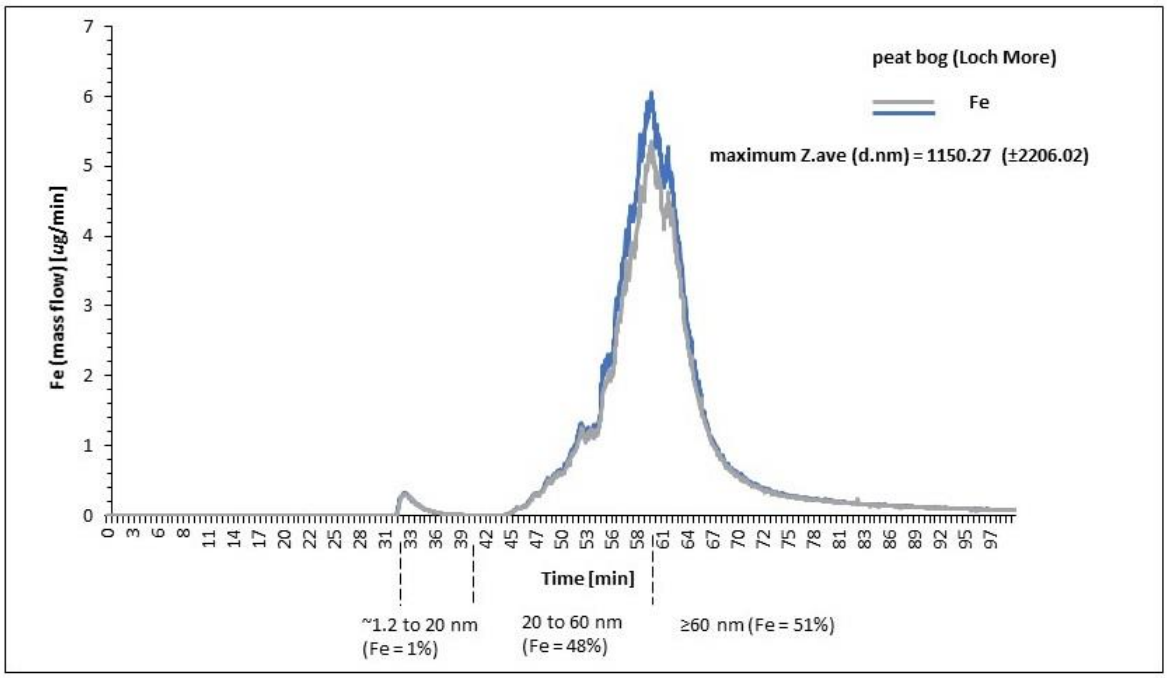

B

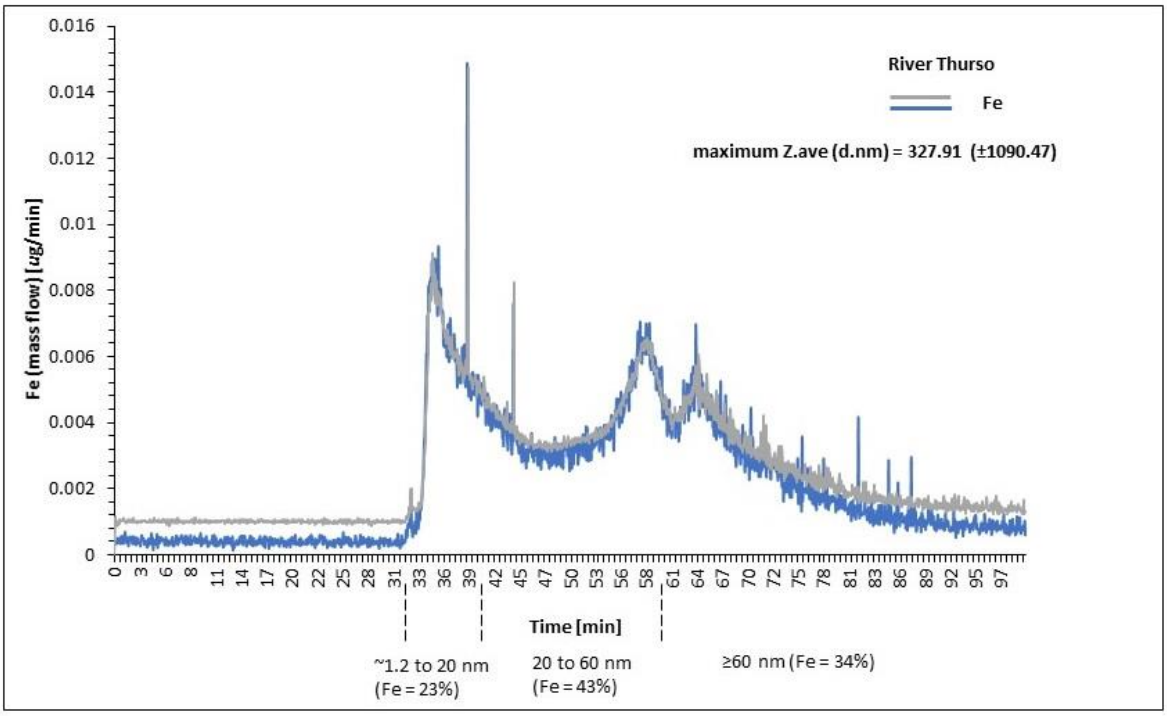

C

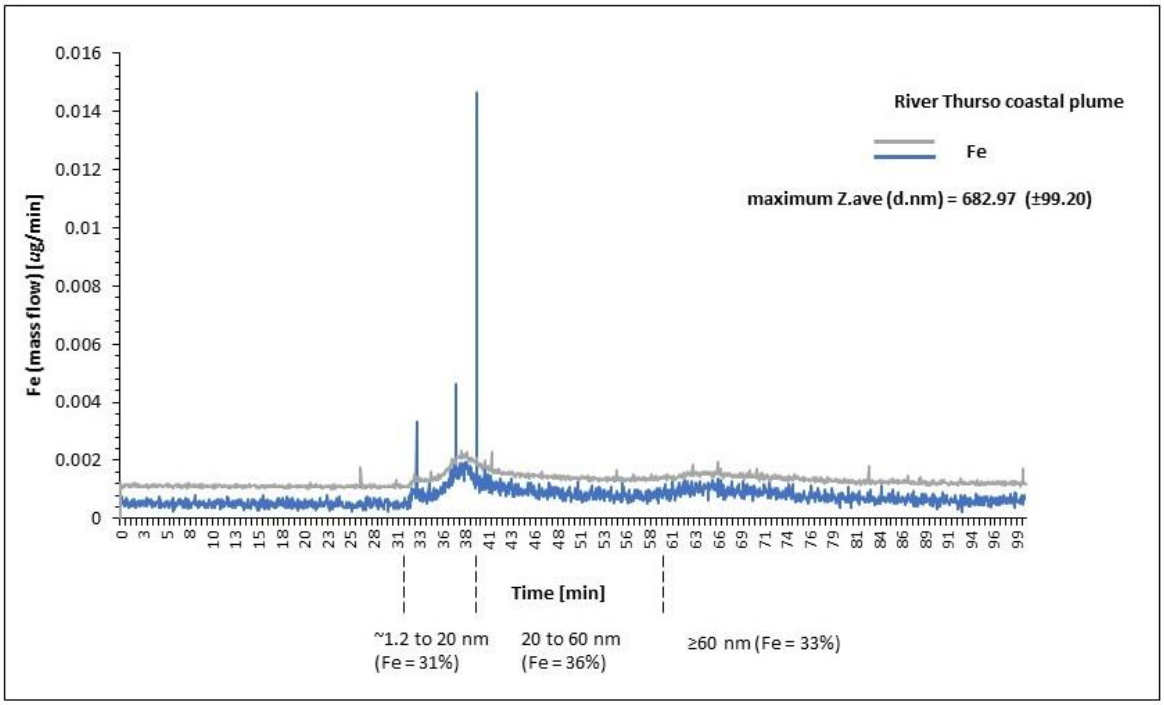
River Thurso coastal plume
Fe
maximum Z.ave (d.nm) = 682.97 (±99.20)
Fe (mass flow) [ug/min]
Time [min]
~1.2 to 20 nm
(Fe = 31%)
20 to 60 nm
(Fe = 36%)
≥60 nm (Fe = 33%)

D

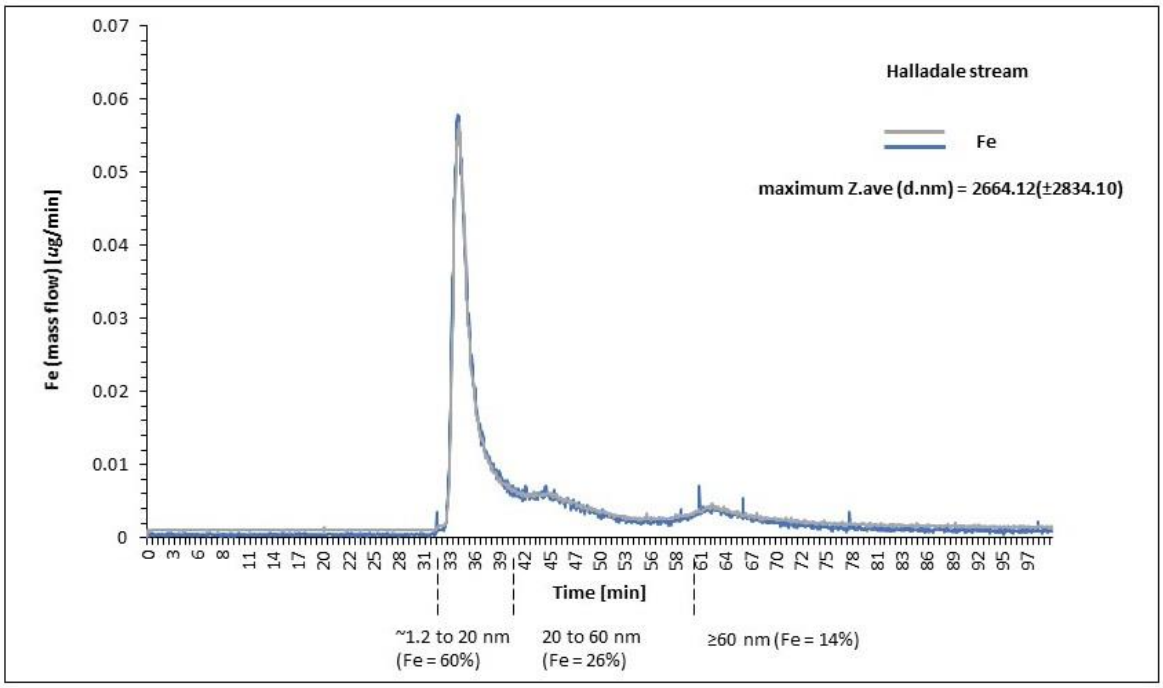
Halladale stream
Fe
maximum Z.ave (d.nm) = 2664.12(±2834.10)
Fe (mass flow) [ug/min]
Time [min]
~1.2 to 20 nm
(Fe = 60%)
20 to 60 nm
(Fe = 26%)
≥60 nm (Fe = 14%)

E

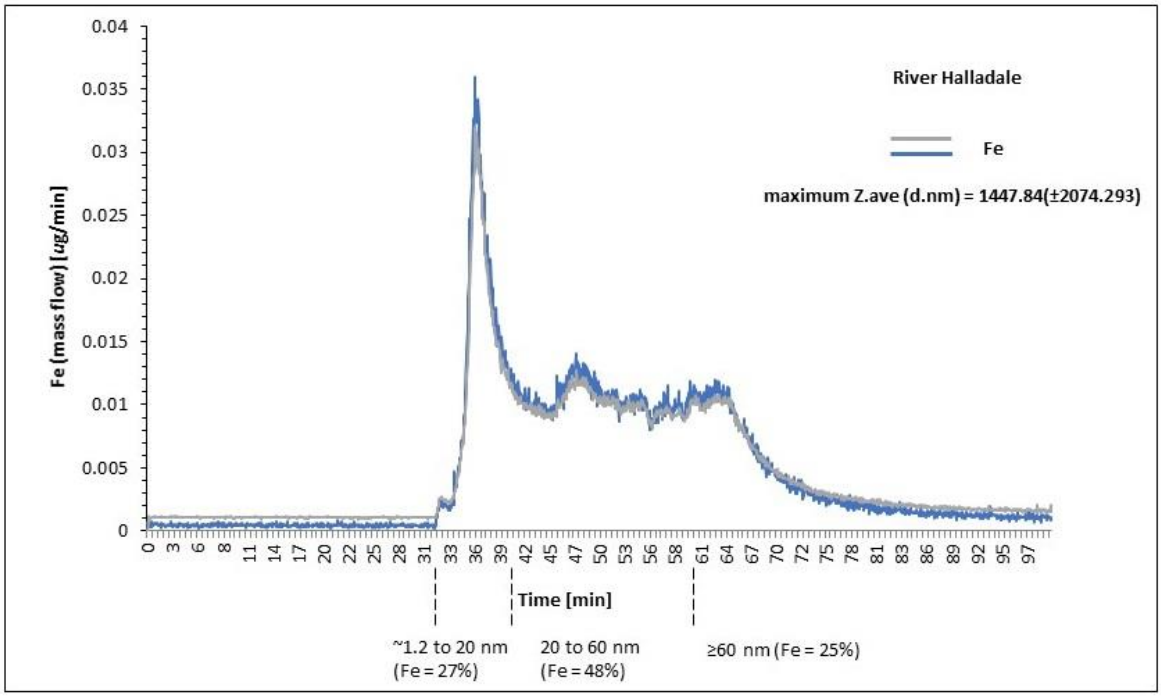

F

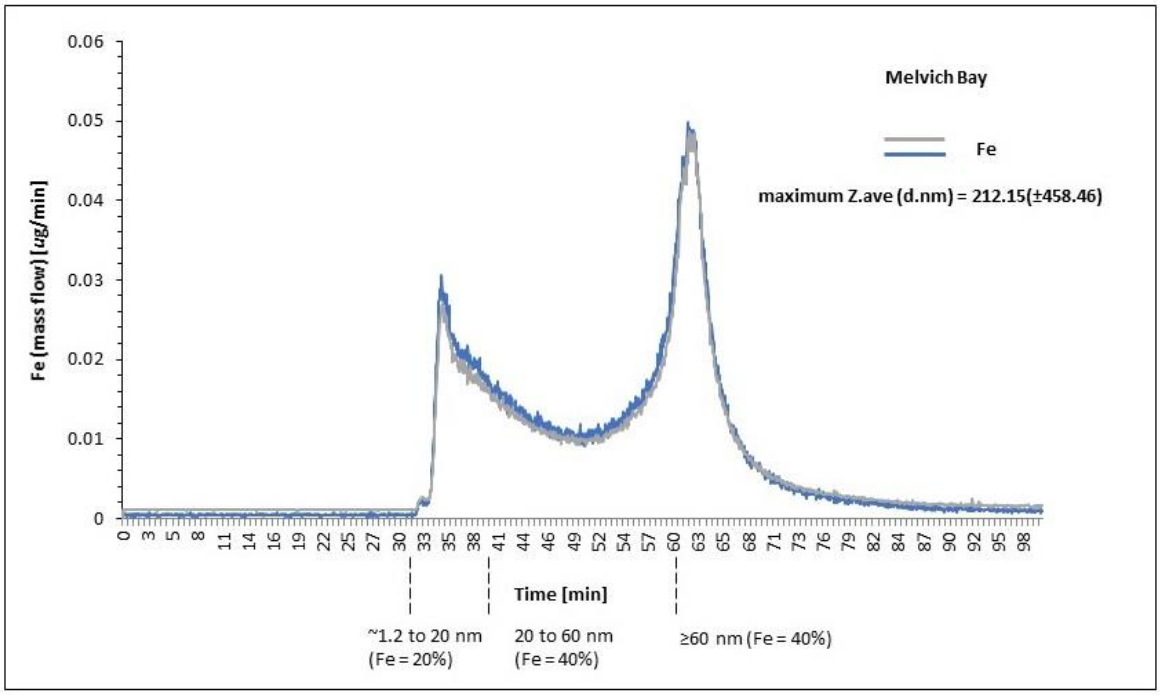

Figure 4.10. AF4-ICP-MS fractograms: ^{56}Fe and ^{57}Fe mass flow in μg/min. A) Peat Bog, B) River Thurso, C) Thurso estuary D) Halladale stream E) River Halladale and F) Melvich Bay. Maximum particle size by intensity (Z-average) for each sample hydrodynamic diameter (d.nm).

Maximum particle size by intensity (Z-average) for each sample hydrodynamic diameter (d.nm) is shown in the DLS data in Table 4.21. The Thurso catchment fractograms show that most of the iron in the peat bog found in particles that are >20 nm, peaking at ~60 nm. However, there is a small peak evident on the >1.2<20 nm sized fraction. Although this is a small peak relative to the second peak (60 nm), iron concentrations are still elevated compared to the River Thurso and coastal sample. The River Thurso sample is composed of iron bearing particles which are found throughout the eluted size fractions, with peaks at ~2 nm and over the larger 60 nm range. As the river meets the coastal sea, the > 20 nm fraction is significantly depleted as iron is lost, however, there are detectable particles containing iron in the smaller 1.2 and 20 nm sized fractions.

In the Halladale catchment, there is a significant iron spike at ~1.2 nm in the feeder stream sample where most of the iron appears to be found in <20 nm fraction. The larger particulate fraction (>60 nm) holds the least iron concentration in this sample. The River Halladale sustains iron between the 1.2 and 20 nm fraction, however, unlike the feeder stream, there is still evidence of iron-bearing particles over the larger particulate fractions and this sample appears to be fairly polydisperse. The coastal site at Melvich Bay then displays a bimodal distribution of iron containing particles with peaks evident at both ~2 nm and 60 nm. Iron concentrations appear to increase over this catchment compared to the Thurso catchment which decreases from source to sea.

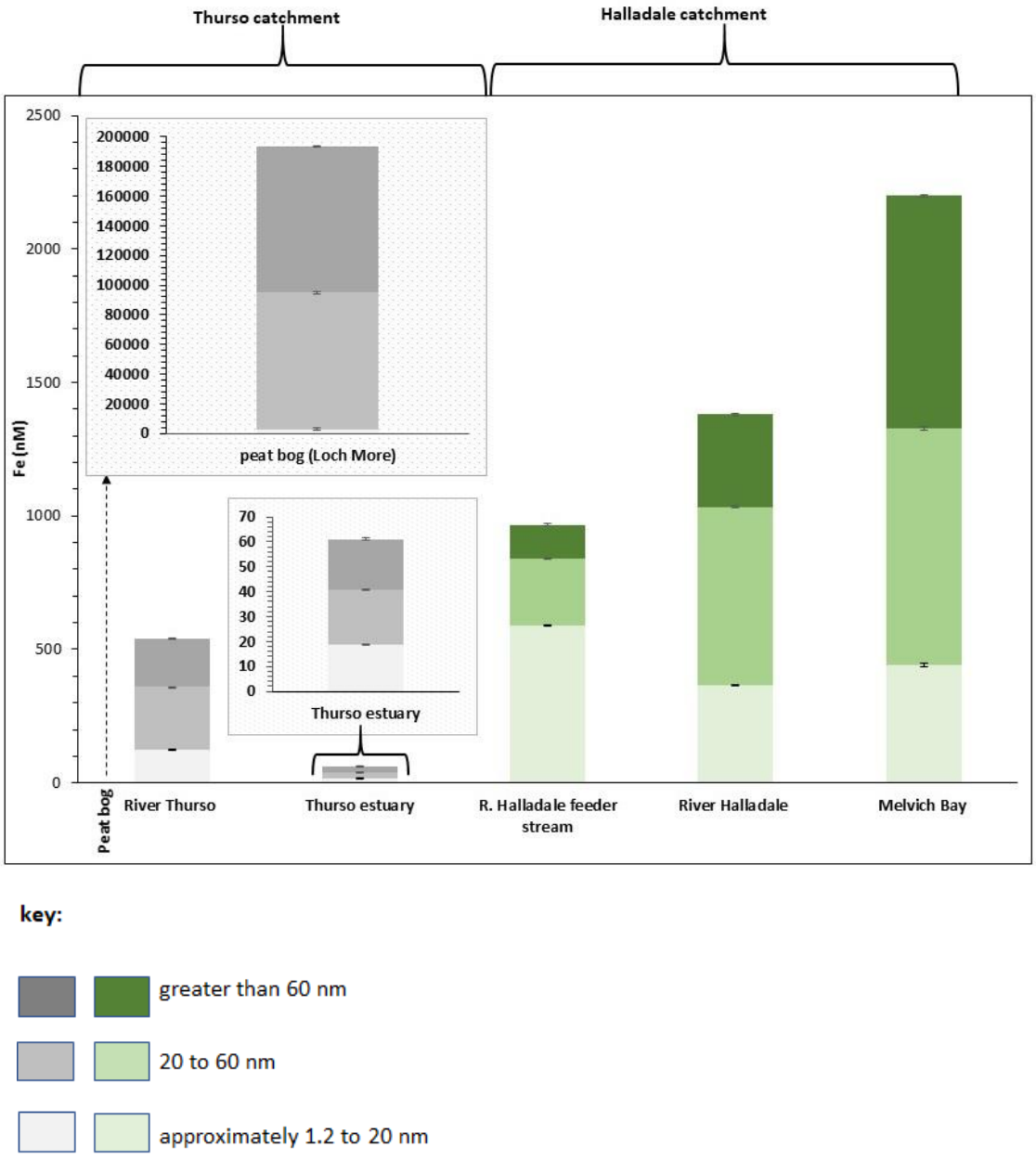

Figure 4.11. Iron concentrations, AF⁴ size fractionation (2018). Fe (nM) for AF⁴-ICP-MS physical size fractionation where: 1st fraction is approximately 1.2 nm to 20 nm; 2nd fraction is >20 nm to 60 nm and 3rd fraction is >60 nm to maximum size detected with Dynamic Light Scattering (DLS)

Fe (nM) for AF^4-ICP-MS 1st fraction: approximately 1.2 nm to 20 nm

A Welch ANOVA was conducted. Significant differences were found in the iron concentrations in the 1st fraction (F(5,4.96)=58581.38, p=0.000). Table 4.22 presents the post-hoc Games-Howell pairwise comparisons.

Table 4.22. AF^4-ICP-MS iron concentrations in 1st fraction (approximately 1.2 nm to 20 nm): grouping Information using the Games-Howell Method and 95% confidence.

Site 1st fraction AF^4-ICP-MS	N	Mean	Grouping
Peat bog	3	2607.55	A
Halladale feeder stream	3	590.00	B
Melvich Bay	3	442.12	C
R. Halladale	3	366.35	D
R. Thurso	3	125.75	E
Thurso estuary	3	18.72	F

Means that do not share a letter are significantly different.

Fe (nM) for AF^4-ICP-MS 2nd fraction: 20 nm to 60 nm

A Welch ANOVA was conducted. Significant differences were found in the iron concentrations in the 2nd fraction (F(5,4.69)=25028.77, p=0.000). Table 4.26 presents the post-hoc Games-Howell pairwise comparisons.

Table 4.23. AF^4-ICP-MS iron concentrations in 2nd fraction (approximately 1.2 nm to 20 nm): grouping Information using the Games-Howell Method and 95% confidence.

Site 2nd fraction AF^4-ICP-MS	N	Mean	Grouping
Peat bog	3	92448.00	A
Melvich Bay	3	885.37	B
R. Halladale	3	667.24	C
Halladale stream	3	247.99	D
R. Thurso	3	233.21	E
Thurso estuary	3	21.9986	F

Means that do not share a letter are significantly different.

Fe (nM) for AF^4-ICP-MS 3rd fraction: greater than 60 nm

A Welch ANOVA was conducted. Significant differences were found in the iron concentrations in the 3rd fraction (F(5,4.75)=27592.36, p=0.000). Table 4.24 presents the post-hoc Games-Howell pairwise comparisons.

Table 4.24. AF^4-ICP-MS iron concentrations in 3rd fraction (greater than 60 nm): grouping Information using the Games-Howell Method and 95% confidence.

Site 3rd fraction AF^4-ICP-MS	N	Mean	Grouping
Peat bog	3	98621.00	A
Melvich Bay	3	871.75	B
R. Halladale	3	345.81	C
R. Thurso	3	183.22	D
Halladale stream	3	128.81	E
Thurso estuary	3	20.36	F

Means that do not share a letter are significantly different.

4.3.3 **Physical size fractionation comparison tables**

Iron concentration in the measured fractions versus mass balance calculation for the greater than 66 nm, less than 450 nm physical size fraction for 2017 where TFF was employed is shown in Table 4.25.

Table 4.25. Iron concentration in the measured fractions versus mass balance calculation for the greater than 66 nm, less than 450 nm physical size fraction for 2017 samples: Tangential flow filtration.

Sampling site	**(A) measured <450 nm *minus* measured <66 nm** (mean *± sd*) **Fe(nM)**	**(B) measured >66 nm<450 nm** (mean *± sd*) **Fe(nM)**	**(A minus B) difference in means Fe(nM)**
River Halladale	6949.65 ± *117.65 minus* 662.83 ± *40.43* = 6286.82	6475.06 ± *41.18*	-188.24
Melvich Bay	6920.99 ± *15.15 minus* 644.79 ± *9.31* = 6276.20	4606.86 ± *472.73*	1669.34
River Thurso	6063.26 ± *18.37 minus* 934.12 ± *2.90* = 5129.14	4393.05 ± *464.32*	736.09

There was a difference in the iron concentration between the two methods for all samples measured (Table 4.25). River Halladale had a lower iron concentration in the measured fraction (A) than was calculated from the two separately measured fractions (A minus B). Higher concentrations were found in the calculated fractions (A minus BB) than in the measured fraction (B) for the other two sampled sites.

Iron concentration in the measured fractions versus mass balance calculation for the greater than 66 nm, less than 450 nm physical size fraction for 2018 where Jumbosep centrifugal devices were employed is shown in Table 4.26.

Table 4.26. Iron concentration in the measured fractions versus mass balance calculation for the greater than 66 nm, less than 400 nm physical size fraction for 2018 samples: Jumbosep centrifugal devices.

Sampling site	**(A)** **measured <400 nm *minus* <66 nm** (mean *± sd*) **Fe(nM)**	**(B)** **measured >400 nm<66 nm** (mean *± sd*) **Fe(nM)**	**Difference in means (A minus B) Fe(nM)**
Peat bog	15317.01 ± *1689.60 minus* 4023.39 ± *177.48* =11294.00	10478.34 ± *45.58*	815.66
River Thurso	1919.37 ± *35.77* minus 409.37 ± *16.88* =1510.03	1361.25 ± *59.89*	148.78
Thurso estuary	139.30 ± *27.19* minus 67.71 ± *39.89* =456.99	550.34 ± *56.62*	-93.35
Halladale stream	3096.67 ± *22.67* minus 3054.49 ±*18.32* =2490.80	2667.60 ± *183.73*	-176.80
River Halladale	2712.47 ± *20.62* minus 761.22 ± *2.25* =92.90	85.41 ± *12.69*	7.49
Melvich Bay	1935.40 ± *62.97* minus 1887.14 ± *221.76* =197.50	174.64 ± *59.10*	22.86

There was a difference in mean Fe for all samples measured for the Jumbosep (2018) size fractionation methods. All samples from sites, excepting Thurso estuary and Halladale stream, had higher iron concentrations in the measured fraction (B) compared to the calculated concentration from the separately measured fractions (A) (Table 4.26).

AF⁴- ICP-MS: total sample iron concentrations comparison with iron in the eluted fractions.

Table 4.27. AF⁴-ICP-MS Fe (nM): comparisons between <5000 nm (<400 nm for River Thurso sample) filtered total sample iron concentration and AF⁴ fractioned iron concentrations. Fractions: 1st (approx. 1.2 nm to 20 nm), 2nd (20 nm to 60 nm) and 3rd (greater than 60 nm).

site	AF⁴ fraction	(A) <5000 nm filtered Fe(nM)	*(A) standard deviation Fe(nM)*	(B) AF⁴ fraction Fe(nM)	*(B) standard deviation Fe(nM)*	Difference (A-B) Fe(nM)
Peat bog	sum of fractions	146834.99	*5372.01*	193676.70	*n/a*	-46841.71
	1st	*n/a*	*n/a*	*2607.55*	*84.12*	*n/a*
	2nd	*n/a*	*n/a*	*92448.49*	*7063.45*	*n/a*
	3rd	*n/a*	*n/a*	*98620.66*	*7377.53*	*n/a*
River Thurso <400 nm filtered	sum of all fractions	1754.86	*53.72*	542.18 (<400 nm fraction)	*n/a*	1212.67
	1st	*n/a*	*n/a*	*125.75*	*11.08*	*n/a*
	2nd	*n/a*	*n/a*	*233.21*	*21.38*	*n/a*
	3rd	*n/a*	*n/a*	*183.22*	*17.82*	*n/a*
Thurso estuary	sum of all fractions	583.76	*28.65*	61.08	*n/a*	522.68
	1st	*n/a*	*n/a*	*18.72*	*4.36*	*n/a*
	2nd	*n/a*	*n/a*	*22.00*	*1.62*	*n/a*
	3rd	*n/a*	*n/a*	*20.36*	*2.05*	*n/a*
Halladale stream	sum of all fractions	3384.37	*71.63*	845.94	*n/a*	2538.43
	1st	*n/a*	*n/a*	*504.11*	*30.85*	*n/a*
	2nd	*n/a*	*n/a*	*222.42*	*19.88*	*n/a*
	3rd	*n/a*	*n/a*	*119.41*	*8.96*	*n/a*
River Halladale	sum of all fractions	2256.24	*89.53*	1379.40	*n/a*	876.85
	1st	*n/a*	*n/a*	*366.35*	*32.14*	*n/a*
	2nd	*n/a*	*n/a*	*667.24*	*54.01*	*n/a*
	3rd	*n/a*	*n/a*	*345.81*	*28.89*	*n/a*
Melvich Bay	sum of all fractions	3294.83	*53.72*	2199.24	*n/a*	1095.59
	1st	*n/a*	*n/a*	*442.12*	*39.60*	*n/a*
	2nd	*n/a*	*n/a*	*885.37*	*75.26*	*n/a*
	3rd	*n/a*	*n/a*	*871.75*	*52.33*	*n/a*

There were differences in the iron concentration for the <5000 nm (total) samples compared to the sum of the AF^4-ICP-MS fractions. The mean values had higher iron concentrations in the total samples for all sites excepting Peat bog where there was a lower concentration in the <5000 sample compared to the summed fractions. It should be noted that the calculation in Table 4.27 ('Difference (A-B)' column) considers only the mean values for the summed fractions.

4.4 **Discussion**

The main aim of the study was to facilitate the development of methods to explore the potential to employ synchrotron Mössbauer (SMS) techniques for the investigation of iron mineralogy in water-borne nanoparticles and colloids in natural waters. The main objectives were to i) quantify iron concentrations in size defined nanoparticle/colloidal fractions ii) determine which particle size fractions iron is associated with for both catchments studied: from source waters, through the rivers to the coastal plume iii) investigate relationships between organic and inorganic carbon concentrations in the nanoparticle/colloidal fractions were quantified and compared to the iron concentration results in the same size fractions and vi) investigate available isolation and concentration techniques for their effectiveness and applicability to SMS sample preparation.

4.4.1 **Particle fractionation**

As discussed in Chapter 1 (section 1.2), it is increasingly recognised that the operationally defined dissolved fraction is not composed of only aqueous phase but also contains nanoparticles and colloids. To better understand biogeochemical cycling and transport of elements it is apparent that the components of the dissolved fraction are identified (Gottselig et al., 2017). For this study, further defining nanoparticle and colloidal containing physical size fractions enabled investigation of iron concentration distribution within the dissolved fraction from terrestrial source waters, rivers and their estuaries.

A variety of particle size fractionation methods were used over this study. This included exploring the use of AF^4-ICP-MS at IBG-3 (Forschungszentrum Jülich) analysis, with a view to its applicability for future iron mineralogical studies on water-borne Fe-OM nanoparticles. The 2018 collected samples were used for this The AF^4-ICP-MS, therefore, effects of long term storage should be considered when analysing the results presented in section 4.3.

Particle size isolation for onward analysis

Vacuum filtration (with filter membranes) was used to isolate the dissolved fraction (operationally defined as less than 450 nm) for samples in both 2017 and 2018. There are known issues with membrane filtration such as the underestimation of particulate matter in the filtrate (Gimbert et al., 2005). Alternative methods to physically isolate the dissolved fraction prior to further fractionation and onward (uncoupled) analyses were explored, however, when consideration was given to the availability of the equipment, and relatively low cost of the filter membranes, the decision was taken to continue with this accepted method.

Two different techniques were used to isolate the less than 66 nm fraction: TFF and Jumbosep centrifugal devices. There were observed losses and gains in iron concentration for the TFF (Table 4.25). One benefit of the TFF is that it has the capacity to deal with relatively large sample volumes as was the case in this study (in excess of 2 L) (Martin et al., 2018, Shah et al., 2020). However, in more dilute waters such as the ocean, the loss or gain of particles could have a significantly impact upon the reliability of iron and other element concentration results. As a result of these observations the decision to use Jumbosep centrifugal devices was made. There were also observed losses and gains in iron concentration when using the Jumbosep devices (Table 4.26). These are likely due to particulate material forming a particle cake on the membrane, resulting in clogging of the membrane pores (Zirkler et al., 2012). This can cause the unintended retention of smaller particles (Gimbert et al., 2005). Amicon Ultra-15 units were used to isolate the less than 2 nm size fraction in the 2018 study. The losses and gains were not

analysed for this study, however, it is expected that there are similar issues with membrane caking and pore clogging as visible accumulation of material on the membrane was observed during processing. It became apparent that alternative size fractionation methods should be investigated for future studies.

Asymmetric flow field flow fractionation (AF^4)

Field flow fractionation (FFF) has been shown to be more successful in terms of particle recovery, than conventional methods, when investigating the distribution of colloids in aquatic environments (Gimbert et al., 2005, Baalousha et al., 2011). In a recent aquatic colloid study, Gottselig et al. (2020) concluded that, despite the potential for membrane interactions, there were no major losses of particles when employing AF^4 coupled to ICP-MS. Similar studies have also shown AF^4 recoveries to be between 70 and 99.5% (Gottselig et al., 2017, Baken et al., 2016).

In this study, the measured <5000 nm (total sample) iron concentrations were greater than the summed fractions measured using AF^4-ICP-MS fractions in all of the samples except for the Peat bog sample which was lower (Table 4.27). The truly dissolved fraction (<1.2 nm in this case) is accepted as the difference between the total sample iron concentration and the iron concentration in sum of the eluted fractions (Gottselig et al., 2020). The Peat bog results appear to be anomalous with the reported recovery data discussed above, however, there are a number of potential explanations. The lower concentration in the total sample measurement could be attributed to sedimentation of larger particles in the sample vial prior to AF^4-ICP-MS for the size fractioned analysis, or possibly a block in the stand alone ICP-MS nebulizer during the total Peat bog sample measurement.

As discussed in Chapter 2 (section 2.4.2), AF^4 can be coupled to a variety of analytical instruments. In addition to this, Hu et al. (2020) have demonstrated the capability to collect the eluted size fractioned particles for onward analyses using stand-alone instrumentation. This reveals the

potential to use AF^4 to collect nanoparticles and colloids from environmental water samples for onward iron mineralogy studies using SMS.

4.4.2 **Iron and carbon**

The first part of this study (2017 sampling) investigated the iron and carbon concentrations in two rivers and one coastal site: River Thurso, River Halladale and its coastal plume at Melvich Bay. The second part of the study, in 2018, extended the sampling to include the River Thurso estuary and two source water sites providing source, river and coastal sites for both river catchments. In the second study, carbon concentrations were measured in equivalent physical size fractions as the colloidal iron concentrations (<400 nm and <66 nm) to facilitate investigation of any relationships between OC, IC and iron concentrations. The results from the two sampling periods revealed differences in the carbon concentrations of both OC and IC. Carbon concentration data in the 2017 study was limited to two river sites and once coastal site and only included one physical size fraction (Figure 4.4).

When interpreting the results from this study it should be acknowledged that the sampling was conducted over two short time periods during 2017 and 2018. This was intentional, allowing time to be spent exploring methods for SMS technique development. To better understand the iron and organic matter dynamics, future studies using these methods should be more extensive and include seasonal studies to investigate fluxes of iron and carbon under different environmental conditions. An example of this can be seen in Muller and Cuscov (2017) and, as discussed in Chapter 1, should ideally also include iron mineralogy.

Iron and carbon, 2017

The 2017 concentrations of OC (<450 nm) were higher in the Thurso River than in the Halladale catchment sites (Table 4.6), and IC (<450 nm) concentrations were higher in the Halladale catchment sites compared to the River Thurso (Table 4.7). There were no significant differences

found in the iron concentration in the less than 450 nm size fraction for the 2017 sites sampled (section 4.3.2, Table 4.4). Two further iron fractions were isolated and measured; the less than 66 nm fraction and the unfiltered samples. There was no significant difference in iron concentration across the sampled sites in the less than 66 nm fraction, however, the unfiltered iron concentrations were significantly different across the three sites (Table 4.8).

Carbon and iron, 2018

Iron concentration data for 2018 is shown in Figure 4.6. Iron was found to be positively correlated with both OC (p=0.018) and IC (p=0.015) in the <400 nm size fraction. There was no significant correlation between IC and OC (p>0.05) (Figure 4.8 and Table 4.8). Both iron and OC concentrations (<400 nm) decreased from source site to coastal site in both catchments (Figures 4.5 and 4.6), consistent with previous studies in this area (Muller and Cuscov, 2017, Muller, 2018). Contrary to the 2017 results, OC was consistently higher in the Halladale catchment sites compared to the equivalent sites in the Thurso catchment. Furthermore, IC concentrations (<400 nm) were higher in the Thurso catchments sites compared to the equivalent Halladale sites. Interestingly, a decrease in IC from source to coast was only observed in the Thurso catchment. The highest IC concentration in the Halladale catchment was found in the coastal site and the lowest in the source (Figure 4.5 and Table 4.11).

Iron and OC were found to be positively correlated (p=0.000) in the less than 66 nm size fraction. There was no correlation between iron and IC nor between IC and OC (p>0.05) (Figure 4.7). The less than 66 nm iron (Table 4.15) and OC (Table 4.11) concentrations followed a similar source to coast reduction in concentration as the less than 400 nm fraction in the Thurso catchment. The same trend was not observed in the Halladale catchment. IC concentrations (<66 nm) in the Halladale catchment were highest in Melvich Bay and lowest in the source site, however, the Thurso catchment IC reduced in concentration from source to sea similar to the less than 400 nm fraction (Table 4.11). Iron in the truly dissolved fraction (<2 nm) reduced from source to sea in the

Thurso catchment, consistent with the other size fractions (<66 nm and <400 nm). The iron concentration in the coastal site for the Halladale catchment was higher than the river which, is consistent with the trend observed in the less than 66 nm fraction but not the less than 400 nm fraction. It should be acknowledged that there were no available data for the Halladale stream source site. Iron concentrations in the unfiltered samples followed the same trend of reducing iron concentration from source sites to coastal sites, however the concentrations in the Halladale source and river sites were not significantly different (Table 4.17). The trend in iron concentration in the unfiltered samples, over both catchments, was also observed in the data from the less than 5000 nm fraction prior to AF^4-ICP-MS (Table 4.20). Further research is needed understand the reasons for this. It is likely that the differences in geology, land cover, use and practices within the catchments will have an influence (Krachler et al., 2016) as will associated fluvial processes.

The fractograms in Figure 4.10 show iron concentration associated with the particle size distribution for the 2018 samples. AF^4 reveals a more detailed insight onto the components of the operationally dissolved fraction and can also be used to analyse samples containing larger colloids as is shown in Table 4.24. The DLS measurements revealed particle sizes in excess of 2000 nm for the samples analysed using AF^4- ICP-MS (section 4.2.6), possibly due to aggregation during storage.

4.4.3 **Conclusion**

This study contributed to the development of SMS methods, informing sample preparation. In addition to this the iron concentration studies have investigated concentrations in physically defined nanoparticle and colloidal size fractions, contributing to understanding of iron and carbon transport through fluvial networks to the coastal ocean. However, both sampling campaigns were conducted over short time periods (2 days) during the Springtime (March and April). The limited sampling was intentional, allowing time to be spent exploring methods for SMS technique development. To better understand the iron and organic matter dynamics, future studies should

be more extensive and cover a longer time period to investigate the effects of seasonality, similar to the research presented by Muller and Cuscov (2017) or Gottselig (2020). As discussed in Chapters 1 and 2, the investigation of environmental iron-bearing nanoparticles and colloids should ideally include iron mineralogy.

5. Investigation of environmental iron nanoparticles and colloids with the ^{57}Fe Synchrotron Mössbauer Source – a proof-of-concept study

5.1 Introduction

This chapter presents the development and success of a novel method to collect energy domain Mössbauer spectra of waterborne environmental iron-bearing nanoparticles and colloids using the Synchrotron Mössbauer Source (SMS), Nuclear Resonance Beamline at the European Synchrotron Radiation Facility, France. The mineralogy of nanoparticles and colloids in the operationally defined dissolved size fraction, greater than 60 nm and below 400 nm, is described. This study presents the capability, and potential employment of these SMS methods to investigate water-borne iron-bearing nanoparticles in a diversity of environments.

As discussed in Chapter 1, iron plays a key role in global biogeochemical cycles. In aquatic systems, interactions tend to involve iron-bearing nanoparticles (<100 nm) and fine colloids (<450 nm) which, are often amorphous (Hochella, 2008, Caraballo et al., 2015). There are repeated calls for physically size fractioned iron measurements to be accompanied by investigation of iron speciation and mineralogy, and other associated characteristics, which might influence iron transport, delivery to oceans and behaviour in water environments (Hawkings et al., 2014, Bagard et al., 2011, von der Heyden et al., 2012, Von Der Heyden and Roychoudhury, 2015, Von Der Heyden et al., 2019). These particles are often difficult to characterise mineralogically using conventional geochemical techniques (Schröder et al., 2016). Studies have examined the success of a variety of these analytical methods, however, even with the latest techniques available in X-ray absorption spectroscopy (XAS), they have been unable to fully define the associated mineralogy (Von Der Heyden et al., 2019, Hawkings et al., 2014). Hawkings et al. (2014) investigated the export of glacial (meltwater) iron in three defined size fractions they described as suspended sediment bound iron (particles greater than 450 nm), colloidal/nanoparticulate iron

(less than 0.45 μm, greater than 20 nm) and 'truly dissolved' iron (less than 20 nm). They found that the fluxes of suspended sediment iron to the ocean were significantly higher than previously estimated, higher than aeolian dust, and also had the potential to be more bioavailable. Additionally, they suggested that the colloidal/nanoparticulate iron in glacial melt was likely to contribute increasing fluxes of potentially bioavailable iron to the oceans as climate warms, however, were unable to fully describe the iron speciation and mineralogy (Hawkings et al., 2014, Hawkings, 2016). In a more recent study involving the investigation of mineralogy of aquatic iron nanoparticles, Von Der Heyden et al. (2019) review of some of the analytical methodologies currently employed and offer an overview of their success using Fe L-Edge X-ray Absorption Spectroscopy. Despite the significance of this paper in the contribution to research in this field, the mineralogy is still not fully defined and is presented as broad groupings of ferrous, ferric and magnetite classes of iron(bearing) nanoparticles (10–100 nm). The authors conclude that, because of the diverse mineralogy and speciation of aquatic nanoparticles, further work should continue to focus on the iron-bearing nanoparticle speciation, biogeochemical behaviour and ecotoxicological impacts. Von Der Heyden et al. (2019) present a useful, albeit brief, review of a selection of methods, however, have not addressed the success of Mössbauer spectroscopy (MBS) for iron mineralogical determination or explored the potential of Synchrotron Mössbauer Source (SMS).

Mössbauer spectroscopy is a valuable technique for the investigation of mineralogy in iron bearing nanoparticles and colloids. It is successful in resolving the mineralogy in particles, even those in non-crystalline phases and in the superparamagnetic size range (<30 nm) (Gütlich et al., 2010, Gütlich et al., 2012, Hepburn et al., 2020). By employing low temperature measurements, taking superparamagnetic materials below their blocking temperature, MBS is able to characterise them in a magnetically ordered state (Novak et al.). Despite its ongoing value and successful use to investigate a variety of materials, conventional Mössbauer spectroscopy (MBS) does not prove the most suitable of techniques for investigating some environmental samples,

particularly those in a water environment. This is often due to the dilute nature of the iron content within the sample matrix. Indeed, there are a number of variables that should be given consideration prior to embarking on MBS measurements, including: sample size, particle size, iron concentration, amorphicity/crystallinity of particles and sample matrix composition and structure e.g. solid or liquid. It should also be noted that MB only measures ^{57}Fe and that the ^{57}Fe isotope is present at only 2.20% in natural abundance (Poitrasson, 2007). Prepared conventional MB samples with diameters of less than 100 μm present difficulties as focussing radiation from radioactive sources and can often be coupled with small concentrations of iron in a sample; the time to obtain a good quality spectrum as the measurement time is directly proportional to the amount of Fe in a sample. This means that measurement success is sample dependent and is often intrinsically linked to sample preparation methods (Potapkin et al., 2012, Schröder et al., 2016). Therefore, although conventional Mössbauer spectroscopy is well suited for the mineralogical characterization of nanoparticles, the dilute nature of the <400 nm fraction in natural waters likely pose issues in sample preparation and measurement success due to the dilute nature of iron in natural waters. In some cases, particularly in saline waters, sample preparation requires filtration exceeding 100s, or indeed 1000 litres of seawater, to gain enough material for a conventional MBS measurement. This is because the dilute nature of these nanoparticles and (fine)colloids in natural water environments constrains the resultant sample volume by yielding a mass of material to achieve only microscopic sample volumes and MB requires an optimal amount of 10 mg Fe cm^2 in a given sample (Schröder et al., 2016). Even in river systems with a high iron load, initial sample volumes still require filtration of water volumes in the range of 10s to 100s of litres. Collecting large sample volumes is simply not viable if we are to successfully define iron mineralogy and its spatial and temporal interactions, understand transport mechanisms, and influences upon biogeochemical cycles and environmental processes.

To demonstrate the challenges to optimise Fe concentrations in samples initial calculations of the volume of water needed to achieve this based on known iron concentrations, a worked example

from an existing study follows: Fe concentrations in the <0.2 μm (described as 'dissolved') physical size fraction, from a creek in the north east of Scotland where iron is 2.64 mg L^{-1} (47274 nM) (Krachler et al., 2016) would mean potentially filtering at least 4 to 5 L of creek water. In more iron dilute systems such as those with higher salinity, for example Loch Etive with ~20 psu (Chapter 3), where the 400 nm has an iron concentration of 0.05 mg L^{-1} (<900 nM), means filtering ~200 L of water. In addition to this, Muller (2018) presented a table of measured iron concentration data of total dissolved iron (shown in the table as Fe^{T}) in marine waters. In this table, the studies presented are from waters where the speciation of iron is likely controlled by humic ligands, as is also expected of the sample waters in this present study (note that two of the entries in the table are from the River Thurso coastal plume which was also a sample site for the study presented in this thesis).

The data presented in Table 5.1 from Muller (2018) demonstrates the dilute nature of iron in the operationally defined 'dissolved' fraction from a selection of studies, over a range of salinities. These data show the total iron concentrations in some sample higher salinity waters as being less than 1 nM in the total defined *dissolved* fraction (as defined in the Table 5.1). It should be noted that this is the *total dissolved fraction* and, therefore, to begin to then probe iron speciation and mineralogy within further physically constrained nanoparticle and colloidal size ranges adds a further *diluting* factor to the process. However, as was explained in the introduction to this chapter, characterising the iron in particles over colloidal size ranges is paramount if we are to better understand the influences on or from biogeochemical interactions, and demonstrates the need to further develop methods to facilitate these investigations (Raiswell and Canfield, 2012).

Table 5.1. Iron concentrations from marine waters: Total Fe in marine waters, where humic ligands are expected to control iron speciation (adapted from Muller (2018)).

region	depth (m)	filter (μm)	salinity (PSU)	*Fe_T (nM)	reference
Transpolar Drift, Arctic Ocean	0-200	0.2	34.0-34.5	0.7 - 4.4	(Slagter et al., 2017)
Nansen & Amundsen Basins, Arctic Ocean	500-4000	0.2	34.8-35.0	0.4 - 0.7	(Slagter et al., 2017)
Thurso River plume, NE Atlantic (November)	1	0.4	29.4-34.9	86 - 573	(Batchelli et al., 2010)
Thurso River plume, NE Atlantic (4 seasons)	1	0.4	4.8-34.8	82 - 5824	(Muller and Cuscov, 2017)
Mersey River outflow, Irish Sea	15	0.2	30.0-34.0	2 - 9	(Laglera and van den Berg, 2009)
Mersey estuary, Irish Sea	surface	0.2	18.8-32.2	5 - 85	(Abualhaija et al., 2015)
Mediterranean Sea	0-100	0.2	37.5-38.9	0.3 - 3.0	(Gerringa et al., 2017)
Mediterranean Sea	100-3000	0.2	38.3-39.2	0.2 - 1.4	(Gerringa et al., 2017)

**Fe_T is total Fe, below the stated filter size in table, from published values in the cited articles.*

In contrast to the capabilities described above for conventional Mössbauer spectroscopy which, can only collimate i.e. filter out non-parallel gamma rays, the ^{57}Fe Synchrotron Mössbauer Source (SMS) has a micron-sized diameter beam which, can be focussed to a spot size of 10 μm x 5 μm with high luminosity (without beam loss), provides a high data quality output, fundamental to investigate microscopic samples (Potapkin et al., 2012, Rüffer and Chumakov, 1996). The benefit of the SMS over conventional MB for this study is that microscopic sample volumes can be measured, thereby opening up the field of Mössbauer spectroscopy to investigate iron mineralogy and speciation in fairly iron dilute, but biogeochemically relevant systems, such as the oceans.

Additionally, SMS measurements are considerably faster than conventional MBS. The ^{57}Fe Synchrotron Mössbauer Source (SMS) at ID18, ESRF has been previously used to determine iron speciation and mineralogy in environmental samples (Schröder et al., 2016) and in microscopic sample volumes (Potapkin et al., 2012, Smirnov et al., 1997). However, until this study, SMS had not been employed to investigate water borne iron bearing environmental nanoparticles and nanoparticles within the operationally defined dissolved fraction.

In a pilot study, Schröder et al. (2016) demonstrated measuring river-borne environmental particles using the Synchrotron Mössbauer Source (SMS) for a larger particle physical size fraction i.e. larger than the operationally defined dissolved fraction. The pilot study by Schröder et al. (2016) obtained spectra from quartz fibre (nominal pore size of 0.7 μm) filter membrane 'cakes' which had been prefiltered using vacuum filtration on 100 μm nylon mesh. These results shown by Schröder et al. (2016) (shown in figure 5.1) helped to confirm the potential to employ SMS for the mineralogical investigation of nanoparticles and fine colloids in riverine and coastal environments. By measuring a larger particle size fraction (>700 nm<100000 nm) they provided the motivation for this current work; to develop methods that would facilitate investigation of smaller sized water-borne environmental colloids and nanoparticles within a physically size defined range.

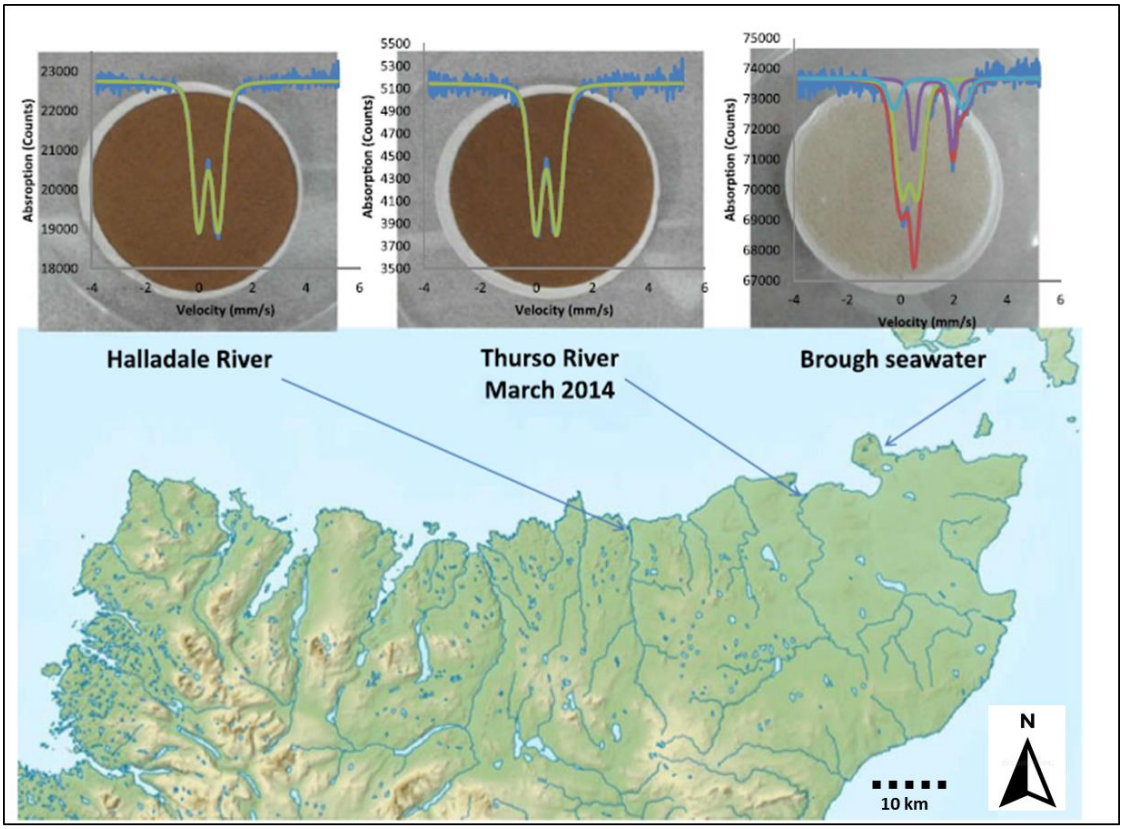

Figure 5.1. **Figure (adapted) from Schröder et al. (2016): SMS spectra on the > 700 nm particulate** size fraction: '*Map showing the northern coastline of Scotland, North is to the top. Arrows indicate sampling locations. The filters from the peat-draining Halladale and Thurso rivers are covered in dark material representing their high organic matter load. The coastal seawater filtrate is pale in comparison. Mossbauer spectra for the Halladale and Thurso rivers are identical and represent ferric iron (green doublet), most likely superparamagnetic iron (oxyhydr)oxides. The coastal seawater sample (Brough) contained 40 % of ferrous iron (purple and light blue doublets), most of it in the calcium-iron carbonate ankerite (purple doublet)*'.

Recent research has shown the ability of terrestrially derived, naturally occurring, organic-matter associated iron-bearing nanoparticles and (fine)colloids, within the operationally defined dissolved fraction (<450 nm), to transcend the salinity zone and be delivered by rivers and creeks to the coastal ocean (Krachler et al., 2010, Krachler et al., 2016, Batchelli et al., 2010, Muller and Cuscov, 2017, Muller, 2018). The studies in this thesis (Chapters 3 and 4) demonstrate that the majority of iron in the operationally defined dissolved fraction, carried by rivers to the coastal sea,

is found in the nanoparticle/colloidal size fraction, and is above the 'truly dissolved' cut off of 2 nm. It was therefore necessary to develop a successful isolation and particle enrichment process to investigate the nanoparticulate and colloidal fractions using SMS techniques. It was deemed important to constrain initial sample volumes to a few litres of river water. Small volumes allowed for spatial and temporal variation to be maintained which, be lost with large sample volumes. Additionally, it is not practicable to collect large volumes of water in the relatively small-scale rivers and streams of interest which are a feature of the Flow Country in the North East of Scotland. Initial water sample volumes had to be sufficient to accumulate a mass of material, accommodated in a small volume vessel whilst remaining feasible in terms of iron concentration for a potentially successful SMS measurement. Therefore, iron concentration measurements by physical size fraction were paramount to inform the planning stages of the SMS sample preparation (Chapter 3 and 4) to inform initial water sample volumes.

SMS Measurements were carried out at the Nuclear Resonance beamline ID18, European Synchrotron Radiation Facility. Development of sample preparation method for the measurement of water borne nanoparticles and colloids using the Synchrotron Mössbauer Source required method development and technique selection in to achieve the following: particle physical size fractionation, enrichment of the isolated particles, development of a sample holder and cryostat mount for SMS measurement and methods for optimal sample preparation.

5.2 Methods

5.2.1 Sampling sites

The Flow Country sample waters explored in this study (Chapter 4) provide a starting point to begin to investigate the mineralogy of iron in natural water environments using SMS, adding to the understanding of biogeochemical cycling for climate vulnerable high latitude systems such as boreal peatlands and potentially sea ice and glacial melt inputs to the oceans. The initial development of the SMS method was performed on waters known to be rich in iron in the

operationally defined dissolved fraction. A known high iron content was expected to increase the possibility of encountering iron bearing nanoparticles and colloids than there would be in a more iron dilute matrix such as sea water, with the intention to later fine tune the methods to encompass such environments. This strategy was adopted to enable a proof-of-concept of the methods to be developed, and to provide a starting point for optimising them to investigate more dilute systems. Other advantages of selecting the sampling sites were for the reasons described in the introduction to this chapter, including: (i) the development could be performed on relatively small sample volumes of water and (ii) any resultant data produced could add to the existing and ongoing iron related research in this geographical area.

Successful SMS measurements were obtained for two samples isolated from the greater than 2 nm and smaller than 400 nm physical size fraction: Loch More peat bog (waters) and River Thurso water, within the River Thurso catchment, North East Scotland. It is in this size fraction, above the truly dissolved fraction where most of the iron is held in these samples (see results in Chapter 4). The sample sites were selected because they are shown to be significant sources of iron and organic matter to the coastal ocean (Krachler et al., 2010, Krachler et al., 2016, Muller and Tankéré-Muller, 2012, Muller and Cuscov, 2017, Batchelli et al., 2010, Schröder et al., 2016). River Thurso catchment data, iron and carbon concentrations are described in more detail in Chapter 4.

5.2.2 **Sample collection**

In the summer of 2017, the Scientists at the Nuclear Resonance Beamline, ID18 (ESRF) hosted me for an internship (6 weeks) which, was also financially assisted by a Marine Alliance for Science and Technology Scotland (MASTS) Postdoctoral and Early Career Researcher Exchanges (PECRE) award. This provided an opportunity to discuss the intention of the project with them and to test the first samples. To prepare for this opportunity the first sampling campaign was undertaken in April 2017. The samples were used for the development of the isolation and concentration steps as described in Chapter 4 and the first tests using SMS were undertaken. The initial testing and

development steps are described below. Based on the results of the initial testing at ID18 in June 2017, beamtime was awarded for July 2018. Sampling for the awarded beamtime (experiment EV-310) was then conducted over the dates 21 to 23 March 2018. It should be noted that this study was conducted in early spring. Muller and Tankéré-Muller (2012) conducted a series of sample collections over the period of a year and found that the water chemical parameters were affected by season. Despite this knowledge, it was proposed that for the purposes of this study i.e. to test the suitability of these methods for investigation of iron phases using synchrotron based Mössbauer techniques, it was acceptable to limit the sampling to a short window of time. Full sampling protocols and results are described in Chapters 3 and 4.

5.2.3 Sample preparation for ^{57}Fe Synchrotron Mössbauer technique: enrichment of nanoparticles and colloids

The methods for physical size fractionation are described fully in Chapter 4, as are the results for the iron concentration within each physically sized fraction. The iron concentration results presented in Chapter 4 informed the development of the SMS methods presented here. Samples were processed through a 3-stage filtration and concentration procedure, as described. In addition, further concentration to enrich the nanoparticle/colloidal fractions was needed to prepare the samples for SMS measurement. These added steps effectively reduced the water content of the sample, optimizing the success of the SMS measurement. This further concentration step is described below.

5.2.4 Isolation and concentration of physical size fractions

The centrifugal devices, Jumbosep (66 nm filter membrane) and Amicon (2 nm filter membrane) used for the SMS beamtime preparation provided reasonably efficient concentration and particle recovery (see Chapter 4, section 4.3.3). Additionally, their components, and the ability to clean them to a high standard to allow for trace metal analysis were the reasons for their selection on this occasion. This selection also allowed for processing of aliquots for iron concentration

measurements, whilst retaining an identical system for water removal from the samples for SMS measurements. In this way the iron concentrations in the enriched fractions could also be measured without introducing further contamination or physical alteration to the processed samples. Isolation and concentration of two physical size fractions were processed: greater than 2 nm, less than 66 nm and greater than 66 nm, less than 400 nm. The SMS preparation process steps are described bin Figures 5.1 and 2.

Stage 1: vacuum filtration to isolate the 400 nm physical size fraction using (trace metal clean) 0.4 μm track-etched polycarbonate membrane filters.

Stage 2: the 400 nm filtrate from stage 1 was further physically size fractionated to concentrate the 66 nm to 400 nm fraction. This was achieved by feeding the 400 nm filtrate into acid clean Jumbosep™ Centrifugal Devices with clean, preconditioned (with sample water) low protein-binding Omega™ membranes with polysulfone housing (molecular weight cut off (MWCO) 66 nm).

Stage 3: The final stage of processing, to isolate the greater than 2 nm less than 66 nm physical size fraction, was achieved by further centrifugation using acid clean, preconditioned (with sample water) 2 nm Amicon units (regenerated cellulose membrane with a 15 mL starting sample volume).

At each processing stage an aliquot of each sample was retained and stored in acid clean Thermo Scientific Nalgene Round-bottom tubes for complete digestion and elemental analysis using Inductively Coupled Plasma Mass Spectrometry (ICP-MS).

Stage 4: To enrich (effectively, further water removal) the nanoparticle/colloidal slurry for SMS measurement, the Amicon units were subject to a series of feeds, each being 12-15 mL in volume. Both the 2 nm to 66 nm (from step 3 above) and the 66 nm to 400 nm retentate from the Jumbosep units (stage 2) were centrifuged in the Amicon units.

Stage 5: The retentate ‘’slurry’’ from stage 4 was then drawn up into a borosilicate glass capillary (by capillary action) and frozen ready for SMS measurement.

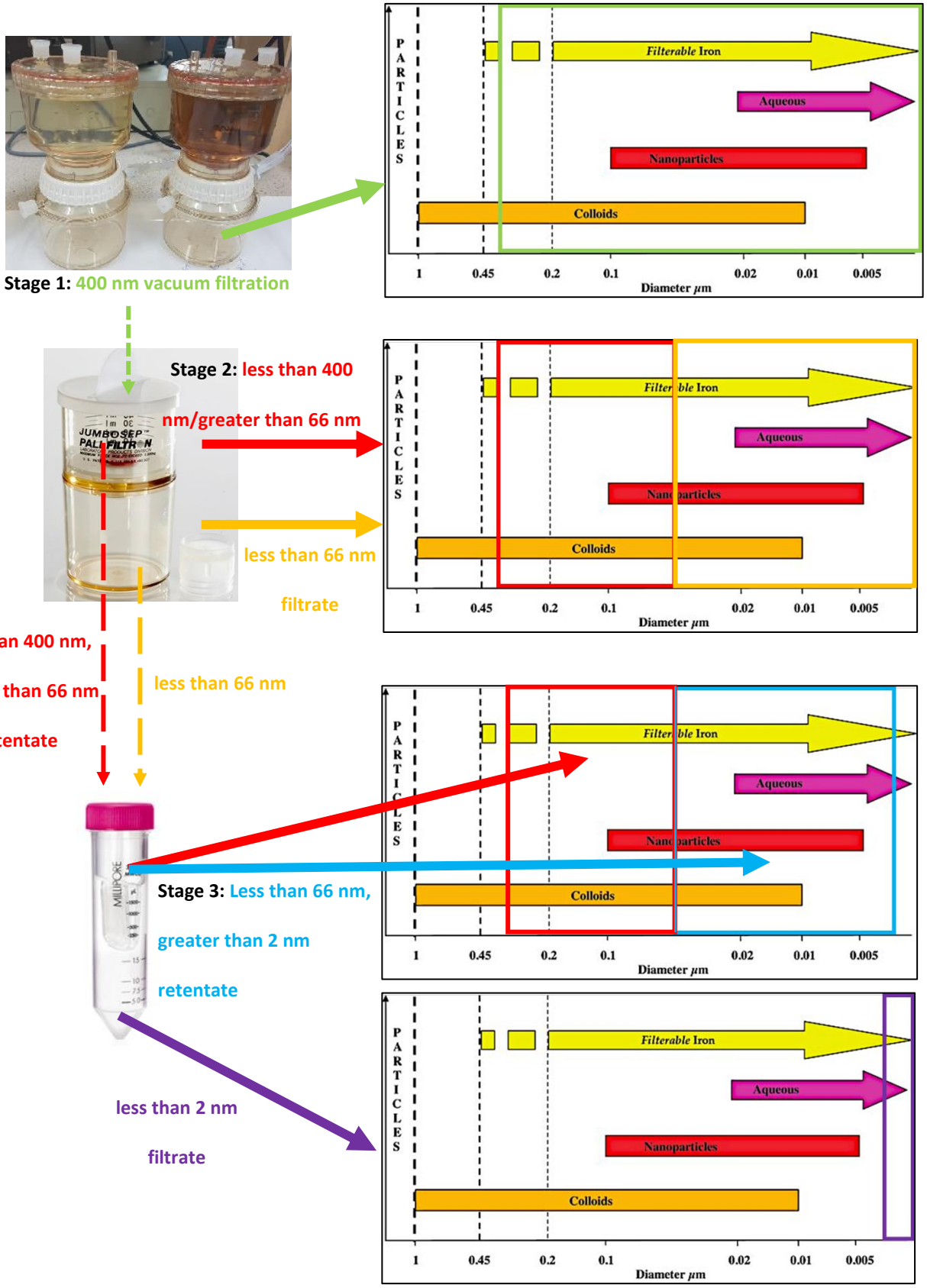

Figure 5.1. Isolation and enrichment of nanoparticles/fine colloids for iron concentration measurements using ICP-MS and in preparation for SMS measurement.

Stage 1: vacuum filtration to isolate the 400 nm physical size fraction. **Stage 2:** concentration of the 66 nm to 400 nm fraction. **Stage 3:** isolation of the greater than 2 nm less than 66 nm physical size fraction. The physical size schematic is adapted from Raiswell and Canfield (2012).

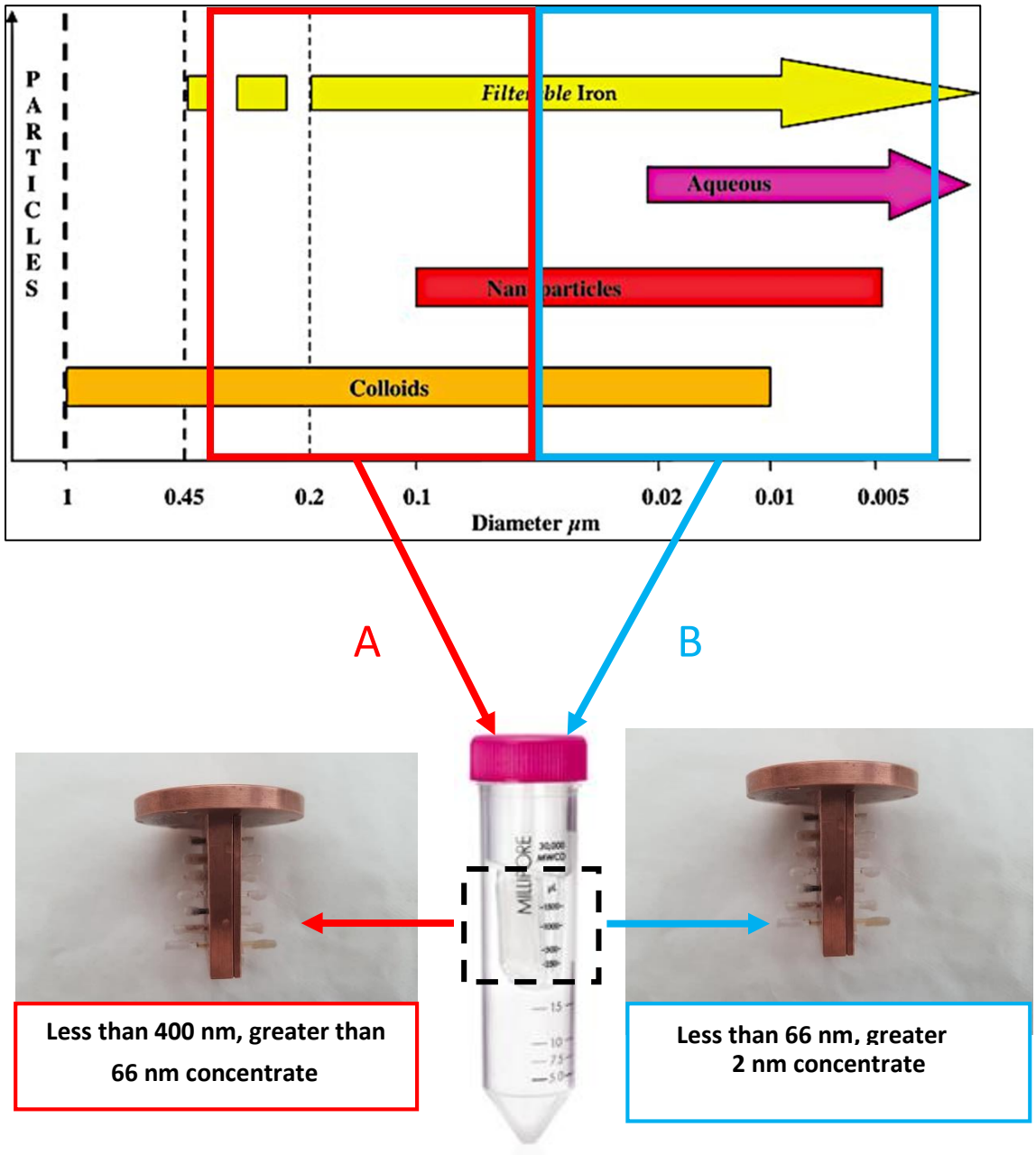

Figure 5.2. Enrichment of nanoparticle/colloidal fractions for SMS measurement.

Enrichment of the nanoparticle/colloidal slurry for SMS measurement: Amicon units (middle bottom photograph) were subject to a series of feeds for physical size fractions (A) and (B). Each retentate (A &B) was drawn up into a borosilicate glass capillary (by capillary action) and frozen ready for SMS measurement (Figure 5.2). The capillaries were then loaded into the OFHC copper sample holder cryostat mount (bottom photographs: left and right). The physical size schematic is adapted from Raiswell and Canfield (2012).

5.2.5 **Sample holder and cryostat mount development**

When considering the sample holder for SMS measurement there were some immediate considerations. These included: using a material that would tolerate temperatures down to 4.2 K, the ability to load the sample into the vessel, a route for the beam to reach the sample with minimal attenuation by the vessel, capability to retain the sample within the vessel before and during SMS measurement and the ease of alteration to the length of the vessel to accommodate different sample lengths based on relative, pre-measured element (particularly iron) concentrations. The cost limitations were also considered as manufacturing a prototype sample vessel could be costly, and it was decided to employ a readily available, inexpensive option for the initial tests. For these reasons borosilicate glass capillaries were chosen. Borosilicate glass has low coefficients of thermal expansion, which suggested it would be ideal for the low temperature measurements needed for successful SMS measurements (Bouras et al., 2009). In addition, a range of borosilicate glass capillaries is readily available, they are easy to clean, the constituents and capabilities are well documented and they are relatively inexpensive. The dimensions of the capillaries purchased for this experiment were: internal bore diameter 1.36 mm; diameter (external) 1.8 to 2 mm; wall thickness 0.28 to 0.32 mm; maximum internal volume ~145.27 mm^3. It is possible to shorten these to better match the sample length (i.e. the sample thickness if the beam is directed through the internal bore), or indeed to select off the shelf or bespoke capillaries with a range of different dimensions.

SMS experiments should consider the following sample preparation: i) the beam should pass through the inner bore of the capillary; ii) the sample container should be long enough to reach the calculated optimum sample thickness; iii) as much water as possible should be removed . Also, because the samples are in suspension and need be frozen for SMS, a cryostat is needed during measurements. The cryostat is also needed to facilitate measurements down to liquid helium temperature (4.2K) as the samples are nanoparticulate and amorphous and therefore expected to display superparamagnetic behaviour. Measurements at 4.2 K take place below the superparamagnetic blocking temperature to gain full mineralogical information.

5.2.6 **Cryostat Mount Design**

The cryostat mount design was developed in conjunction with the ESRF, ID18 beamline scientists (Dr A. Chumakov and Dr D. Bessas) who then produced the technical drawings (Appendices for Chapter 5) that were used to produce the cryostat mount to specification using oxygen-free high thermal conductivity (OFHC) copper (Figure 5.3) by Dunblane Light Engineering (DLE) Limited Company, Fallin, Scotland.

Figure 5.3. Photograph of completed OHFC copper cryostat mount prepared for introduction to the beam, ID18, ESRF, July 2018 (photograph credit: D. Wood).

SMS samples are shown photograph in Figure 5.3 (7 samples), loaded into borosilicate glass capillaries and housed in the oxygen-free high thermal conductivity (OFHC) copper cryostat sample holder and mount ready for SMS measurement.

5.3 **SMS measurement**

SMS spectra were collected at the Nuclear Resonance beamline ID18 using the nuclear monochromator as described by Potapkin et al. (2012) at the European Synchrotron Radiation Facility (Rüffer and Chumakov, 1996). The nuclear resonant monochromator employs pure nuclear reflections of an iron borate ($^{57}FeBO_3$) crystal. This provides ^{57}Fe resonant radiation at 14.4 keV within a bandwidth of ~6 neV, which is tunable in energy over a range of about ±0.6 μeV. In contrast to radioactive sources, the beam emitted by the SMS is fully resonant, up to 99% polarized, has high brilliance and can be focused to a 10 μm × 5 μm minimum spot size (Potapkin et al., 2012). Measurements were at low temperatures by employing a cryostat. The benefit of measuring at low temperature for these samples is two-fold. Firstly, although the samples had been condensed, removing much of the water, the particles remained in suspension and needed to be frozen to create a solid matrix, essential for Mössbauer measurement (Long and Grandjean, 2003). Furthermore, because the samples contained iron-bearing amorphous nanoparticles and colloids, which display superparamagnetic behaviour, measurements at 4.2 K, below the superparamagnetic blocking temperature allows the acquisition of full mineralogical information.

5.3.1 **Introduction of sample to beam during EV-10, ID18, ESRF**

The SMS set up for experiment EV-310, July 2018 is shown below (Figure 5.4). This is the full optical scheme for SMS (adapted from Potapkin et al. (2012)), however, the figure has been adapted to include the sample introduction for this experiment (beam direction is right to left in this example).

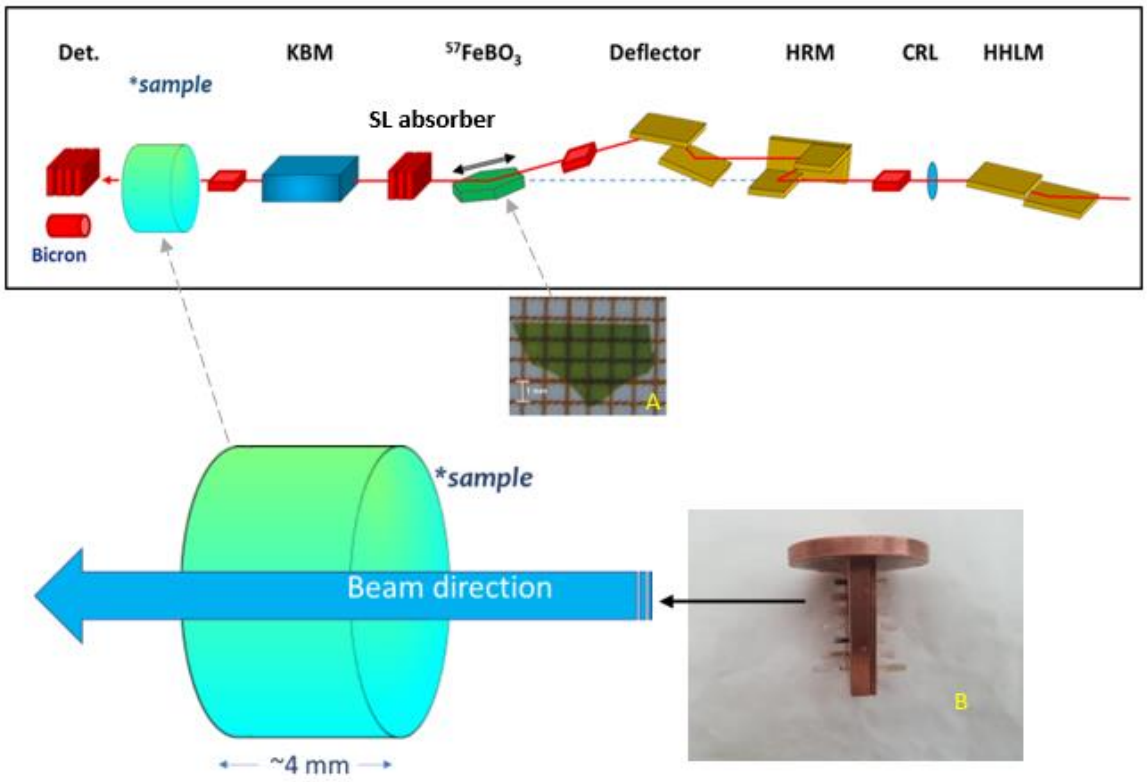

Figure 5.4. Example set up of beamline ID18,ESRF adapted from Potapkin et al. (2012) with example sample construction (photograph B, credit: D Wood).

Figure 5.4 presents the optical scheme for the Synchrotron Mössbauer Source : HHLM is the high-heat-load monochromator; CRL is the compound refractive lens; HRM is the high-resolution monochromator; deflector (the deflector for the (111) reflection can be obtained using two reflections: Si(422) and Si(531)); $^{57}FeBO_3$, high-quality single-crystal platelet (photograph A from Potapkin et al. (2012)); SL absorber is the single line absorber; KBM are the Kirkpatrick–Baez mirrors; sample represents the sample within the cryostat; Det. is the detector. The samples are housed in a borosilicate glass capillary, secured in a custom made OFHC (oxygen-free high thermal conductivity) mount (photograph B) within the cryostat in the beamline hutch.

5.3.2 **Introduction of samples for measurement**

The nanoparticle/colloidal fractions shown in Figure 5.2 were collected as retentate in the Amicon Ultra 15 units and transferred to capillary tubes (acid clean borosilicate glass, cut to appropriate length for estimated sample thickness) for SMS measurement. The prepared samples were then frozen and housed within the cryostat mount, ready for introduction to the cryostat within the beamline's experimental cabin (Figure 5.5).

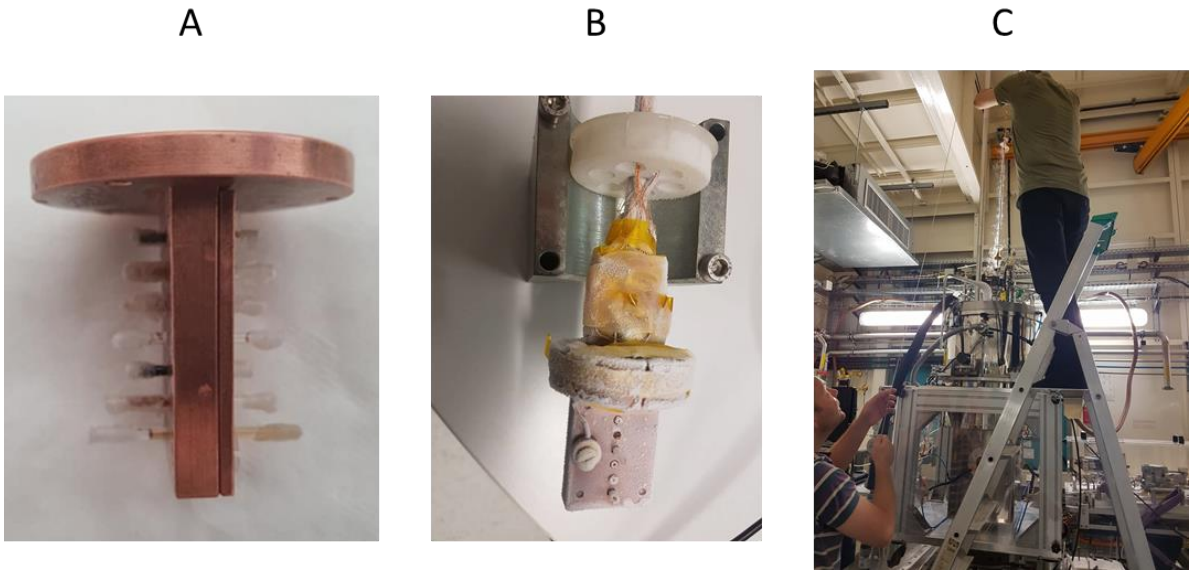

Figure 5.5. Samples prepared for SMS measurement. Photographs: A) pre-loaded borosilicate glass capillaries housed in OFHC cryostat mount & B) pre-frozen loaded capillaries in OFHC cryostat mount attached to sample mount holder (custom produced by DLE (Dunblane Light Engineering Limited Company, Fallin, Scotland) oxygen-free high thermal conductivity (OFHC) copper mount based on design produced by ID18 in collaboration, photograph C) loading the samples into the cryostat for introduction to the beam (ID18, ESRF, Grenoble, July 2018). (Photographs by D Wood, ID18, ESRF, 2018).

Firstly, the sample holder was measured to locate the sample holder slots then samples were loaded and each sample was preliminarily measured to locate its centre for SMS measurement.

SMS linewidth was controlled between each sample measurement with the collection of a single line spectrum of $K_2Mg^{57}Fe(CN)_6$ and the velocity scale was calibrated using natural iron foil.

5.3.3 **SMS spectral analysis**

Mössbauer spectra were calibrated using natural iron foil data provided by ID18, ESRF and evaluated with Recoil (University of Ottawa, Canada) using the Voigt-based fitting routine (Rancourt and Ping, 1991). Mössbauer parameters were compared to published literature values for Fe (oxyhydr)oxides taken from Cornell and Schwertmann (2003) and Murad and Schwertmann (1984).

5.4 **Results**

5.4.1 **SMS sample variables**

As described in the methods section, the samples underwent water removal for SMS measurement. Table 7.5.1 shows the mass fractions and absorption coefficients for the River Thurso (2018 sampling) and using ICP-MS data for total Fe and other element concentrations. Ideal absorber (sample) thickness was determined following the examples and calculations shown in Gütlich (2010) where the mass absorption coefficient (μ_e) can be calculated using the following equation:

$$\mu_e = \Sigma\, c_i \mu_i$$

Mass absorption coefficients ($cm^2\ g^{-1}$) were calculated using methods described in Gütlich (2010) and Long et al. (1983). Mass absorption coefficients table can be found in Appendices for Chapter 5 (section 7.5.1).

Example: River Thurso water physical size fraction >66 nm<400 nm (^{57}Fe (Energy 14.41 keV), EV-310, ID18, ESRF, 2018). Using μ_e for H_2O = 1.7 $cm^2\ g^{-1}$ from Gütlich (2010). The total mass absorption coefficient (based on concentrations of known elements only) for this sample is found

to be μ_e = 1.699 cm^2 g^{-1}. The ideal absorber thickness is given by $t'_{opt} = 2/\mu_e$ (for low nonresonant background, Nb<<N∞) as described by Gütlich et al. (2010), giving an ideal absorber thickness of (t'_{opt} = 2/1.699 cm^2 g^{-1}) or 1.18 g cm^{-2}, and the natural Fe in the sample is 0.21 mg Fe cm^2. This iron concentration is less than the recommended ideal absorber, which is uniform with a thickness of ~10 mg/cm^2 of natural Fe (Klingelhoefer et al., 2003).

5.4.2 **SMS spectra (March 2018 sampling)**

Preliminary sample scans were performed at the beginning of the experiment to make an initial assessment on which samples to target, thereby maximising the success of achieving successful measurement in the amount of beamtime that was available. The measurements allow the location of each sample (capillary) to be logged making it easier to locate them for measurement. In figure 5.6, the shape of the cryostat mount is visible where the peaks represent the X-ray passing through the sample slots.

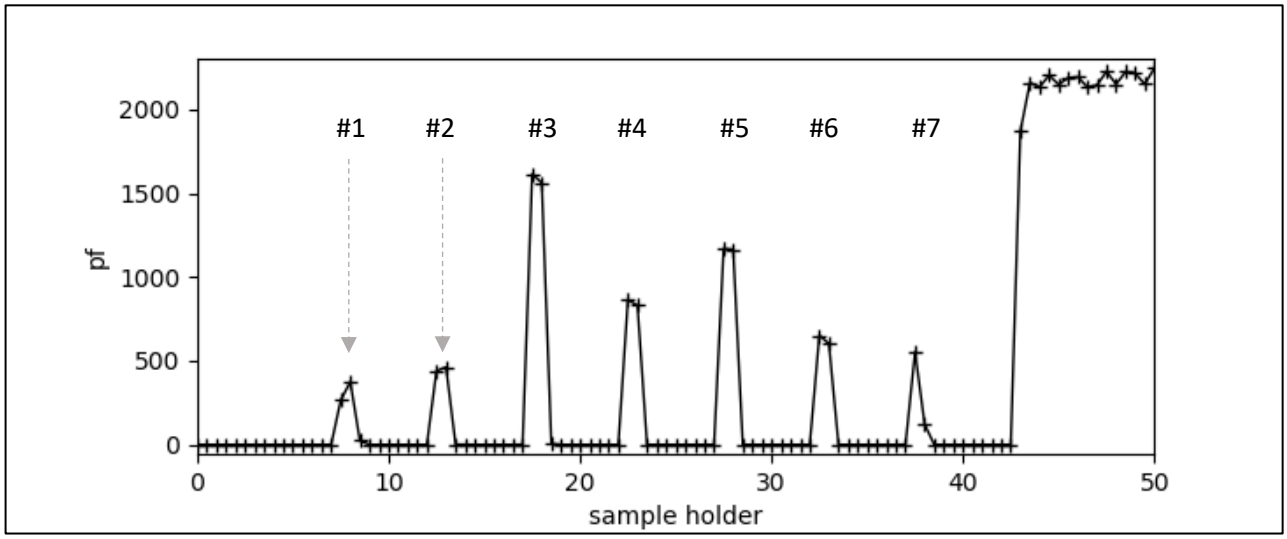

Figure 5.6. Preliminary measurements (scans) SMS, EV-310, ID18, ESRF, July 2018: focal spots for each sample within the cryostat mount (x-axis is the motor (units = mm); y-axis are counts (pf is the counter name). #1 to #7 are the positions of the 7 samples.

Table 5.2. Mössbauer fitting parameters for peat bog and River Thurso: A is T=77 K and B is T=4.2 K.

A: Measurements at 77 K			
sample	**phase**	**δ (mm s^{-1})**	**ΔE_Q (mm s^{-1})**
peat bog (1)	Be	0.25	0.41
peat bog (2)	Fe^{3+}	0.48	0.78
River Thurso (1)	Be	0.25	0.41
River Thurso (2)	Fe^{3+}	0.55	1.13

B: Measurements at 4.2 K					
Sample	**phase**	**δ (mm s^{-1})**	**ΔE_Q (mm s^{-1})**	**B_{hf} (T)**	**Area (%)**
peat bog (1)	Be	0.25	0.41	-	22
peat bog (2)	Fe^{3+}	0.61	0.10	45.69	22
River Thurso (1)	Be	0.25	0.41	-	28
River Thurso (2)	Fe^{3+}	0.47	1.37	-	27
River Thurso (3)	Fe^{3+}	0.57	0.04	46.63	34

Figures 5.7 to 5.10 show the fitted SMS spectra collected for the two samples: River Thurso and Loch More peat bog water in the isolated size fraction at controlled temperatures of T=77 K and T= 4.2 K.

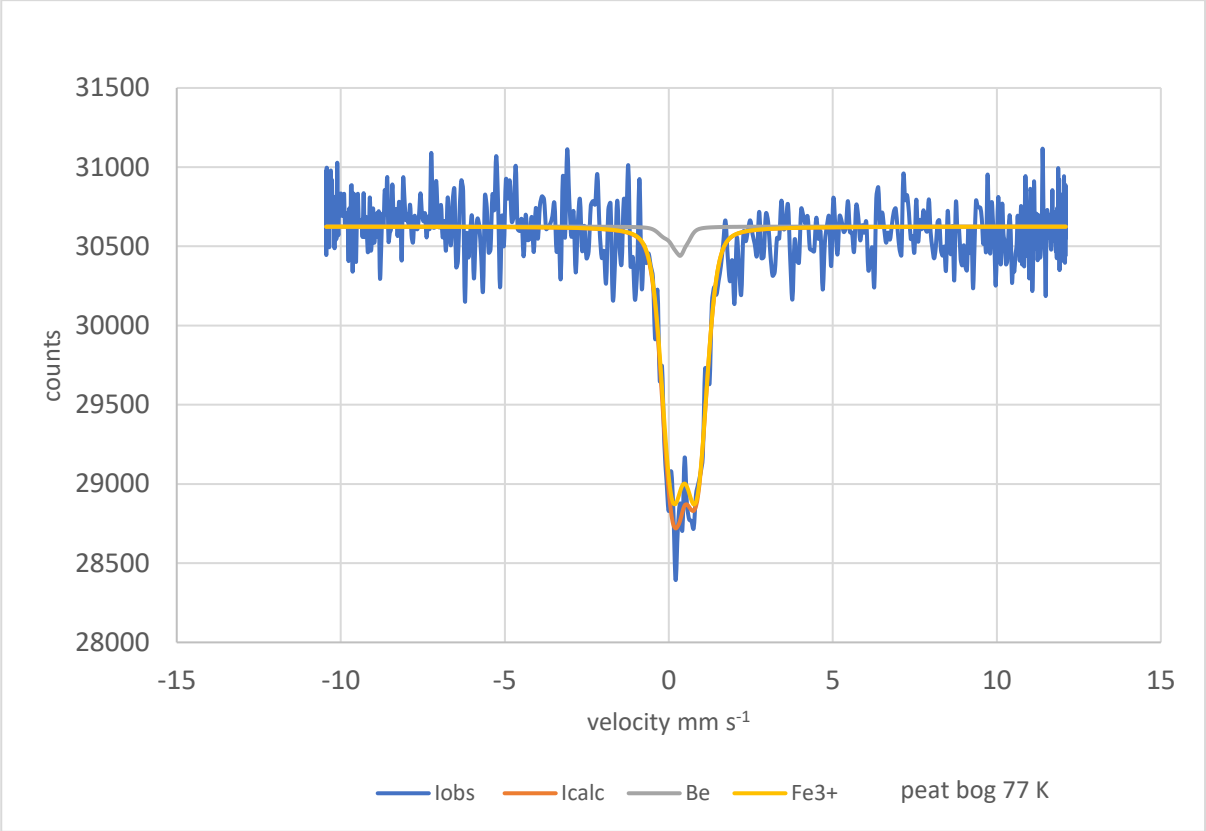

Figure 5.7. Ev-310, ID18, ESRF SMS Mössbauer spectrum for Loch More peat bog surface water and filtered particles sizes >100 kDa (66 nm) <0.4 μm (400 nm) at T=77 K. The blue line shows the measured spectrum; the grey line is background signal from Fe in the Be lenses of the SMS setup; the yellow line represents Fe^{3+} in a superparamagnetic Fe (oxyhydr)oxide. Measurement time was 3 hrs 47 minutes.

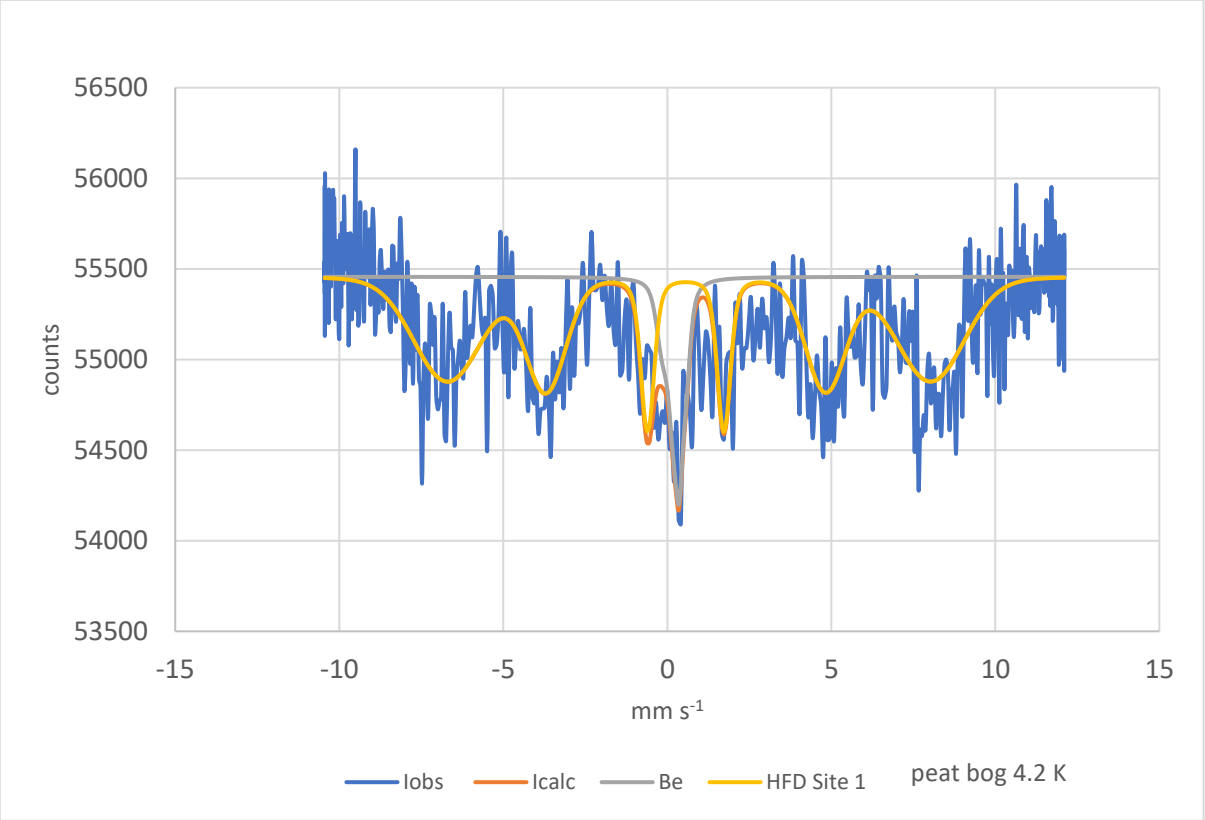

Figure 5.8. Ev-310, ID18, ESRF SMS Mössbauer spectrum for Loch More peat bog surface water and filtered particles sizes of >100 kDa (66 nm)<0.4 μm (400 nm) at T=4.2 K. The blue line shows the measured spectrum; the grey line is background signal from Fe in the Be lenses of the SMS setup; the yellow sextet represents Fe^{3+} in a magnetically ordered Fe (oxyhydr)oxide, most consistent with lepidocrocite. Measurement time was 5 hrs 7 minutes.

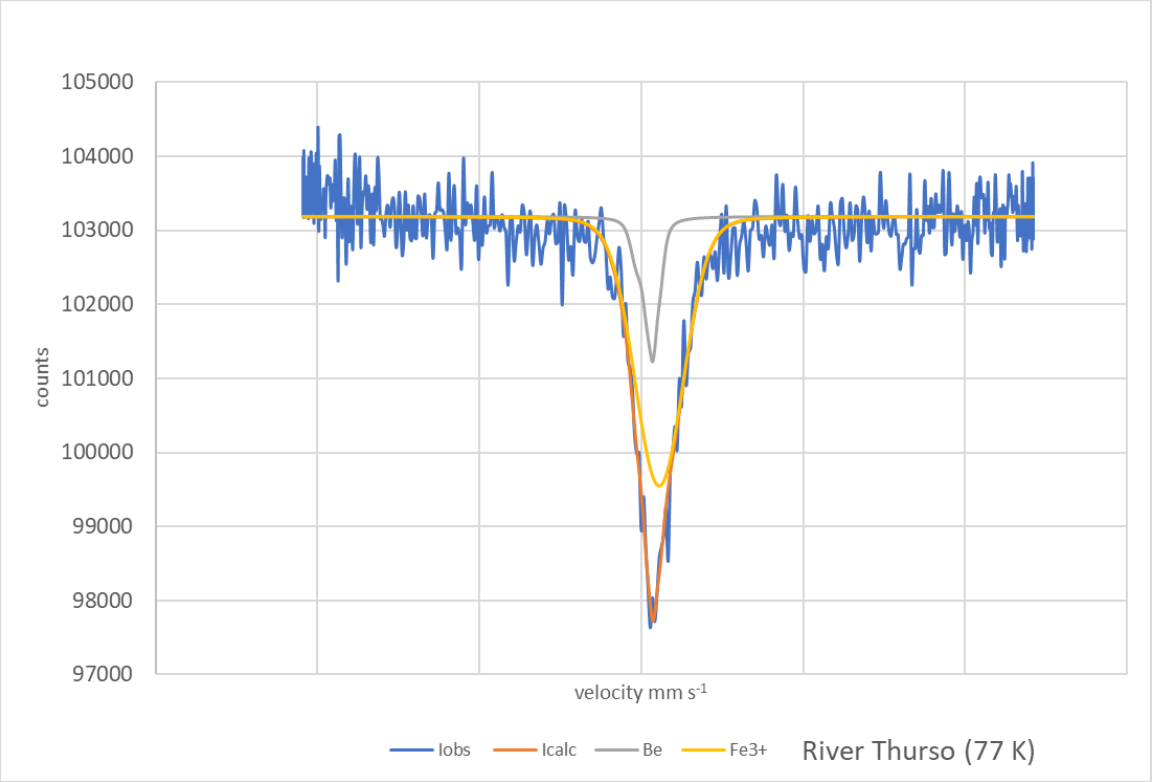

Figure 5.9. Ev-310, ID18, ESRF SMS Mössbauer spectrum for River Thurso water and filtered particle sizes of >100 kDa (66 nm)<0.4 μm (400 nm) at T=77 K. The blue line shows the measured spectrum; the grey line is background signal from Fe in the Be lenses of the SMS setup; the yellow line represents Fe^{3+} in a superparamagnetic Fe (oxyhydr)oxide. Measurement time was 3 hrs 55 minutes.

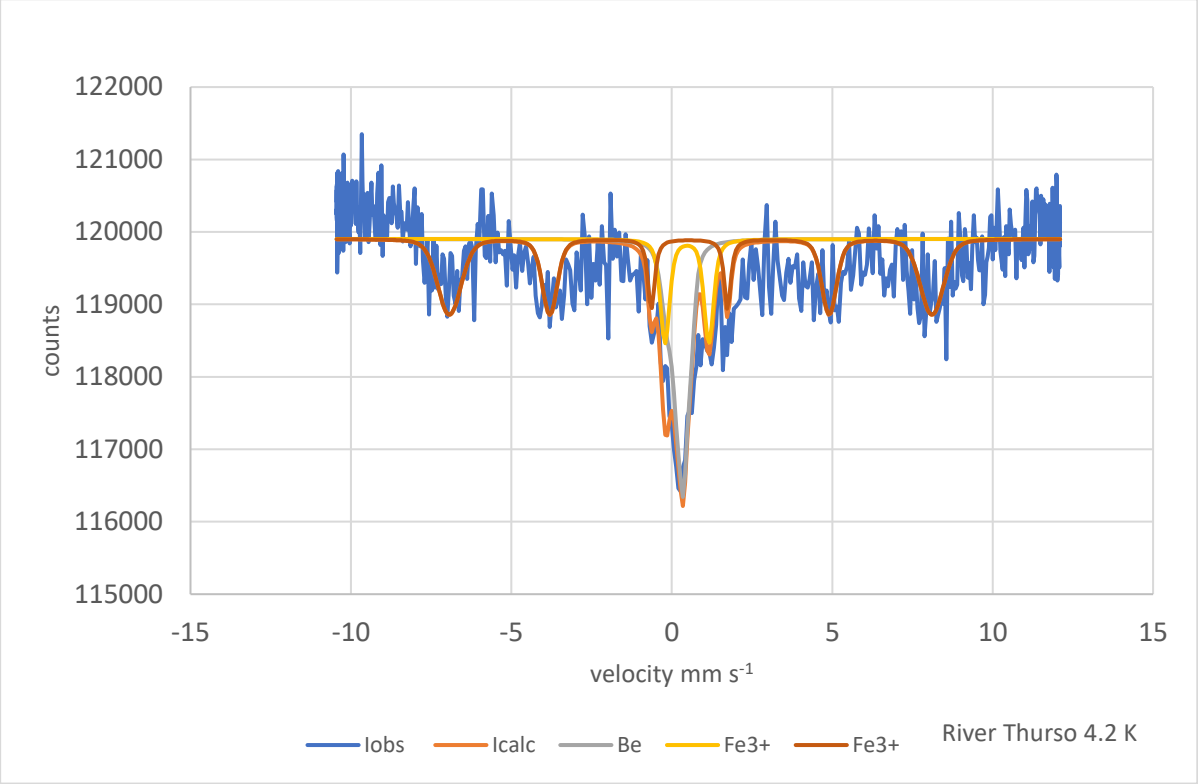

Figure 5.10. Ev-310, ID18, ESRF SMS Mössbauer spectrum for River Thurso water filtered particles sizes of >100 kDa (66 nm)<0.4 μm (400 nm) at T=4.2 K. The blue line shows the measured spectrum; the grey line is background signal from Fe in the Be lenses of the SMS setup; the yellow doublet represents remaining (super)paramagnetic Fe^{3+} and the orange sextet is Fe^{3+} in a magnetically ordered Fe (oxyhydr)oxide, most consistent with lepidocrocite. Measurement time was less than 6 hours.

5.5 Discussion

This study investigated the ability to employ the SMS at ID18, ESRF for the mineralogical characterisation of iron in water-borne environmental nanoparticles and colloids and has shown that SMS has been successful in the determination of the speciation and mineralogy of waterborne environmental iron nanoparticles and colloids. Previous thesis chapters explored the techniques and methods used to isolate and concentrate these particles from natural water samples. Here the methods employed are discussed in relationship to the outcomes of the SMS

experiment to better inform any future SMS studies on these environmental particles.

5.6 **Iron speciation and mineralogy**

Lepidocrocite has been assigned to the magnetically ordered components of the samples measured at 4.2 K i.e. the 2nd component of peat bog ((2) Fe^{3+}) and the 3rd component of River Thurso ((3) Fe^{3+}) as these data are consistent with the Mössbauer measurements presented by Murad and Schwertmann (1984). Lepidocrocite has a low Néel temperature of around 77 K (Murad and Schwertmann, 1984), Hirt (2002) suggests 52 K. At room temperature (RT) it shown to be is paramagnetic (Cornell and Schwertmann, 2003, Murad and Schwertmann, 1984). This study has not incorporated RT measurements due to the environmental nature of the samples, as discussed in the method development. However, despite the lack of data at RT, the 77 K measurements for the samples do not display fully magnetically ordered components. It is suggested that this might be due to the small particle sizes in the sample matrix, and the expectancy that naturally occurring iron (hydr)oxides are poorly crystalline as these can hinder full mineralogical determination. Additionally the influence of organic components upon mineral phase transformation has been shown to influence crystal morphology (Larese-Casanova et al., 2010). It might be expected that the samples in this study present a higher quadrupole splitting compared to more crystalline samples measured in other studies (Cornell and Schwertmann, 2003, Murad and Schwertmann, 1984). It should also be considered that, at around Néel temperature, atypical Mössbauer spectra might be produced, therefore, measurement well below this is recommended (Murad and Schwertmann, 1984).

Table 5.3. Comparison of the measured peat bog and River Thurso magnetically ordered Mössbauer parameters for Fe^{3+} (Lepidocrocite) in this study, alongside published (Lepidocrocite) data from Cornell and Schwertmann (2003) and references therein:

Cornell and Schwertmann (2003)	measuring temperature = 4.2 K	isomer shift = 0.47 mm s^{-1}	quadrupole splitting = 0.02 mm s^{-1}	hyperfine field = 45.8 T
Cornell and Schwertmann (2003)	measuring temperature = 4.2 K	isomer shift = 0.25 mm s^{-1}	quadrupole splitting = 0.02 mm s^{-1}	hyperfine field = 45.4 T ('*well crystalline natural sample*')
This study - River Thurso Fe^{3+} (3)	measuring temperature = 4.2 K	isomer shift = 0.57 mm s^{-1}	quadrupole splitting = 0.04 mm s^{-1}	hyperfine field = 46.63 T
This study – peat bog Fe^{3+} (2)	measuring temperature = 4.2 K	isomer shift = 0.61 mm s^{-1}	quadrupole splitting = 0.01 mm s^{-1}	hyperfine field = 45.69 T

The parameters presented in Table 5.3 show a higher quadrupole splitting for the peat bog waters compared to the River Thurso, an indication that the peat bog comprises particles possibly displaying a higher amorphicity than the river particles. However, additional techniques to investigate morphology, for example Transmission Electron Microscopy (as discussed in Chapter 2, section 2.4.5), should be applied to better understand if these assumptions are indeed founded.

The analysis and fitting parameters of the obtained data provided SMS spectra for the oxyhydroxide lepidocrocite (*γ*-FeO(OH) within both the peat bog waters and River Thurso in the nanoparticle/colloidal (66 to 400 nm) physical size fraction. Lepidocrocite is an iron mineral which was found to be a significant component of ochres that precipitated from low-pH (<5) waters in mine drainage (Bowell and Bruce, 1995). Loch More peat bog water pH value was recorded at 6.74 (± 0.35) (Chapter 4, section 4.3). Peat bogs (sphagnum-dominated) are naturally acidic

(Clymo, 1984). Lepidocrocite is most commonly encountered in primary iron mineral weathering and is also found in iron ore deposits. It is present in hydrological environments, for example it can form in the presence of water in steel pipes and tanks, hence it's alternative name hydrohematite. This mineral can be formed where there are distinct changes in redox potential which, favours free Fe^{2+} release from the lattice of iron containing silicates with a (near) ~neutral soil reaction (i.e. slow oxidation) (Raiswell, 2011). An example of this would be an environment with high soil organic matter (Alekseev and Alekseeva, 2000), as is found in peat bogs. This information about the formation of lepidocrocite aligns well with its presence in the peat bog and river water samples investigated in this study.

Particle size

There are observed differences between the peat bog and River Thurso samples Mössbauer data. There are also other differences amongst the other results for these samples such as particle size range. It should be noted that the particle size measurements were done using AF^4-ICP-MS and dynamic light scattering after a period of cold storage. Therefore, there could have been changes due to aggregation and/or disaggregation within the samples and affecting the measured particle size. A range of other variables might also explain the differences in the results, such as microbial activity or location within the catchment i.e. peat bog (source) versus river. These two environments are recognised to often display differences including redox conditions, pH, biogeochemical cycling, carbon and other element concentrations and speciation (Krachler et al., 2016, Kritzberg et al., 2014, Herzog et al., 2017, Von Der Heyden et al., 2019).

Measured iron concentrations at the time of filtration for the two sample locations are an order of magnitude higher in the less than 400 nm size fraction for the peat bog sample compared to the River Thurso sample. In the SMS spectra for the River Thurso (Figures 5.9 and 5.10) and Peat Bog (Figures 5.7 and 5.8), differences in the mineralogy found between the two samples can be seen. Although both contain Fe^{3+} in lepidocrocite, the River Thurso sample still shows doublet

(Fe^{3+}) at 4.2 K which, could be linked to the iron in the smaller particle size range found for the river compared to the peat bog. This might suggest the presence a more amorphous (transitional) Fe phase in the smaller size fraction (Li et al., 2011, Hinshaw, 2004). Further analysis is needed to determine why this other phase is present in the river alone, and indeed if there might be a relationship to particle size. It should be noted that these samples were not fully investigated using SMS and there is the potential for other Fe phases to be revealed that might have been missed in the achieved measurements.

Proposed adaptations to optimise sample preparation and measurement might allow for more comprehensive datasets. Future SMS investigation might also benefit from the addition of AF^4 coupled to ICP-MS or DLS, and possible collection of collection of the eluted particles which could then be prepared for SMS. This was previously discussed in Chapter 4 (section 4.4.1). this method is yet to be fully investigated, however, there is the potential for it to provide a solution to mitigate any storage associated changes to particle size (aggregation/disaggregation), and to better align the iron mineralogy with particle size. A suite of complementary analyses should form part of future SMS investigation to facilitate the investigation of where the iron Fe-OM particles as was suggested by Von Der Heyden (2019).

5.6.1 **SMS method development**

Beamtime

Experiment EV-310 was a proof-of-concept study. This constrained the parameters for the standard beamtime application made to the ESRF to facilitate test samples. Despite the time constraints, this experiment was successful in defining mineralogy in the samples and provided an opportunity to assess sample preparation to inform future studies. It is suggested that future beamtime application should factor estimated measurement times for each sample based on the measurements from this study and accounting for any future sample preparation optimisation. It

is expected that significant data would have been collected for some of the remaining samples if they had been measured for a longer time.

Optimisation for future studies should consider alteration to the sample dimensions, increased enrichment of particles (water removal from the sample matrix) and adjustment of the beam focus. This should ensure optimal use of future beamtime awarded for sample measurement and include reasoned estimations of the measurement times per sample based on the observations made in the methods and results sections of this chapter.

Sample preparation optimisation and SMS measurement

There were some known reasons and some untested assumptions for data collection issues for these samples. Firstly, there may not have been sufficient iron in the sample (see ideal sample thickness calculations in results section). Additionally, as there was only one measurement per sample, and given the small spot size of the beam compared to the capillary bore area, it is a possibility that a successful attempt of measurement was missed. Furthermore, the samples may have been compromised in two ways: i) shattering of some capillaries was observed, possibly caused by sudden temperature change and compounded by overly long capillary length not being fully housed within the OFHC casing and, ii) it is possible that some borosilicate glass filings were included in the sample matrix. This is likely from the process of shortening the capillary length after sample loading in order to prevent the capillary damage, likely due to temperature change.

Sample optimisation

The results of this study suggest further optimisation of sample preparation is needed. The optimum (ideal) sample thickness is the thickness that will allow for measurement, using Mössbauer spectroscopy, to be conducted successfully in the shortest time period (Long et al., 1983). Calculations for optimum thickness are partially dependent upon a number of known parameters. Samples for Mössbauer absorption measurements should contain sufficient

concentration of the ^{57}Fe isotope (relative abundance in nature of ^{57}Fe is 2.21% (Rickard, 2012)) and the γ-radiation must be able to penetrate the sample matrix (Gütlich et al., 2010). Mössbauer gamma rays are soft (energy: E_0 ~14.4 keV) (Saito et al., 2019), and are therefore susceptible to being absorbed by nonresonant mass absorption. The decision to direct the beam along the internal bore of the borosilicate glass capillary negates part of this issue.

Despite being able to overcome this issue by accessing the sample matrix alone, there is still a case to optimise the thickness of the sample being measured. The thickness of a sample affects both the strength of the Mössbauer signal and the intensity of the detected radiation due to the nonresonant mass absorption within the sample matrix. In the River Thurso sample the natural Fe in the sample is 0.21 mg Fe cm^2. An ideal absorber has ~10 mg/cm^2 of natural Fe and is uniform (Klingelhoefer et al., 2003). This paucity of iron demonstrates the need to further optimise sample preparation and sample holder construction.

Consideration should also be given to the other components (elements) in the sample, in conjunction with the optimisation of "thin" absorbers, as has been described by Long et al. (1983) and Gütlich et al. (2010). Mössbauer absorbers (the sample) should ideally be homogenous and devoid of areas where the sample material is missing. Care should be taken when preparing samples, especially for those in this type of study sample due to the water content, additionally, care should be taken to ensure there are no void spaces in the capillary prior to freezing. For future SMS measurements, increased initial sample water volumes might provide a higher iron content (sample dependent), and a higher ratio of particulate matter to water in the sample could further enrich the particles of interest.

Freeze drying is another option which might be considered for future SMS application, however, this technique introduces other limitations: small sample volumes and the ability to safely freeze dry with no significant loss of sample; the capillary action would be lost with no liquid matrix and an alternative sample vessel would need sought out and to ensure the sample was unable to

move during SMS measurement. As discussed, by applying the optimum sample thickness to the sample preparation procedure the sample holder can be constructed to accommodate both the beam spot size and the desired thickness of the sample, thus ensuring full measurement of the sample in the minimal measurement time with maximal signal to noise ratio (Gütlich et al., 2010).

Sample preparation for SMS measurement should therefore include consideration of altering the dimensions of the samples i.e. capillary dimensions, removing more of the pore water and using a different capillary material to mitigate it shattering (possibly due to thermal expansion) which appeared to occur when the sample capillary was longer than the cryostat mount sample slot and also to prevent borosilicate glass particles from infiltrating the sample matrix when the capillary is cut to size. The dimensions of the sample capillary used in this study had an internal bore diameter of 1360 μm (r = 680 μm). Therefore, the beam had access to a sample with an area of 1.45267×10^{6} μm. As discussed in the introduction to this chapter, the minimum spot size the beam can be focused to is 10 μm x 5 μm and a sample diameter of <100 μm is possible for SMS measurements (Potapkin et al., 2012). Comparing the sample surface area to the beam size demonstrates the vast sample area available to measure as is shown in Figure 5.11. Consequently, much of the sample is missed by the beam, limiting data collection.

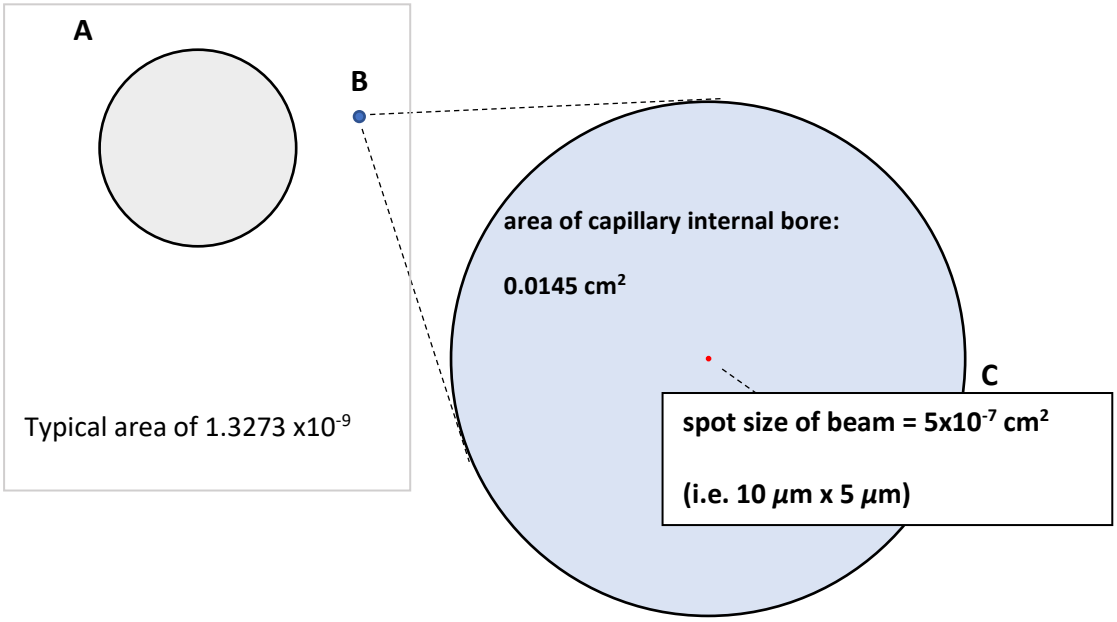

Figure 5.11.Sample dimensions for conventional Mössbauer spectroscopy and SMS: A) typical dimensions of a standard filter membrane used for conventional Mössbauer spectroscopy (at Mössbauer Spectroscopy laboratory for Earth and Environment at the University of Stirling), B) internal bore accessible area for beam for the capillaries used for this experiment (EV-310) (scale is 1:200) and C) enlarged area of capillary bore as in B) with beam spot size (scaled to relative internal bore area and beam spot size).

Capillaries with a smaller internal bore are available. Figure 5.12 shows an example of how adjusting the capillary internal bore to be similar to that of the beam spot size might accommodate optimised SMS measurements. This capillary dimension change would provide the possibility to collect data for a full sample area. This would mean that the majority the sample could be accessed by the beam thereby avoiding the situation described in Figure 5.11.

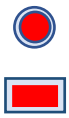

Possible example: borosilicate glass capillary with an internal bore diameter similar to the spot size of the beam. The outer circle or rectangle represents the capillary and the inner red shape, the beam.

Figure 5.12. Optimisation of sample dimensions to allow full sample access of the beam. Proposed capillary options for future SMS measurements showing end view of capillary bore (blue) and beam spot size (red).

Although changing to a capillary with a smaller internal bore (diameter) might appear an ideal option for this application, another possible challenge is then presented. When sufficient water has been removed from the sample to achieve an optimised measurement, the ability to successfully load the sample into the internal bore of the capillary might be compromised. This sample optimisation is planned for testing prior to further beamtime application.

There are possible options for filling the capillary, if capillary action is compromised. These include, pre-loading a filling needle with the sample, or employing a glass cannula attached to a micro-syringe. The smallest possible inner diameter of capillaries accessed online ranges at 4- 5 μm with differing wall thicknesses and standard manufacturing lengths of 1060 and 1500 mm. However, there are manufacturers who will make capillaries to specified dimensions. By using this approach (custom designed), it should be possible to obtain capillaries with inner diameter and wall thickness to fit the existing cryostat mount sample slots and avoiding extra costs. This should allow for testing of the optimal internal bore dimensions for SMS measurement whilst retaining the capability to load the sample into the existing cryostat mount.

Any change to the capillary material should consider ease of alteration to the capillary length, and also the associated thermal properties i.e. the ability for the material to withstand low temperatures down to 4.2 K in order to gain full mineralogical information. It is also suggested there may be a possibility to alter the beam size so that it is not as focussed. This option should be

explored in the first instance as it could facilitate measurement of a larger sample area and negate capillary dimension alterations. It should be acknowledged, however, that any alteration to the beam focus should be investigated alongside any possible trade off for data acquisition and time constraints.

As has been discussed over Chapters 3 and 4, future studies sampling campaigns would benefit from encompassing seasonality and changes through environmental boundaries e.g. salinity transects in river plumes and glacial or sea ice melt. This will help to elucidate the role these particles might play in biogeochemical cycling in source to sea transport. Here it is expected that Fe-OM particles might be delivering a pool of potentially bioavailable (through photochemical reduction, (siderophore) dissolution and/or protozoan grazing) iron to the coastal oceans or the sea shelf (Krachler et al., 2015, Krachler et al., 2016). Optimisation of the method could enhance SMS capabilities to include more iron dilute systems such as glaciers and glacial melt, sea ice, deep oceans and hydrothermal vents where definitive mineralogy has been shown to be lacking.

5.7 **Conclusions**

The experiment EV-310 at ID18, ESRF successfully demonstrated the ability to employ SMS to investigate iron speciation and mineralogy in water-borne environmental nanoparticles and colloids within the operationally defined dissolved size fraction of natural waters. These water-borne, often amorphous, particles are shown in the literature to be complicated to characterise and defining iron mineralogy is particularly difficult (Chapters 1 and 2). SMS has the potential to contribute to our understanding of Fe-OM influences, and iron interactions with biogeochemical cycles, as these are expected to differ from the behaviour of mineral standards observed in existing experimental models (Von Der Heyden et al., 2019).

Despite the need to optimise the sample preparation, the success of the method has been demonstrated for the first time during this experiment. The data obtained has given insight into

preparing for future SMS measurement of iron-bearing water borne nanoparticles and colloids and has hopefully given impetus to future SMS beamtime application success. This study presents the ability of the SMS to provide iron mineralogy data without the requirements of reference standards which, are often needed for other methods (Chapter 2, section 2.4.7).

The results presented in this chapter are from beamtime experiment EV-310 at the European Synchrotron Radiation Facility (ESRF). The potential for future employment of SMS to further elucidate iron mineralogy associated with (natural) environmental nanoparticles and fine colloids has now been established, however, optimisation of the methods is needed. Ongoing development of this technique should provide insight into the role of iron in biogeochemical systems. SMS has the potential to define iron mineralogy in a diversity of environments where achieving only microscopic sample volumes is achievable, for example surface and deep oceans, returned samples from extraterrestrial locations, hydrothermal vents, sea ice and glacial melt.

6. Summary, conclusions and outlook

The research has shown the success of the developed Synchrotron Mössbauer techniques to provide definitive mineralogy in water-borne environmental nanoparticles and colloids. The process of the method development provided insight into the effectiveness of particle size fractionation methods over a range of particles size fractions, and explored isolation and concentration techniques, investigating sample loss and providing recommendations for future studies. The studies also presented iron and carbon data and explored relationships, over catchments and particle size ranges.

Iron and carbon

The studies in Chapters 3 and 4 focused on iron concentrations from terrestrials sources to coastal sites. The initial purpose of these iron concentration investigations was to determine where, within the operationally dissolved physical size fraction, iron was associated with natural nanoparticles and colloids. The initial study was not as successful as anticipated in covering a full salinity transect, however, it was informative and highlighted limitations to the development of the SMS method. These included: limitations of physical size fractionation and concentration of particles, trace iron concentrations and the need for clean laboratory space, contamination issues for iron dilute samples, and storage versus processing capabilities.

As a result of the Loch Etive study, a decision to develop the methods in a more iron rich environment was made. This decision was taken to mitigate the low iron concentration issues with regard to sample processing times and volumes and also took account of contamination issues. Despite not having a clean laboratory facility, trace metal cleaning and clean lab practices were adopted as far as possible. Future studies should include this to avoid contamination of dilute samples, particularly when, as the intention for SMS, sea water is being processed or analysed. This led to the decision to locate the future sampling to the Flow Country.

There are many existing studies on organic matter and iron here, and research is ongoing due to the vulnerability of peatlands in this area (Andersen et al., 2018). The existing research was extremely informative when planning the sampling campaigns, and the ongoing interest in this geographical area suggested that future studies using SMS might be a good addition to the growing body of knowledge.

Data gathered in the Chapter 3 and 4 studies was used to inform the development of the SMS methods described in Chapter 5. However, it has also shown that, within the operationally dissolved size fraction of the studied waters, most of the iron is found in nanoparticles and colloids and that these particles sustain through rivers to the coastal mixing zones. Further studies at higher salinities should be done in order to reveal the extent of the transport.

Additionally, the Flow Country studies in Chapter 4 reveal iron associations with both organic and inorganic carbon, however, these relationships are shown to vary in their strength over catchments, and particle size ranges. It would be advantageous to add organic matter characterisation to the studies. In doing so, if combined with iron mineralogy there is the potential to elucidate the mechanisms involved in Fe-OM associations and transport in aquatic environments. Further studies are needed to understand these relationships and it is suggested that they are approached from a multi-elemental perspective. The addition of the SMS method to add iron mineralogy to ongoing research would close knowledge gaps that are highlighted in the existing research such as the association of iron and humic and fulvic substances (Muller, 2018, Philippe and Schaumann, 2014, Pokrovsky et al., 2016).

The studies in this project were constrained by time and funding availability. Therefore, the sampling campaigns were constricted to a very narrow window of time and the data gathered only provides a snapshot of the catchments studied. Ideally long-term studies over paired catchments would allow for better insight into Fe-OM water-borne particles (Gottselig et al., 2017). Catchment

studies should include other variables which contribute the chemistry of rivers. However, this requires collaboration and funding.

Particle isolation and concentration

Chapter 4 provides an analysis of particle size isolation methods: TFF, Jumbosep Centrifugal Devices, Amicon Centrifugal units and AF^4 coupled to ICP-MS. The investigation revealed that there were instances of both sample loss and sample gain for all of the methods, however, concluded that the use of AF^4- ICP-MS had a number of advantages. The recovery rate has been shown to be in excess of 90% (Gottselig et al., 2020), and it provides sample specific data that can be used to identify the components in the dissolved fraction of water i.e. elemental concentrations and particle size data. AF^4 can be coupled to other instrumentation such as DLS or carbon analysers (Leeman et al., 2015, Jirsa et al., 2013). There is also the capability to collect the eluted size fractions for onward stand-alone analyses and it is suggested that this is explored for its applicability to the SMS method, replacing the previously tested filtration devices which had greater limitations. There are questions that need addressed, however. Ideally, the sample volume would need to be sufficient to provide SMS suitable iron concentrations as described in Chapter 5 (Schröder et al., 2016, Gütlich et al., 2010). Would there be a need to remove water from the matrix? If so, then a method for that would need to be found or developed. It is suggested that this option is worth exploring seriously. AF^4 coupled to ICP-MS would provide iron and other element concentrations in the selected size fractions using an identical system for each sample, mitigating filtration and instrument error. It should also limit the possibility of contamination from excess processing. If achievable, the combined methods, including onward SMS, has improved potential for further development, and for successful investigation of more iron dilute systems such as oceans, sea ice and glacial melt waters.

Optimising the SMS method for introduction to the beam

Despite the success of the developed SMS methods there is still an apparent need to further optimise them. This is particularly pertinent for future iron mineralogical studies in more dilute environments such as sea water. The direction of the development should focus on optimising sample preparation and beam introduction methods presented in Chapter 5 (5.6.1).

It is recommended that to gain further insight into this development, an extended study should be carried out, similar to the studies presented in Chapters 3 and 4. Ideally, continuing to investigate source, river and coastal sites. Iron mineralogy should ideally form part of nanoparticle and colloid studies investigating elemental fluxes of other elements and organic matter (Hochella et al., 2008, Raiswell and Canfield, 2012).

There are numerous options to consider with regard to optimising the sample holder, as discussed in Chapter 5. These include efforts being made to remove more water by exploring the filtration methods above. Once the particles are isolated, ultrafiltration units can be used as they were for this project, however, there are other available options such as the Rocket Evaporator, which is able to concentrate large sample volumes of water rapidly and without the previously discussed membrane filtration issues (Hirave et al., 2020).

After water removal there are also a number of ways to optimise the sample vessel by changing its dimensions to ensure that the beam is focused on the full sample, or by adjusting the beam focus to achieve the same result. If changing the sample vessel, then consideration must be given to the ability to load it with the sample. This is, however, a relatively low cost option. If changing the beam focus then there is a risk that the measurement time will over extended (Potapkin et al., 2012, McCammon, 1994). It is apparent that there needs to be a balance between these two variables.

When considering the use of SMS in the future there is an advantage to the costs involved in the use of the method. If beamtime is awarded by the ESRF the costs are covered and that part of the

research should not need further external funding, however, the future of the SMS research project is dictated by whether beamtime is awarded or not. Also, the length of beam time is crucial and if sample preparation is not fully optimised, opportunities for data collection will likely be lost.

This project has developed and shown that these novel SMS methods are capable of providing definitive mineralogy for water-borne Fe-OM nanoparticles and colloids, and also revealed that Fe (oxyhydr)oxide particles are associated with suspended particles in river waters. Going forward the SMS method has applicability in a variety of environmental settings where other techniques not yet provided definitive mineralogy (Von Der Heyden et al., 2019). There is the potential to develop SMS for the determination of iron mineralogy in microscopic samples that are held in an aqueous matrix, such as sea water, lake waters, sea ice or glacial melt. Chapter 2 considered a variety of techniques to investigate water-borne environmental iron-bearing nanoparticles and it was clear that the techniques, including other synchrotron techniques, have not yet been developed sufficiently to provide definitive mineralogy for these particles.

The priorities for the future of the SMS methods are to optimise sample collection, size fractionation and particle concentration methods in collaboration with multi-element/OM investigations. Ideally, long term studies involving seasonal influences and over paired catchments. In the meantime, the immediate priority is to explore the optimisation options for sample introduction to the beam.

References

ABAZARI, A. M., SAFAVI, S. M., REZAZADEH, G. & VILLANUEVA, L. G. 2015. Modelling the Size Effects on the Mechanical Properties of Micro/Nano Structures. *Sensors (Basel).*

ABUALHAIJA, M. M., WHITBY, H. & VAN DEN BERG, C. M. G. 2015. Competition between copper and iron for humic ligands in estuarine waters. *Marine Chemistry,* 172**,** 46-56.

AKBARZADEH, A., SAMIEI, M. & DAVARAN, S. 2012. Magnetic nanoparticles: preparation, physical properties, and applications in biomedicine. *Nanoscale Research Letters,* 7**,** 1-13.

ALEKSEEV, A. O. & ALEKSEEVA, T. V. 2000. On the lepidocrocite formation in soils. *Eurasian Soil Science,* 33**,** 1053-1060.

ALI, A., ZAFAR, H., ZIA, M., HAQ, I. U., PHULL, A. R., ALI, J. S. & HUSSAIN, A. 2016. Synthesis, characterization, applications, and challenges of iron oxide nanoparticles. *Nanotechnology Science and Applications,* 9**,** 49-67.

AMSTAD, E., GILLICH, T., BILECKA, I., TEXTOR, M. & REIMHULT, E. 2009. Ultrastable iron oxide nanoparticle colloidal suspensions using dispersants with catechol-derived anchor groups. *Nano letters,* 9**,** 4042-4048.

AMSTAD, E., TEXTOR, M. & REIMHULT, E. 2011. Stabilization and functionalization of iron oxide nanoparticles for biomedical applications. *Nanoscale,* 3**,** 2819-2843.

ANDERSEN, R., COWIE, N., PAYNE, R. J. & SUBKE, J.-A. 2018. The Flow Country peatlands of Scotland. *Mires and Peat*.

ANGELAKERIS, M., LI, Z.-A., SAKELLARI, D., SIMEONIDIS, K., SPASOVA, M. & FARLE, M. 2014. Can commercial ferrofluids be exploited in AC magnetic hyperthermia treatment to address diverse biomedical aspects? *In:* NIARCHOS, D., HADJIPANAYIS, G. & KALOGIROU, O. (eds.) *Jems 2013 - Joint European Magnetic Symposia.*

ANGELICO, R., CEGLIE, A., HE, J. Z., LIU, Y. R., PALUMBO, G. & COLOMBO, C. 2014. Particle size, charge and colloidal stability of humic acids coprecipitated with Ferrihydrite. *Chemosphere,* 99**,** 239-47.

ANSCHUTZ, A. J. & PENN, R. L. 2005. Reduction of crystalline iron(III) oxyhydroxides using hydroquinone: Influence of phase and particle size. *Geochemical Transactions,* 6**,** 60-66.

AUDSLEY, A., AROSIO, R. & HOWE, J. A. 2016. A geomorphological reconstruction of the deglaciation of Loch Etive during the Loch Lomond Stadial. *Scottish Journal of Geology,* 52**,** 55-63.

BAALOUSHA, M. 2009. Aggregation and disaggregation of iron oxide nanoparticles: Influence of particle concentration, pH and natural organic matter. *Sci Total Environ,* 407**,** 2093-101.

BAALOUSHA, M., MANCIULEA, A., CUMBERLAND, S., KENDALL, K. & LEAD, J. R. 2008. Aggregation and surface properties of iron oxide nanoparticles: influence of pH and natural organic matter. *Environmental Toxicology and Chemistry,* 27**,** 1875-1882.

BAALOUSHA, M., STOLPE, B. & LEAD, J. R. 2011. Flow field-flow fractionation for the analysis and characterization of natural colloids and manufactured nanoparticles in environmental systems: a critical review. *Journal of Chromatography A,* 1218**,** 4078-4103.

BAER, D. R., GASPAR, D. J., NACHIMUTHU, P., TECHANE, S. D. & CASTNER, D. G. 2010. Application of surface chemical analysis tools for characterization of nanoparticles. *Analytical and bioanalytical chemistry,* 396**,** 983-1002.

BAGARD, M. L., CHABAUX, F., POKROVSKY, O. S., VIERS, J., PROKUSHKIN, A. S., STILLE, P., RIHS, S., SCHMITT, A. D. & DUPRE, B. 2011. Seasonal variability of element fluxes in two Central Siberian rivers draining high latitude permafrost dominated areas. *Geochimica Et Cosmochimica Acta,* 75**,** 3335-3357.

BAKEN, S., REGELINK, I. C., COMANS, R. N. J., SMOLDERS, E. & KOOPMANS, G. F. 2016. Iron-rich colloids as carriers of phosphorus in streams: A field-flow fractionation study. *Water research,* 99**,** 83-90.

BALASUBRAMANIAN, C., JOSEPH, B., GUPTA, P., SAINI, N. L., MUKHERJEE, S., DI GIOACCHINO, D. & MARCELLI, A. 2014. X-ray absorption spectroscopy characterization of iron-oxide nanoparticles synthesized by high temperature plasma processing. *Journal of Electron Spectroscopy and Related Phenomena,* 196**,** 125-129.

BANCROFT, G. M. 1973. *Mössbauer spectroscopy: An introduction for inorganic chemists and geochemists*, Halsted Press.

BARRETO, J. A., O'MALLEY, W., KUBEIL, M., GRAHAM, B., STEPHAN, H. & SPICCIA, L. 2011. Nanomaterials: Applications in Cancer Imaging and Therapy. *Advanced Materials,* 23**,** H18-H40.

BATCHELLI, S., MULLER, F. L. L., CHANG, K.-C. & LEE, C.-L. 2010. Evidence for strong but dynamic iron− humic colloidal associations in humic-rich coastal waters. *Environmental science & technology,* 44**,** 8485-8490.

BOURAS, N., MADJOUBI, M. A., KOLLI, M., BENTERKI, S. & HAMIDOUCHE, M. 2009. Thermal and mechanical characterization of borosilicate glass. *Physics Procedia,* 2**,** 1135-1140.

BOWELL, R. J. & BRUCE, I. 1995. Geochemistry of iron ochres and mine waters from Levant Mine, Cornwall. *Applied Geochemistry,* 10**,** 237-250.

BRAUNSCHWEIG, J., BOSCH, J. & MECKENSTOCK, R. U. 2013. Iron oxide nanoparticles in geomicrobiology: from biogeochemistry to bioremediation. *New biotechnology,* 30**,** 793-802.

BREITBARTH, E., ACHTERBERG, E. P., ARDELAN, M. V., BAKER, A. R., BUCCIARELLI, E., CHEVER, F., CROOT, P. L., DUGGEN, S., GLEDHILL, M. & HASSELLÖV, M. 2010. Iron biogeochemistry across marine systems–progress from the past decade. *Biogeosciences,* 7**,** 1075-1097.

BRYANT, H. C., ADOLPHI, N. L., HUBER, D. L., FEGAN, D. L., MONSON, T. C., TESSIER, T. E. & FLYNN, E. R. 2011. Magnetic properties of nanoparticles useful for SQUID relaxometry in biomedical applications. *Journal of Magnetism and Magnetic Materials,* 323**,** 767-774.

CARABALLO, M. A., MICHEL, F. M. & HOCHELLA, M. F. 2015. T he rapid expansion of environmental mineralogy in unconventional ways: Beyond the accepted definition of a mineral, the latest technology, and using nature as our guide. *American Mineralogist,* 100**,** 14-25.

CARDELL, C. & GUERRA, I. 2016. An overview of emerging hyphenated SEM-EDX and Raman spectroscopy systems: Applications in life, environmental and materials sciences. *TrAC Trends in Analytical Chemistry,* 77**,** 156-166.

CARTER, C. B. & WILLIAMS, D. B. 2016. *Transmission electron microscopy: Diffraction, imaging, and spectrometry*, Springer.

CARVELL, J., AYIETA, E., GAVRIN, A., CHENG, R., SHAH, V. R. & SOKOL, P. 2010. Magnetic properties of iron nanoparticle.

CHAN, C. S., FAKRA, S. C., EDWARDS, D. C., EMERSON, D. & BANFIELD, J. F. 2009. Iron oxyhydroxide mineralization on microbial extracellular polysaccharides. *Geochimica Et Cosmochimica Acta,* 73**,** 3807-3818.

CHARETTE, M. A. & SHOLKOVITZ, E. R. 2002. Oxidative precipitation of groundwater-derived ferrous iron in the subterranean estuary of a coastal bay. *Geophysical research letters,* 29**,** 85-1.

CHARLET, L., SCHEINOST, A. C., TOURNASSAT, C., GRENECHE, J. M., GEHIN, A., FERNANDEZ-MARTINEZ, A., COUDERT, S., TISSERAND, D. & BRENDLE, J. 2007. Electron transfer at the mineral/water interface: Selenium reduction by ferrous iron sorbed on clay. *Geochimica Et Cosmochimica Acta,* 71**,** 5731-5749.

CHATTERJEE, J., HAIK, Y. & CHEN, C.-J. 2003. Size dependent magnetic properties of iron oxide nanoparticles. *Journal of Magnetism and Magnetic Materials,* 257**,** 113-118.

CHEKLI, L., PHUNTSHO, S., ROY, M., LOMBI, E., DONNER, E. & SHON, H. K. 2013. Assessing the aggregation behaviour of iron oxide nanoparticles under relevant environmental conditions using a multi-method approach. *Water Res,* 47**,** 4585-99.

CHEKLI, L., ZHAO, Y. X., TIJING, L. D., PHUNTSHO, S., DONNER, E., LOMBI, E., GAO, B. Y. & SHON, H. K. 2015. Aggregation behaviour of engineered nanoparticles in natural waters: characterising aggregate structure using on-line laser light scattering. *J Hazard Mater,* 284**,** 190-200.

CHIANG, I. W., BRINSON, B. E., HUANG, A. Y., WILLIS, P. A., BRONIKOWSKI, M. J., MARGRAVE, J. L., SMALLEY, R. E. & HAUGE, R. H. 2001. Purification and characterization of single-wall carbon nanotubes (SWNTs) obtained from the gas-phase decomposition of CO (HiPco process). *Journal of Physical Chemistry B,* 105**,** 8297-8301.

CHUPAKOV, A. V., CHUPAKOVA, A. A., MOREVA, O. Y., SHIROKOVA, L. S., ZABELINA, S. A., VOROBIEVA, T. Y., KLIMOV, S. I., BROVKO, O. S. & POKROVSKY, O. S. 2017. Allochthonous and autochthonous carbon in deep, organic-rich and organic-poor lakes of the European Russian subarctic. *Boreal Environment Research,* 22**,** 213-230.

CINI, A., MANNINI, M., TOTTI, F., FITTIPALDI, M., SPINA, G., CHUMAKOV, A., RÜFFER, R., CORNIA, A. & SESSOLI, R. 2018. Mössbauer spectroscopy of a monolayer of single molecule magnets. *Nature communications,* 9**,** 480.

CLAUDIO, C., DI IORIO, E., LIU, Q., JIANG, Z. & BARRON, V. 2017. Iron Oxide Nanoparticles in Soils: Environmental and Agronomic Importance. *Journal of Nanoscience and Nanotechnology,* 17**,** 4449-4460.

CLYMO, R. S. 1984. Sphagnum-dominated peat bog: a naturally acid ecosystem. *Philosophical Transactions of the Royal Society of London. B, Biological Sciences,* 305**,** 487-499.

COLOMBO, M., CARREGAL-ROMERO, S., CASULA, M. F., GUTIERREZ, L., MORALES, M. P., BOEHM, I. B., HEVERHAGEN, J. T., PROSPERI, D. & PARAK, W. J. 2012. Biological applications of magnetic nanoparticles. *Chemical Society Reviews,* 41**,** 4306-4334.

CORNELL, R. M. & SCHWERTMANN, U. 2003. *The iron oxides: structure, properties, reactions, occurrences and uses*, John Wiley & Sons.

CUTTER, G., ANDERSSON, P., CODISPOTI, L., CROOT, P., FRANCOIS, R., LOHAN, M. C., OBATA, H. & RUTGERS VD LOEFF, M. 2010. Sampling and sample-handling protocols for GEOTRACES cruises. GEOTRACES.

DA SILVA, M. G. F. 2016. Optical properties and crystallization behaviour of some MnO and/or Fe2O3-containing silicate glasses and glass-ceramics. *Journal of Non-Crystalline Solids,* 447**,** 223-232.

DAI, M.-H. & MARTIN, J.-M. 1995. First data on trace metal level and behaviour in two major Arctic river-estuarine systems (Ob and Yenisey) and in the adjacent Kara Sea, Russia. *Earth and Planetary Science Letters,* 131**,** 127-141.

DANESHVAR, E. 2015. Dissolved iron behavior in the Ravenglass Estuary waters, an implication on the early diagenesis. *Universal Journal of Geoscience,* 3**,** 1-12.

DE BAAR, H. J. W. 2001. Distributions, sources and sinks of iron in seawater. *The biogeochemistry of iron in seawater***,** 123-253.

DE JONG, J., SCHOEMANN, V., LANNUZEL, D., CROOT, P., DE BAAR, H. & TISON, J. L. 2012. Natural iron fertilization of the Atlantic sector of the Southern Ocean by continental shelf sources of the Antarctic Peninsula. *Journal of Geophysical Research: Biogeosciences,* 117.

EBERLE, A. L., MIKULA, S., SCHALEK, R., LICHTMAN, J., TATE, M. L. K. & ZEIDLER, D. 2015. High-resolution, high-throughput imaging with a multibeam scanning electron microscope. *Journal of microscopy,* 259**,** 114-120.

EKSTRÖM, S. M., REGNELL, O., READER, H. E., NILSSON, P. A., LÖFGREN, S. & KRITZBERG, E. S. 2016. Increasing concentrations of iron in surface waters as a consequence of reducing conditions in the catchment area. *Journal of Geophysical Research: Biogeosciences,* 121**,** 479-493.

EMERSON, D., RODEN, E. & TWINING, B. 2012. The microbial ferrous wheel: iron cycling in terrestrial, freshwater, and marine environments. *Frontiers in microbiology,* 3**,** 383.
ERICKSON, H. P. 2009. Size and shape of protein molecules at the nanometer level determined by sedimentation, gel filtration, and electron microscopy. *Biological procedures online,* 11**,** 32.
FARAJI, M., YAMINI, Y. & REZAEE, M. 2010. Magnetic Nanoparticles: Synthesis, Stabilization, Functionalization, Characterization, and Applications. *Journal of the Iranian Chemical Society,* 7**,** 1-37.
FILGUEIRAS, A. V., LAVILLA, I. & BENDICHO, C. 2002. Chemical sequential extraction for metal partitioning in environmental solid samples. *Journal of Environmental Monitoring,* 4**,** 823-857.
FREY, P. A. & REED, G. H. 2012. The Ubiquity of Iron. *ACS Chemical Biology,* 7**,** 1477-1481.
FROGGETT, S. J., CLANCY, S. F., BOVERHOF, D. R. & CANADY, R. A. 2014. A review and perspective of existing research on the release of nanomaterials from solid nanocomposites. *Particle and Fibre Toxicology,* 11.
FU, D., KEECH, P. G., SUN, X. & WREN, J. C. 2011. Iron oxyhydroxide nanoparticles formed by forced hydrolysis: dependence of phase composition on solution concentration. *Physical Chemistry Chemical Physics,* 13**,** 18523-18529.
GAFFNEY, P. P. J., HANCOCK, M. H., TAGGART, M. A. & ANDERSEN, R. 2020. Restoration of afforested peatland: Immediate effects on aquatic carbon loss. *Science of The Total Environment,* 742**,** 140594.
GERRINGA, L. J. A., SLAGTER, H. A., BOWN, J., VAN HAREN, H., LAAN, P., DE BAAR, H. J. W. & RIJKENBERG, M. J. A. 2017. Dissolved Fe and Fe-binding organic ligands in the Mediterranean Sea–GEOTRACES G04. *Marine Chemistry,* 194**,** 100-113.
GHAZANFARI, M. R., KASHEFI, M., SHAMS, S. F. & JAAFARI, M. R. 2016. Perspective of Fe3O4 Nanoparticles Role in Biomedical Applications. *Biochemistry Research International*.
GIDDINGS, J. C. 1993. Field-flow fractionation: analysis of macromolecular, colloidal, and particulate materials. *Science,* 260**,** 1456-1465.
GIMBERT, L. J., HAYGARTH, P. M., BECKETT, R. & WORSFOLD, P. J. 2005. Comparison of centrifugation and filtration techniques for the size fractionation of colloidal material in soil suspensions using sedimentation field-flow fractionation. *Environmental science & technology,* 39**,** 1731-1735.
GONZALEZ, A. G., POKROVSKY, O. S., JIMENEZ-VILLACORTA, F., SHIROKOVA, L. S., SANTANA-CASIANO, J. M., GONZALEZ-DAVILA, M. & EMNOVA, E. E. 2014. Iron adsorption onto soil and aquatic bacteria: XAS structural study. *Chemical Geology,* 372**,** 32-45.
GONZALEZ-GALVEZ, D., JANER, G., VILAR, G., VILCHEZ, A. & VAZQUEZ-CAMPOS, S. 2017. The Life Cycle of Engineered Nanoparticles. *Adv Exp Med Biol,* 947**,** 41-69.
GOTTSELIG, N., AMELUNG, W., KIRCHNER, J. W., BOL, R., EUGSTER, W., GRANGER, S. J., HERNÁNDEZ-CRESPO, C., HERRMANN, F., KEIZER, J. J. & KORKIAKOSKI, M. 2017. Elemental composition of natural nanoparticles and fine colloids in European forest stream waters and their role as phosphorus carriers. *Global Biogeochemical Cycles,* 31**,** 1592-1607.
GOTTSELIG, N., BOL, R., NISCHWITZ, V., VEREECKEN, H., AMELUNG, W. & KLUMPP, E. 2014. Distribution of phosphorus-containing fine colloids and nanoparticles in stream water of a forest catchment. *Vadose zone journal,* 13.
GOTTSELIG, N., SOHRT, J., UHLIG, D., NISCHWITZ, V., WEILER, M. & AMELUNG, W. 2020. Groundwater controls on colloidal transport in forest stream waters. *Science of The Total Environment,* 717**,** 134638.
GUO, H. & BARNARD, A. S. 2013. Naturally occurring iron oxide nanoparticles: morphology, surface chemistry and environmental stability. *Journal of Materials Chemistry A,* 1**,** 27-42.

GUO, L. & SANTSCHI, P. H. 2007. Ultrafiltration and its applications to sampling and characterisation of aquatic colloids. *IUPAC Series on Analytical and Physical Chemistry of Environmental Systems,* 10**,** 159.

GUPTA, A. K. & GUPTA, M. 2005. Synthesis and surface engineering of iron oxide nanoparticles for biomedical applications. *Biomaterials,* 26**,** 3995-4021.

GÜTLICH, P., BILL, E. & TRAUTWEIN, A. X. 2010. *Mössbauer spectroscopy and transition metal chemistry: fundamentals and applications*, Springer Science & Business Media.

GÜTLICH, P., SCHRÖDER, C. & SCHÜNEMANN, V. 2012. Mössbauer spectroscopy - An indispensable tool in solid state research. *Spectroscopy Europe,* 24**,** 21-32.

HARTLAND, A., LEAD, J. R., SLAVEYKOVA, V., O'CARROLL, D. & VALSAMI-JONES, E. 2013. The environmental significance of natural nanoparticles. *Nature education knowledge,* 4**,** 7.

HAWKINGS, J. 2016. Ironing out glacial sediment reactivity on I08. *Diamond,* 2016.

HAWKINGS, J. R., WADHAM, J. L., TRANTER, M., RAISWELL, R., BENNING, L. G., STATHAM, P. J., TEDSTONE, A., NIENOW, P., LEE, K. & TELLING, J. 2014. Ice sheets as a significant source of highly reactive nanoparticulate iron to the oceans. *Nature Communications,* 5**,** 8.

HENDY, I. L. 2015. Ironing out carbon export to the deep ocean. *Proceedings of the National Academy of Sciences,* 112**,** 306-307.

HEPBURN, L. E., BUTLER, I. B., BOYCE, A. & SCHRÖDER, C. 2020. The use of operationally-defined sequential Fe extraction methods for mineralogical applications: A cautionary tale from Mössbauer spectroscopy. *Chemical Geology***,** 119584.

HERZOG, S. D., PERSSON, P. & KRITZBERG, E. S. 2017. Salinity effects on iron speciation in boreal river waters. *Environmental science & technology,* 51**,** 9747-9755.

HERZOG, S. D., PERSSON, P., KVASHNINA, K. & KRITZBERG, E. S. 2020. Organic iron complexes enhance iron transport capacity along estuarine salinity gradients of Baltic estuaries. *Biogeosciences,* 17**,** 331-344.

HINSHAW, L. 2004. *Tailings and Mine Waste'04: Proceedings of the Eleventh Tailings and Mine Waste Conference, 10-13 October 2004, Vail, Colorado, USA*, CRC Press.

HINTERWIRTH, H., WIEDMER, S. K., MOILANEN, M., LEHNER, A., ALLMAIER, G., WAITZ, T., LINDNER, W. & LÄMMERHOFER, M. 2013. Comparative method evaluation for size and size-distribution analysis of gold nanoparticles. *Journal of separation science,* 36**,** 2952-2961.

HIRAVE, P., GLENDELL, M., BIRKHOLZ, A. & ALEWELL, C. 2020. Compound-specific isotope analysis with nested sampling approach detects spatial and temporal variability in the sources of suspended sediments in a Scottish mesoscale catchment. *Science of The Total Environment***,** 142916.

HIRST, C., ANDERSSON, P. S., SHAW, S., BURKE, I. T., KUTSCHER, L., MURPHY, M. J., MAXIMOV, T., POKROVSKY, O. S., MORTH, C. M. & PORCELLI, D. 2017. Characterisation of Fe-bearing particles and colloids in the Lena River basin, NE Russia. *Geochimica Et Cosmochimica Acta,* 213**,** 553-573.

HIRT, A. M., LANCI, L., DOBSON, J., WEIDLER, P. & GEHRING, A. U. 2002. Low-temperature magnetic properties of lepidocrocite. *Journal of Geophysical Research: Solid Earth,* 107**,** EPM-5.

HOCHELLA, M. F. 2008. Nanogeoscience: From Origins to Cutting-Edge Applications. *Elements,* 4**,** 373-379.

HOCHELLA, M. F., LOWER, S. K., MAURICE, P. A., PENN, R. L., SAHAI, N., SPARKS, D. L. & TWINING, B. S. 2008. Nanominerals, mineral nanoparticles, and Earth systems. *Science,* 319**,** 1631-1635.

HOO, C. M., STAROSTIN, N., WEST, P. & MECARTNEY, M. L. 2008. A comparison of atomic force microscopy (AFM) and dynamic light scattering (DLS) methods to characterize nanoparticle size distributions. *Journal of Nanoparticle Research,* 10**,** 89-96.

HOPWOOD, M. J., STATHAM, P. J., SKRABAL, S. A. & WILLEY, J. D. 2015. Dissolved iron (II) ligands in river and estuarine water. *Marine Chemistry,* 173**,** 173-182.
HU, J. D., ZEVI, Y., KOU, X. M., XIAO, J., WANG, X. J. & JIN, Y. 2010. Effect of dissolved organic matter on the stability of magnetite nanoparticles under different pH and ionic strength conditions. *Sci Total Environ,* 408**,** 3477-89.
HU, Y., CRIST, R. M. & CLOGSTON, J. D. 2020. The utility of asymmetric flow field-flow fractionation for preclinical characterization of nanomedicines. *Analytical and Bioanalytical Chemistry,* 412**,** 425-438.
HUANG, L., WENG, X., CHEN, Z., MEGHARAJ, M. & NAIDU, R. 2014. Green synthesis of iron nanoparticles by various tea extracts: Comparative study of the reactivity. *Spectrochimica Acta Part A: Molecular and Biomolecular Spectroscopy,* 130**,** 295-301.
HUE, H. V. 2015. Crystallization of Amorphous Iron Nano-particles by Means of Molecular Dynamics Simulation. *Int J Nano Stud Technol,* 4**,** 88-92.
HUFSCHMID, R., ARAMI, H., FERGUSON, R. M., GONZALES, M., TEEMAN, E., BRUSH, L. N., BROWNING, N. D. & KRISHNAN, K. M. 2015. Synthesis of phase-pure and monodisperse iron oxide nanoparticles by thermal decomposition. *Nanoscale,* 7**,** 11142-11154.
HUNTER, K. A., LEONARD, M. R., CARPENTER, P. D. & SMITH, J. D. 1997. Aggregation of iron colloids in estuaries: a heterogeneous kinetics study using continuous mixing of river and sea waters. *Colloids and Surfaces A: Physicochemical and Engineering Aspects,* 120**,** 111-121.
IRAVANI, S. 2011. Green synthesis of metal nanoparticles using plants. *Green Chemistry,* 13**,** 2638-2650.
ISLAM, M. R., BACH, L. G., TRAN THI, N. & LIM, K. T. 2013. Covalent ligation of gold coated iron nanoparticles to the multi-walled carbon nanotubes employing click chemistry. *Journal of Alloys and Compounds,* 561**,** 201-205.
JAIN, G., CAPOZZI, C. J. & XU, J. J. 2003. Nanosized amorphous iron oxyhydroxide for reversible lithium intercalation. *Journal of the Electrochemical Society,* 150**,** A806-A810.
JAIN, T. K., MORALES, M. A., SAHOO, S. K., LESLIE-PELECKY, D. L. & LABHASETWAR, V. 2005. Iron oxide nanoparticles for sustained delivery of anticancer agents. *Molecular pharmaceutics,* 2**,** 194-205.
JEANDEL, C., PEUCKER-EHRENBRINK, B., JONES, M. T., PEARCE, C. R., OELKERS, E. H., GODDERIS, Y., LACAN, F., AUMONT, O. & ARSOUZE, T. 2011. Ocean margins: The missing term in oceanic element budgets? *Eos, Transactions American Geophysical Union,* 92**,** 217-218.
JICKELLS, T. D., AN, Z. S., ANDERSEN, K. K., BAKER, A. R., BERGAMETTI, G., BROOKS, N., CAO, J. J., BOYD, P. W., DUCE, R. A. & HUNTER, K. A. 2005. Global iron connections between desert dust, ocean biogeochemistry, and climate. *science,* 308**,** 67-71.
JILBERT, T., TVÄRMINNE ZOOLOGICAL STATION, U. O. H., J.A.PALMÉNINTIE 260, 10900 HANKO, FINLAND, TOM.JILBERT@HELSINKI.FI, ASMALA, E., TVÄRMINNE ZOOLOGICAL STATION, U. O. H., J.A.PALMÉNINTIE 260, 10900 HANKO, FINLAND, DEPARTMENT OF BIOSCIENCE – APPLIED MARINE ECOLOGY AND MODELLING, A., FREDERIKSBORGVEJ 399, 4000 ROSKILDE, DENMARK, 0000-0002-9150-1227, SCHRÖDER, C., BIOLOGICAL AND ENVIRONMENTAL SCIENCES, F. O. N. S., UNIVERSITY OF STIRLING, STIRLING FK9 4LA, SCOTLAND, UK, 0000-0002-7935-6039, TIIHONEN, R., TVÄRMINNE ZOOLOGICAL STATION, U. O. H., J.A.PALMÉNINTIE 260, 10900 HANKO, FINLAND, MYLLYKANGAS, J.-P., TVÄRMINNE ZOOLOGICAL STATION, U. O. H., J.A.PALMÉNINTIE 260, 10900 HANKO, FINLAND, 0000-0001-5259-6852, VIRTASALO, J. J., 0000-0002-9712-3642, KOTILAINEN, A., PELTOLA, P., BOLIDEN RÖNNSKÄR, S., SWEDEN, EKHOLM, P., HIETANEN, S., TVÄRMINNE ZOOLOGICAL STATION, U. O. H., J.A.PALMÉNINTIE 260, 10900 HANKO, FINLAND & 0000-0002-1572-8294 2018. Impacts of flocculation on the distribution and diagenesis of iron in boreal estuarine sediments. *Biogeosciences,* 15**,** 1243-1271.

JIRSA, F., NEUBAUER, E., KITTINGER, R., HOFMANN, T., KRACHLER, R., VON DER KAMMER, F. & KEPPLER, B. K. 2013. Natural organic matter and iron export from the Tanner Moor, Austria. *Limnologica,* 43**,** 239-244.

JOURNET, E., DESBOEUFS, K. V., CAQUINEAU, S. & COLIN, J.-L. 2008. Mineralogy as a critical factor of dust iron solubility. *Geophysical Research Letters,* 35.

KARAKOTI, A. S., HENCH, L. L. & SEAL, S. 2006. The potential toxicity of nanomaterials—the role of surfaces. *Jom,* 58**,** 77-82.

KASHUBA, A. B. & POKROVSKY, V. L. 1993. STRIPE DOMAIN-STRUCTURES IN A THIN FERROMAGNETIC FILM. *Physical Review B,* 48**,** 10335-10344.

KAY, A. L., CROOKS, S. M., DAVIES, H. N. & REYNARD, N. S. 2011. An assessment of the vulnerability of Scotland's river catchments and coasts to the impacts of climate change: Work Package 1 Report.

KELLER, A. A., WANG, H., ZHOU, D., LENIHAN, H. S., CHERR, G., CARDINALE, B. J., MILLER, R. & JI, Z. 2010. Stability and aggregation of metal oxide nanoparticles in natural aqueous matrices. *Environmental science & technology,* 44**,** 1962-1967.

KLINGELHOEFER, G., MORRIS, R. V., BERNHARDT, B., RODIONOV, D., DE SOUZA JR, P. A., SQUYRES, S. W., FOH, J., KANKELEIT, E., BONNES, U. & GELLERT, R. 2003. Athena MIMOS II Mössbauer spectrometer investigation. *Journal of Geophysical Research: Planets,* 108.

KOHOUT, T., ČUDA, J., FILIP, J., BRITT, D., BRADLEY, T., TUČEK, J., SKÁLA, R., KLETETSCHKA, G., KAŠLÍK, J., MALINA, O., ŠIŠKOVÁ, K. & ZBOŘIL, R. 2014. Space weathering simulations through controlled growth of iron nanoparticles on olivine. *Icarus,* 237**,** 75-83.

KOVALCHUK, N. M. & STAROV, V. M. 2012. Aggregation in colloidal suspensions: Effect of colloidal forces and hydrodynamic interactions. *Advances in colloid and interface science,* 179**,** 99-106.

KRACHLER, R., KRACHLER, R. F., VON DER KAMMER, F., SÜPHANDAG, A., JIRSA, F., AYROMLOU, S., HOFMANN, T. & KEPPLER, B. K. 2010. Relevance of peat-draining rivers for the riverine input of dissolved iron into the ocean. *Science of the Total Environment,* 408**,** 2402-2408.

KRACHLER, R., KRACHLER, R. F., WALLNER, G., HANN, S., LAUX, M., RECALDE, M. F. C., JIRSA, F., NEUBAUER, E., VON DER KAMMER, F. & HOFMANN, T. 2015. River-derived humic substances as iron chelators in seawater. *Marine chemistry,* 174**,** 85-93.

KRACHLER, R., KRACHLER, R. F., WALLNER, G., STEIER, P., EL ABIEAD, Y., WIESINGER, H., JIRSA, F. & KEPPLER, B. K. 2016. Sphagnum-dominated bog systems are highly effective yet variable sources of bio-available iron to marine waters. *Science of the Total Environment,* 556**,** 53-62.

KRITZBERG, E. S. & EKSTRÖM, S. M. 2012. Increasing iron concentrations in surface waters–a factor behind brownification? *Biogeosciences,* 9**,** 1465-1478.

KRITZBERG, E. S., VILLANUEVA, A. B., JUNG, M. & READER, H. E. 2014. Importance of boreal rivers in providing iron to marine waters. *PLoS One,* 9**,** e107500.

LAGLERA, L. M. & VAN DEN BERG, C. M. G. 2009. Evidence for geochemical control of iron by humic substances in seawater. *Limnology and Oceanography,* 54**,** 610-619.

LALONDE, K., MUCCI, A., OUELLET, A. & GÉLINAS, Y. 2012. Preservation of organic matter in sediments promoted by iron. *Nature,* 483**,** 198.

LANNUZEL, D., VANCOPPENOLLE, M., VAN DER MERWE, P., DE JONG, J., MEINERS, K. M., GROTTI, M., NISHIOKA, J. & SCHOEMANN, V. 2016. Iron in sea ice: Review and new insights. *Elem Sci Anth,* 4.

LARESE-CASANOVA, P., HADERLEIN, S. B. & KAPPLER, A. 2010. Biomineralization of lepidocrocite and goethite by nitrate-reducing Fe (II)-oxidizing bacteria: effect of pH, bicarbonate, phosphate, and humic acids. *Geochimica et Cosmochimica Acta,* 74**,** 3721-3734.

LAUDERDALE, J. M., BRAAKMAN, R., FORGET, G., DUTKIEWICZ, S. & FOLLOWS, M. J. 2020. Microbial feedbacks optimize ocean iron availability. *Proceedings of the National Academy of Sciences,* 117**,** 4842-4849.

LEEMAN, M., STORM, M. U. & NILSSON, L. 2015. Practical Applications of Asymmetrical Flow Field-Flow Fractionation (AF4): A Review. *LCGC Europe,* 28**,** 642-651.
LI, Q., KARTIKOWATI, C. W., HORIE, S., OGI, T., IWAKI, T. & OKUYAMA, K. 2017. Correlation between particle size/domain structure and magnetic properties of highly crystalline Fe3O4 nanoparticles. *Scientific Reports,* 7.
LI, Y.-L., ZHU, S.-Y. & DENG, K. 2011. Mössbauer hyperfine parameters of iron species in the course of Geobacter-mediated magnetite mineralization. *Physics and Chemistry of Minerals,* 38**,** 701.
LILLY, A. B. N. & DONNELLY, D. 2012. Map of soil organic carbon in top soils of Scotland. Map prepared for EU project GS-SOIL-Assessment and strategic development of INSPIRE compliant Geodata-Services for European Soil Data. ECP-2008-GEO-318004.
LIMPENS, J., BERENDSE, F., BLODAU, C., CANADELL, J. G., FREEMAN, C., HOLDEN, J., ROULET, N., RYDIN, H. & SCHAEPMAN-STRUB, G. 2008. Peatlands and the carbon cycle: from local processes to global implications–a synthesis. *Biogeosciences,* 5**,** 1475-1491.
LINDSAY, R., CHARMAN, D. J., EVERINGHAM, F., O'REILLY, R. M., PALMER, M. A., ROWELL, T. A. & STROUD, D. A. 1988. The flow country: the peatlands of Caithness and Sutherland. Joint Nature Conservation Committee.
LINGAMDINNE, L. P., CHANG, Y.-Y., YANG, J.-K., SINGH, J., CHOI, E.-H., SHIRATANI, M., KODURU, J. R. & ATTRI, P. 2017. Biogenic reductive preparation of magnetic inverse spinel iron oxide nanoparticles for the adsorption removal of heavy metals. *Chemical Engineering Journal,* 307**,** 74-84.
LIU, J., DAI, C. & HU, Y. 2018. Aqueous aggregation behavior of citric acid coated magnetite nanoparticles: Effects of pH, cations, anions, and humic acid. *Environ Res,* 161**,** 49-60.
LOH, P. S., REEVES, A. D., HARVEY, S. M., OVERNELL, J. & MILLER, A. E. J. 2008. The fate of terrestrial organic matter in two Scottish sea lochs. *Estuarine, Coastal and Shelf Science,* 76**,** 566-579.
LOHRKE, J., BRIEL, A. & MÄDER, K. 2008. Characterization of superparamagnetic iron oxide nanoparticles by asymmetrical flow-field-flow-fractionation.
LONG, G. J., CRANSHAW, T. E. & LONGWORTH, G. 1983. The ideal Mössbauer effect absorber thickness. *Mössbauer Effect Reference and Data Journal,* 6**,** 42-49.
LONG, G. J. & GRANDJEAN, F. 2003. Mössbauer Spectroscopy: Introduction.
LONG, G. J. & GRANDJEAN, F. 2013. *Mössbauer spectroscopy applied to magnetism and materials science*, Springer Science & Business Media.
LU, P., NUHFER, N. T., KELLY, S., LI, Q., KONISHI, H., ELSWICK, E. & ZHU, C. 2011. Lead coprecipitation with iron oxyhydroxide nano-particles. *Geochimica Et Cosmochimica Acta,* 75**,** 4547-4561.
LUEF, B., FAKRA, S. C., CSENCSITS, R., WRIGHTON, K. C., WILLIAMS, K. H., WILKINS, M. J., DOWNING, K. H., LONG, P. E., COMOLLI, L. R. & BANFIELD, J. F. 2013. Iron-reducing bacteria accumulate ferric oxyhydroxide nanoparticle aggregates that may support planktonic growth. *Isme Journal,* 7**,** 338-350.
LYUBUTIN, I. S., BASKAKOV, A. O., STARCHIKOV, S. S., SHIH, K.-Y., LIN, C.-R., TSENG, Y.-T., YANG, S.-S., HAN, Z.-Y., OGARKOVA, Y. L., NIKOLAICHIK, V. I. & AVILOV, A. S. 2018. Synthesis and characterization of graphene modified by iron oxide nanoparticles. *Materials Chemistry and Physics,* 219**,** 411-420.
MAGRO, M., LIGUORO, M. D., FRANZAGO, E., BARATELLA, D. & VIANELLO, F. 2018. The surface reactivity of iron oxide nanoparticles as a potential hazard for aquatic environments: A study on Daphnia magna adults and embryos. *Scientific Reports,* 8**,** 13017.
MAHMOUDI, M., SANT, S., WANG, B., LAURENT, S. & SEN, T. 2011. Superparamagnetic iron oxide nanoparticles (SPIONs): development, surface modification and applications in chemotherapy. *Advanced drug delivery reviews,* 63**,** 24-46.

MAHOWALD, N. M., BAKER, A. R., BERGAMETTI, G., BROOKS, N., DUCE, R. A., JICKELLS, T. D., KUBILAY, N., PROSPERO, J. M. & TEGEN, I. 2005. Atmospheric global dust cycle and iron inputs to the ocean. *Global biogeochemical cycles,* 19.

MAI, W. 2012. Fundamental theory of atomic force microscopy. *Recuperado el,* 4.

MANCIULEA, A., BAKER, A. & LEAD, J. R. 2009. A fluorescence quenching study of the interaction of Suwannee River fulvic acid with iron oxide nanoparticles. *Chemosphere,* 76**,** 1023-7.

MARTIN, J. H. 1990. Glacial-interglacial CO2 change: The iron hypothesis. *Paleoceanography,* 5**,** 1-13.

MARTIN, T. J., GOODHEAD, A. K., SNAPE, J. R. & DAVENPORT, R. J. 2018. Improving the ecological relevance of aquatic bacterial communities in biodegradability screening assessments. *Science of The Total Environment,* 627**,** 1552-1559.

MCCAMMON, C. A. 1994. A MOSSBAUER MILLIPROBE - PRACTICAL CONSIDERATIONS. *Hyperfine Interactions,* 92**,** 1235-1239.

MCKEE, D., CUNNINGHAM, A. & JONES, K. J. 2002. Optical and hydrographic consequences of freshwater run-off during spring phytoplankton growth in a Scottish fjord. *Journal of plankton research,* 24**,** 1163-1171.

MODENA, M. M., RÜHLE, B., BURG, T. P. & WUTTKE, S. 2019. Nanoparticle characterization: What to measure? *Advanced Materials,* 31**,** 1901556.

MORI, C., SANTOS, I. R., BRUMSACK, H.-J., SCHNETGER, B., DITTMAR, T. & SEIDEL, M. 2019. Non-conservative behavior of dissolved organic matter and trace metals (Mn, Fe, Ba) driven by porewater exchange in a subtropical mangrove-estuary. *Frontiers in Marine Science,* 6**,** 481.

MORTON, D., ROWLAND, C., WOOD, C., MEEK, L., MARSTON, C., SMITH, G., WADSWORTH, R. & SIMPSON, I. 2011. Final Report for LCM2007-the new UK land cover map. Countryside Survey Technical Report No 11/07.

MOURDIKOUDIS, S., PALLARES, R. M. & THANH, N. T. K. 2018. Characterization techniques for nanoparticles: Comparison and complementarity upon studying nanoparticle properties. *Nanoscale,* 10**,** 12871-12934.

MULLER, F. L. L. 2018. Exploring the potential role of terrestrially derived humic substances in the marine biogeochemistry of iron. *Frontiers in Earth Science,* 6**,** 159.

MULLER, F. L. L. & TANKÉRÉ-MULLER, S. P. C. 2012. Seasonal variations in surface water chemistry at disturbed and pristine peatland sites in the Flow Country of northern Scotland. *Science of the Total Environment,* 435**,** 351-362.

MULLER, F. O. L. L. & CUSCOV, M. 2017. Alteration of the copper-binding capacity of iron-rich humic colloids during transport from peatland to marine waters. *Environmental science & technology,* 51**,** 3214-3222.

MURAD, E. 2018. *Mössbauer Spectroscopy of Environmental Materials and Their Industrial Utilization*.

MURAD, E. & SCHWERTMANN, U. 1984. The influence of crystallinity on the Mössbauer spectrum of lepidocrocite. *Mineralogical Magazine,* 48**,** 507-511.

NEAMTU, M., NADEJDE, C., HODOROABA, V.-D., SCHNEIDER, R. J., VERESTIUC, L. & PANNE, U. 2018. Functionalized magnetic nanoparticles: Synthesis, characterization, catalytic application and assessment of toxicity. *Scientific Reports,* 8**,** 6278.

NISCHWITZ, V. & GOENAGA-INFANTE, H. 2012. Improved sample preparation and quality control for the characterisation of titanium dioxide nanoparticles in sunscreens using flow field flow fractionation on-line with inductively coupled plasma mass spectrometry. *Journal of Analytical Atomic Spectrometry,* 27**,** 1084-1092.

NISCHWITZ, V., GOTTSELIG, N., MISSONG, A., MEYN, T. & KLUMPP, E. 2016. Field flow fractionation online with ICP-MS as novel approach for the quantification of fine particulate carbon in stream water samples and soil extracts. *Journal of Analytical Atomic Spectrometry,* 31**,** 1858-1868.

NOVAK, P., PECHOUSEK, J., MALINA, O., NAVARIK, J. & MACHALA, L. Liquid nitrogen cryostat for the low-temperature Mössbauer spectra measurements. 2014. American Institute of Physics, 67-71.

OLDHAM, V. E., MILLER, M. T., JENSEN, L. T. & LUTHER III, G. W. 2017. Revisiting Mn and Fe removal in humic rich estuaries. *Geochimica et Cosmochimica Acta,* 209**,** 267-283.

OLEINIKOVA, O. V., SHIROKOVA, L. S., DROZDOVA, O. Y., LAPITSKIY, S. A. & POKROVSKY, O. S. 2018. Low biodegradability of dissolved organic matter and trace metals from subarctic waters. *Science of the Total Environment,* 618**,** 174-187.

OVERNELL, J., BRAND, T., BOURGEOIS, W. & STATHAM, P. J. 2002. Manganese dynamics in the water column of the upper basin of Loch Etive, a Scottish fjord. *Estuarine, Coastal and Shelf Science,* 55**,** 481-492.

PATSULA, V., MOSKVIN, M., DUTZ, S. & HORÁK, D. 2016. Size-dependent magnetic properties of iron oxide nanoparticles. *Journal of Physics and Chemistry of Solids,* 88**,** 24-30.

PHILIPPE, A. & SCHAUMANN, G. E. 2014. Interactions of dissolved organic matter with natural and engineered inorganic colloids: a review. *Environ Sci Technol,* 48**,** 8946-62.

POITRASSON, F. 2007. Does planetary differentiation really fractionate iron isotopes? *Earth and Planetary Science Letters,* 256**,** 484-492.

POKROVSKY, O. S. 2016. Measuring and Estimating Fluxes of Carbon, Major and Trace Elements to the Arctic Ocean. *In:* MUELLER, L., SHEUDSHEN, A. K. & EULENSTEIN, F. (eds.) *Novel Methods for Monitoring and Managing Land and Water Resources in Siberia.* Cham: Springer Int Publishing Ag.

POKROVSKY, O. S., DUPRE, B. & SCHOTT, J. 2005. Fe-Al-organic colloids control of trace elements in peat soil solutions: Results of ultrafiltration and dialysis. *Aquatic Geochemistry,* 11**,** 241-278.

POKROVSKY, O. S., GALY, A., SCHOTT, J., POKROVSKI, G. S. & MANTOURA, S. 2014. Germanium isotope fractionation during Ge adsorption on goethite and its coprecipitation with Fe oxy(hydr)oxides. *Geochimica Et Cosmochimica Acta,* 131**,** 138-149.

POKROVSKY, O. S., KARLSSON, J. & GIESLER, R. 2018. Freeze-thaw cycles of Arctic thaw ponds remove colloidal metals and generate low-molecular-weight organic matter. *Biogeochemistry,* 137**,** 321-336.

POKROVSKY, O. S., MANASYPOV, R. M., LOIKO, S. V. & SHIROKOVA, L. S. 2016. Organic and organo-mineral colloids in discontinuous permafrost zone. *Geochimica Et Cosmochimica Acta,* 188**,** 1-20.

POKROVSKY, O. S., SHIROKOVA, L. S., ZABELINA, S. A., VOROBIEVA, T. Y., MOREVA, O. Y., KLIMOV, S. I., CHUPAKOV, A. V., SHORINA, N. V., KOKRYATSKAYA, N. M., AUDRY, S., VIERS, J., ZOUTIEN, C. & FREYDIER, R. 2012. Size Fractionation of Trace Elements in a Seasonally Stratified Boreal Lake: Control of Organic Matter and Iron Colloids. *Aquatic Geochemistry,* 18**,** 115-139.

PONYIK, C. A., WU, D. T. & WILLIAMS, S. K. R. 2013. Separation and composition distribution determination of triblock copolymers by thermal field-flow fractionation. *Analytical and bioanalytical chemistry,* 405**,** 9033-9040.

POTAPKIN, V., CHUMAKOV, A. I., SMIRNOV, G. V., CELSE, J.-P., RUEFFER, R., MCCAMMON, C. & DUBROVINSKY, L. 2012. The Fe-57 Synchrotron Mossbauer Source at the ESRF. *Journal of Synchrotron Radiation,* 19**,** 559-569.

POULTON, S. W. & CANFIELD, D. E. 2005. Development of a sequential extraction procedure for iron: implications for iron partitioning in continentally derived particulates. *Chemical Geology,* 214**,** 209-221.

PRODAN, A. M., ICONARU, S. L., CIOBANU, C. S., CHIFIRIUC, M. C., STOICEA, M. & PREDOI, D. 2013. Iron oxide magnetic nanoparticles: characterization and toxicity evaluation by in vitro and in vivo assays. *Journal of Nanomaterials,* 2013**,** 5.

PYRZ, W. D. & BUTTREY, D. J. 2008. Particle size determination using TEM: a discussion of image acquisition and analysis for the novice microscopist. *Langmuir,* 24**,** 11350-11360.
PÉREZ-GUZMÁN, L., BOGNER, K. R. & LOWER, B. H. 2010. Earth's ferrous wheel. *Nat. Educ. Knowl,* 3**,** 32.
RAHMAN, M. M., KHAN, S. B., JAMAL, A., FAISAL, M. & AISIRI, A. M. 2011. Iron oxide nanoparticles. *Nanomaterials.* InTech.
RAISWELL, R. 2006. Towards a global highly reactive iron cycle. *Journal of Geochemical Exploration,* 88**,** 436-439.
RAISWELL, R. 2011. Iceberg-hosted nanoparticulate Fe in the Southern Ocean: Mineralogy, origin, dissolution kinetics and source of bioavailable Fe. *Deep Sea Research Part II: Topical Studies in Oceanography,* 58**,** 1364-1375.
RAISWELL, R. & CANFIELD, D. E. 2012. THE IRON BIOGEOCHEMICAL CYCLE PAST AND PRESENT. *Geochemical Perspectives,* 1**,** 1-220.
RAISWELL, R., HAWKINGS, J., ELSENOUSY, A., DEATH, R., TRANTER, M. & WADHAM, J. 2018. Iron in glacial systems: speciation, reactivity, freezing behavior, and alteration during transport. *Frontiers in Earth Science,* 6**,** 222.
RANCOURT, D. G. & PING, J. Y. 1991. Voigt-based methods for arbitrary-shape static hyperfine parameter distributions in Mössbauer spectroscopy. *Nuclear Instruments and Methods in Physics Research Section B: Beam Interactions with Materials and Atoms,* 58**,** 85-97.
RATHGEB, A., CAUSON, T., KRACHLER, R. & HANN, S. 2016. Determination of size-dependent metal distribution in dissolved organic matter by SEC-UV/VIS-ICP-MS with special focus on changes in seawater. *Electrophoresis,* 37**,** 1063-1071.
RAWAT, S., PULLAGURALA, V. L. R., ADISA, I. O., WANG, Y., PERALTA-VIDEA, J. R. & GARDEA-TORRESDEY, J. L. 2018. Factors affecting fate and transport of engineered nanomaterials in terrestrial environments. *Current Opinion in Environmental Science & Health,* 6**,** 47-53.
REICHEL, V., KOVÁCS, A., KUMARI, M., BERECZK-TOMPA, É., SCHNECK, E., DIEHLE, P., PÓSFAI, M., HIRT, A. M., DUCHAMP, M. & DUNIN-BORKOWSKI, R. E. 2017. Single crystalline superstructured stable single domain magnetite nanoparticles. *Scientific Reports,* 7**,** 45484.
REINSCH, B. C., FORSBERG, B., PENN, R. L., KIM, C. S. & LOWRY, G. V. 2010. Chemical Transformations during Aging of Zerovalent Iron Nanoparticles in the Presence of Common Groundwater Dissolved Constituents. *Environmental Science & Technology,* 44**,** 3455-3461.
RIBEIRO, J., DABOIT, K., FLORES, D., KRONBAUER, M. A. & SILVA, L. F. O. 2013. Extensive FE-SEM/EDS, HR-TEM/EDS and ToF-SIMS studies of micron-to nano-particles in anthracite fly ash. *Science of the Total Environment,* 452**,** 98-107.
RICHES, J. & DRENNAN, J. 2006. 3 - Nanostructure characterisation using electron-beam techniques. *In:* HANNINK, R. H. J. & HILL, A. J. (eds.) *Nanostructure Control of Materials.* Woodhead Publishing.
RICKARD, D. 2012. Iron isotope fractionation in sedimentary sulfides.
RIEDEL, T., ZAK, D., BIESTER, H. & DITTMAR, T. 2013. Iron traps terrestrially derived dissolved organic matter at redox interfaces. *Proceedings of the National Academy of Sciences,* 110**,** 10101-10105.
RIJKENBERG, M. J. A., MIDDAG, R., LAAN, P., GERRINGA, L. J. A., VAN AKEN, H. M., SCHOEMANN, V., DE JONG, J. T. M. & DE BAAR, H. J. W. 2014. The distribution of dissolved iron in the West Atlantic Ocean. *PloS one,* 9**,** e101323.
RUBASINGHEGE, G., LENTZ, R. W., SCHERER, M. M. & GRASSIAN, V. H. 2010. Simulated atmospheric processing of iron oxyhydroxide minerals at low pH: Roles of particle size and acid anion in iron dissolution. *Proceedings of the National Academy of Sciences of the United States of America,* 107**,** 6628-6633.

RÜFFER, R. & CHUMAKOV, A. I. 1996. Nuclear resonance beamline at ESRF. *Hyperfine Interactions,* 97**,** 589-604.
SABALE, S., KANDESAR, P., JADHAV, V., KOMOREK, R., MOTKURI, R. K. & YU, X. Y. 2017. Recent developments in the synthesis, properties, and biomedical applications of core/shell superparamagnetic iron oxide nanoparticles with gold. *Biomaterials Science,* 5**,** 2212-2225.
SAITO, M., KANAYA, T. & MASHITA, R. 2019. Synchrotron Radiation-Based Quasi-Elastic Scattering Using Mössbauer Gamma Ray with neV-Energy Resolution. *High-Resolution Inelastic X-Ray Scattering.* IntechOpen.
SALTER, I., SCHIEBEL, R., ZIVERI, P., MOVELLAN, A., LAMPITT, R. & WOLFF, G. A. 2014. Carbonate counter pump stimulated by natural iron fertilization in the Polar Frontal Zone. *Nature Geoscience,* 7**,** 885.
SALVADÓ, J. A., TESI, T., ANDERSSON, A., INGRI, J., DUDAREV, O. V., SEMILETOV, I. P. & GUSTAFSSON, Ö. 2015. Organic carbon remobilized from thawing permafrost is resequestered by reactive iron on the Eurasian Arctic Shelf. *Geophysical Research Letters,* 42**,** 8122-8130.
SASAKI, S., NAKAMURA, K., HAMABE, Y., KURAHASHI, E. & HIROI, T. 2001. Production of iron nanoparticles by laser irradiation in a simulation of lunar-like space weathering. *Nature,* 410**,** 555.
SASSI, M., PEARCE, C. I., BAGUS, P. S., ARENHOLZ, E. & ROSSO, K. M. 2017. First-Principles Fe L-2,L-3-Edge and O K-Edge XANES and XMCD Spectra for Iron Oxides. *Journal of Physical Chemistry A,* 121**,** 7613-7618.
SCHEINOST, A. C. & CHARLET, L. 2008. Selenite reduction by mackinawite, magnetite and siderite: XAS characterization of nanosized redox products. *Environmental Science & Technology,* 42**,** 1984-1989.
SCHRÖDER, C., KOHLER, I., MUELLER, F. L. L., CHUMAKOV, A. I., KUPENKO, I., RUEFFER, R. & KAPPLER, A. 2016. The biogeochemical iron cycle and astrobiology. *Hyperfine Interactions,* 237.
SCHRÖDER, C., BAILEY, B., KLINGELHOEFER, G. & STAUDIGEL, H. 2006. Fe Mössbauer spectroscopy as a tool in astrobiology. *Planetary and Space Science,* 54**,** 1622-1634.
SCHWERTMANN, U. 1991. Solubility and dissolution of iron oxides. *Plant and soil,* 130**,** 1-25.
SCOTTI, A., LIU, W., HYATT, J. S., HERMAN, E. S., CHOI, H. S., KIM, J. W., LYON, L. A., GASSER, U. & FERNANDEZ-NIEVES, A. 2015. The CONTIN algorithm and its application to determine the size distribution of microgel suspensions. *The Journal of chemical physics,* 142**,** 234905.
SHAH, N. K., IVONE, R., SHEN, J. & MEENACH, S. A. 2020. A comparison of centrifugation and tangential flow filtration for nanoparticle purification: A case study on acetalated dextran nanoparticles. *Particuology,* 50**,** 189-196.
SHENG, G., YANG, P., TANG, Y., HU, Q., LI, H., REN, X., HU, B., WANG, X. & HUANG, Y. 2016. New insights into the primary roles of diatomite in the enhanced sequestration of UO22+ by zerovalent iron nanoparticles: An advanced approach utilizing XPS and EXAFS. *Applied Catalysis B: Environmental,* 193**,** 189-197.
SHOLKOVITZ, E. R. 1978. The flocculation of dissolved Fe, Mn, Al, Cu, NI, Co and Cd during estuarine mixing. *Earth and Planetary Science Letters,* 41**,** 77-86.
SHOLKOVITZ, E. R., BOYLE, E. A. & PRICE, N. B. 1978. The removal of dissolved humic acids and iron during estuarine mixing. *Earth and Planetary Science Letters,* 40**,** 130-136.
SINGH, A. K. 2016. Chapter 4 - Experimental Methodologies for the Characterization of Nanoparticles. *Engineered Nanoparticles.* Boston: Academic Press.
SINGH, A. K., SRIVASTAVA, O. N. & SINGH, K. 2017. Shape and size-dependent magnetic properties of Fe 3 O 4 nanoparticles synthesized using piperidine. *Nanoscale research letters,* 12**,** 298.

SLAGTER, H. A., READER, H. E., RIJKENBERG, M. J. A., VAN DER LOEFF, M. R., DE BAAR, H. J. W. & GERRINGA, L. J. A. 2017. Organic Fe speciation in the Eurasian Basins of the Arctic Ocean and its relation to terrestrial DOM. *Marine Chemistry,* 197**,** 11-25.

SMEATON, C., AUSTIN, W. E. N., DAVIES, A., BALTZER, A., HOWE, J. A. & BAXTER, J. M. 2017. Scotland's forgotten carbon: a national assessment of mid-latitude fjord sedimentary carbon stocks. *Biogeosciences*.

SMIRNOV, G. V., VAN BÜRCK, U., CHUMAKOV, A. I., BARON, A. Q. R. & RÜFFER, R. 1997. Synchrotron Mössbauer source. *Physical Review B,* 55**,** 5811.

SMITA, S., GUPTA, S. K., BARTONOVA, A., DUSINSKA, M., GUTLEB, A. C. & RAHMAN, Q. 2012. Nanoparticles in the environment: assessment using the causal diagram approach. *Environmental Health,* 11**,** S13.

SOIL SURVEY OF SCOTLAND, S. 1981. Soil Maps of Scotland at a scale of 1: 250 000. Macaulay Institute for Soil Research Aberdeen.

STOLPE, B., GUO, L., SHILLER, A. M. & AIKEN, G. R. 2013. Abundance, size distributions and trace-element binding of organic and iron-rich nanocolloids in Alaskan rivers, as revealed by field-flow fractionation and ICP-MS. *Geochimica et Cosmochimica Acta,* 105**,** 221-239.

STOLPE, B., LAPWORTH, D. J., LEAD, J., GUO, L., SHILLER, A. M. & GOODDY, D. C. 2012. Iron-rich nanoparticle formation and importance for trace metal transport in groundwater and Arctic rivers.

STOOKEY, L. L. 1970. Ferrozine---a new spectrophotometric reagent for iron. *Analytical chemistry,* 42**,** 779-781.

SUN, Y. P., LI, X. Q., CAO, J. S., ZHANG, W. X. & WANG, H. P. 2006. Characterization of zero-valent iron nanoparticles. *Advances in Colloid and Interface Science,* 120**,** 47-56.

TAGLIABUE, A., BOWIE, A. R., BOYD, P. W., BUCK, K. N., JOHNSON, K. S. & SAITO, M. A. 2017. The integral role of iron in ocean biogeochemistry. *Nature,* 543**,** 51.

TAO, N. R., WANG, Z. B., TONG, W. P., SUI, M. L., LU, J. & LU, K. 2002. An investigation of surface nanocrystallization mechanism in Fe induced by surface mechanical attrition treatment. *Acta Materialia,* 50**,** 4603-4616.

TEJA, A. S. & KOH, P.-Y. 2009. Synthesis, properties, and applications of magnetic iron oxide nanoparticles. *Progress in Crystal Growth and Characterization of Materials,* 55**,** 22-45.

TEO, B. K. 2012. *EXAFS: basic principles and data analysis*, Springer Science & Business Media.

TESSIER, A., CAMPBELL, P. G. C. & BISSON, M. 1979. Sequential extraction procedure for the speciation of particulate trace metals. *Analytical chemistry,* 51**,** 844-851.

TIRAFERRI, A., CHEN, K. L., SETHI, R. & ELIMELECH, M. 2008. Reduced aggregation and sedimentation of zero-valent iron nanoparticles in the presence of guar gum. *Journal of Colloid and Interface Science,* 324**,** 71-79.

UGLOV, V. V., DOROSHEVICH, I. L., KVASOV, N. T., REMNEV, G. E. & SHYMANSKI, V. I. 2016. On physical properties of nanoparticles: size effect and scale of nanoobjects. *Physica Status Solidi C: Current Topics in Solid State Physics, Vol 13 No 10-12,* 13**,** 903-907.

VANCE, M. E., KUIKEN, T., VEJERANO, E. P., MCGINNIS, S. P., HOCHELLA, M. F., JR., REJESKI, D. & HULL, M. S. 2015. Nanotechnology in the real world: Redeveloping the nanomaterial consumer products inventory. *Beilstein J Nanotechnol,* 6**,** 1769-80.

VASYUKOVA, E. V., POKROVSKY, O. S., VIERS, J., OLIVA, P., DUPRE, B., MARTIN, F. & CANDAUDAP, F. 2010. Trace elements in organic- and iron-rich surficial fluids of the boreal zone: Assessing colloidal forms via dialysis and ultrafiltration. *Geochimica Et Cosmochimica Acta,* 74**,** 449-468.

VD KAMMER, F., BABOROWSKI, M. & FRIESE, K. 2005. Field-flow fractionation coupled to multi-angle laser light scattering detectors: applicability and analytical benefits for the analysis of environmental colloids. *Analytica chimica acta,* 552**,** 166-174.

VIOLLIER, E., INGLETT, P. W., HUNTER, K., ROYCHOUDHURY, A. N. & VAN CAPPELLEN, P. 2000. The ferrozine method revisited: Fe (II)/Fe (III) determination in natural waters. *Applied geochemistry,* 15**,** 785-790.

VON DER HEYDEN, B., ROYCHOUDHURY, A. & MYNENI, S. 2019. Iron-rich nanoparticles in natural aquatic environments. *Minerals,* 9**,** 287.

VON DER HEYDEN, B. P. & ROYCHOUDHURY, A. N. 2015. A review of colloidal iron partitioning and distribution in the open ocean. *Marine Chemistry,* 177**,** 9-19.

VON DER HEYDEN, B. P., ROYCHOUDHURY, A. N., MTSHALI, T. N., TYLISZCZAK, T. & MYNENI, S. C. B. 2012. Chemically and Geographically Distinct Solid-Phase Iron Pools in the Southern Ocean. *Science,* 338**,** 1199-1201.

WANG, H., ZHAO, X., HAN, X., TANG, Z., SONG, F., ZHANG, S., ZHU, Y., GUO, W., HE, Z., GUO, Q., WU, F., MENG, X. & GIESY, J. P. 2018. Colloidal stability of Fe3O4 magnetic nanoparticles differentially impacted by dissolved organic matter and cations in synthetic and naturally-occurred environmental waters. *Environ Pollut,* 241**,** 912-921.

WASSILKOWSKA, A., CZAPLICKA-KOTAS, A., ZIELINA, M. & BIELSKI, A. AN ANALYSIS OF THE ELEMENTAL COMPOSITION OF MICRO-SAMPLES USING EDS TECHNIQUE ANALIZA SKŁADU PIERWIASTKOWEGO W MIKROOBSZARZE PRZY UŻYCIU TECHNIKI EDS.

WAYCHUNAS, G. A., KIM, C. S. & BANFIELD, J. F. 2005. Nanoparticulate iron oxide minerals in soils and sediments: unique properties and contaminant scavenging mechanisms. *Journal of nanoparticle research,* 7**,** 409-433.

WELLS, M. L. & GOLDBERG, E. D. 1994. The distribution of colloids in the North Atlantic and Southern Oceans. *Limnology and Oceanography,* 39**,** 286-302.

WESTERHOFF, P., ATKINSON, A., FORTNER, J., WONG, M. S., ZIMMERMAN, J., GARDEA-TORRESDEY, J., RANVILLE, J. & HERCKES, P. 2018. Low risk posed by engineered and incidental nanoparticles in drinking water. *Nature Nanotechnology,* 13**,** 661.

WIESNER, M. R., LOWRY, G. V., JONES, K. L., HOCHELLA, J. M. F., DI GIULIO, R. T., CASMAN, E. & BERNHARDT, E. S. 2009. Decreasing uncertainties in assessing environmental exposure, risk, and ecological implications of nanomaterials. ACS Publications.

WIGGINTON, N. S., HAUS, K. L. & HOCHELLA JR, M. F. 2007. Aquatic environmental nanoparticles. *Journal of Environmental Monitoring,* 9**,** 1306-1316.

WU, W., HE, Q. & JIANG, C. 2008. Magnetic Iron Oxide Nanoparticles: Synthesis and Surface Functionalization Strategies. *Nanoscale Research Letters,* 3**,** 397-415.

WU, W., WU, Z., YU, T., JIANG, C. & KIM, W.-S. 2015. Recent progress on magnetic iron oxide nanoparticles: synthesis, surface functional strategies and biomedical applications. *Science and Technology of Advanced Materials,* 16**,** 023501.

YANG, R., SU, H., QU, S. & WANG, X. 2017. Capacity of humic substances to complex with iron at different salinities in the Yangtze River estuary and East China Sea. *Scientific reports,* 7**,** 1381.

YANG, S., ZONG, P., REN, X., WANG, Q. & WANG, X. 2012. Rapid and highly efficient preconcentration of Eu(III) by core-shell structured Fe3O4@humic acid magnetic nanoparticles. *ACS Appl Mater Interfaces,* 4**,** 6891-900.

YANG, Y. & WESTERHOFF, P. 2014. Presence in, and Release of, Nanomaterials from Consumer Products. *In:* CAPCO, D. G. & CHEN, Y. (eds.) *Nanomaterial: Impacts on Cell Biology and Medicine.* Berlin: Springer-Verlag Berlin.

YOUNG, R. J. & MOORE, M. V. 2005. Dual-beam (FIB-SEM) systems. *Introduction to Focused Ion Beams.* Springer.

YÜCEL, M., GARTMAN, A., CHAN, C. S. & LUTHER III, G. W. 2011. Hydrothermal vents as a kinetically stable source of iron-sulphide-bearing nanoparticles to the ocean. *Nature Geoscience,* 4**,** 367.

ZACHARA, J. M., KUKKADAPU, R. K., FREDRICKSON, J. K., GORBY, Y. A. & SMITH, S. C. 2002. Biomineralization of poorly crystalline Fe(III) oxides by dissimilatory metal reducing bacteria (DMRB). *Geomicrobiology Journal,* 19**,** 179-207.

ZHAN, H., BIAN, Y. N., YUAN, Q., REN, B. Z., HURSTHOUSE, A. & ZHU, G. C. 2018. Preparation and Potential Applications of Super Paramagnetic Nano-Fe3O4. *Processes,* 6.

ZHANG, S., WANG, S. & SHAN, X.-Q. 2001. Effect of sample pretreatment upon the metal speciation in sediments by a sequential extraction procedure. *Chemical Speciation & Bioavailability,* 13**,** 69-74.

ZHANG, X., LIN, S., CHEN, Z. L., MEGHARAJ, M. & NAIDU, R. 2011. Kaolinite-supported nanoscale zero-valent iron for removal of Pb2+ from aqueous solution: Reactivity, characterization and mechanism. *Water Research,* 45**,** 3481-3488.

ZHU, W. Z., YANG, G. P. & ZHANG, H. H. 2017. Photochemical behavior of dissolved and colloidal organic matter in estuarine and oceanic waters. *Sci Total Environ,* 607-608**,** 214-224.

ZIRKLER, D., LANG, F. & KAUPENJOHANN, M. 2012. "Lost in filtration"—The separation of soil colloids from larger particles. *Colloids and Surfaces A: Physicochemical and Engineering Aspects,* 399**,** 35-40.

7. Appendices

7.2 Appendices for Chapter 2

Table 7.1. Iron bearing nanoparticles: considerations for choice of characterisation techniques and instrumentation. All searches were conducted over timespan 1900 to 2020 inclusive. The table reflects citations to source items indexed within Web of Science Core Collection and limited to the top 50 cited highest times cited where returned results exceeded n=50. Instruments and techniques included are compiled from those cited in the discovered literature.

Search terms by topic(s)	Instrument or technique
Mineralogy (*mineralogy* refined by: *techniques* AND *bulk characterization*)	Powder X-ray diffraction (XRD), transmission electron microscopy (TEM), X-ray computed tomography (CT) & μCT, visible and near-infrared reflectance spectroscopy (VNIR), Wavelength-Dispersive X-ray fluorescence (WD-XRF), Fourier-transform infrared spectroscopy (FTIR), mineralogy mapping using Energy-Dispersive Scanning Electron Microscopy (EDS-SEM/SEM-EDX/SEM-EDS), X-ray absorption spectroscopies (XAS) e.g. X-ray Absorption Near-Edge Structure (XANES), EXAFS techniques, X-ray microprobe techniques, infrared Raman spectroscopies, nuclear and magnetic spectroscopies, low-energy electron diffraction, X-ray reflectivity, X-ray standing wave methods, X-ray photoelectron and Auger electron spectroscopies, secondary ion mass spectrometry, scanning tunnelling and atomic force microscopies, laser confocal microscopy, environmental scanning electron microscopy,

	sequential extraction techniques, Mössbauer spectroscopy, Thermogravimetric Analysis.
Nanoparticle mineralogy *(mineralogy refined by: particles AND techniques AND characterization AND nanoparticles)*	XRD (μXRD), FTIR, SEM-EDX, Raman spectroscopy, Mössbauer spectroscopy, microscopy techniques, standard mineral magnetic techniques, XAS methods (XANES, EXAFS), TEM, Scanning transmission electron microscopy (STEM), Focused ion beam–scanning electron microscopy (FIB–SEM), micro X-ray fluorescence, High Resolution-Transmission Electron microscopy (HR-TEM)/EDS/selected-area diffraction pattern (SAED), Field Emission-Scanning Electron Microscopy (FE-SEM)/EDS) analysis, Electron probe micro-analyser (EPMA)(with WDS), sequential extraction techniques.
Environmental nanoparticle (mineralogy) *(environmental nanoparticles refined by mineralogy AND characterisation)*	XRD, HR-TEM, HR-TRM/EDS/SAED, Raman spectroscopy, FE-SEM, NMR, Mössbauer spectroscopy, synchrotron methods (including (μ-) XRD, XRF, XAS), infrared techniques, X-ray microprobe techniques, nuclear and magnetic spectroscopies Particle-induced X-ray emission (PIXE), scanning tunnelling and atomic force microscopies, FIB, AFM.
Iron bearing nanoparticles (mineralogy) *(nanoparticles refined by iron AND mineralogy)*	scanning electron microscopy (SEM), TEM/HR-TEM/STEM (mode), electron microprobe, X-ray diffraction (XRD including μ-), X-ray absorption fine structure (XAFS) spectroscopy (including XANES and EXAFS), sequential extraction techniques, synchrotron X-ray total scattering, low temperature magnetic measurements, Mössbauer spectroscopy, (microscopic) XRF, Electron energy-loss spectroscopy (e.g. TEM-EDS & EELS), XPS, NMR, AFM.

Iron bearing environmental nanoparticles (mineralogy) *(environmental nanoparticles OR natural nanoparticles refined by iron AND mineralogy)*	Microfocused XAFS (e.g. μ-EXAFS, μ-XANES) XAS methods (EXAFS, XANES), (μ-)XRF, (μ-)XRD, TEM, HR-TEM, FE-SEM, NMR, Scanning Transmission X-ray Microscopy (STXM), Mössbauer spectroscopy and Synchrotron Mössbauer techniques (SMS).
Iron bearing nanoparticles in aquatic environments (mineralogy) **(***nanoparticles refined by iron AND aquatic AND environment AND natural)*	XAS and μXAS techniques, Mössbauer spectroscopy and Synchrotron Mössbauer techniques (SMS).

7.2.1 **Abbreviations list for Table 2.2**

Transmission electron microscopy (**TEM**), X-ray powder diffraction (µXRD), Dynamic light scattering (**DLS**), Nanoparticle tracking analysis (**NTA**), High resolution-Transmission electron microscopy (**HR-TEM**), Scanning electron microscopy (**SEM**), Atomic Force Microscopy (**AFM**), X-ray Absorption Spectroscopy (**XAS**), Extended X-ray absorption fine structure (**EXAFS**), Near edge X-ray absorption fine structure (**XANES**), Ferromagnetic resonance (**FMR**), Differential centrifugal sedimentation (**DCS**), Inductively coupled plasma mass spectrometry (**ICP-MS**), Ultraviolet–visible spectroscopy (**UV-Vis**), Matrix-assisted laser desorption/ionization (**MALDI**), Nuclear magnetic resonance spectroscopy (**NMR**), Tunable Resistive Pulse Sensing (**TRPS**), Elliptically polarized light

scattering (**EPLS**), X-ray photoelectron spectroscopy (**XPS**), ICP- Optical Emission Spectrometry (**ICP-OES**), SEM-Energy-dispersive X-ray spectroscopy (**SEM-EDX**), Magnetic force microscopy (**MFM**), Low-energy ion scattering (**LEIS**), Scanning Transmission Electron Microscopy (**STEM**), Small-Angle X-ray Scattering (**SAXS**), Nanoparticle tracking analysis (**NTA**), Differential thermal analysis (**DTA**), Electron energy loss spectroscopy (**EELS**), Fourier transformation infrared spectroscopy (**FTIR**), Secondary ion mass spectrometry (**SIMS**), Thermogravimetric analysis (**TGA**), Magnetic small-angle neutron scattering (**SANS**), Brunauer, Emmett and Teller theory (**BET**), Electrophoretic mobility (**EPM**), Resonant Mass Measurement-Micro Electro-Mechanical Systems (**RMM-MEMS**), Particle tracking analysis (**PTA**), Differential centrifugal sedimentation (**DCS**), Sp-ICP-MS, electron backscatter diffraction (**EBSD**), UV-vis-near-IR spectroscopy (**UV-Vis-NIR**), Electron energy loss spectroscopy-Scanning Transmission Electron Microscopy (**EELS-STEM**), superconducting quantum interference device (**SQUID**), Vibrating Sample Magnetometer (**VSM**), X-ray magnetic circular dichroism (**XMCD**), Asymmetrical flow field-flow fractionation (**AF^4**).

7.3 Appendices for Chapter 3

7.3.1 Physical size parameters

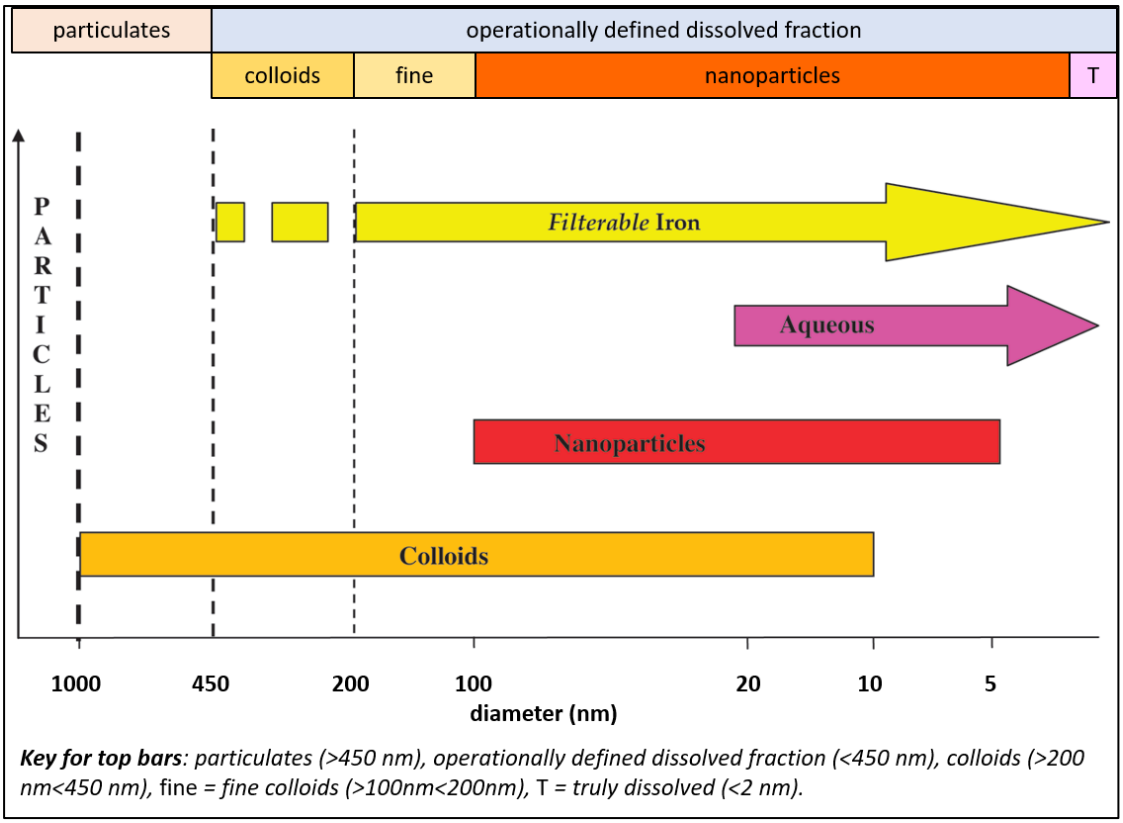

***Key for top bars**: particulates (>450 nm), operationally defined dissolved fraction (<450 nm), colloids (>200 nm<450 nm),* fine *= fine colloids (>100nm<200nm),* T *= truly dissolved (<2 nm).*

Figure 7.1. Operationally defined physical size fractions: *filterable iron* diagram, adapted from Raiswell and Canfield (2012). Physical size fractions as defined by Raiswell and Canfield (2012) are shown in the bottom section of the diagram and the top two bars show the defined physical size fractions relative to this study.

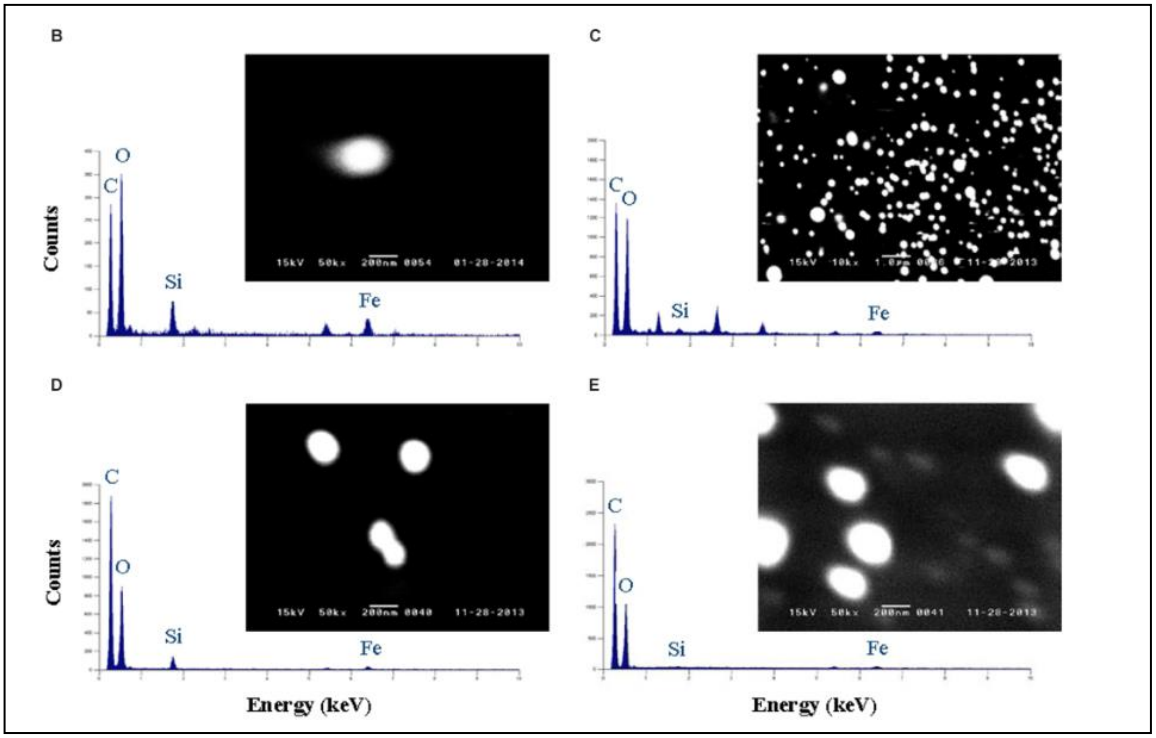

Figure 7.2. Spherical particles detected and measured by Muller and Cuscov (2017): ***images are Wet scanning electron microscopy (WETSEM) showing aquatic organic colloids and are accompanied in each figure (labelled B to E) with the corresponding energy dispersive X-ray analysis (EDXA) for water samples collected from River Thurso catchment and its estuary: 0 psu (images C and E) and at 30 psu (images B and D)*** **(Muller and Cuscov, 2017).**

7.3.2 **Acid Digest**

Protocols provided by SAMS

Unless otherwise indicated, hotplate temperature is 120 °C. Acid-cleaned 15 mL Teflon vials with 6 M hydrochloric acid (HCl) were leached on the hotplate for min 30 mins, followed by rinsing in DI. The vials were left to dry on the outside. Samples were shaken to suspend all particles and an aliquot 10 ml into 15 ml Teflon vial. This was evaporated to dryness on the hotplate (~24 hours). High purity reagents were used throughout the following processes.

Removal of organics

Organics were removed by adding concentrated hydrogen peroxide (H_2O_2) to the cold sample vials, loosely capped and left to react for approximately 30 mins, capped and fluxed for 30 mins (checked for gas build up) then left to flux on hotplate overnight. Samples were then evaporated to dryness.

Digestion of silicates

Concentrated hydrofluoric acid (HF) and concentrated nitric acid (HNO_3) were added to the sample vials in a 4:1 ratio, capped tightly and fluxed for 2 days then evaporated to dryness. Concentrated HNO_3 (0.2 mL) was added, dried down and repeated twice more. The vial was left to cooldown, 5 ml 2% HNO_3 and indium aliquot, capped tightly and fluxed for 30 mins. Once the samples were checked for full digestion.

7.3.3 Ferrozine assay calibration curves

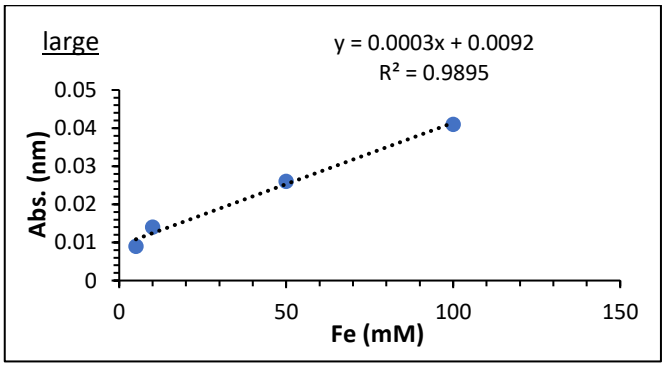

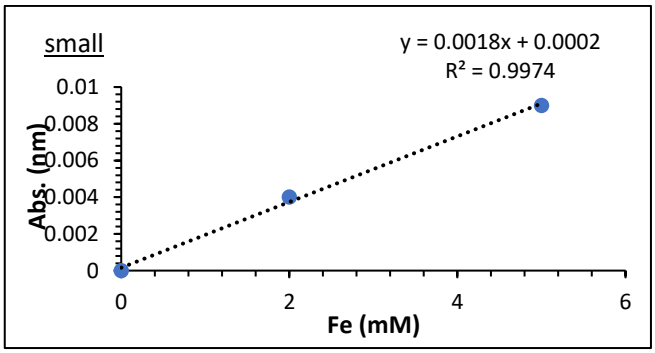

Figure 7.3. Ferrozine assay calibration curves.

7.4 Appendices for Chapter 4

7.4.1 **AF^4- ICP-MS elution times.** Injection volume = 0.005 L (Gottselig et al., 2014, Nischwitz et al., 2016).

fraction name	physical size	peak name	elution time (s)
1st fraction	1 kDa (approximately 1.2 nm) to 20 nm	1st peak	32.0 to 39.9
2nd fraction	greater than 20 nm, less than 60 nm	2nd peak	40.0 to 59.9
3rd fraction	greater than 60 nm	3rd peak	60.0 to 95.0

Calibration data regression parameters for AF^4 data:

AF^4 data (standards matrix) (Nischwitz and Goenaga-Infante, 2012).

Calibration data					Reference	V.Nischwitz, H. Goenaga-Infante		J. Anal. At. Spectrom., 2012, 27, 1084–1092	
Regression Parameters									
	Al27	Si28	Si29	P31	Ca43	Ca44	Mn55	Fe56	Fe57
Slope	268.539569	106.72852	6.1294357	20.48843	1.823695	29.42658	3202.503	4034.657	87.8326245
Intercept	270.693762	145.93617	4.3292005	20.42636	-3.368008	-48.06286	3206.7951	-2897.292	-27.731126
Flow rates:									
HPLC					f_H	0.5	mL/min		
Post-Col.	0.2	mL	4.9166667	min	f_A	0.041	mL/min		

7.5 Appendices for Chapter 5

7.5.1 Mass absorption coefficients

Table 7.2. Mass absorption coefficients from Gütlich (2010): '*Values taken from Long, G.J., Cranshaw, T.E., Longworth, G.: In: Stevens, J.G., Stevens, V.E., White, R.M., Gibson, J.L. (eds.) Mössbauer Effect Reference and Data Journal, p. 42. Mössbauer Effect Data Center, North Carolina (1983)*'.

Atom	No.	Mass (Da)	μ_e (cm^2 g^{-1})	Atom	No.	Mass (Da)	μ_e (cm^2 g^{-1})
H	1	1.008	0.387	Tc	43	98.91	35.5
He	2	4.003	0.194	Ru	44	101.07	37.5
				Rh	45	102.91	38
Li	3	6.941	0.23	Pd	46	106.4	41
Be	4	9.012	0.32	Ag	47	107.87	44
B	5	10.810	0.51	Cd	48	112.41	46
C	6	12.011	0.87				
N	7	14.007	1.4	In	49	114.82	49
O	8	15.999	2.2	Sn	50	118.69	54
F	9	18.998	2.7	Sb	51	121.75	56
Ne	10	20.179	4.0	Te	52	127.60	60
				I	53	126.91	61
Na	11	22.990	5.2	Xe	54	131.30	67
Mg	12	24.305	6.8				
Al	13	26.982	9.0	Cs	55	132.91	71
Si	14	28.086	12.4	Ba	56	137.33	75
P	15	30.974	14.2	La	57	138.91	76
S	16	32.062	17.0	Ce	58	140.12	77
Cl	17	35.453	20.0	Pr	59	140.10	81
Ar	18	39.948	21.0	Nd	60	144.24	88
				Pm	61	(145)	92
K	19	39.098	27.0	Sm	62	150.42	96
Ca	20	40.080	32.5				
Sc	21	44.956	33	Eu	63	151.96	100
Ti	22	47.900	42	Gd	64	157.25	104
V	23	50.941	43	Tb	65	158.93	107
Cr	24	51.996	48	Dy	66	162.50	110
M	25	54.938	53	Ho	67	164.93	115
Fe	26	55.847	64	Er	68	167.26	120
Co	27	58.933	66	Tm	69	168.93	127
Ni	28	58.700	75	Yb	70	173.04	133
Cu	29	63.546	82	Lu	71	174.97	139
Zn	30	65.380	92				
				Hf	72	178.49	145
Ga	31	69.72	97	Ta	73	180.95	150
Ge	32	72.59	102	W	74	183.85	155
As	33	74.92	126	Re	75	186.20	160
Se	34	78.96	110	Os	76	190.23	165
Br	35	79.90	130	Ir	77	192.22	172
Pb	82	207.2	120	Pt	78	195.09	178
Kr	36	83.80	126	Au	79	196.96	191
				Hg	80	200.59	165
Rb	37	85.47	21.0				
Sr	38	87.62	24.5	Tl	81	204.37	123
				Pb	82	207.2	120
Y	39	88.91	26.0	Bi	83	208.98	123
Zr	40	91.22	28.0	Po	84	(209)	126
Nb	41	92.91	29.5	At	85	(210)	140
Mo	42	95.94	34.0	Rn	86	(222)	60

7.5.2 **Cryostat mount – technical drawings: Oxygen-free high thermal conductivity (OFHC) copper sample holder/mount and clamp for cryostat (drawings produced by ID18, ESRF, Grenoble in collaboration).**

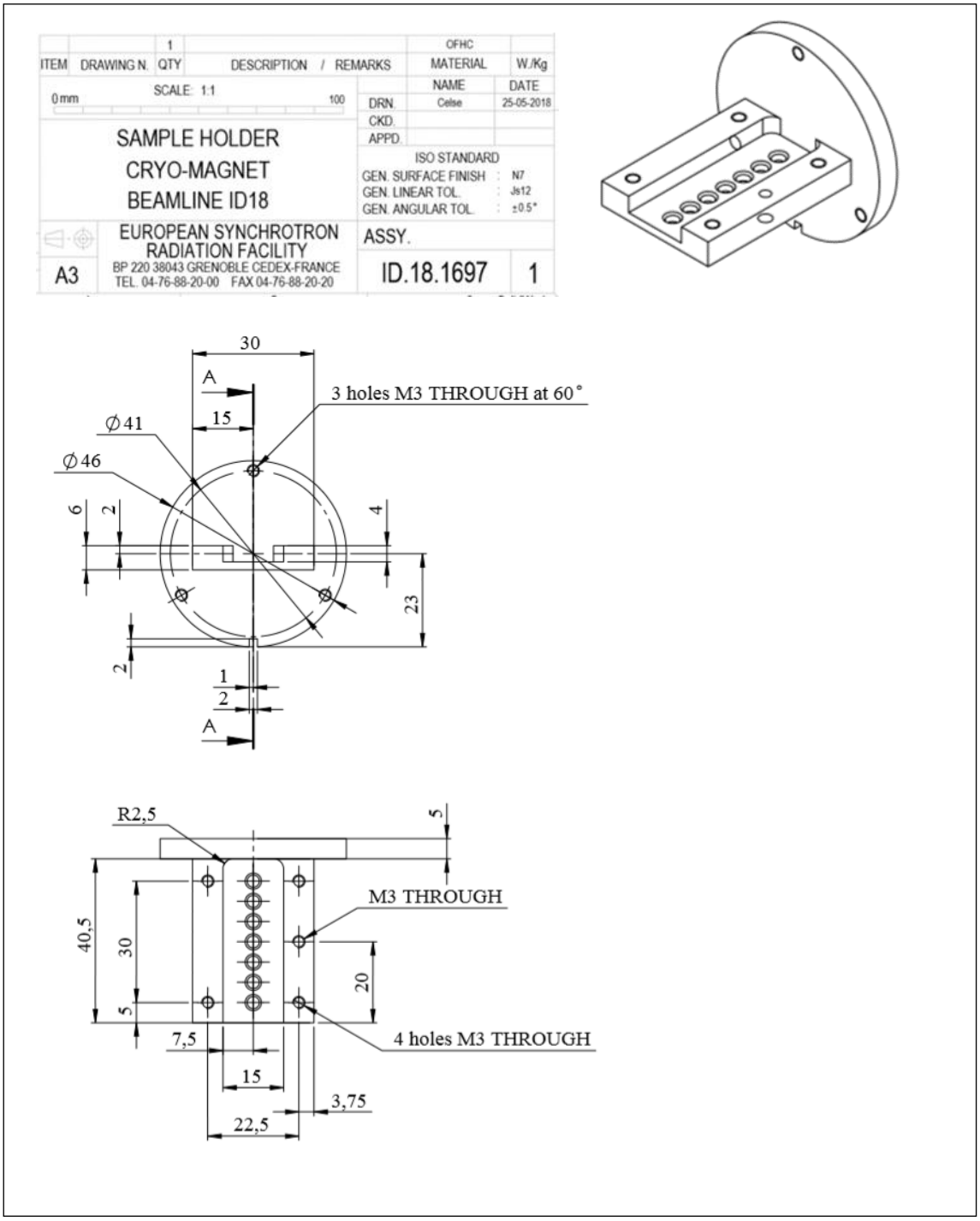

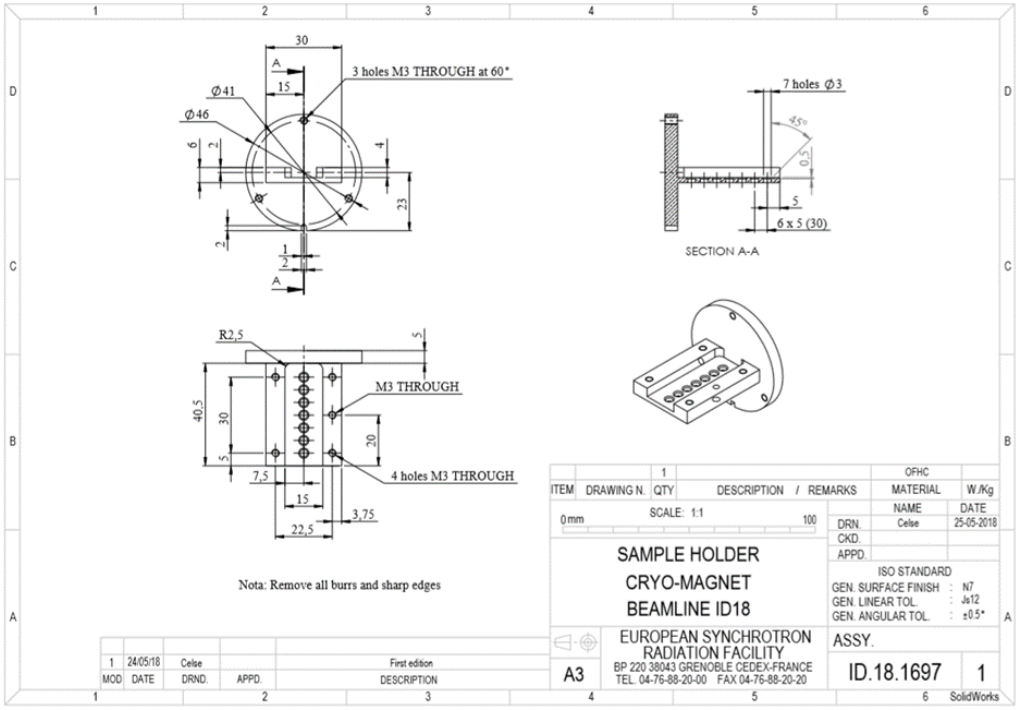
30
3 holes M3 THROUGH at 60°
Ø41
Ø46
7 holes Ø3
45°
SECTION A-A
6 x 5 (30)
R2,5
M3 THROUGH
4 holes M3 THROUGH
Nota: Remove all burns and sharp edges
SAMPLE HOLDER
CRYO-MAGNET
BEAMLINE ID18
EUROPEAN SYNCHROTRON RADIATION FACILITY
BP 220 38043 GRENOBLE CEDEX-FRANCE
TEL. 04-76-88-20-00 FAX 04-76-88-20-20
ASSY.
ID.18.1697
A3
SCALE: 1:1
ISO STANDARD
GEN. SURFACE FINISH : N7
GEN. LINEAR TOL. : Js12
GEN. ANGULAR TOL. : ±0.5°
First edition
SolidWorks

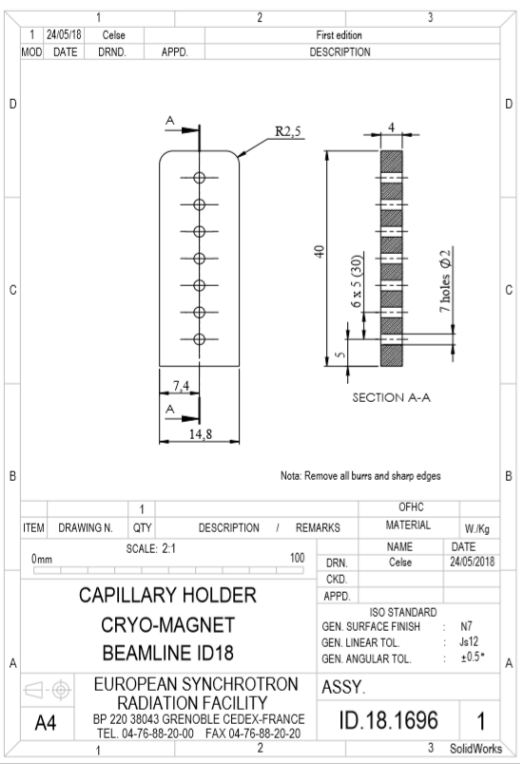
R2,5
7,4
14,8
4
40
6 x 5 (30)
7 holes Ø2
SECTION A-A
Nota: Remove all burns and sharp edges
CAPILLARY HOLDER
CRYO-MAGNET
BEAMLINE ID18
EUROPEAN SYNCHROTRON RADIATION FACILITY
BP 220 38043 GRENOBLE CEDEX-FRANCE
TEL. 04-76-88-20-00 FAX 04-76-88-20-20
ASSY.
ID.18.1696
A4
SCALE: 2:1
ISO STANDARD
GEN. SURFACE FINISH : N7
GEN. LINEAR TOL. : Js12
GEN. ANGULAR TOL. : ±0.5°
First edition
SolidWorks

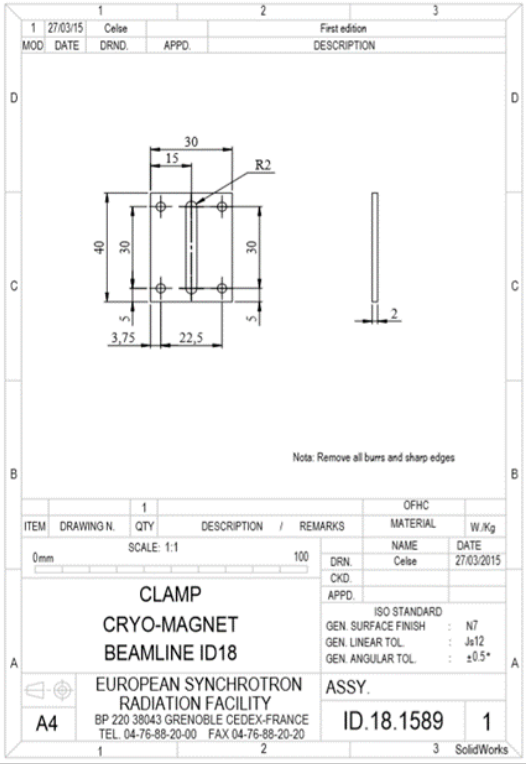
30
15
R2
40
30
3,75
22,5
2
Nota: Remove all burns and sharp edges
CLAMP
CRYO-MAGNET
BEAMLINE ID18
EUROPEAN SYNCHROTRON RADIATION FACILITY
BP 220 38043 GRENOBLE CEDEX-FRANCE
TEL. 04-76-88-20-00 FAX 04-76-88-20-20
ASSY.
ID.18.1589
A4
SCALE: 1:1
ISO STANDARD
GEN. SURFACE FINISH : N7
GEN. LINEAR TOL. : Js12
GEN. ANGULAR TOL. : ±0.5°
First edition
SolidWorks

7.5.3 **EV-310, SMS lab book. ID18, ESRF, July 2018.**

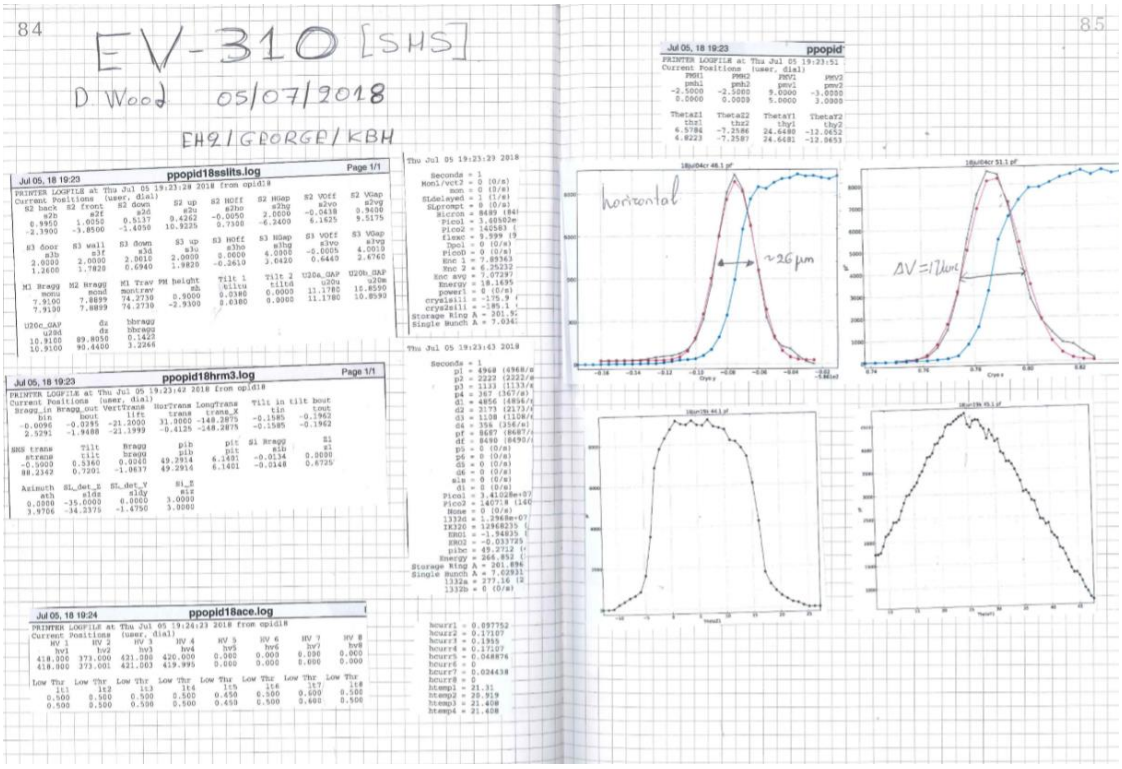

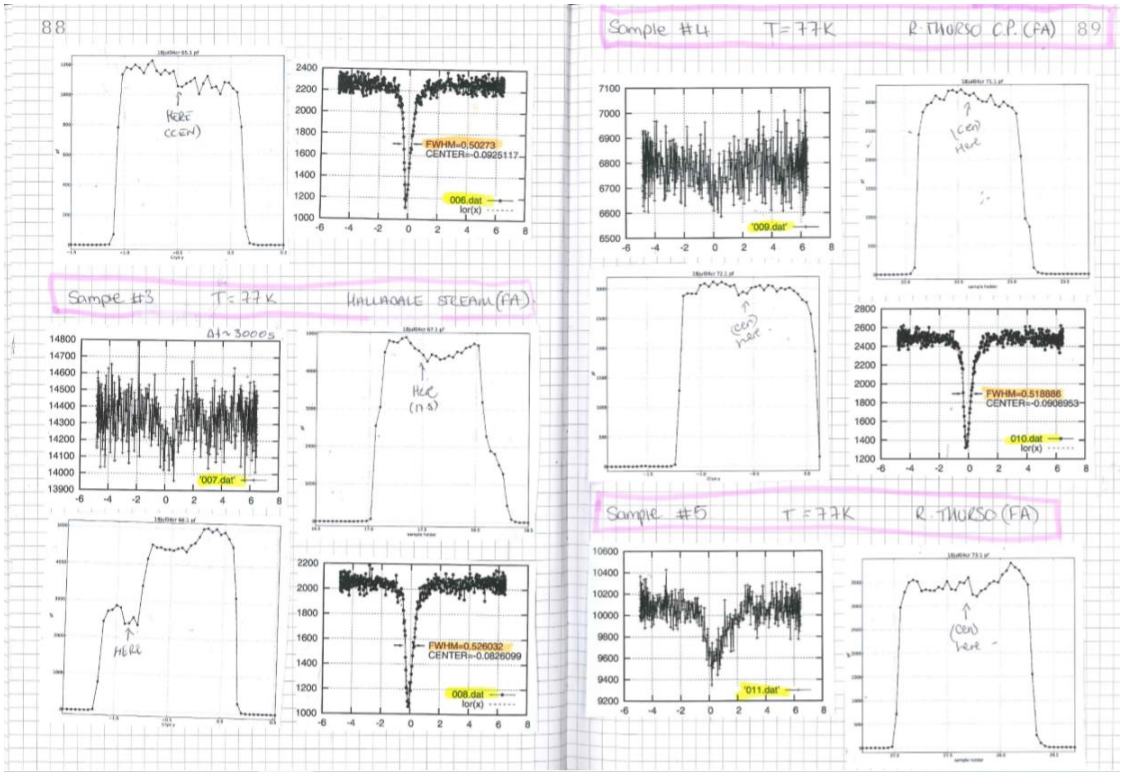
88
Sample #3 T=77K HALLADALE STREAM (FA)
Δt ~ 3000s
FWHM=0.50273
CENTER=-0.0925117
006.dat
007.dat
008.dat
FWHM=0.526032
CENTER=-0.0826099
Sample #4 T=77K R. THURSO C.P. (FA) 89
009.dat
010.dat
FWHM=0.518886
CENTER=-0.0906953
Sample #5 T=77K R. THURSO (FA)
011.dat

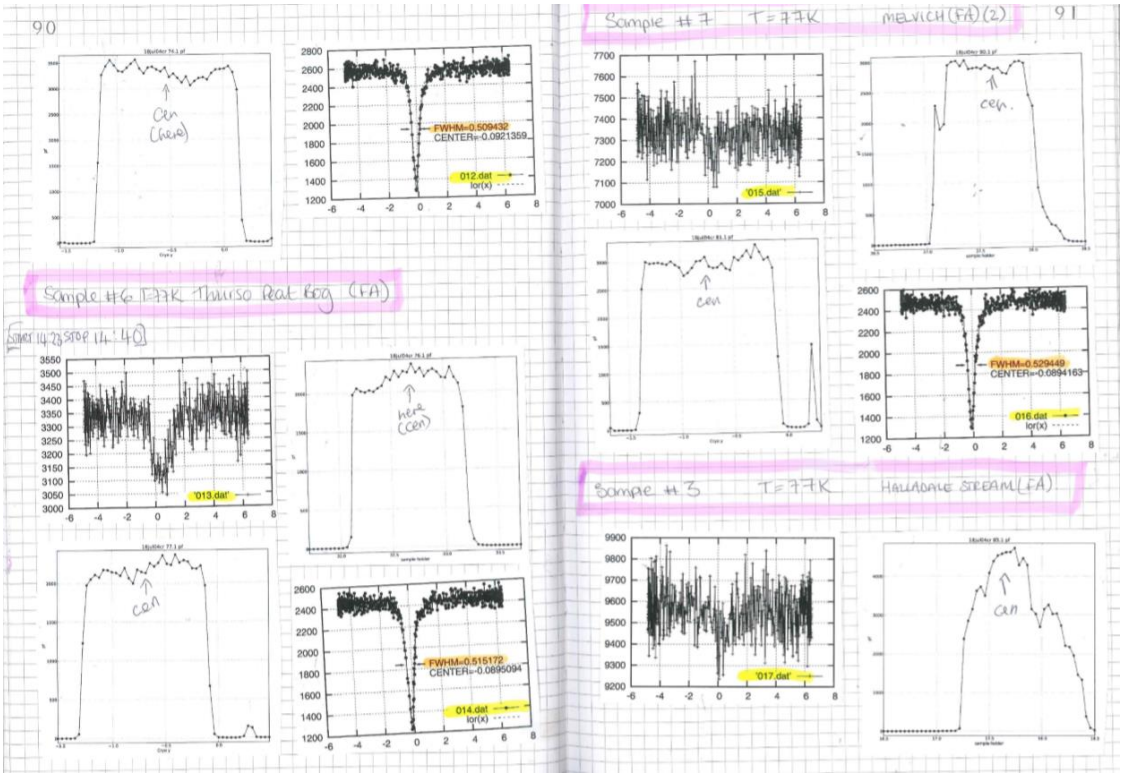
90
Sample #6 T=77K Thurso Peat Bog (FA)
FWHM=0.509432
CENTER=-0.0921359
012.dat
013.dat
014.dat
FWHM=0.515172
CENTER=-0.0895094
Sample #7 T=77K MELVICH (FA) (2) 91
015.dat
016.dat
FWHM=0.529449
CENTER=-0.0894163
Sample #3 T=77K HALLADALE STREAM (FA)
017.dat

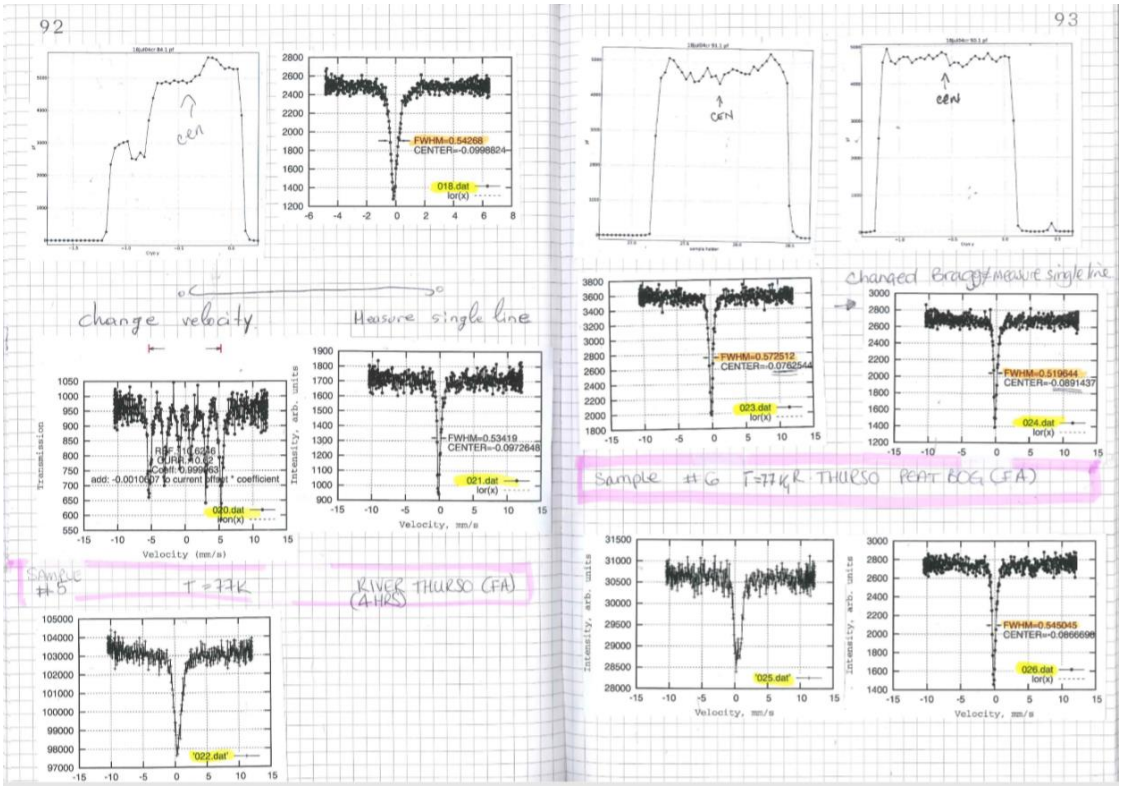
92
CEN
FWHM=0.54268
CENTER=-0.0998824
018.dat
lor(x)
change velocity
Measure single line
Transmission
Intensity, arb. units
RBF: 1.106238
CURR: 4.0.03
Coeff: 0.999963
add: -0.0010007 to current offset * coefficient
020.dat
lor(x)
Velocity (mm/s)
FWHM=0.53419
CENTER=-0.0972648
021.dat
lor(x)
Velocity, mm/s
Sample #5 T=77K
RIVER THURSO (FA)
(4 HRS)
'022.dat'
93
CEN
CEN
changed Bragg & measure single line
FWHM=0.572512
CENTER=-0.0762544
023.dat
lor(x)
FWHM=0.519644
CENTER=-0.0891437
024.dat
lor(x)
Sample #6 T=77K R. THURSO PEAT BOG (FA)
Intensity, arb. units
'025.dat'
Velocity, mm/s
FWHM=0.545045
CENTER=-0.0866698
026.dat
lor(x)
Velocity, mm/s

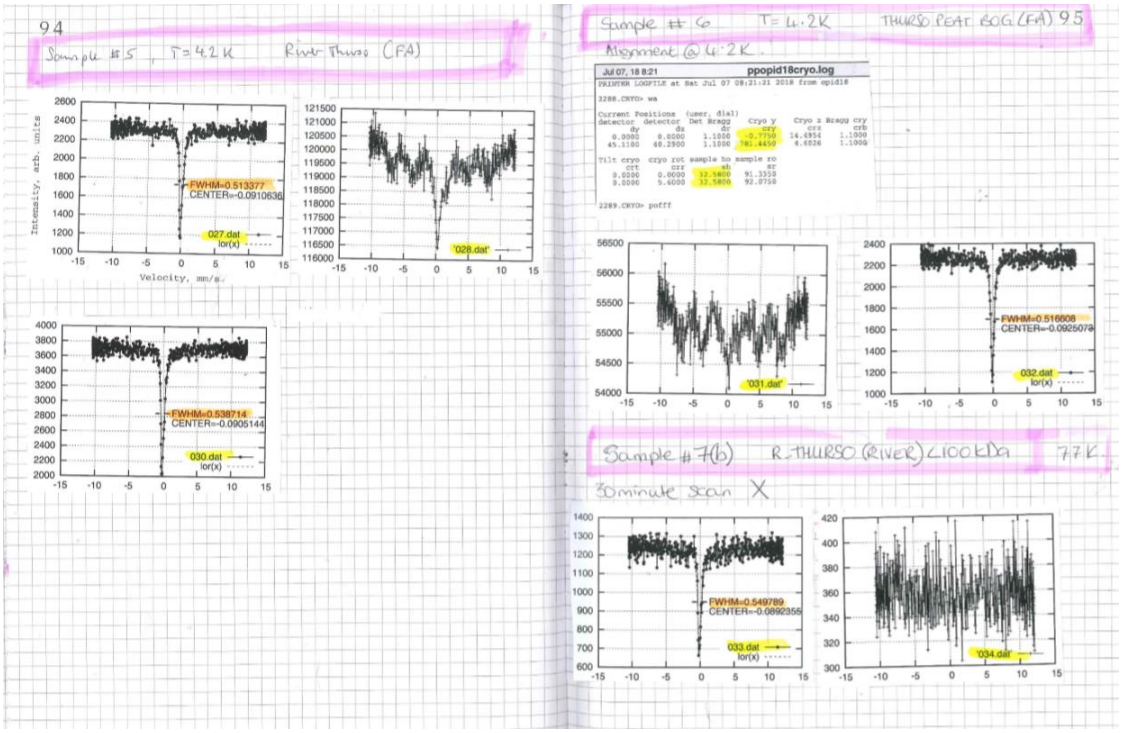
94
Sample #5 T=4.2K River Thurso (FA)
Intensity, arb. units
FWHM=0.513377
CENTER=-0.0910636
027.dat
lor(x)
Velocity, mm/s
'028.dat'
FWHM=0.538714
CENTER=-0.0905144
030.dat
lor(x)
Sample #6 T=4.2K THURSO PEAT BOG (FA) 95
Alignment @ 4.2K
Jul 07, 18 8:21 ppopid18cryo.log
PRINTER LOGFILE at Sat Jul 07 08:21:21 2018 from opid18
2288.CRYO> wa
Current Positions (user, dial)
Detector detector Det Bragg Cryo y Cryo z Bragg cry
dy da dc cry crz crb
0.0080 0.8080 1.1000 -0.7750 14.4954 1.1000
45.3180 40.2900 1.1000 701.4450 4.6026 1.1000
Tilt cryo cryo rot sample ho sample ro
crt crz sh sr
0.0090 0.0090 32.5800 91.3350
9.0090 5.6000 32.5800 92.0750
2289.CRYO> pofff
'031.dat'
FWHM=0.516608
CENTER=-0.0925079
032.dat
lor(x)
Sample #7(b) R. THURSO (RIVER) 2100KDa 77K
30minute scan X
FWHM=0.549789
CENTER=-0.0892355
033.dat
lor(x)
'034.dat'

96

Sample #3(b) Thuesо RWER c100kDa
(* burst capillary in liquid nitrogen) 77K

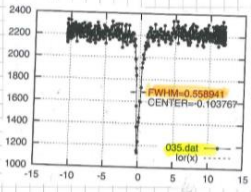

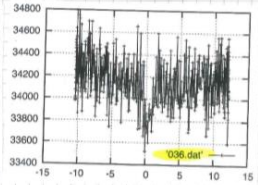

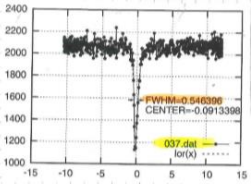

Sample#3(b) T=47K Thuzso RIVER c100kDa

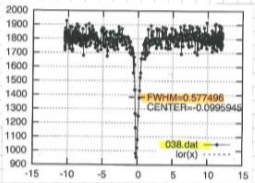

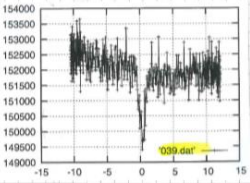

97